清華大學
Tsinghua University

香港科技大學
THE HONG KONG
UNIVERSITY OF SCIENCE
AND TECHNOLOGY

CSVE

The 1st International Symposium on Soil Dynamics and Geotechnical Sustainability

7-9th August 2016, HKUST, Hong Kong

Editors: Gang Wang, Ga Zhang and Duruo Huang
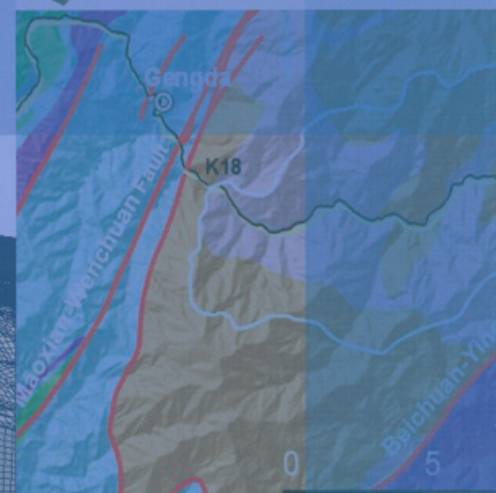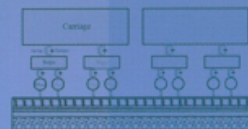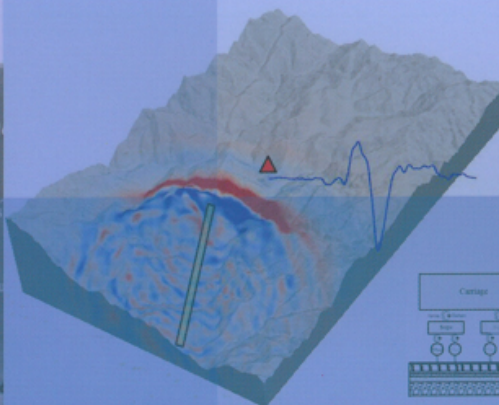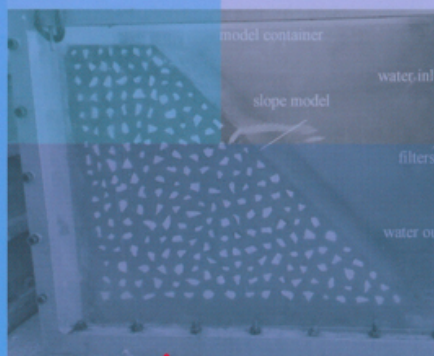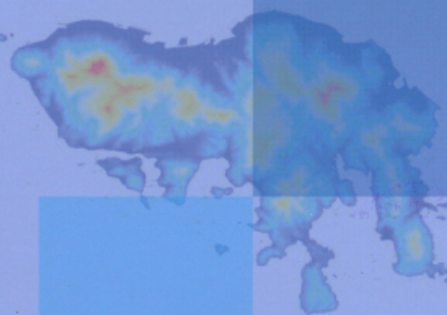
The 1st International Symposium on Soil Dynamics and Geotechnical Sustainability

Editors

Gang Wang

The Hong Kong University of Science and Technology

Ga Zhang

Tsinghua University

Duruo Huang

The Hong Kong University of Science and Technology

Preface

The 1st International Symposium on Soil Dynamics and Geotechnical Sustainability (ISSDGS 2016) was held successfully on August 7-9, 2016 at the Hong Kong University of Science and Technology. The event was jointly organized by HKUST, Tsinghua University, the Soil Dynamics Committee of the Chinese Society for Vibration Engineering, and Chinese Institution of Soil Mechanics and Geotechnical Engineering, China Civil Engineering Society. The Symposium was also supported by TC203 (Geotechnical Earthquake Engineering) and TC210 (Dams & Embankments) of the International Society for Soil Mechanics and Geotechnical Engineering (ISSMGE), American Society of Civil Engineers Hong Kong Section, Hong Kong Institute of Engineers Geotechnical Division, Hong Kong Geotechnical Society, Institution of Civil Engineers Hong Kong Association, and Hong Kong Society of Theoretical and Applied Mechanics. The financial support from K.C. Wong Education Foundation, HKUST Jockey Club Institute for Advanced Study is highly appreciated.

The last decades have seen tremendous development of civil infrastructure around the world. It has become increasingly important to improve the sustainability of geotechnical systems for harmonious development of man and nature, especially in face of the frequent occurrences of natural disasters. The theme of the symposium focused on the challenges and opportunities in soil dynamics for geotechnical sustainability and resilience. The symposium provided an excellent opportunity for researchers and engineers in different areas to meet and share new ideas, achievements, experiences and lessons through presentations and discussions. Among those who participated in the symposium were many prominent scholars from the United States, Japan, the United Kingdom, Canada, Indian, Iran and China. As HKUST is striving to become a global leader in sustainability education and research, the campus is just the appropriate venue to host such a timely event.

The symposium consisted of two plenary lectures, 11 invited keynote lectures, 19 invited theme lectures and many other technical presentations on a variety of scientific topics in the frontiers of soil dynamics and geotechnical sustainability, including: seismic hazard and geo-risk analysis, seismic reconnaissance and post-earthquake reconstruction of key infrastructure, ground failure, slope stability, liquefaction of soils, seismic analysis and design of geotechnical systems, modeling cyclic behavior of soils, soil-structure interaction analysis, failure mechanism, physical and numerical modeling of localized deformation in geomaterials, landslide and debris flow dynamics and mitigation, innovative and sustainable construction technology as well as offshore geotechnics. The credit goes to all authors and presenters who made the symposium a successful event. We are also grateful to faculty, staff and students of the Department of Civil and Environmental Engineering, HKUST, and colleagues from the Department of Hydraulic Engineering, Tsinghua University. It is their contributions and support that made organising the symposium a most rewarding experience.

Gang Wang and Ga Zhang

Chairman of the Organising Committee

ORGANISATION

Symposium Chairman

Prof. Ga Zhang, Tsinghua University, China
Prof. Gang Wang, HKUST, HKSAR

Secretary General

Dr. Duruo Huang, HKUST, HKSAR

International Advisory Committee

Prof. Brendon Bradley, University of Canterbury, NZ
Prof. Russell Green, Virginia Tech, USA
Prof. Nicholas Sitar, Univ. California, Berkeley, USA
Prof. Zhaohui (Joey) Yang, University of Alaska Anchorage, USA
Prof. Chu-Han Zhang, Tsinghua University, China

Organising Committee

Prof. Deepankar Choudhury, IIT Bombay, India
Prof. Yumin Chen, Hohai University, China
Prof. Clarence Choi, HKUST, HKSAR
Prof. Shideah Dashti, University of Colorado, USA
Prof. Lijun Deng, University of Alberta, Canada
Prof. Shijin Feng, Tongji University, China
Dr. Duruo Huang, HKUST, HKSAR (Secretary)
Prof. C. Ledezma, Pontifical Catholic University, Chile
Prof. Run Liu, Tianjin University, China
Prof. Charles W.W. Ng, HKUST, HKSAR
Prof. Tong Qiu, Penn State University, USA
Prof. Armin Stuedlein, Oregon State University, USA
Prof. Gang Wang, HKUST, HKSAR (Chairman)
Prof. Jinting Wang, Tsinghua University, China
Prof. J.P. Wang, HKUST, HKSAR
Prof. Y.H. Wang, HKUST, HKSAR
Prof. Jun Yang, University of Hong Kong, China
Prof. Ga Zhang, Tsinghua University, China (Chairman)
Prof. Limin Zhang, HKUST, HKSAR (Vice-Chairman)
Prof. Jidong Zhao, HKUST, HKSAR
Prof. Chao Zhou, HKUST, HKSAR
Prof. Yuande Zhou, Tsinghua University, China
Prof. Bin Zhu, Zhejiang University, China

TABLE OF CONTENTS

3. Theme Lectures

4. Parallel Sessions

TURNING DISASTER INTO KNOWLEDGE

J. D. Bray[*], E.M. Rathje[+], and J. D. Frost[#],
[*] University of California, Berkeley, CA, USA
[+] University of Texas, Austin, TX, USA
[#] Georgia Institute of Technology, Atlanta, GA, USA

BRIEF INRODUCTION, METHODOLOGY AND KEY RESULTS

Geotechnical engineering is an experience-driven discipline. Field observations are particularly important, because it is difficult to replicate in the laboratory the characteristics and response of soil deposits built by nature over thousands of years. Furthermore, much of the data generated by a major disaster is perishable, so it is critical that it is collected soon after an event occurs. Detailed mapping and surveying of damaged and undamaged areas provides the data for the well-documented case histories that drive the development of many of the design procedures used by geotechnical engineers. Thus, documenting the key lessons learned from major extreme events around the world contributes significantly to advancing research and practice in geotechnical engineering. This is one of the primary objectives of the US National Science Foundation (NSF)-sponsored Geotechnical Extreme Events Reconnaissance (GEER) Association.

Many of the currently employed analytical methods utilized to evaluate geotechnical hazards, such as liquefaction-induced ground failure and its effects on building and buried utilities performance, rain-induced landslides and their effects on residential areas and transportation systems, and hurricane-induced storm surge and its effects on levee and coastal protection surface systems, could be enhanced. Well documented case histories that describe both poor and good performance during extreme events are critical to advancing the profession. For example, prevalent liquefaction triggering procedures are based primarily on empirical methods (e.g., Idriss & Boulanger 2008). Simplified seismic slope and embankment displacement procedures (e.g., Bray & Travasarou 2007) are not used by engineers until they have been shown to capture the observed performance of earth/waste structures during earthquakes. These and other commonly employed engineering procedures require continual re-evaluation and revision as important case histories are documented.

Even more importantly, new unanticipated observations from major events often define alternative research directions. As an example, the results of recent studies of soil liquefaction, especially those involving soils with a significant amount of fines, have been largely motivated by observations of liquefaction and ground softening documented by GEER reconnaissance efforts after earthquakes in Turkey and Taiwan. The careful documentation of liquefaction following the 1999 Kocaeli earthquake (Bray & Stewart 2000) provided much of the data that advanced the profession's understanding of liquefaction/cyclic ground softening of fine-grained soils and led to important new criteria for evaluating the liquefaction potential of these soils (e.g., Bray & Sancio 2006). If the geotechnical engineering profession is not prepared to look for and find new "geotechnical insights" following future events, important research insights and opportunities will be lost. Important advancements are possible through research of these effects after future extreme events if their consequences are captured carefully and comprehensively.

The geotechnical engineering profession has a rich tradition of understanding the need to develop and to apply new technologies and techniques that document in detail the effects of

extreme events on urban infrastructure (e.g., Bray & Frost 2010). The significant experience of geotechnical engineers in documenting the effects of natural hazards and their leadership in implementing new technologies in reconnaissance activities, positions them to work closely with other professionals to document the effects of extreme events and to advance the practice of geotechnical engineering through learning the lessons from these disasters.

CONCLUSIONS

Understanding and knowledge can be advanced through the documentation of the effects of extreme events. Recent GEER post-event reports illustrate what effective post-event geotechnical engineering reconnaissance can accomplish. These efforts succeeded in large part because of the value that geotechnical engineers place on learning from disasters and on developing well-documented case histories that form the cornerstone of understanding for the geotechnical engineering profession. The death and destruction resulting from recent events emphasizes society's need to improve its resilience. Unfortunately, extreme events will happen. It would be unfortunate if the geotechnical engineering profession did not capture the perishable data that enables it to understand which design procedures result in good performance and which procedures still need improvement. With this enhanced understanding and with robust empirical data, researchers can advance the practice of geotechnical engineering using GEER documentation of extreme events (GEER 2016).

ACKNOWLEDGEMENTS

REFERENCES

Bray, J.D., and Stewart, J. P. (2000). "Damage Patterns and Foundation Performance in Adapazari," Chapter 8 of the *Kocaeli, Turkey Earthquake of August 17, 1999 Reconnaissance Report*, in *Earthquake Spectra* J., Suppl. A to V. 16, EERI, pp. 163-189.

Bray, J.D. and Sancio, R.B. (2006). "Assessment of the Liquefaction Susceptibility of Fine-Grained Soils," *J. of Geotechnical and Geoenvironmental Engineering*, ASCE, V. 132, No. 9, pp. 1165-1177.

Bray, J.D. and Travasarou, T. (2007). "Simplified Procedure for Estimating Earthquake-Induced Deviatoric Slope Displacements," *J. of Geotechnical and Geoenvironmental Engineering*, ASCE, V. 133, No. 4, pp. 381-392.

Bray, J.D. and Frost, J.D., Eds. (2010). "Geo-engineering Reconnaissance of the 2010 Maule, Chile Earthquake," a report of the NSF- Sponsored GEER Association Team, primary authors: Arduino et al., GEER-022, Ver. 2, May, 2010, http://www.geerassociation.org/.

Geotechnical Extreme Events Reconnaissance (GEER) Association [2016]. Website for Dissemination for GEER Activities, http://www.geerassociation.org/.

Idriss, I.M., and Boulanger, R.W. [2008]. *Soil Liquefaction During Earthquakes*. Earthquake Engineering Research Institute, MNO-12, Oakland, CA.

SEISMIC ANALYSIS AND DESIGN OF RETAINING STRUCTURES

Nicholas Sitar
Edward G. Cahill and John R. Cahill Professor
Civil & Environmental Engineering, UC Berkeley
Berkeley, CA, USA, sitar@berkeley.edu

BRIEF INRODUCTION, METHODOLOGY AND KEY RESULTS

Earth retaining structures, excavation bracing and basement walls have historically performed well under seismic loading, even when they were designed for less intense ground motion or static loading only. The results from recent experimental and numerical analyses show that the observed seismic load increments are a function of the ground motion, wall type and the depth of embedment (Wagner and Sitar, 2016). The dynamic earth pressure increment distribution for deep basement structures is highly non-linear in contrast with shorter retaining structures (<6.5 m in height) for which the dynamic earth pressure increment was observed to increase linearly with depth (Sitar et al., 2012; Mikola & Sitar, 2013; Candia & Sitar, 2013). The point of application of the dynamic earth pressure resultant varies between 1/3 H and 0.6 H above the base of the wall, as recommended by most current design procedures. Most importantly, the depth of embedment can be incorporated in traditional limit equilibrium analyses by calculating a seismic coefficient, k_{MHEA}, as the maximum of the average acceleration within the backfill over the depth of the basement structure. Results from previous centrifuge experiments and the experimental results of this study were found to be in good agreement with the seismic earth pressure coefficient, ΔK_{ae}, obtained using the Okabe (1924) pseudo-static Coulomb wedge analysis and the methodology proposed by Seed & Whitman (1970). This suggests that some of the current procedures recommended for design overestimate seismic loads on retaining structures not necessarily through inherent conservatism in the methods, but rather due to overly conservative choice of seismic demand input. Therefore, for retaining structures not permitted to translate or rotate, the use of k_{MHEA} is proposed as an alternative to using the peak ground acceleration (PGA) or some fraction thereof. Also, this definition of the seismic coefficient is consistent with that recommended by Anderson et al. (2008) and Bray et al. (2010).

Figure 1 is a plot of the dynamic increment of earth pressure, ΔK_{ae}, versus the seismic coefficient computed in the numerical model and obtained in the experiments. Analytical solutions by Okabe (1924)0, Seed & Whitman (1970), and Wood (1973) are also shown for reference. The results from the numerical modeling reflect the trend of increasing dynamic earth pressure with increasing seismic coefficient. This data show that numerical models can reproduce the results of a centrifuge experiments when the models are properly calibrated with realistic soil behavior. As can be seen, there is a good agreement between the observed and computed dynamic load compared to the dynamic load computed using the Okabe (1924) and Seed & Whitman (1970) methods for $k_{MHEA} \lesssim 0.4$ and for deep structures. Moreover, the Wood (1973) significantly overestimates the computed and experimentally observed seismic load increment.
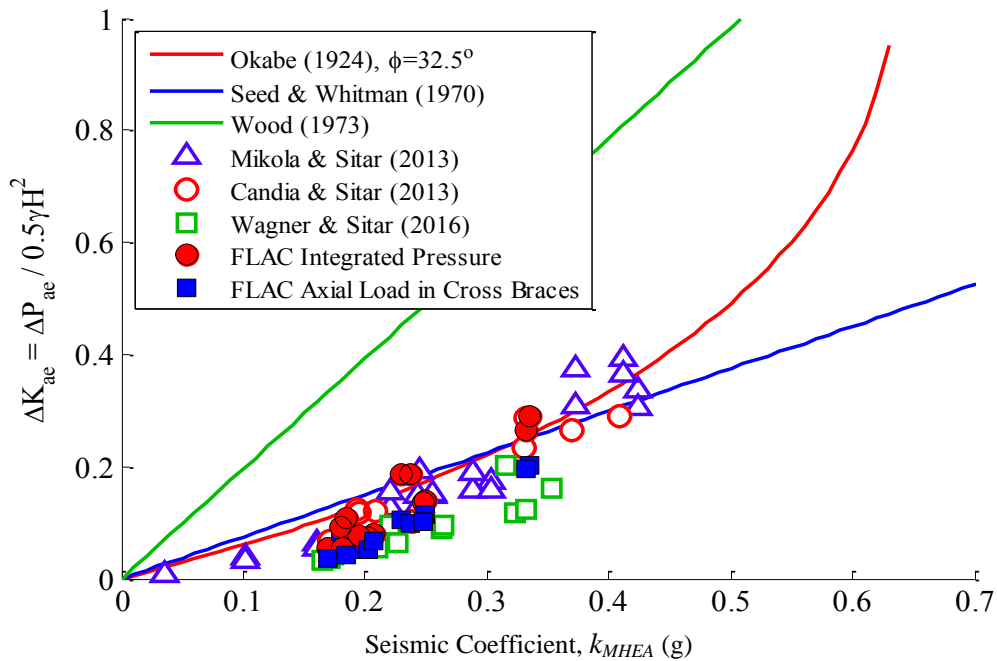
Figure 1 Computed and observed coefficient of dynamic earth pressure increment versus seismic coefficient, k_{MHEA} (from Wagner and Sitar, 2016).

CONCLUSIONS

Overall, evaluating static and dynamic earth pressure on retaining structures is a complex problem with a variety of competing and complementary effects to consider. In the recent studies centrifuge experiments were used to replicate the basic response of an idealized retaining structure systems. However, ultimately, further observations of performance in future seismic events and data from instrumented, full scale structures are highly desirable in order to fully validate these results. While numerical modeling offers a means to identify important aspects of the earth pressure problem, the results are sensitive to the input parameters, the boundary conditions, and the initialization of the process. Therefore, numerical models should be calibrated against real data whenever possible in order to ascertain their veracity.

REFERENCES

Anderson, D.G., Martin, G.R., Lam, I., Wang, J.N. (2008). Seismic Analysis and Design of Retaining Walls, Buried Structures, Slopes, and Embankments *(NCHRP Report 611)*. Transportation Research Board, Washington, DC.

Bray, J.D., Rathje, E.M., Augello, A.J., Merry, S.M. (1998). "Simplified seismic design procedures for geosynthetic-lined, solid waste landfills," *Geosynthetics International*, **5** (1-2), 203-235.

Candia, G., Sitar, N. (2013). Seismic Earth Pressures on Retaining Structures in Cohesive Soils. *Report No. UCB GT 13-02*, August 2013, p. 161, DOI:10.4231/D34746R4K

Mikola, R.G., Sitar, N. (2013). Seismic earth pressures on retaining structures in cohesionless soils. Report No. UCB GT 13-01, March 2013, p. 217, DOI: 10.13140/RG.2.1.1524.1446

Okabe, S. (1924). "General theory of earth pressure and seismic stability of retaining wall and dam." *Journal of the Japanese Society of Civil Engineers*, 10 (6), 1277-1323.

Seed, H.B., Whitman, R.V. (1970). Design of Earth Retaining Structures for Dynamic Loads. ASCE Specialty Conference, Lateral Stresses in the Ground and Design of Earth Retaining Structures. Cornell University, Ithaca, New York, 103-147.

Sitar, N., Mikola, R.G., Candia, G. (2012). "Seismically induced lateral earth pressures on retaining structures and basement walls." Keynote Lecture, Geotechnical Engineering State of the Art and Practice, Keynote Lectures from GeoCongress 2012, GSP 226, ASCE, 2012.

Whitman, R.V. (1991). "Seismic Design of Earth Retaining Structures." Proceedings, Second International Conference on Recent Advances in Geotechnical Earthquake Engineering and Soil Dynamics, St. Louis, Missouri, 1767-1778.

Wagner, N. Sitar, N. (2016). Seismic Earth Pressure on Basement Walls with Cohesionless Backfill. Report No. UCB GT 16-02, June 2016, DOI:10.21418/G8WC7H

Wood, J.H. (1973). Earthquake-Induced Soil Pressures on Structures. Report EERL 73-05, Earthquake Engineering Research Laboratory, California Institute of Technology, Pasadena, CA.

SOIL LIQUEFACTION - RECENT ADVANCES IN OUR UNDERSTANDING

S.P.G. Madabhushi
University of Cambridge, Cambridge

LIQUEFACTION BEHAVIOUR OF SANDS

Earthquake induced soil liquefaction continues to inflict considerable damage on man-made structures as witnessed in many of the earthquakes like the Tohuku earthquake in Japan, Christchurch earthquakes of 2011 in New Zealand or even more recently the Muisine earthquake of 2016 in Ecuador. Historically liquefaction was thought to be an undrained event given the relatively short duration of earthquake loading. Accordingly the undrained cyclic triaxial tests were considered as representative tests to study the liquefied soil behaviour. Constitutive models were developed based on the observations from such tests. In contrast to this, the Critical State frame work was used in Cambridge to explain the liquefied soil behaviour as shown in Figure 1. According to this, liquefied soil in near zero effective stress state should reach the 'Fracture Surface' leading to opening up of fissures that lead to sand boils and other liquefaction phenomena, Madabhushi and Haigh (2012). Further, the permeability of liquefied soil and hence its compressibility must increase. Haigh et al (2012) have shown that, at very low effective stresses (<1 kPa) the permeability of different types of sands does increase significantly as shown in Figure 2, as the soil stress state reaches the fracture line in Figure 1.
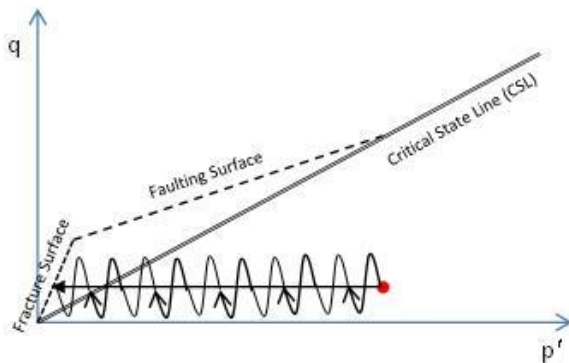
Figure 1: Critical State framework for soil liquefaction (*after Muhunthan and Schofield, 2000*)
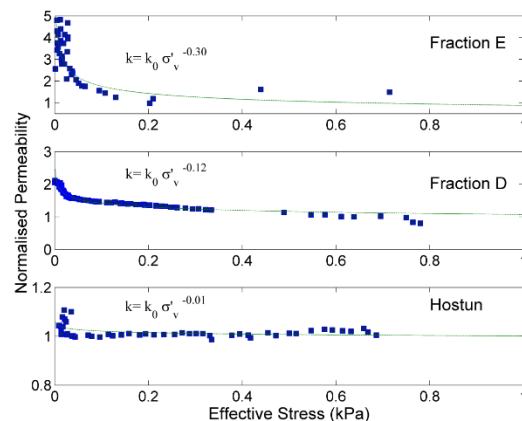
Figure 2: Change in permeability at very low effective stresses (*after Haigh et al, 2012*)

In the last decade dynamic centrifuge modelling was used extensively to study the soil liquefaction problem. Centrifuge test data on settlement of level beds of saturated, loose Fraction E sand (RD~50%) as shown in Figure 3 indicate that the co-seismic settlement is much larger than the post-seismic settlement due to reconsolidation (Coelho et al, 2007), despite the excess pore pressures staying high within the soil. Again this suggests that at very low effective stresses i.e. in near-liquefied state the soil's permeability and its compressibility increase. More recently, Adamidis and Madabhushi (2016a) have looked at the shallow foundations on liquefiable layers of saturated sand. Using a combination of the high-speed

imaging and PIV techniques, they were able to obtain the volumetric and shear strains below the shallow foundations that were accumulated over an earthquake event similar to the one shown in Figure 3. These volumetric and shear strains are plotted in Figure 4 with brighter colours indicating larger strain amplitudes. As expected there is a concentration of shear strains that accumulate at the edge of the shallow foundation. Further, it can be clearly seen that both volumetric strains and shear strains are present, confirming that even during the shaking event the soil suffers volumetric strains and hence is ***not*** in an undrained condition.
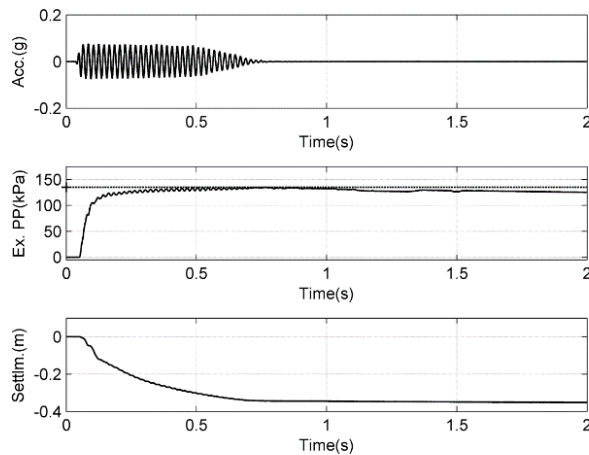
Figure 3: Results from the centrifuge test on a level soil bed with a RD of 50%
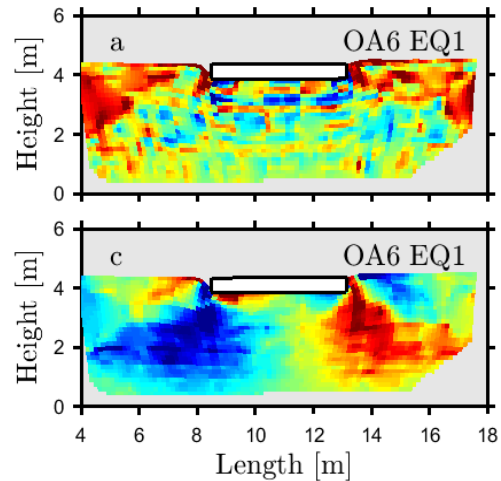
Figure 4: Volumetric and shear strains below foundation on shallow liquefiable layer

Following up from this work, Adamidis and Madabhushi (2016b) have carried out a novel series of centrifuge tests in which a 'triaxial chamber' is created within the centrifuge model as shown in Figure 5. The drainage in and out of the chamber is controlled carefully through a control valve system. The chamber is created using latex sheet and is therefore able to deform during shaking allowing the soil within to shear. The behaviour of soil within the chamber is compared directly to that in the 'free-field', by placing miniature instruments like PPT's and accelerometers exactly at the same elevation within the model. Some of the typical results from this centrifuge test are presented here. In Figures 6a and 6b the shear stress τ and the shear strain γ are plotted against time for the location in the chamber and in the free-field. In Figure 6c, the $\tau - \sigma'_v$ plot is presented for the chamber location and the free-field. In this figure it can be seen that the stress path taken by the soil in the free-field is very different to the soil within the 'triaxial chamber', although both soil elements start at the same location. The soil in the free-field loses its vertical effective stress very quickly

Figure 5: A centrifuge model with a 'triaxial chamber'

and cycles close to the zero value. The soil within the 'triaxial chamber' initially sees a drop in vertical effective stress but then seems to regain some effective stress with further cycles and finishes up at about 25 kPa of vertical effective stress. Clearly this indicates quite a different behaviour compared to the free-field soil. Similarly Figures 6d and 6e show the τ - γ
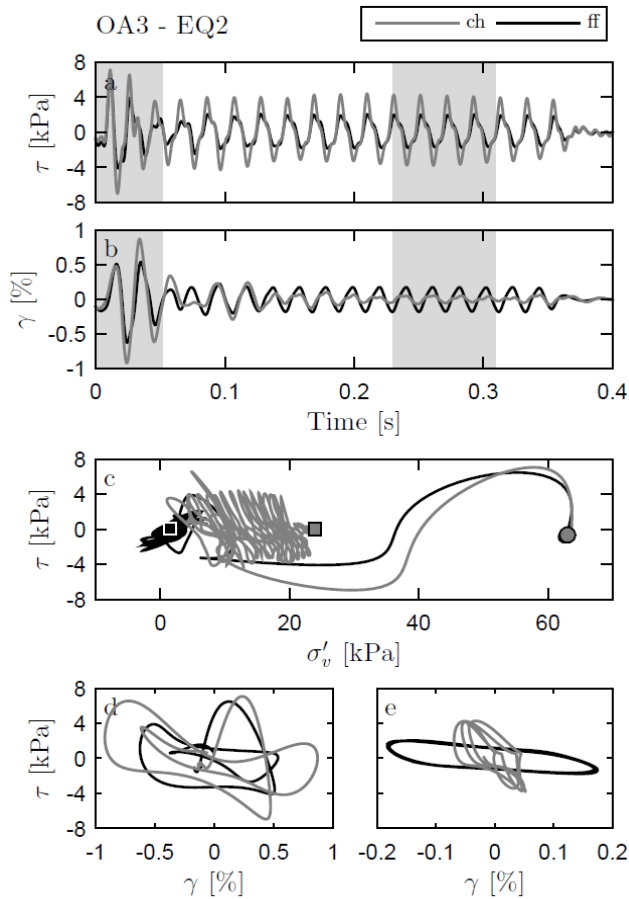
Figure 6: Stress-strain plots in centrifuge test OA3

plots for the initial cycles (left) and towards the end of shaking i.e. post liquefaction (right). In these figures it can be seen that during the initial period of shaking, the shear stress-strain behaviour is broadly similar at large strains (up to 0.8%). As the soil liquefies, the shear strain amplitudes drop off to less than 0.2% as do the shear stress levels. Towards the end of shaking i.e. in the post-liquefaction period, the soil in the free-field shows a very flat response with large strain amplitudes and very low shear stresses, suggesting a large drop in the soil stiffness as seen in Figure 6e.

In contrast, the soil within the 'triaxial chamber' suffers smaller shear strain amplitudes and is able to mobilise larger shear stresses, indicating that the soil in the chamber has gained some stiffness towards the end of shaking. This is also reflected in Figure 6c, introduced earlier where this soil is able to gain some vertical effective stress as the shaking progressed.

It must be pointed out that gradient of the vertical effective stress is the same in the free-field and in the 'triaxial chamber' as this is a centrifuge test. Comparing the overall behaviour between the free-field and the soil within the 'triaxial chamber' it can be seen that by simply restricted the flow of pore fluid i.e. controlling the fluid boundary conditions can create vast differences in soil behaviour enclosed in the chamber relative to that in the free-field. In the free-field the pore fluid is able to drain upwards especially with increased permeability when the soil is close to the fully liquefied state. Within the 'triaxial chamber' the excess pore pressures quickly equilibrate forming a small water film at the top of the chamber.

CONCLUSIONS

1. Soil liquefaction continues to be a major issue as witnessed in many of the recent earthquakes. Research in this area should focus on the fundamental behaviour of liquefied soil and the best practices in modelling this behaviour.
2. In this paper some of the basic tenants of 'soil liquefaction' are challenged. Historic perspectives that treat liquefaction as an 'undrained event' are shown to be incorrect, even during the co-seismic period. Increases in the permeability and soil compressibility at very low effective stresses, as predicted by the Critical State framework, play a major role in the behaviour of liquefied ground.
3. Centrifuge test data shows that co-seismic settlements of level ground are much larger than post-seismic settlements. Similarly tests on shallow foundations show the existence of volumetric shear strains that accumulate throughout the shaking period.
4. Further, novel centrifuge tests have shown that free-field behaviour is very different from that of soil enclosed in a 'triaxial chamber'. This shows the important role drainage plays in determining the behaviour of liquefied soils.

8

REFERENCES

Adamidis, O. and Madabhushi, G.S.P., (2016a), "Response of shallow foundations to successive earthquake-induced liquefaction events", Proc. 1st International Conference on Natural Hazards & Infrastructure, 28-30 June, 2016, Chania, Greece.

Adamidis, O. and Madabhushi, G.S.P., (2016b), "Post-liquefaction reconsolidation of sand", *Proceedings of Royal Society A, Mathematical, Physical and Engineering Sciences*, 472:20150745; DOI: 10.1098/rspa.2015.0745.

Coelho, P.A.L.F., Haigh, S.K., Madabhushi, S.P.G. and O'Brien, A.S., (2007), "Post-earthquake behaviour of footings when using densification as a liquefaction resistance measure", *Ground Improvement Journal*, Vol. 11, Issue 1, pp 45-53.

Haigh S.K., Eadington, J. & Madabhushi, S.P.G., (2012), "Permeability and stiffness of sands at very low effective stresses", *Geotechnique*, 62(1), pp. 69-75.

Madabhushi, S.P.G. and Haigh, S.K., (2012), "How well do we understand earthquake induced liquefaction?" *Indian Geotechnical Journal*, Vol. 42, Issue 3, pp. 150-160.

Muhunthan, B. and Schofield, A.N., (2000), "Liquefaction and dam failures", Proc. GeoDenver, Denver, Colorado, USA.

RATE-DEPENDENT UH MODEL FOR SOILS

Y. P. Yao

Beihang University, Beijing, China

INTRODUCTION

The stress-strain relation of soil is time-dependent, which is referred to as rheology or viscosity of soil. In the geotechnical engineering, the rheology of soil may cause uneven settlements of foundations and decreases of long-term strength of slopes. If the rheology is neglected or underestimated in the design and construction of geotechnical engineering, it will leave a hidden danger to the normal operation and safety of engineering. Therefore, the rheology of soil has been always a research focus in soil mechanics. In recent years, with the rapid development of our domestic economy, an increasing number of infrastructure projects (e.g., airports and high-speed railway) are being constructed in the soft-clay geological environment around the sea, rivers and lakes. The rheology of soil is being paid more and more attentions.

The experimental phenomena related to the rheology of soil mainly include the creep and the strain rate effect. The experimental result about creep shows that creep makes the normally consolidated soil to be overconsolidated. The experimental result about the strain rate effect indicates that the overconsolidated soil exhibits different overconsolidation degrees under different strain loading rates. These experimental results prove that the rheology and the overconsolidation of soil are closely linked. Therefore, a reasonable rheological constitutive model should be capable of considering both the rheology and the overconsolidation, and reflecting the interconversion between them.

The UH (unified hardening) model is a constitutive model for overconsolidated clay. By incorporating a time-dependent hardening rule into the UH model, an elasto-visco-plastic (EVP) constitutive model that can simultaneously describe the rheology and the overconsolidation is built. The new model is called the rate-dependent UH model. The rate-dependent UH model is then generalized to the three-dimensional stress condition by the transformed stress method.

UH MODEL AND ITS EXTENSIONS

The UH model is based on the relationship between the current yield surface and the reference yield surface. A current yield surface is used to describe overconsolidated behaviour, and a reference yield surface to describe the yield characteristics corresponding to normally consolidated clays. The UH model can model many characteristics of overconsolidated clays well, including stress–strain relationships, shear dilatancy, strain-hardening and softening, and stress path dependence behaviour. The key feature of the model is the adoption of a unified hardening parameter that is independent of stress paths. Based on the SMP criterion and the corresponding transformed stress method, the proposed model can be applied conveniently to three-dimensional stress states. Compared with the Cam-clay model, the UH model requires only one additional clay parameter, the slope of the Hvorslev envelope.

The UH model has been extended to consider influences of some external factors (temperature and suction), complicated characteristics (anisotropy, structural and small-strain properties) and complicated loading paths (cyclic loading, and various drainage conditions, namely asymptotic states). Moreover, the UH model has been embedded into the commercial numerical analysis software and applied to the geotechnical engineering analysis.

RATE-DEPENDENT UH MODEL

The rate-dependent UH model is built on the basis of the UH model. In developing the rate-dependent UH model, first the time effects on clays were connected with the change of overconsolidation degree according to the concepts of aging time and the instant normal compression line. This made it convenient to combine a logarithmic creep function with the reloading function of the UH model, and, thus, an isotropic EVP relationship was built.
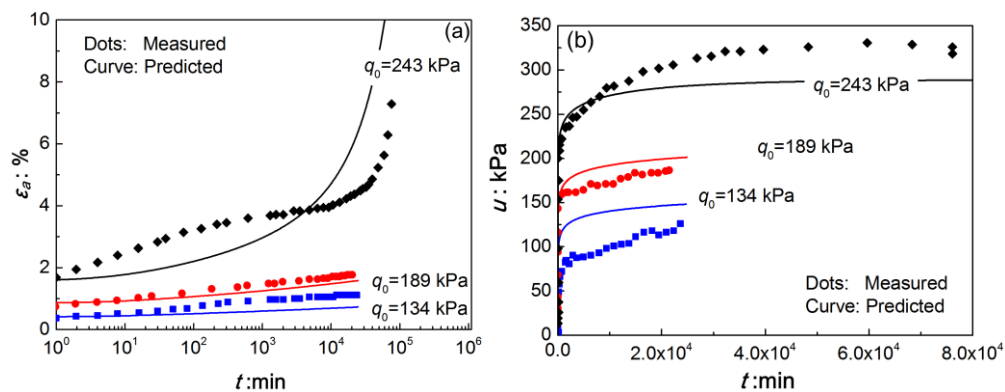
Figure 1: Simulation for triaxial undrained creep, (a) axial strain-time relation, (b) pore pressure-time relation
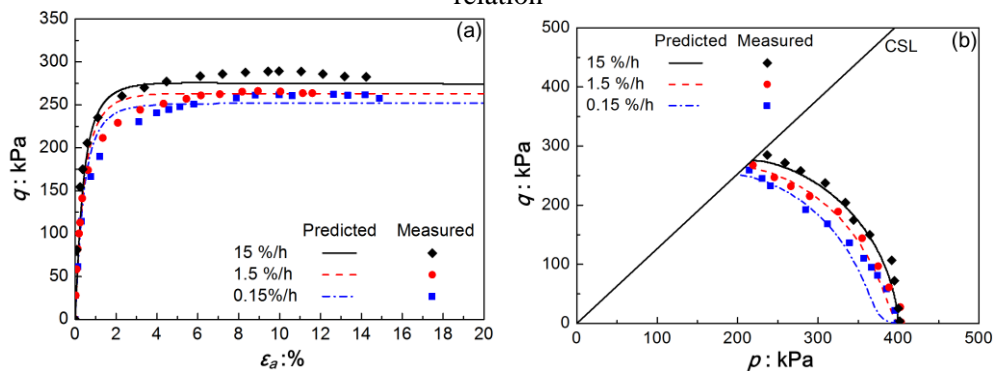
Figure 2: Simulation for triaxial undrained compression under different constant strain rates on normally consolidated clay, (a) stress-strain relation, (b) stress path
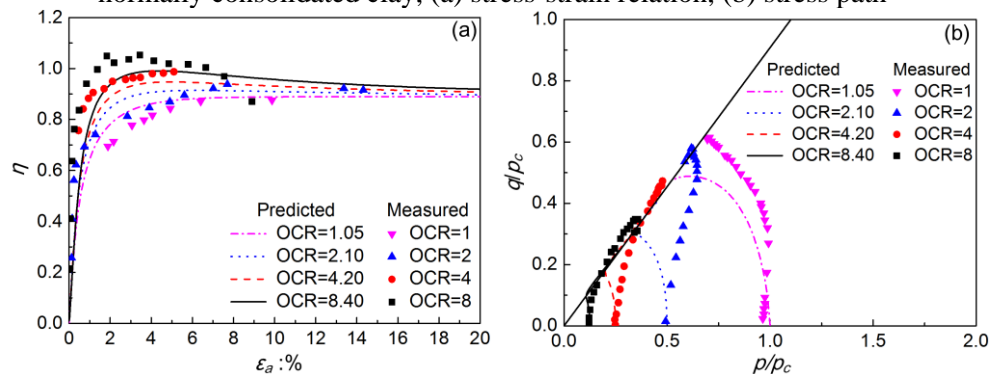
Figure 3: Simulation for triaxial undrained compression under a constant strain rate on clays with different OCRs, (a) stress-strain relation, (b) stress path

Second, a time variable derived from the isotropic EVP relationship was embedded into the

current yield function of the UH model, and, thereby, a time-dependent current yield function is proposed. Based on the time-dependent current yield function and the flow rule, an EVP
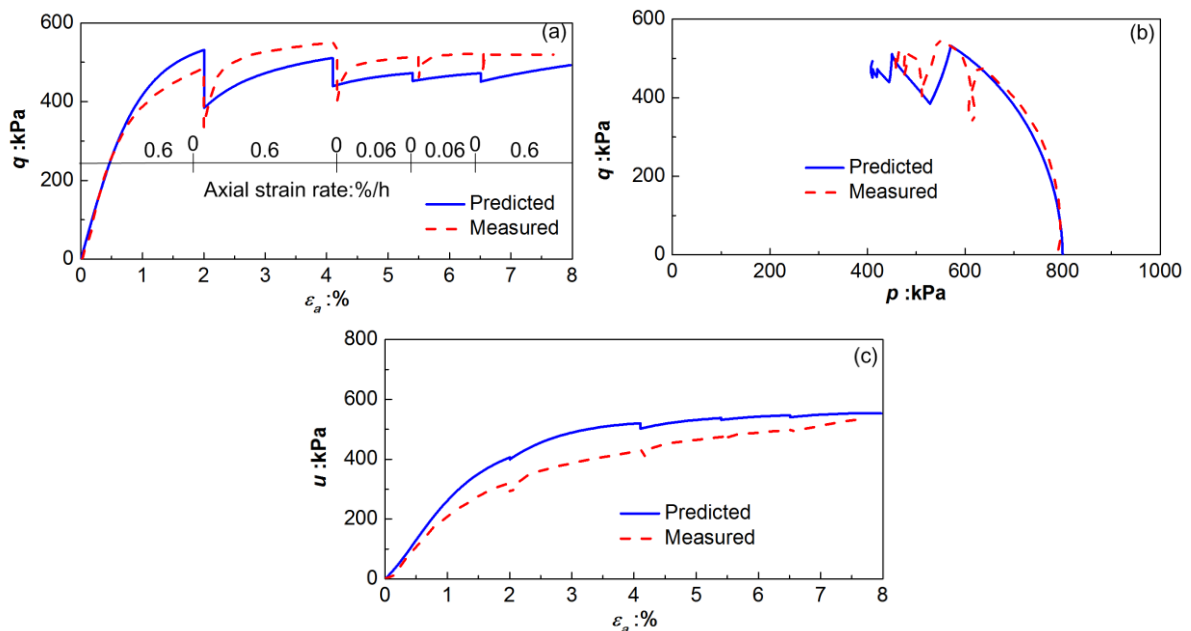
Figure 4: Simulation for triaxial undrained compression at the stage-changed strain rate, (a) stress-strain relation, (b) stress path, (c) pore pressure-strain relation

model for triaxial compression stress states was built. The EVP model for triaxial compression stress states then was extended to a three-dimensional EVP model for general stress states through the transformed stress method.

The proposed three-dimensional EVP model can describe time-dependent behaviours, such as creep, relaxation, and loading rate effect, for both normally consolidated and overconsolidated clays, with two additional parameters compared with the modified Cam-clay model. Finally, numerous experimental results in the literature (such as the results of triaxial undrained creep tests, triaxial undrained compression and extension tests at the constant strain rate, and triaxial undrained tests at the stage-changed strain rate) were used to validate the rate-dependent UH model, as shown as Figures 1 to 4.

CONCLUSIONS

A new three-dimensional EVP constitutive model, i.e. the rate-dependent UH model is built on the basis of the UH model. By comparing the simulated results of the rate-dependent UH model with laboratory results, it can be found the rate-dependent UH model can reflect most overconsolidated and viscous behaviour of soils, such as strain softening, dilatancy, as well as creep, relaxation, and strain rate effect under triaxial condition. Besides, the rate-dependent UH model needs only two more material constants than the modified Cam-clay model. In comparison with other EVP models, the rate-dependent UH model adopts fewer material constants.

ACKNOWLEDGEMENTS

REFERENCES

Matsuoka, H., Yao, Y. P., Sun, D. A. (1999). "The Cam-clay models revised by the SMP criterion." *Soils Found.*, 39(1), 81-95.

Yao, Y. P., Sun, D. A. (2000). "Application of Lade's criterion to Cam-clay model." *J. Eng. Mech.*, 126(1), 112-119.

Yao, Y. P., Sun, D. A., Luo, T. (2004). "A critical state model for sands dependent on stress and density." *Int. J. Num. Anal. Met. Geo.*, 28(4): 323–337.

Yao, Y. P., Zhou, A. N., Lu, D. C. (2007). "Extended transformed stress space for geomaterials and its application." *J. Eng. Mech.*, 133(10): 1115–1123.

Yao, Y. P., Hou, W., Zhou, A. N. (2008). "Constitutive model for overconsolidated clays." *Sci. China-Technol. Sc.*, 51(2): 179–191.

Yao, Y. P., Sun, D. A., Matsuoka, H. (2008). "A unified constitutive model for both clay and sand with hardening parameter independent on stress path." *Comp. Geotech.*, 35(2): 210–222.

Yao, Y. P., Hou, W., Zhou, A. N. (2009). "UH model: three-dimensional unified hardening model for overconsolidated clays." *Geotechnique*, 59(5), 451-469.

Yao, Y. P., Yang, Y. F., Niu, L. (2011). "UH model considering temperature effects." *Sci. China-Technol. Sc.*, 54(1): 190–202.

Yao, Y. P., Gao, Z. W., Zhao, J. D., Wan, Z. (2012). "Modified UH model: constitutive modelling of overconsolidated clays based on a parabolic Hvorslev envelope." *J. Geotech. Geoenviron. Eng.*, 138(7), 860-868.

Yao, Y. P., Kong, Y. X. (2012). "Extended UH model: three-dimensional unified hardening model for anisotropic clays." *J. Eng. Mech.*, 138(7), 853-866.

Yao, Y. P., Cui, W. J., Wang, N. D. (2013a). "Three-dimensional dissipative stress space considering yield behavior in deviatoric plane." *Sci. China-Technol. Sc.*, 56(8), 1999-2009.

Yao, Y. P., Niu, L., Cui, W. J. (2013b). "Unified hardening (UH) model for overconsolidated unsaturated soils." *Can. Geotech. J.*, 51(7), 810-821.

Yao, Y. P., Zhou, A. N. (2013). "Non-isothermal UH model: A thermo-elastoplastic model for clays." *Geotechnique,* 63(15), 1328-1345.

Yao, Y. P., Kong, L. M., Hu, J. (2013). "An elastic-viscous-plastic model for overconsolidated clays." *Sci. China-Technol. Sc.*, 2013, 56(2): 441–457.

Yao, Y. P., Kong, L. M., Zhou, A. N., Yin, J. H. (2014). "Time-dependent unified hardening model: three-dimensional elastoviscoplastic constitutive model for clays." *J. Eng. Mech.*, 2014, doi: 10.1061/(ASCE)EM.1943-7889.0000885.

Yao, Y. P., Wang, N. D. (2014). "Transformed stress method for generalizing soil constitutive models." *J. Eng. Mech.*, 140(3), 614-629.

Yin, J. H., Zhu, J. G., Graham, J. (2002). "A new elastic viscoplastic model for time-dependent behaviour of normally and overconsolidated clays: theory and verification." *Can. Geotech. J.*, 39(1), 157-173.

Yin, Z. Y., Chang, C. S., Karstunen, M., Hicher, P. Y. (2010). "An anisotropic elastic-viscoplastic model for soft clays." *Int. J. Solids Struct.*, 47(5), 665-677.

Zhu, J. G. (2000). "Experimental study and elastic visco-plastic modelling of the time-dependent stress-strain behaviour of Hong Kong marine deposits." Ph.D. thesis, The Hong Kong Polytechnic University, Hong Kong.

SUBSEQUENT DEVELOPMENT OF ROCK-FILLED CONCRETE DAM

Feng Jin, Hu Zhou, Ga Zhang and Yuande Zhou
Tsinghua University, Beijing, China

BRIEF INRODUCTION, METHODOLOGY AND KEY RESULTS

The rock-filled concrete (RFC) is an innovative mass concrete technology developed by Tsinghua University in 2003 (Jin and An, 2003; Jin *et al.* 2005; An *et al.* 2014). It is formed by pouring fresh Self-Compacting Concrete (SCC) into pre-placed stone layers to fill the void among the stones. More than 1.5×10^6 m^3 RFC have been poured in more than 100 projects since 2005. Figure 1 shows the construction procedures of RFC. The picture of Baijia RFC arch dam, completed in 2015, is shown in Figure 2.
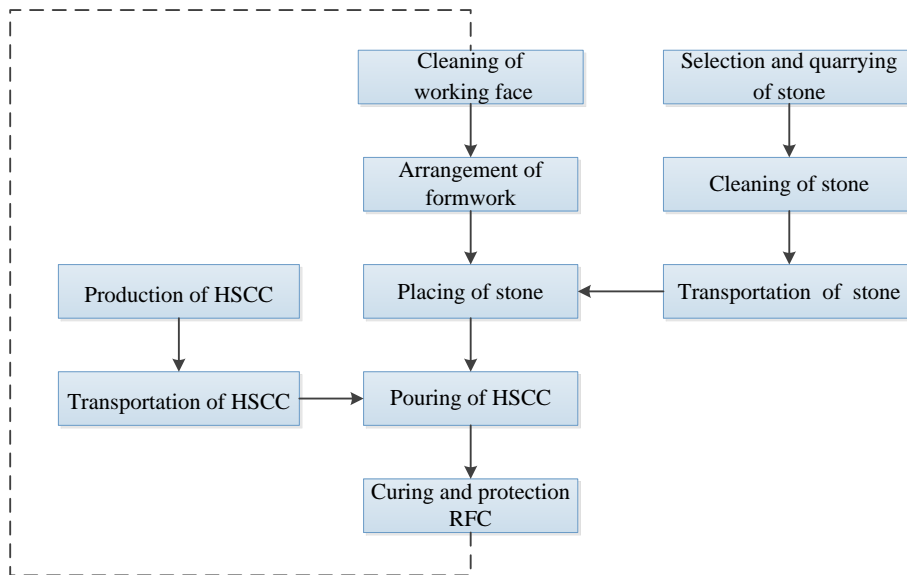
Figure 1: The flow chart of Rock-Filled Concrete

Figure 2: Baijia RFC arch dam completed in 2015

One of the key features of RFC is the compacting ability of SCC in the stone layers (also called Rock-fill). Using large aggregates (grain size > 30 cm), the RFC technology presents many advantages, such as less cement usage, less deformation, less hydration heat, no vibration, faster construction speed, and less CO_2 emission. However, there are also significant challenges: (1) whether SCC can effectively fill the spaces between aggregates, and (2) whether the interfaces between SCC and rocks will become a weak part and threaten the strength and durability of RFC. To address these challenges, some numerical and physical simulation were performed (Xie *et al.* 2014; Wang *et al.* 2016). Figure 3 shows an experiment setup designed and fabricated to simulate SCC flow in rock skeleton by using self-compacting mortar (SCM) and large aggregates. The test box is divided into two chambers by a release door. SCM first flows into chamber 1 and then flows through the aggregate skeleton packed in chamber 2 after the release door is lifted. The effects of different factors (aggregate size, yield stress, etc.) on the filling capacity of SCC and the properties of RFC were investigated on the basis of filling rate, cross-section porosity, and interface microstructure. Figure 4 shows variation of porosity in the interfacial transition zone (ITZ) between mortar and aggregate, measured from aggregate surface using different SCM.
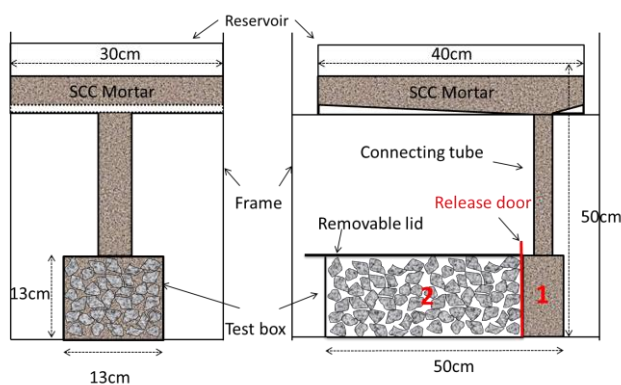
Figure 3 Design profile of a RFC test
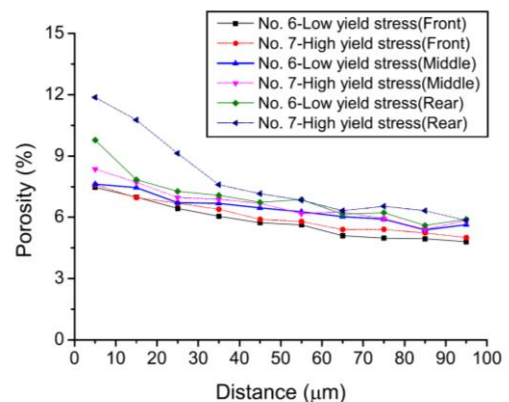
Figure 4 ITZ porosities of different SCM

Based on these studies, a new idea of innovative dam type was further developed most recently. The key point is to combine the RFC technology with the rockfill dam. The mechanical properties of the new dam materials, maybe called Cemented Rockfill, fall between those of concrete and rockfill materials. In generally, it belongs to a granular material, but is strengthened by cemented. Some preliminary tests were performed. New methods for predicting the mechanical properties of the new material should be developed.

CONCLUSIONS

1. RFC technology has been well developed in recent years. More and more RFC dams have been built. The maximum height of RFC dams will soon reach 100 m in the near future.
2. Based on the studies on the fluidity of SCC in the rockfill, an innovative technique of dam construction is developed. The new material belongs to a structuralized strengthened granular material. New methods for predicting the mechanical properties of the new material should be developed.

ACKNOWLEDGEMENTS

REFERENCES

An, X., Wu, Q., Jin, F., Huang, M., Zhou, H., Chen, C., Liu, C. (2014), "Rock-filled concrete, the new norm of SCC in hydraulic engineering in China", *Cement and Concrete Composites* 54 89-99.

Jin, F., An, X. (2003), "Construction Method of Rock-Filled Concrete Dams", Chinese Patent No. ZL03102674.5

Jin, F., An, X., Shi, J., Zhang, C. (2005), "Study on rock-fill concrete dam", *J. Hydraul. Eng.* 36, pp1347–1352.

Wang, Y., Xie, Y. and Jin, F. (2016), "Influences of casting procedure and aggregate size on the ITZ properties, compressive strength and water permeability of rock-filled concrete", *J. Construction & Building Materials* ASCE. 28

Xie, Y., Corr, D.J., Chaouche, M., Jin, F., Shah, S.P. (2014), "Experimental study of filling capacity of self-compacting concrete and its influence on the properties of rock-filled concrete", *Cement Concrete Research* 56 pp121-128

DISTRIBUTION AND FATE OF EARTHQUAKE-INDUCED LANDSLIDES NEAR THE EPICENTRE OF THE WENCHUAN EARTHQUAKE

L.M. Zhang*, and S. Zhang[+]
* Hong Kong University of Science of Technology, Hong Kong, China
[+] Technological Higher Education Institute of Hong Kong, Hong Kong, China

BRIEF INTRODUCTION, METHODOLOGY AND KEY RESULTS

More than 60,000 landslides were triggered by the magnitude Mw 7.9 Wenchuan earthquake in China in 2008, with 25-30,000 fatalities caused by the earthquake-induced landslides. The majority of these landslides were distributed along the Yingxiu–Beichuan fault. After the earthquake, many of the landslide deposits reactivated during rainstorms, inducing a chain of hazards including slides and rock falls, large-scale debris flows, landslide dams, flooding due to dam breach, increased sedimentation, change of river course, and scouring. These hazards evolved either separately or as an integrated system known as cascading landslide hazards (Zhang et al. 2014a).
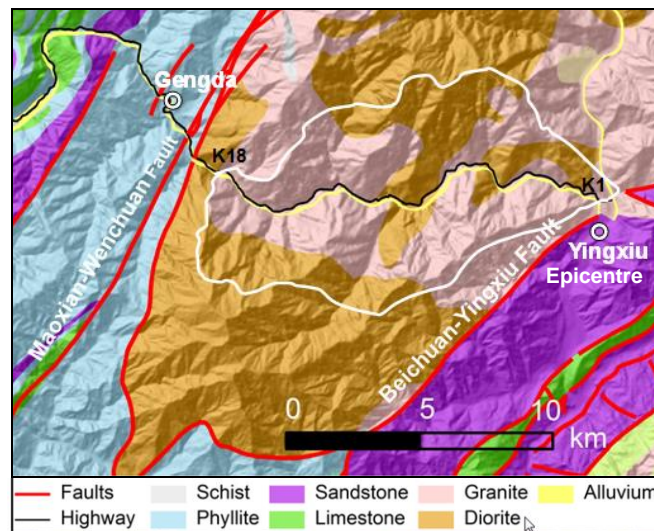
Figure 1: Geological conditions and faults near the epicenter of the Wenchuan earthquake.

An extensive research on the distribution and fate of earthquake-triggered landslides was conducted in a study area near the epicentre of the Wenchuan earthquake, Yingxiu, along the Province Road PR303 (Figure 1). The highway goes across four faults and is partly located on the hanging wall of the Yingxiu-Beichuan fault where strong ground motions were up to a peak horizontal ground acceleration of 0.96 g (Li et al., 2008). The geological setting between Yingxiu and Gengda from K1 to K18 is shown in Figure 1. Widespread co-seismic landslides were triggered on both sides of the highway during the earthquake, and a large number of rain-induced landslides and debris flows occurred in the first seven years after the earthquake. Some landslides blocked the Yuzixi River, forming landslide dams. The collapse of the landslide dams caused floods and cut off the highway repeatedly. The riverbed along the road rose due to the accumulation of sediments. These cascading hazards not only caused

losses of life and property, but also initiated a fundamental transformation of the natural environment. Such transformation is expected to last for many years. Understanding the distribution and fate of these earthquake-induced landslides has significant implications for sustainability and risk management.

Digital image interpretation techniques and field verifications were combined to characterize the landslides in the study area. We mapped the earthquake-induced landslides along PR303 near the epicentre and the rain-induced landslides and debris flows, and compared the distribution characteristics of the earthquake-induced landslides and the rain-induced landslides (Zhang et al. 2014b). We also traced the movements of the landslide deposits on the hillslopes and in channels in the first seven years after the earthquake, and budgeted the soil volumes as the soil deposits moved down the hillslopes either as landslides or as debris flows.

New computational tools have been developed to analyse the triggering and movements of landslides in the study area (Chen and Zhang 2014), to simulate the mobility and entrainment of debris flows (Chen and Zhang 2015), and to assess the risks posed by the cascading landslides (Zhang et al. 2012; Chen et al. 2016).

The distributions of the volume of landslides along the highway shortly after the earthquake in 2008 and after the rainstorm in 2010 are shown in Figure 2. The total volume of the 305 hill-slope deposits shortly after the Wenchuan earthquake was 54.30 million m^3 and the total volume of the channel deposits was 12.39 million m^3. The August 2010 storm triggered 351 fresh landslides but the total volume of these landslides was significantly smaller than that triggered by the earthquake in 2008 (Figure 2). As time goes on, the volume of the hillslope deposits became smaller while the volume of the channel deposits became larger. Part of the soil deposits became river sediment after moving into the Yuzixi River.
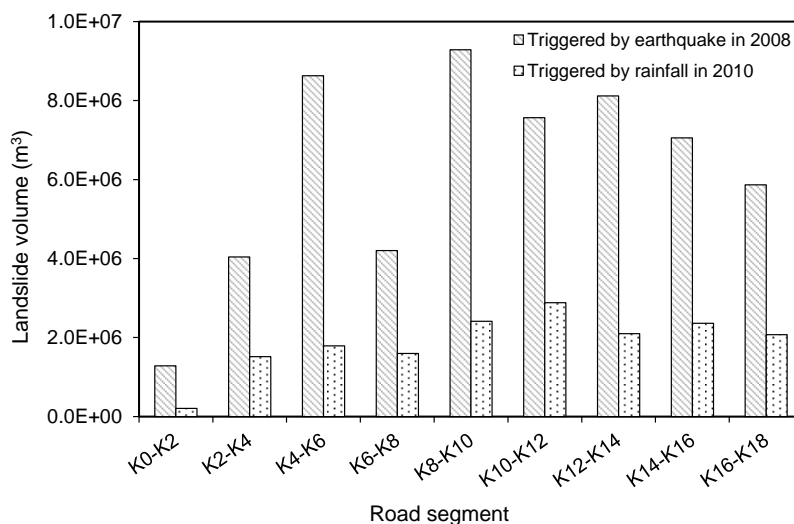
Figure 2: Volumes of landslides triggered by the earthquake in 2008 and the storm in 2010.

CONCLUSIONS

1. During the Wenchuan earthquake, 305 hill-slope deposits and 28 channel deposits were triggered in the 85 km^2 study area near the epicentre of the Wenchuan earthquake. The total volume of the hill-slope deposits and channel deposits were 54.3 million m^3 and 12.39 million m^3, respectively. The August 2010 storm triggered a total of 351 fresh rain-induced landslides with a total volume of 16.94 million m^3. The earthquake-induced landslides were mainly distributed at slope angles of 30-50°. The fresh rain-induced landslides in 2010 were mainly distributed at slightly smaller slope angles between 20°

and 40°. The earthquake-induced landslides were steeper, which can probably be attributed to topographic amplification of ground motions and lower external loads required to trigger instability of materials on steeper slopes. In addition, the earthquake-induced landslides occurring under dry condition could pose steeper slope angles than the rain-induced landslides did.

2. During the storm events in the first seven years after the earthquake, some of the hillslope deposits evolved into channel deposits and the materials in the channels gradually moved forward to the gully mouth. The volume of the hillslope loose deposits decreased while the volume of the channel deposits increased over time. The mass transport rates were 24.5%, 16.3% and 12.1% during the rainstorms in 2010, 2011 and 2013, respectively. The quantities of the sediment that contributed to the aggraded riverbed were approximately 1.2×10^6 m^3 in year 2010, 0.7×10^6 m^3 in year 2011, and 1.5×10^6 m^3 in year 2013, respectively. Such mass movement process indicates that the mass is redistributed with time or rearranged in space.

3. Approximately 90% of the erodible material still remains on the hillslope and channels; hence the landslide risks are still rather high and a longer-term monitoring and investigation of the earthquake- and rain-induced landslides is needed.

ACKNOWLEDGEMENTS

REFERENCES

Chen, H. X., and Zhang, L. M. (2015). "EDDA 1.0: integrated simulation of debris flow erosion, deposition and property changes." *Geoscientific Model Development* 8, pp. 829–844. www.geosci-model-dev.net/8/829/2015/; doi:10.5194/gmd-8-829-2015.

Chen, H. X., and Zhang, L. M. (2014). "A physically-based distributed cell model for predicting regional rainfall-induced slope failures." *Engineering Geology* 176, pp. 79–92.

Chen, H. X., Zhang, S., Peng, M., and Zhang, L. M. (2016). "A physically-based multi-hazard risk assessment platform for regional rainfall-induced slope failures and debris flows." *Engineering Geology* 203, pp. 15–29.

Li, X. J., Zhou, Z. H., and Yu, H. Y. (2008). "Strong motion observations and recordings from the great Wenchuan Earthquake." *Earthquake Engineering and Engineering Vibration* 7, pp. 235-246.

Zhang, L. M., Zhang, S., and Huang, R. Q. (2014a). "Multi-hazard scenarios and consequences in Beichuan, China: The first five years after the 2008 Wenchuan earthquake." *Engineering Geology* 180, pp. 4-20.

Zhang, S., Zhang, L. M., and Glade, T. (2014b). "Characteristics of earthquake- and rain-induced landslides near the epicentre of Wenchuan Earthquake." *Engineering Geology* 175, pp. 58–73.

Zhang, S., Zhang, L. M., Peng, M., Zhang, L. L., Zhao, H. F., and Chen, H. X. (2012). "Assessment of risks of loose landslide deposits formed by the 2008 Wenchuan earthquake." *Natural Hazards and Earth System Sciences* 12, pp. 1381–1392.

EVALUATING RISK DUE TO LIQUEFACTION: LESSONS LEARNED FROM RECENT EARTHQUAKES AND NEW DEVELOPMENTS

Russell A. Green and Brett W. Maurer
Virginia Tech, Blacksburg, Virginia, USA

BRIEF INRODUCTION, METHODOLOGY AND KEY RESULTS

Whitman (1971), and Seed and Idriss (1971), first developed the "simplified" liquefaction evaluation procedure to compute the factor of safety against liquefaction (FS) at a given depth in the soil profile. While the simplified procedure predicts liquefaction triggering at a specific depth, it does not predict the severity of liquefaction manifestation at the ground surface, which more directly correlates to damage potential due to liquefaction. To fill this gap, Iwasaki et al. (1978) proposed the liquefaction potential index (LPI) to better characterize the damage potential of liquefaction, where LPI is computed as:

$$\text{LPI} = \int_0^{20m} \text{F} \cdot \text{w}(z) dz \qquad (1)$$

In this expression, $F = 1 - FS$ for $FS \leq 1$ and $F = 0$ for $FS > 1$, where FS is obtained from a variant of the simplified liquefaction evaluation procedure mentioned above, and w(z) is a depth weighting function given by $w(z) = 10 - 0.5z$, where z = depth in meters below the ground surface. Thus, it is assumed that the severity of liquefaction manifestation is proportional to the thickness of a liquefied layer; the amount by which FS is less than 1.0; and the proximity of the layer to the ground surface.

Researchers evaluating LPI during recent earthquakes have found its performance to be inconsistent, ranging from largely erroneous (Lee et al., 2003) to generally consonant but inaccurate for a non-trivial percent of sites (Toprak and Holzer, 2003). For example, Maurer et al. (2014) assessed the performance of LPI during the 2010-2011 Canterbury, New Zealand, Earthquake Sequence (CES); prediction-errors from the $M_w 7.1$ Darfield and $M_w 6.2$ Christchurch earthquake are shown in Figure 1, where over-predictions indicate the observed severity of liquefaction manifestation was less than predicted. It can be seen in Figure 1 that while LPI performance was generally good, liquefaction severity was significantly over-predicted for a portion of the study-area. Given the inconsistent efficacy of the existing LPI framework and criterion for assessing risk due to liquefaction, further research is warranted.

Independent of the LPI framework and its potential shortcomings, Ishihara (1985) recognized the influence of the non-liquefied capping layer (or crust) on the severity of surficial manifestation of liquefaction. He plotted observations of liquefaction surface effects using the thicknesses of the non-liquefied crust, H_1, and the liquefied strata, H_2, and proposed boundary curves for predicting liquefaction manifestation as a function of H_1, H_2, and peak ground acceleration (PGA). Ishihara (1985) initially proposed a single boundary curve, shown in Figure 2a, using data from sites subjected to a PGA of 200 gal (~0.2g); incorporating the work of others, a series of curves was then proposed corresponding to different PGAs, as shown in Figure 2b. The proposed boundary curves indicate that for a given PGA, there is a limiting H_1 beyond which surface manifestations do not form regardless of H_2. The importance of the non-liquefiable crust (i.e., H_1) on the severity of

surficial liquefaction manifestation (or lack thereof) is not directly accounted for in the LPI framework. However, a shortcoming of the Ishihara H_1-H_2 framework is the difficulty in its implementation for profiles that cannot be easily characterized in terms of H_1 and H_2.
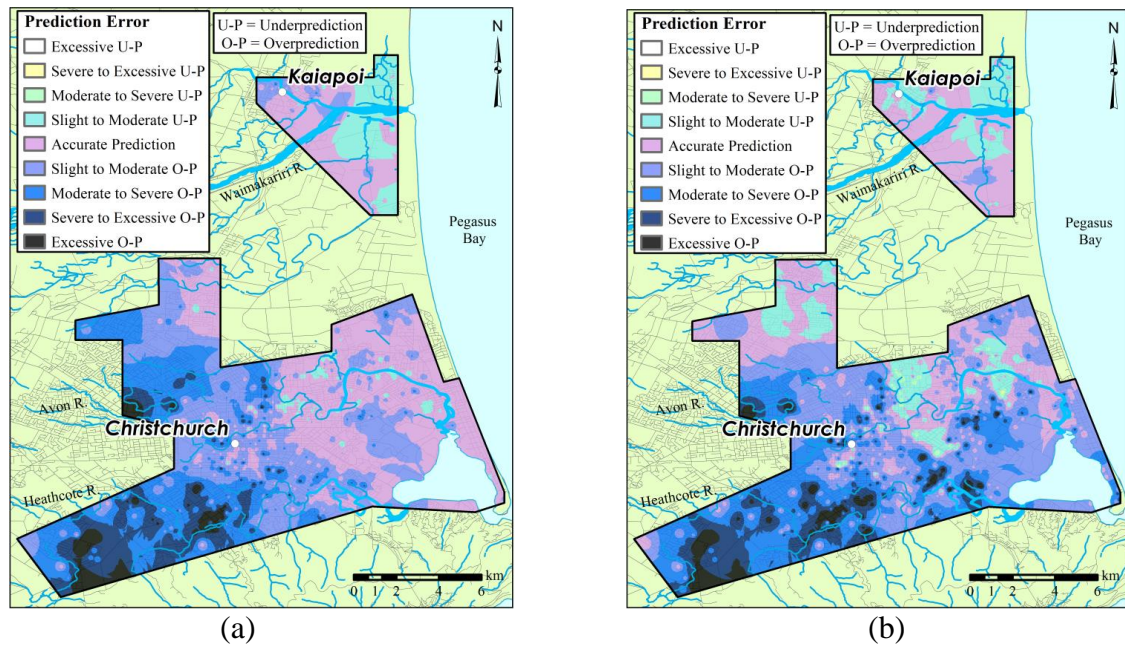
Figure 1: Liquefaction severity prediction errors for the (a) $M_w7.1$ Darfield and (b) $M_w6.2$ Christchurch New Zealand earthquakes (Maurer et al., 2014).

In an effort to capture the positive aspects of both the LPI and Ishihara H_1-H_2 liquefaction damage potential frameworks, Maurer et al. (2015a) proposed the LPI_{ISH} framework, which is a mathematical merger of the two frameworks (van Ballegooy et al., 2015):

$$\text{LPI}_{ISH} = \int_{H_1}^{20m} F(FS) \frac{25.56}{z} dz \tag{2a}$$

where

$$F(FS) = \begin{cases} 1 - FS & \text{if } FS \leq 1 \bigcap H_1 \cdot m \, (FS) \leq 3 \\ 0 & \text{otherwise} \end{cases} \tag{2b}$$

and

$$m(FS) = \exp\left(\frac{5}{25.56(1-FS)}\right) - 1 \tag{2c}$$

In Eqn. (2), H_1 is defined the same as H_1 in the Ishihara (1985) framework, and z is the depth to the layer of interest in meters below the ground surface. The most notable differences in the LPI and LPI_{ISH} frameworks are that the latter accounts for the relative thickness of the liquefied stratum and the non-liquefied crust on surficial manifestations via the additional criterion on F when $FS \leq 1$ and the depth weighting factor is proportional to $1/z$ (which is implied by the shape of the Ishihara H_1-H_2 curves), as opposed be being linear. Specific to the depth weighting factor, in the LPI_{ISH} framework shallower liquefied layers contribute more to surficial manifestations than predicted by the LPI framework.

To assess the relative efficacy of the LPI versus LPI_{ISH} frameworks, Maurer et al. (2015a) analyzed 60 case histories from the 1989 Loma Prieta (USA), 1994 Northridge (USA), 1999

Kocaeli (Turkey), 1999 Chi-Chi (Taiwan), 2010 Darfield (New Zealand), and 2011 Christchurch (New Zealand) earthquakes. The results showed that LPI and LPI$_{ISH}$ performed equally well in predicting true positives (i.e., cases where manifestations were observed as predicted), with 94% of such cases correctly identified with either index. However, LPI$_{ISH}$ demonstrated improvement over LPI in reducing false positives (i.e., cases where manifestations were predicted but not observed), with LPI framework having a false positive prediction rate of 69% versus 0% for LPI$_{ISH}$ framework. Furthermore, Maurer et al. (2016) analyzed data from the approximately 7000 case histories from the CES. The results again showed that LPI$_{ISH}$ framework had superior predictive capabilities over LPI framework.

Despite the superior performance of the LPI$_{ISH}$ framework, both the LPI and LPI$_{ISH}$ frameworks consistently over-predicted the severity of the surficial liquefaction manifestations in profiles having interbedded plastic silt or clay layers, inferred from analysis of CPT soundings (Maurer et al., 2015b). The plastic soils likely limit propagation of liquefied soil to the ground surface, thus minimizing surficial manifestations. Additionally, neither the LPI nor the LPI$_{ISH}$ frameworks were able to accurately predict the severity of lateral spreading. This is not surprising because topographic factors influencing severity of lateral spreading are not included in either the LPI or LPI$_{ISH}$ frameworks. As such, further development of the LPI$_{ISH}$ framework is needed to properly account for the characteristics of the non-liquefied layers in a profile on severity of surficial manifestations and topographic factors that influence the severity of lateral spreading. This work is in process.
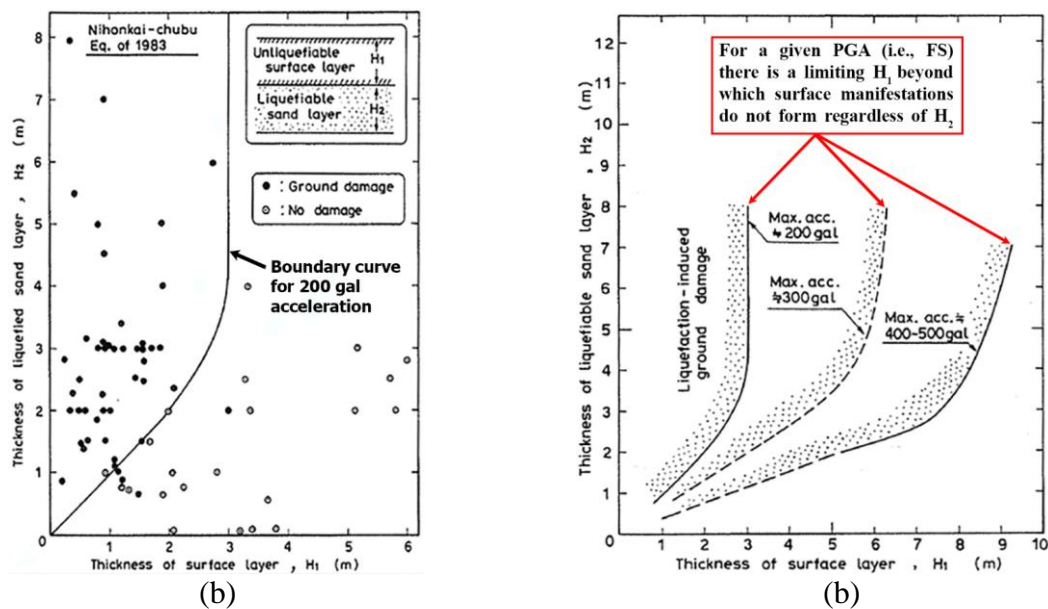
Figure 2: (a) Conditions of subsurface soil stratification discriminating between occurrence and non-occurrence of ground rupturing due to liquefaction (200 gal PGA); (b) Boundary curves proposed for identification of liquefaction-induced damage. (Ishihara, 1985).

CONCLUSIONS

The Ishihara (1985) H_1-H_2 curves were used to derive an alternative index for assessing liquefaction hazard, LPI$_{ISH}$. The H_1-H_2 curves imply that (1) a power-law depth weighting function is more appropriate than the linear form used in the LPI framework; and (2) the F-parameter (see Eqn. 2b) should account for the limiting thickness of the non-liquefiable crust, beyond which surface manifestations do not form regardless of the thickness of the underlying liquefiable strata. LPI$_{ISH}$ was derived to incorporate these improvements. Its performance was evaluated using liquefaction case histories from the global database and from the CES and compared to that of the LPI framework. LPI$_{ISH}$ was found to be consonant

with observed surface effects and showed improvement over the existing LPI procedure in reducing false-positive predictions (i.e., cases where manifestations were predicted but not observed). However, despite the superior performance further development of the LPI$_{ISH}$ framework is needed to properly account for the characteristics of the non-liquefied layers in a profile on severity of surficial manifestations and topographic factors that influence the severity of lateral spreading. This work is in process.

ACKNOWLEDGEMENTS

REFERENCES

Ishihara, K. (1985). "Stability of natural deposits during earthquakes." *Proc. 11th Intern. Conf. on Soil Mechanics and Foundation Engineering*, San Francisco, CA, USA, 1, pp. 321-376.

Iwasaki, T., Tatsuoka, F., Tokida, K., and Yasuda, S. (1978). "A practical method for assessing soil liquefaction potential based on case studies at various sites in Japan." *Proc. 2nd Intern. Conf. on Microzonation*, San Francisco, CA, USA, pp. 885-896.

Lee, D.H., Ku, C.S., and Yuan, H. (2003). "A study of liquefaction risk potential at Yuanlin, Taiwan." *Engineering Geology*, 71, pp. 97-117.

Maurer, B.W., Green, R.A., Cubrinovski, M., and Bradley, B.A. (2014). "Evaluation of the Liquefaction Potential Index for Assessing Liquefaction Hazard in Christchurch, New Zealand." *Journal of Geotechnical and Geoenvironmental Engineering*, ASCE, 140(7).

Maurer, B.W., Green, R.A., and Taylor, O.-D.S. (2015a). "Moving Towards an Improved Index for Assessing Liquefaction Hazard: Lessons from Historical Data." *Soils and Foundations*, JGS, 55(4), pp. 778-787.

Maurer, B.W., Green, R.A., Cubrinovski, M., and Bradley, B.A. (2015b). "Fines-Content Effects on Liquefaction Hazard Evaluation for Infrastructure in Christchurch, New Zealand." *Soil Dynamics and Earthquake Engineering*, 76, pp. 58-68.

Maurer, B.W., Green, R.A., Cubrinovski. M., and Bradley, B.A. (2016). "Lessons in Liquefaction Hazard Assessment Resulting from the Canterbury, New Zealand, Earthquake Sequence." Geotechnical and Structural Congress 2016, Phoenix, AZ, 14-17 February. (*abstract*)

Seed, H.B. and Idriss, I.M. (1971). "Simplified procedure for evaluating soil liquefaction potential." *Journal of the Soil Mechanics and Foundation Division*, ASCE, 97(9), pp. 1249-1273.

Toprak, S. and Holzer, T. (2003). "Liquefaction potential index: field assessment." *Journal of Geotechnical and Geoenvironmental Engineering*, ASCE, 129(4), pp. 315-322.

van Ballegooy, S., Green, R.A., Lees, J., Wentz, F., and Maurer, B.W. (2015). "Assessment of Various CPT Based Liquefaction Severity Index Frameworks Relative to the Ishihara (1985) H_1-H_2 Boundary Curves." *Soil Dynamics and Earthquake Engineering*, 79(Part B), pp. 347–364.

Whitman, R.V. (1971). "Resistance of soil to liquefaction and settlement." *Soils and Foundations*, 11(4), pp. 59-68.

MECHANISM OF INTERACTION BETWEEN DEBRIS FLOWS AND BARRIERS: CENTRIFUGE MODELLING

C. W. W. Ng[1], D. Song[1], C. E. Choi[1], J. S. H. Kwan[2] and R. C. H. Koo[2]

[1] Department of Civil and Environmental Engineering, The Hong Kong University of Science and Technology
[2] Geotechnical Engineering Office, Civil Engineering and Development Department, Hong Kong SAR

BRIEF INRODUCTION

Debris flows surge downhill under large momentum and entrain objects, including boulders, in their paths. To mitigate this hazardous phenomenon, structural countermeasures such as rigid reinforced concrete barriers and steel flexible barriers are commonly installed along the predicted flow paths. These barriers are designed to resist both the bulk flow mass and discrete boulder loading (Volkwein *et al.*, 2011; Proske *et al.,* 2011). For practical designs, the following hydrodynamic equation is commonly used to estimate loading from the bulk flow mass (Kwan 2012):

$$F_{\mathrm{d}} = \alpha \rho v^2 \sin \beta \, hw \tag{1}$$

where F_d is the bulk debris impact force, α is the dynamic pressure coefficient, ρ is the debris density, v is the debris velocity, β is the angle between the barrier and impact orientation, h is the debris thickness and w is the channel width. The main assumptions in the hydrodynamic equation are uniform flows with a constant impact velocity and a constant impact area for incompressible flows. The impact force of boulders on a reinforced concrete wall is usually estimated using Hertzian contact theory (Kwan, 2012; Ng *et al.,* 2016a):

$$F_{\mathrm{b}} = K_{\mathrm{c}} 4000 v^{1.2} r^2 \tag{2}$$

where F_b is the impact force of boulders, K_c is the load reduction factor, v is the boulder velocity and r is the boulder radius. The Hertz equation assumes that during impact strains are within the elastic limit, the contact area is much smaller than the contacting bodies, and the surfaces are frictionless.

Simplified design equations have been proposed and adopted for estimating debris flow loading, but there is no reliable way to verify their performance. This is because of the poor temporal predictability of natural debris flows and the inherent difficulty in modelling debris flows at a realistic scale (Iverson, 2015). These factors have hindered our understanding of the impact mechanisms of debris flows on rigid and flexible barriers. Further complicating matters is that debris flows comprise mixtures of soil, water and boulders. Each component of the debris flow mixture can vitally influence the flow dynamics (Iverson, 1997; Iverson and George, 2014). However, it remains unclear how frictional stress from the solid phase, or how viscous stress from the interstitial fluid influences barrier impact dynamics (Cui *et al.*, 2015). Furthermore, the impact behaviour of the most adverse impact scenario of boulder-entrained flow fronts, via reserve segregation (Zhou and Ng, 2010), remains poorly

understood. To effectively design debris flow barriers, it is necessary to elucidate the fundamental impact behaviour of simplified flows as a starting point, specifically frictional dry sand, viscous fluid, two-phase and bouldery flows.

In order to study the impact of debris flows on barriers systematically in a controlled manner and to ease the interpretation of test data, the centrifuge modelling technique is adopted (Ng, 2014; Ng *et al*., 2016b; Ng *et al.,* 2016c). This technique allows the impact energy, flow volume, and stress state of the flowing sediment to be scaled appropriately, so that meaningful results can be obtained on how debris flows interact with barriers upon impact. In this extended abstract, the influence of flow composition on debris impact on a rigid as well as a novel flexible barrier (Ng *et al*., 2016b) is investigated in a geotechnical centrifuge and major test results are reported and discussed. The differences in the impact dynamics of dry frictional flows, viscous flows, two-phase flows, and boulder-entrained flows are compared and highlighted.

GEOTECHNICAL CENTRIFUGE MODEL TESTS

The 400 g-ton Geotechnical Centrifuge Facility (GCF) at the Hong Kong University of Science and Technology was adopted. This beam centrifuge has an arm radius of 4.2 m (Ng, 2014). All tests were conducted at 22.4g using a model container with plan dimensions of 1245 mm × 350 mm and a depth of 851 mm. A 25° slope with a width of 233 mm and a length of 1000 mm was installed inside the model container. Either a flexible or rigid barrier was installed perpendicularly on the model slope. Figures 1a and 1b show the front view of the 200 mm tall model flexible barrier and the spring elements mounted at the back of a partition to replicate prototype cable load-displacement, respectively. Load cells and laser sensors were installed to measure axial load and displacement in each model flexible barrier cable, respectively. More details of the novel model flexible barrier are available from Ng *et al.* (2016b). To model the impact on a rigid barrier, a cantilevered steel plate was used. The model rigid barrier was 10 mm thick, 200 mm high and 233 mm wide. The rigid barrier was instrumented with strain gauges to measure bending moment. Furthermore, impact kinematics was captured for each centrifuge test using a high-speed camera with a resolution of 1300×1600 pixels and a sampling rate of 640 frames per second.
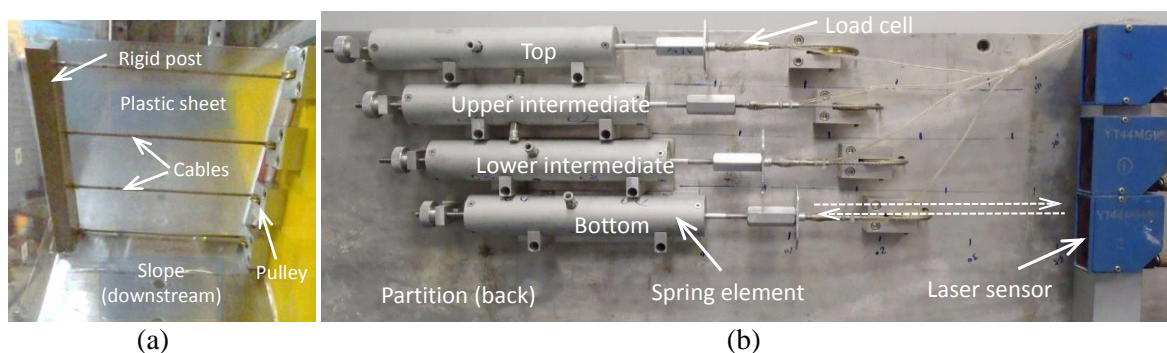
Fig. 1. Model flexible barrier: (a) front view of barrier; (b) spring elements at the back of the partition

Leighton Buzzard (LB) fraction C sand, with a diameter of about 0.6 mm, was used in the tests. The bulk density of sand was about 1530 kg/m^3. The internal and interface friction angles of sand were 31° and 22.6°, respectively. The viscous liquid had a specific viscosity of 11.3 Pa·s and a density similar to that of sand. Sand-liquid mixtures were used to model the two-phase impact on the rigid barrier. Mixtures of LB sand and glass spheres having a diameter of 39 mm were adopted to model boulder-entrained flows. A summary of the tests is given in Table 1.

Table 1. Test programme for rigid and flexible barriers (dimensions in model)

Test ID	Description	Material
FS	Flexible barrier + sand	Dry sand (LB fraction C)
FL	Flexible barrier + liquid	Viscous liquid, viscosity 11.3 Pas
RL		Viscous liquid (Solid fraction 0%)
RSL20	Rigid barrier + sand-liquid mixture	Solid fraction 20%
RSL40		Solid fraction 40%
RSL50		Solid fraction 50%
RB39	Rigid barrier + bouldery debris	Glass sphere (39 mm)
RB39S		Glass sphere (39 mm) and dry sand

KEY RESULTS

All dimensions given in this section are in prototype unless stated otherwise. Figure 2 compares the measured maximum flexible barrier cable loads induced by the impact of a dry sand flow (test FS) and a viscous liquid flow (test FL). A reference line using the hydrodynamic equation (1) with $\alpha = 2.0$ (Kwan and Cheung, 2012) is shown to compare α values of 0.9 and 0.8 back-analysed from the measured loads at the bottom cable for viscous and sand flows, respectively. It should be cautioned that the load corresponding to $\alpha = 2.0$ and the back-analysed α values are calculated based on loaded areas estimated based on the debris impact depth observed from high-speed camera images. A certain level of uncertainty in data interpretation may be considered. The back-analysed α values are slightly less than unity, which is the theoretical value for incompressible flows impacting a constant area of a flexible barrier at a constant and uniform velocity. The slightly higher measured loading from the viscous flow than that from the dry sand flow was likely attributed to the former's significantly lower compressibility.
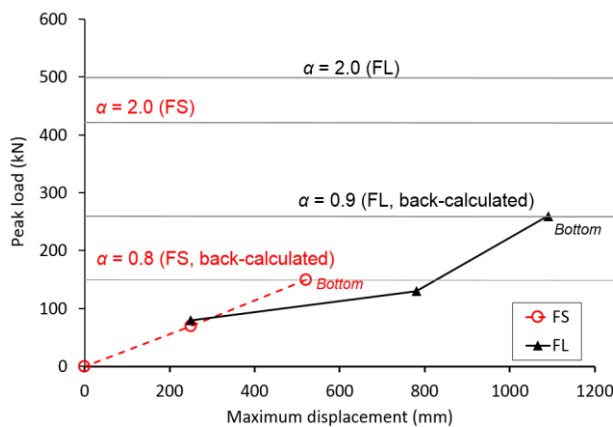
Fig. 2: Maximum flexible barrier cable loads and displacements for single-phase flows
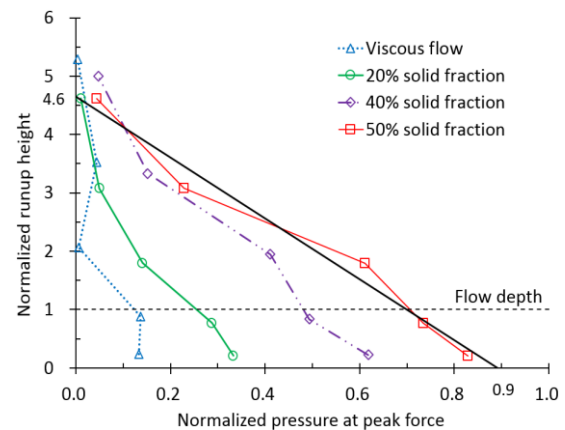
Fig. 3: Rigid barrier pressure profile with barrier height for two-phase flows

Figure 3 shows the normalized impact pressure at peak force for flows with different solid fractions measured along the normalized height of the rigid barrier. The measured pressure was normalized by ρv^2, whereas the run up height was normalized by the flow depth (h) before impact. Flows with a larger fraction of solids induced a larger normalized peak force on the rigid barrier. This is because the static load from dead zones (deposited solids) at the base of the barrier increased with the fraction of solids (Faug *et al.*, 2002).
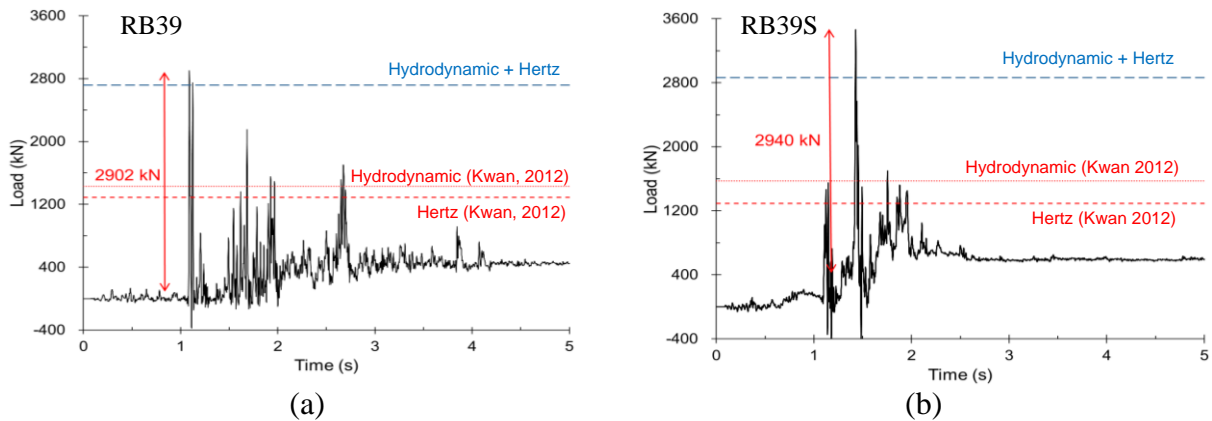
Fig. 4: Impact loads on a rigid barrier from: (a) a boulder flow (RB39) and (b) a boulder-sand flow (RB39S)

Figure 4a shows the measured load from a 0.9 m boulder flow (RB39) impacting the rigid barrier. Reference lines for the hydrodynamic equation (1) for the bulk flow mass (assuming $\alpha = 2.5$ for a rigid barrier), the Hertz equation (2) for a single 0.9 m boulder, and the superposition of Hertz and hydrodynamic loading are shown for comparison purpose. Again, a certain level of uncertainty in data interpretation may be considered in establishing the debris impact depth for calculation of the hydrodynamic loading. Measurements show that a large number of high impulses were induced during the impact process. These recorded impulses were caused by discrete boulder impacts and few of recorded ones were larger than the sum of calculated loads using equations (1) and (2).

Figure 4b shows measured loads from the impact of a boulder-sand flow (RB39S). Slightly fewer impulses were induced on the barrier by the boulder-sand flow than the boulder-only flow (RB39). This may be due to the sand within the voids of the boulder-sand flow attenuating the boulder impulse loads more efficiently. Similar to test RB39, however, very few of recorded ones were larger than the sum of calculated loads using equations (1) and (2).

CONCLUDING REMARKS

A novel series of centrifuge tests of debris flow interaction on barriers were conducted. The results reveal the significance of solid fraction of debris flows in determining the dynamic impact load. Observations of the centrifuge tests provide new insight for rationalise barrier design guidelines.

ACKNOWLEDGEMENTS

REFERENCES

Cui, P., Zeng, C. and Lei, Y. (2015). Experimental analysis on the impact force of viscous debris flow. *Earth Surface Processes and Landforms*, 40(12): 1544-1655.

Iverson, R.M. (1997). The physics of debris flows. *Reviews of geophysics,* 35(3): 245-296.

Faug, T., Lachamp, P. and Naaim, M. (2002). Experimental investigation on steady granular flows interacting with an obstacle down an inclined channel: Study of the dead zone upstream from the obstacle. Application to interaction between dense snow avalanches and defense structures. *Natural Hazards and Earth System Sciences*, 2(3/4): 187-191.

Iverson, R.M. (2015). Scaling and design of landslide and debris-flow experiments. *Geomorphology,* 244, 9-20.

Iverson, R.M. and George, D.L. (2014). A depth-averaged debris-flow model that includes the effects of evolving dilatancy. I. Physical basis. *Proceedings of the Royal Society of London A: Mathematical, Physical and Engineering Sciences,* 470, No. 2170, 20130819.

Kwan, J.S.H. (2012). *Supplementary technical guidance on design of rigid debris-resisting barriers. GEO Report No. 270.* Geotechnical Engineering Office, HKSAR Government.

Kwan, J.S.H. and Cheung, R.W.M (2012). *Suggestions on Design Approaches for Flexible Debris-resisting Barriers*. GEO Report DN 1/2012, 91p.

Ng, C.W.W., Choi, C.E., Su, A.Y., Kwan, J.S.H. and Lam. C. (2016a). Large-scale successive impacts on a rigid barrier shielded by gabions. *Canadian Geotechnical Journal*, (accepted).

Ng, C.W.W., Song, D., Choi, C.E., Koo, C.H. and Kwan, J.S.H. (2016b). A novel flexible barrier for simulating landslide debris impact in centrifuge. *Géotechnique Letters*, (accepted)

Ng, C.W.W., Song, D., Choi, C.E., Liu, L.H.D., Kwan, J.S.H., Koo, R.C.H. and Pun, W.K. (2016c). Impact mechanisms of granular and viscous Flows on rigid and flexible barriers, *Canadian Geotechnical Journal*, (accepted).

Ng, C.W.W. (2014). The state-of-the-art centrifuge modelling of geotechnical problems at HKUST. *Journal of Zhejiang University A (Applied Physics & Engineering)*, 15(1): 1-21.

Proske, D., Suda, J. and Hübl, J. (2011). Debris flow impact estimation for breakers. *Georisk*, 5(2), 143-155.

Volkwein, A., Wendeler, C. and Guasti, G. (2011). Design of flexible debris flow barriers. In *5th International Conference on Debris-Flow Hazards Mitigation: Mechanics, Prediction, and Assessment*, Padua, Italy, 14 to 17 June, 1093-1100.

Zhou, G.D. and Ng, C.W.W. (2010). Numerical investigation of reverse segregation in debris flows by DEM. *Granular Matter* 12(5), 507-516.

TOPOGRAPHIC AMPLIFICATION OF GROUND MOTIONS: A CASE STUDY OF HONG KONG

Gang Wang, Chunyang Du and Duruo Huang

Department of Civil and Environmental Engineering
The Hong Kong University of Science and Technology

BRIEF INRODUCTION

Amplification of seismic waves due to surface topography and subsurface soils has often been observed to cause intensive damage in past earthquakes. Due to its complexity, topography amplification has not yet been considered in most seismic design codes, with a few exceptions such as the Eurocode 8. Using a simplified classification of ridge geometry and slope angle, EU8 prescribes a topographic amplification factor which is frequency-independent and limited to a maximum increase of 40%. On the other hand, significantly larger topography amplification in order of 10 to 20 has been observed through instrumented data. As is against EU8, the topography amplification is also found to be frequency-dependent (Burjanek *et al.* 2014).

Hong Kong is a mountainous region where many buildings and infrastructures were built on hill tops and steep slopes due to paucity of land. The latest Chinese Seismic Code (China Code 2010) prescribes a peak ground acceleration of 0.12 g for the 475-year return period on "rock" outcrop. It is noted that the obtained design ground-motion are only applicable for a level ground. To date, scientifically based standard for seismic design of buildings on steep slopes is still not available. It is expected that the intensity of shaking could be much larger on hill slopes due to topographic amplification. In particular, the amplified spectral accelerations at long periods could have significant implication for designing and evaluating tall buildings on steep slopes.

METHODOLOGY AND KEY RESULTS

Extensive numerical studies have been conducted to improve our understanding of topography amplification in the lack of well instrumented data (e.g. Sitar and Clough 1983, Ashford et al. 1997). In these analyses, simple 2D topography geometries are often used and the soil is assumed to be a uniform viscoelastic material. The numerical simulations usually result in an amplification factor less than 2, which tends to underestimate the field data.

Recently, Du *et al.* (2016) analyzed spectral amplification of ground motions on a 2D rock ridge (Figure 1). The rock is assumed to be elastic with a shear wave velocity Vs=1000 m/s, and the surface soil layer on top of the rock is assumed to be 0 to 10 m deep with Vs=200 m/s. The soil nonlinearity is modelled using the equivalent linear method. The result further confirmed that a low velocity zone near the slope surface can have a significant impact on the amplification of the spectral accelerations (SA). Apparently, such amplification is frequency dependent. Figure 2 compares the "topography amplification effects" (SA at the rock ridge top vs. SA at rock free field, without soils), "soil amplification effects" (SA at free field with soils vs. SA at free field without soils), as well as the "total amplification effects" (SA at ridge top with soils vs SA at free field without soils). The numerical analyses show that the

"total amplification" can be approximated as the "topography amplification" factor multiplies the "soil amplification" factor. In Fig. 2, the estimated vibration period of the soil layer is highlighted using a black line. The fundamental period of the ridge is estimated to be 0.3 s. Amplification of the peak ground acceleration (PGA) varies from 1.5 to 2.5 depending on the thickness of the soil layer. When soil depth is 7.5 m, the period of the soil layer is close to that of the ridge (0.3 s), spectral amplification at that period reaches as large as 4, while amplification of the PGA is around 2 in that case.
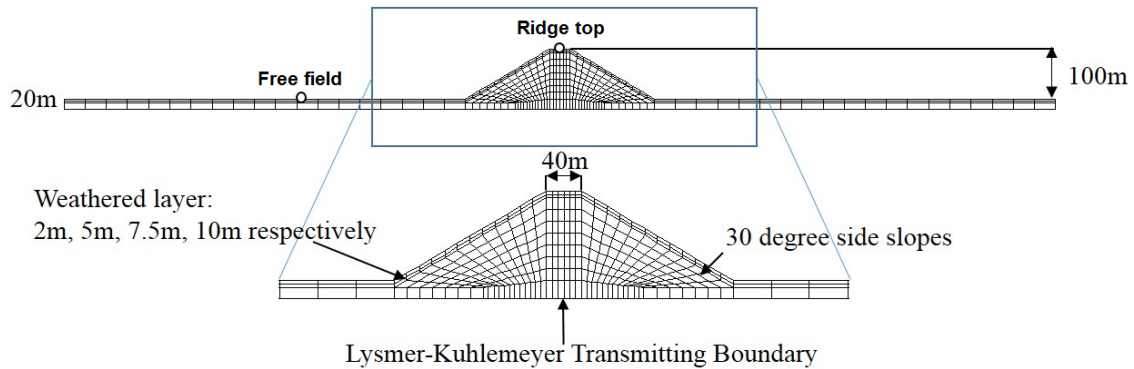
Figure 1: 2D numerical simulation considered weathered soil layers
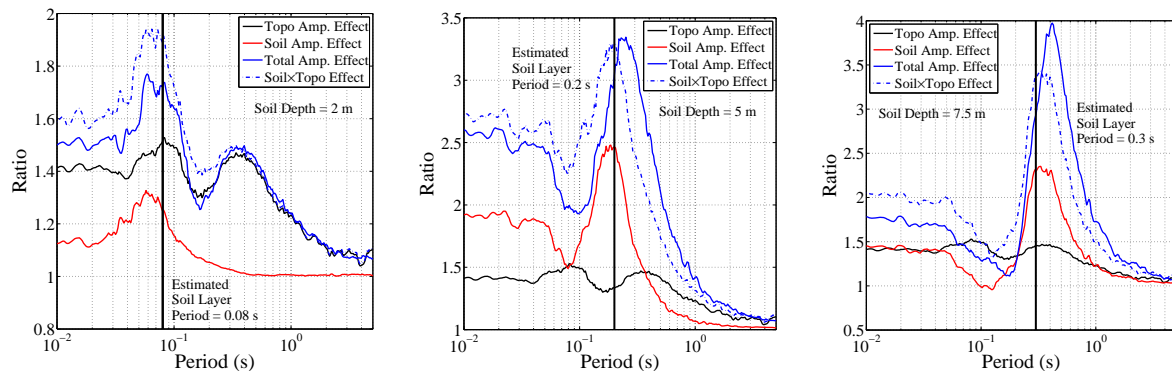
Figure 2: Spectral amplification ratio for cases with different soil depths

Compared with the above simple 2D example, numerical simulations incorporating realistic 3D topography and subsurface soil conditions is more attractive. However, 3D site response analysis is rarely done in the geotechnical community. There are several challenges to be addressed: (1) since 3D topography is complex, it is important to parameterize the ground-motion amplification using simple topographic measures. (2) It is important to find well-instrumented field data to validate and calibrate the numerical modeling; (3) Subsurface soil distribution can be highly heterogeneous and variable. Yet, we typically have little information on the subsurface stratigraphy of a region. It is challenging to adequately quantify the uncertainties associated with the numerical modeling.

In this project, we study ground-motion amplification on 3D topography based on 3D Spectral Element Method (SEM), using Hong Kong as a local testbed site. The SEM is a high-order finite element method that uses a special nodal basis. The SEM method is superior to the commonly used finite-difference method in many ways. The SEM uses a pseudo-spectral method to achieve high accuracy in modeling wave propagation. If a polynomial degree of 4 is used in interpolation, one SEM element per wavelength has been found to be very accurate. In other words, if the element size is 5 m and shear wave velocity is 200 m/s, the highest frequency that SEM can simulate will be up to 40 Hz. As a comparison, the finite difference method will be very expensive since a great number of grid points will be needed to achieve the same accuracy. The SEM can be easily implemented in parallel computing

because its mass matrix is diagonal (Komatitsch and Vilotte 1998). Because of these advantages, the SEM has been recently widely used in global and regional scale wave simulation with a simulation domain up to hundreds of kilometers (He *et al.* 2015).

Figure 3 illustrated a constructed 3D SEM model of the western part of Hong Kong Island. The dimension of the computational domain is 8 km × 9 km. In general, the rocks in Hong Kong Island consist of volcanics intruded by granite. The volcanic and granitic rocks are subjected to extensive weathering. The hill slopes are generally covered by colluvium (0-15 m thick) on the surface, underlain by weathered rocks varying significantly from 10 m to 50 m, but can be up to 90 m locally. The highest point, Victoria Peak, is 554 m above the sea level.
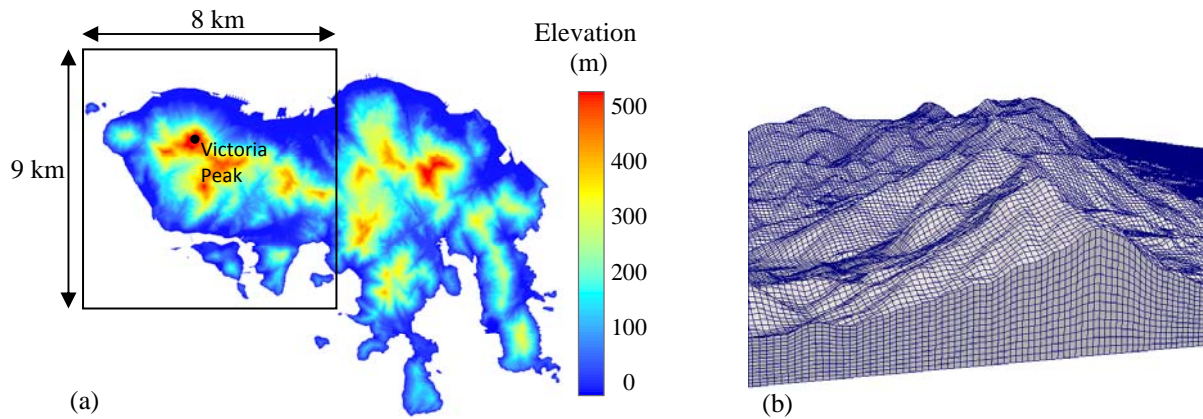
Figure 3: (a) Hong Kong Island elevation map and study region, (b) 3D SEM mesh illustration

High resolution Digital Elevation Model (DEM) is used to extract elevation data in numerical simulations and topographic curvature calculation. The resolution of the elevation model is fine enough to cover the very detailed topographic features. Uniform ground excitation is input at the base of the model. Lysmer-Kuhlemeyer transmitting boundary is implemented to mimic the infinite half space at the bottom, and absorbing boundaries are used on the sides to avoid wave reflection from the boundary. The mesh resolution can accurately capture wave motions well above 10 Hz. Material in the simulation is assumed to be uniform and linearly elastic with Vs=1000 m/s, so only the topography effects is studied at the present stage.

First, Ricker wavelet is used as acceleration input in the simulation, with predominate frequency of the wavelet varying from 0.5 Hz to 5 Hz. The amplification factor is defined as the PGA recorded on the slope surface divided by the PGA recorded on the level ground, as shown in Figure 4.
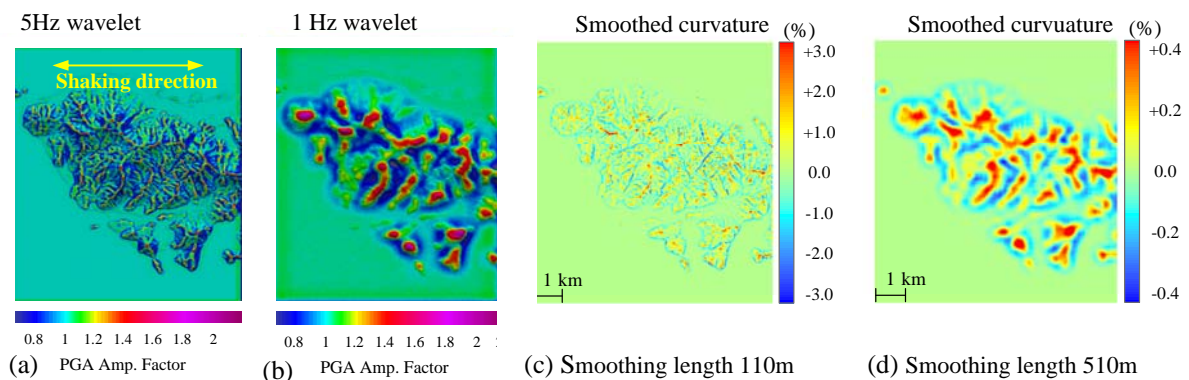
Figure 4: PGA amplification factor maps excited by (a) 5 Hz wavelet; (b) 1 Hz wavelet; (c) and (d): smoothed curvatures using different smoothing lengths

Figs. 4 (a)(b) show amplification factor maps under 5 Hz and 1 Hz wavelet excitation, where the maximum amplicaiton factor is 2.1 and 1.9, respectively. It is obvious that the amplification/de-amplification is closely related to very localized topographic features under the high frequency (5Hz) excitation. Figs. 4(c)(d) compares topographic curvatures smoothed using neighborhood data within different smoothing lengths. Apparently, more localized topography (convex/concave) details can be captured if a shorter smoothing length is used.
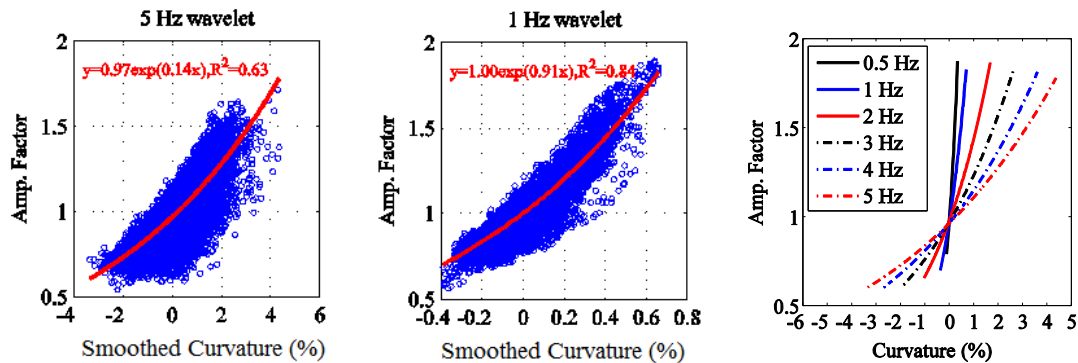
Figure 5: Correlation between amplification factor and smoothed curvature (smoothing length=L/2)

Similar patterns in Fig. 4 suggest a parameteric relationship between the ground-motion amplification and smoothed curvatures. It is found that the amplification factor (AF) can be best correlated with the smoothed curvature (c_s), if half of the input wavelength is used as the smoothing length. The relationship can be cast into an exponential form:

$$AF(L, c_s) = \exp\left[a(L) \times c_s \times 100\right] \qquad (1)$$

where $a(L) = 9.90 \times 10^{-4} L - 0.083$ and L is the wavelength (in meter, $L = V_s/f$). c_s is the curvature smoothed using L/2. Eq. (4) manifests that the frequency-dependent amplification is related to a scale-dependent topographic feature.
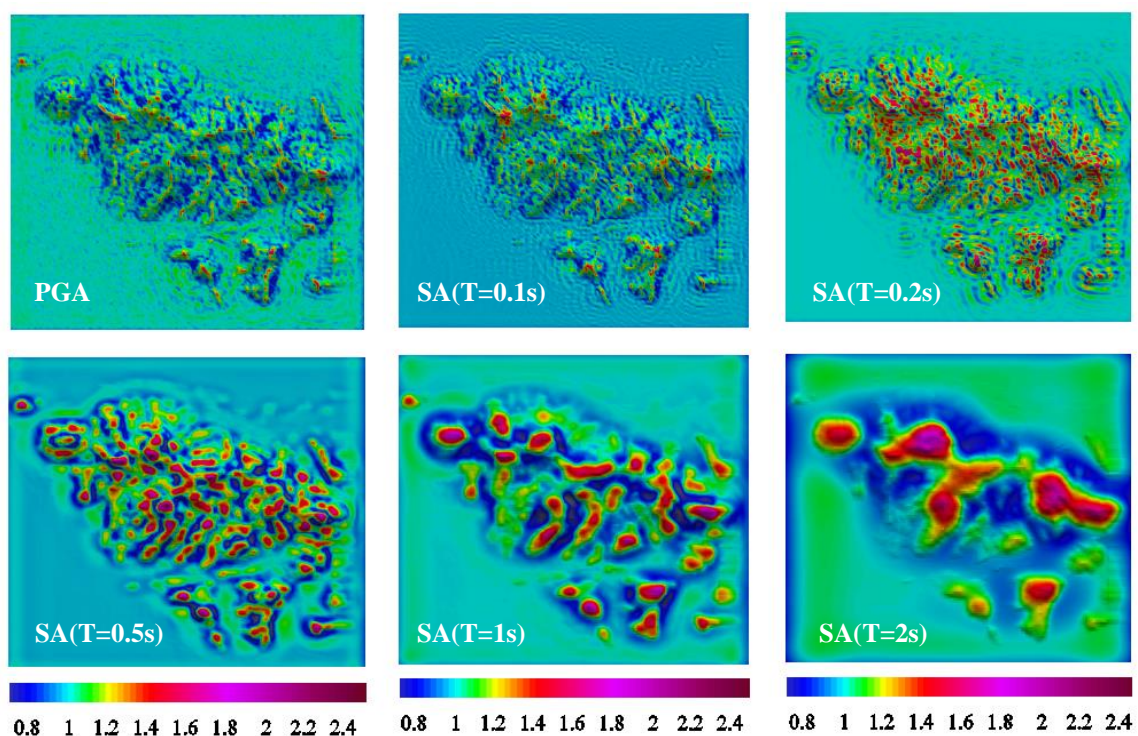
Figure 6: Topography amplification of spectral accelerations at different periods

3D SEM analyses were also conducted using recorded ground motions linearly scaled to fit to the 2475-year-return-period Uniform Hazard Spectrum for Hong Kong (input PGA=0.2 g). Fig. 6 shows the topography amplification of spectral accelerations at different periods (PGA, T=0.1s, 0.2s, 0.5s, 1s, 2s). The amplification pattern is similar to Fig. 4. Maximum amplication factors are 2.2 (PGA, T=0.1 s) to 2.5 (T=0.2 s, 0.5s), 2 (T=1 s) and 1.85 (T=2s).

CONCLUSIONS

We conduct a region-scale 3D numerical simulation to quantify frequency-dependent topographic amplification with a reference to the design ground motions in Hong Kong. The analyses revealed that topography amplification of ground motions is frequency dependent. It can be parameterized using a scale-dependent topographic feature (the smoothed curvature). Amplification of high frequency wave is correlated with curvature smoothed over a small length scale. On the other hand, amplification of long-period waves is correlated with large-scale topography features. The maximum topography amplification generally ranges from 1.8 to 2.5 in the protruded areas, which is larger than EU8 specification. De-amplification of the high-frequency wave is observed in the locally concaved areas even at high elevations.

Inevitably, the numerical simulation will highly depend on the resolution of topography and the subsurface data available. At the present, we are collecting and reviewing borehole information to understand the near-surface geology of the study areas. Emphasis will be placed on investigating the extent of soil cover and weathered rock profiles on the hill top and hill slope, which may have great impact on site amplification as implied by the 2D analyses on simple geometry. Extensive parametric study needs to be performed to quantify the uncertainty of the numerical simulations through varying stratification and properties of soil/rock units.

ACKNOWLEDGEMENTS

REFERENCES

Ashford, S.A., Sitar, N., Lysmer, J. and Deng, N. (1997). "Topographic effects on the seismic response of steep slopes". *Bulletin of the seismological society of America* 87(3),701-709.

Burjanek, J., Edwards, B., Fah, D. (2014). "Empirical evidence of local seismic effects at sites with pronounced topography: a systematic approach." *Geophysical Journal International*, 014.

China Code (2010). "Code for seismic design of buildings", GB50011-2010, Ministry of Construction, P.R. China.

Du, C.Y., Wang, G., Koo, R.C.H., and Kwan, J.S.H. (2016). "Topography effects on design response spectrum", The 7th Guangdong-Hong Kong-Macau Seminars on Earthquake Science and Technology, 7-8 April 2016, Hong Kong (in Chinese).

He, C.H., Wang, J.T., Zhang, C.H., and Jin, F. (2015). "Simulation of broadband seismic ground motions at dam canyons by using a deterministic numerical approach." *Soil Dynamics and Earthquake Engineering* 76. pp.136-144.

Komatitsch, D. and Vilotte, J.P. (1998). "The spectral element method: An efficient tool to simulate the seismic response of 2D and 3D geological structures." *Bulletin of the seismological society of America* 88(2). pp.368-392.

Sitar, N., Clough, G.W. (1983). "Seismic response of steep slopes in cemented soils." *Journal of Geotechnical Engineering* 109, No. 2, pp. 210-227.

SUSTAINABLE LIQUEFACTION MITIGATION: DRIVEN TIMBER DISPLACEMENT PILES

Armin W. Steudlein
Oregon State University, Corvallis, OR, USA

BRIEF INTRODUCTION

Considerable efforts are made by geotechnical engineers and specialty contractors to mitigate the deleterious effects of earthquake-induced liquefaction using various forms of accepted ground improvement methods. However, many methods require the use of mined aggregate or cementitious materials, or some combination of both. These materials allow for efficiencies over less favorable improvement methods, such as full excavation and replacement, but are not as sustainable as other approaches. Commonly-used ground improvement methodologies seek to densify, reinforce, or densify and reinforce liquefiable soils; the latter approach can be achieved using displacement piles. The contractive response of cohesionless soils to displacement pile installation has been recognized for some time (Robinsky and Morrison 1964). Meyerhof (1959) and Broms (1966) have shown that installation of piles in loose sand resulted in some degree of densification up to 6 pile diameters away from the pile. Unfortunately, little research has been performed concerning the magnitude and distribution of densification around displacement piles since then, particularly with regard to the influence of fines content on densification. Timber piling is a renewable material, does not require specialized construction equipment, is durable below the groundwater table, and can mitigate liquefaction when driven to densify and reinforce soils. Studies such as those described herein are required to illustrate the degree of mitigation possible.

METHODOLOGY AND KEY RESULTS

A full-scale field test program of driven timber displacement piles was conducted for the purpose of densification of loose, potentially liquefiable sands and silty sands. Both conventional, and experimental timber piles fitted with pre-fabricated drains (PVDs) to help densify contractive soils during pile installation were assessed in this study. The piles were installed in groups with center-to-center spacing of two to five pile head diameters (Figure 1). Measurements of cone penetration tests (CPTs) revealed the variation of post-installation increases in penetration resistance with decreases in pile spacing (Figure 2). However, long-term measurements showed that pile-spacing dependent reductions in cone penetration resistance following installation can occur, which have been attributed to relaxation of horizontal stresses. Preliminary relationships between the average area replacement ratio and change in corrected cone tip resistance were developed. Pre- and post-improvement standard penetration tests conducted in each of the treated zones confirmed the long-term degree of densification noted using the CPT. Measured pre- and post-installation shear wave velocities indicated that the soil fabric of the previously aged sands was effectively destroyed, and that reduction small strain stiffness is possible in tandem with densification.

Full-scale, controlled blasting field tests were also conducted to study the response of the densified and reinforced ground to blast-induced excess pore pressures. Controlled blasting of
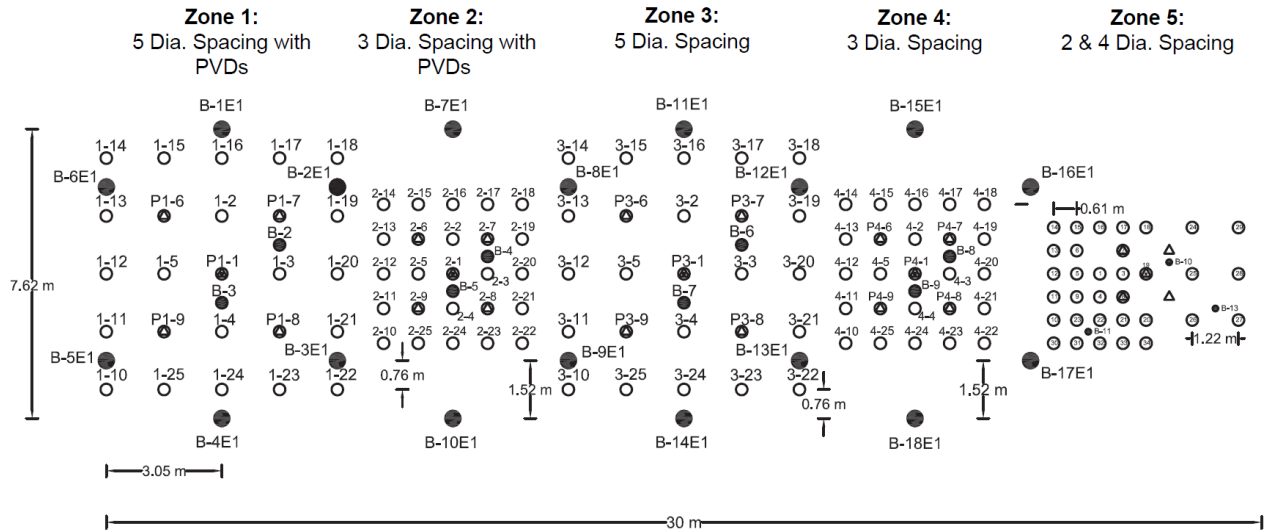
Figure 1: Site layout including pile locations, initial in-situ tests, and blast casing locations.
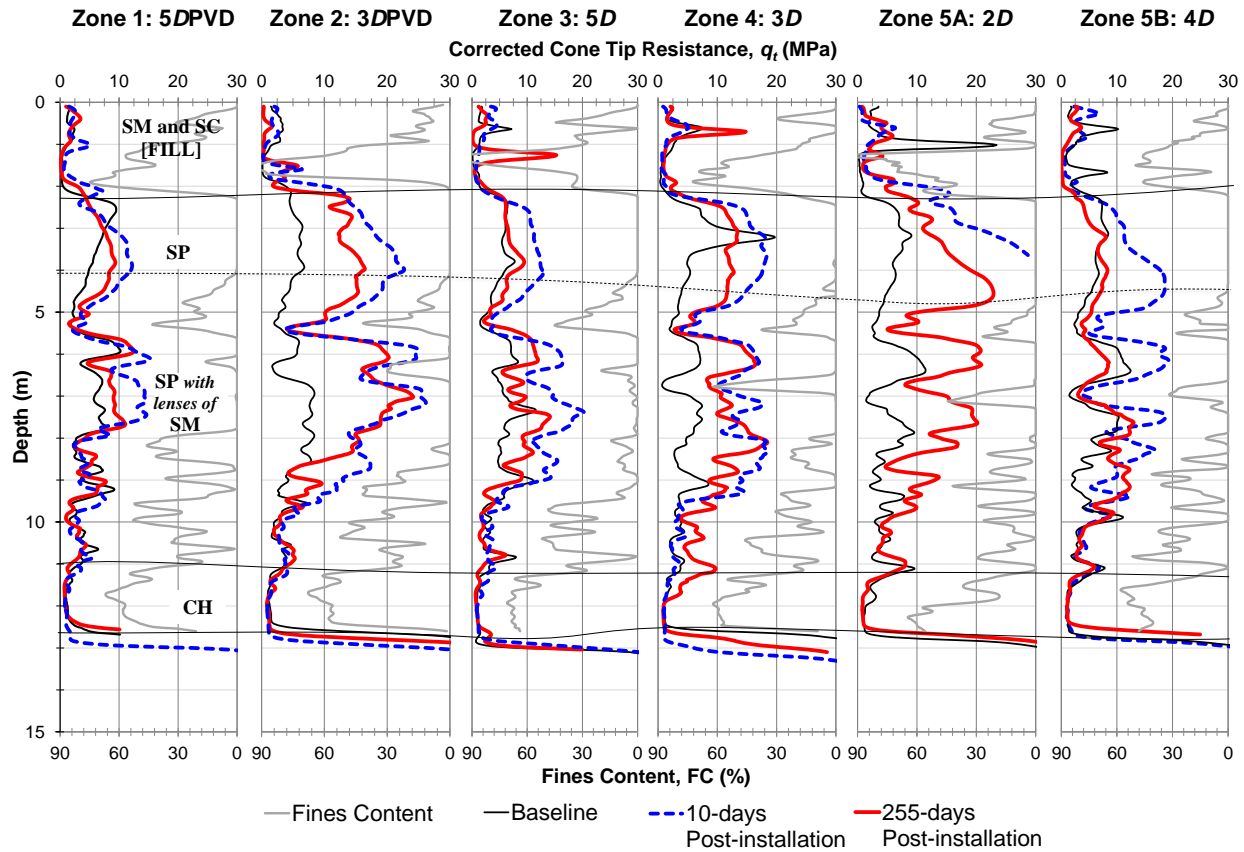
Figure 2: Comparison of corrected cone tip resistance before and 10 and 255 days following pile installation, along with the fines content estimated using the site-specific FC correlation. The average depths of the inner nine piles are 12.1, 9.3, 11.7, 11.1, 10.6, and 11.5 m for Zones 1, 2, 3, 4, 5A, 5B, respectively (adapted from Stuedlein et al. 2016).

unimproved ground using sufficient explosive charges to induce liquefaction and the resulting post-liquefaction settlements measured provided a baseline for comparison against the improved ground. Excess pore pressures generated during blasting in the improved ground were observed to be smaller than that in the unimproved ground, and resulted in

settlements that were generally one-sixth to one-third of that measured in the unimproved ground. Piles tipped into a dense bearing layer settled significantly less than those in the surrounding soil, whereas those that were not founded in a competent layer settled as much as the surrounding soil. Importantly, measured excess pore pressures pointed to a change in response from contractive to dilative during execution of the cyclic detonation pattern, indicating that the improved ground mobilized significant strength during blasting (Figure 3). Finite element analyses calibrated to the unimproved ground response and altered to reflect the observed densification and cyclic resistance produced good estimates of the generation and dissipation of excess pore pressures for the conventional

Figure 3: Example comparison of excess pore pressure response measured for the unimproved control zone to that of improved ground at depths of 4.8 to 5.3 m.

displacement pile-reinforced ground. The results of this field trial are used to illustrate that shear strain compatibility between the improved ground and the displacement piles did not occur during the blast-induced ground motions, indicating that a central assumption in reinforcement-based liquefaction mitigation techniques should be discontinued. The experimental findings in this paper may be broadly applied to displacement piles constructed of materials other than timber.

CONCLUSIONS

A full scale experimental program was conducted to evaluate the degree of liquefaction mitigation possible with driven displacement piling. The test program included various in-situ tests, ranging from penetration testing to controlled blasting. In-situ tests showed the relationship between area replacement ratio or spacing and the degree of densification. Compared to an unimproved control zone, the timber pile treated area performed significantly better to blasting, with lower and dilative excess pore pressures and reduced deformations.

REFERENCES

Broms, B. (1966). "Methods of calculating the ultimate capacity of piles – a summary." *Sols-Soils*, 5(18–19), pp. 21-32.

Meyerhof, G. G. (1959). "Compaction of sands and bearing capacity of piles," *J. Soil Mech. Fndns. Div.*, Vol. 85, *SM6*, pp. 1-30.

Robinsky, E.I. and Morrison, C.F. (1964) "Sand Displacement and Compaction around Model Friction Piles," *Can. Geo. J.*, 1(2), pp. 81 – 93.

Stuedlein, A.W., Gianella, T.N., and Canivan, G. (2016) "Densification of Granular Soils using Conventional and Drained Timber Displacement Piles," *J. Geotech. Geoenv. Engrg.*, *in Press (available online).*

RECENT ADVANCES IN DESIGN OF COMBINED PILE-RAFT FOUNDATION SYSTEM UNDER EARTHQUAKE CONDITIONS

Deepankar Choudhury and Ashutosh Kumar

Department of Civil Engineering, Indian Institute of Technology Bombay, Powai, Mumbai 400076, India. Email: dc@civil.iitb.ac.in, ashusingh@iitb.ac.in

BRIEF INTRODUCTION, METHODOLOGY AND KEY RESULTS

High rise buildings are usually subjected to vertical load due to the superstructure, horizontal load and overturning moment due to wind and earthquake events. Pile foundation is the preferred choice in such loading scenarios. In conventional design, the contribution of raft or pile cap is ignored even if they rest on competent soil strata due to limited understanding of the complex soil-structure interaction and unavailability of validated method of analysis. Recently, several researchers started incorporating the contribution from raft in load sharing for both vertical and lateral loading cases, leading to rise in the demand for performance-based design of the combined foundation system, namely, combined pile-raft foundation (CPRF). This paper discusses recent advances in the analysis and design of CPRF system subjected to earthquake loading conditions. Figure 1 shows the basic mechanism of working principle of CPRF system for static loading conditions as given in the ISSMGE Combined Pile-Raft Foundation Guideline by Katzenbach and Choudhury (2013).
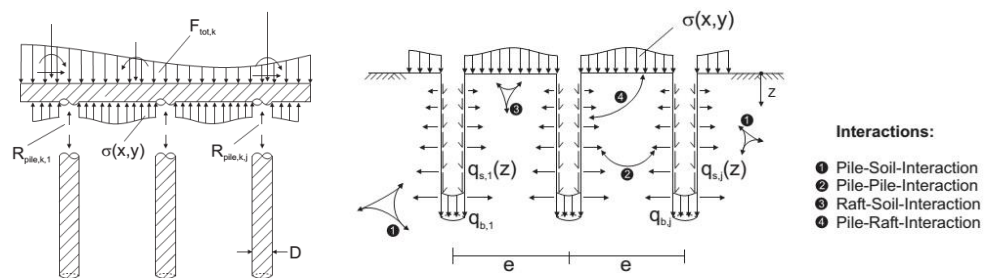
Figure 1: Soil-structure interaction in Combined Pile-Raft Foundation (CPRF) system under static loading conditions (Katzenbach and Choudhury, 2013)
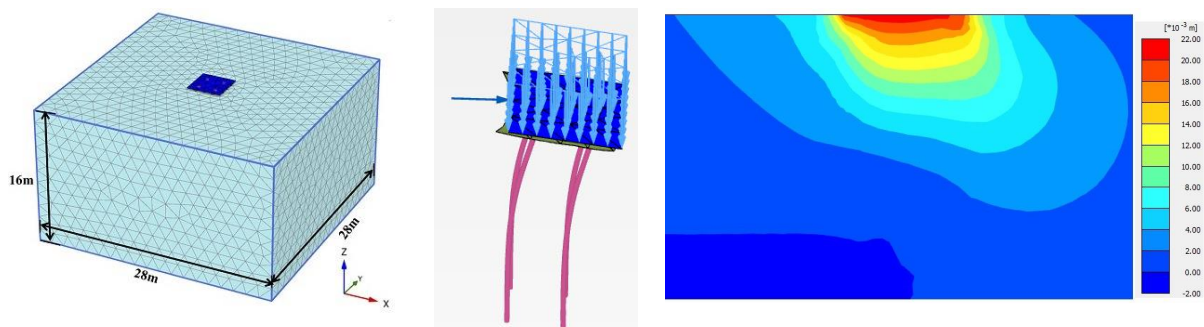
Figure 2: (a) Discretised model of CPRF (b) deformed CPRF model (c) horizontal displacement contour under earthquake loading in PLAXIS3D (Kumar et al. 2016)

Recent research work by Horikoshi et al. (2003) discussed the load sharing mechanism of individual components of CPRF under earthquake excitation. Thereafter, many researchers like Kitiyodom and Matsumoto (2003), Sawada and Takemura (2014), Kumar and Choudhury (2016), Kumar et al. (2016) and Katzenbach et al. (2016) made fruitful contributions to discuss the effect of earthquake loadings on CPRF. Figure 2 shows the discretised CPRF model subjected to 1989 Loma Gilroy earthquake load with deformed shape and deformation contour. The load carried by push-in and pull-out pile under the effect of lateral loading changes with a change in the height of application of lateral load, as shown in Figure 3. Banerjee et al. (2014) stated that lateral bending moment and shear is entirely dependent upon pile rigidity, as shown in Figure 4.
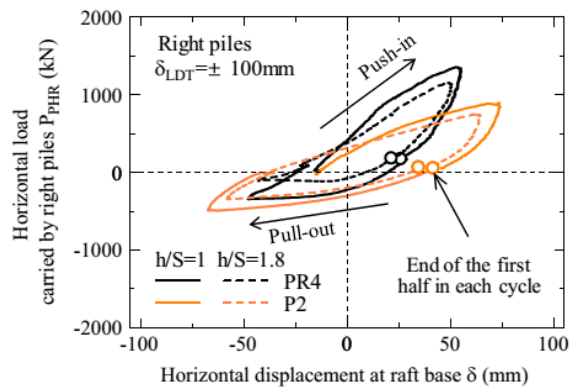
Figure 3: Variation of horizontal load in piles (Sawada and Takemura, 2014)
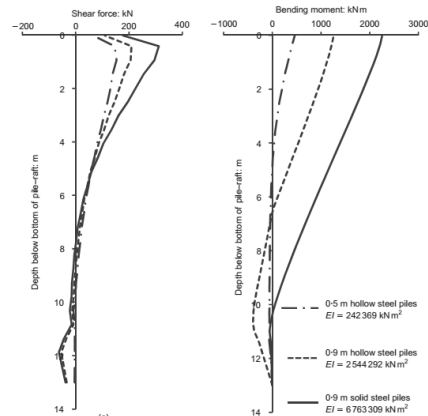
Figure 4: Shear force and bending moment profile under 0.1g (Banerjee et al. 2014)

SUMMARY

The estimation of displacement response and stress resultants like bending moment, shear and axial forces are highly important factors for the design of CPRF. Pile shares a maximum percentage of the lateral load which is unlike the case of vertical load. Initially, soil-raft interaction dominates the lateral load sharing response but at a later stage, pile-soil interaction plays an important role.

REFERENCES

Banerjee, S., Goh. S. H. and Lee, F. H. (2014). "Earthquake-induced bending moment in fixed-head piles in soft clay." *Géotechnique* 64, No. 6, pp. 431-446.

Horikoshi, K., Matsumtoto, T., Hashizume, Y. and Watanabe, T. (2003). "Performance of piled raft foundation subjected to dynamic loading." *Int. J. Phy. Mod. Geotech.* 2, 51-62.

Kitiyodom, P. and Matsumoto, T. (2003). "A simplified analysis method for piled raft foundations in non-homogeneous soils." *Int. J. of Num. and Ana. Meth. Geomechanics* 27, No. 2, pp. 85–109.

Katzenbach, K. and Choudhury, D. (2013). "*ISSMGE Combined Pile-Raft Foundation Guideline*." ISSMGE Technical Committee TC 212 - Deep Foundations, 1-28.

Kumar, A., Choudhury, D. and Katzenbach, R. (2016). "Effect of Earthquake on Combined Pile-Raft Foundation." *International Jounral of Geomechanics*, ASCE, pp. 1–16, 10.1061/(ASCE)GM.1943-5622.0000637.

Kumar, A. and Choudhury, D. (2016). "DSSI analysis of pile foundations for an oil tank in Iraq." *Proc. of the ICE – Geotechnical Engineering, ICE* 169, No. 2, pp. 129–138.

Katzenbach, R., Leppla, S and Choudhury, D. (2016). "*Foundation Systems for High-Rise Structures*" CRC Press, Taylor and Francis Group, UK. (ISBN: 978-1-4978-4477-5), pp. 1-256.

Sawada, K. and Takemura, J. (2014). Centrifuge model tests on piled raft foundation in sand subjected to lateral and moment loads. *Soils and Foundations* 54, No. 2, pp. 126–140.

SLOPE FAILURE EVALUATIONS IN VIEW OF ENERGY

Takaji Kokusho
Professor Emeritus, Chuo University, Tokyo, Japan

SLOPE FAILURES IN VIEW OF ENERGY

Slope failures are normally evaluated by force equilibrium in a potentially sliding soil mass. This can evaluate a safety factor against failure, but cannot predict sliding deformation essential in risk evaluation of slope failures. The Newmark method can evaluate residual displacement of a rigid soil block along a fixed slip surface, though sliding soil may not necessarily behave as a rigid body but deforms continuously developing to flow-type failures.

In order to evaluate slope failures including the flow-type, an energy approach was proposed by the present authors (Kokusho & Kabasawa 2003). In that method, four energies; potential energy change $-\delta E_p$ (minus sign because δE_p always decreases during failure), earthquake energy contributing to slope failure E_{EQ}, dissipated energy in a sliding soil mass E_{DP}, and kinetic energy E_K of the sliding soil mass or their increments are correlated by the following equations;

$$-\delta E_p + E_{EQ} = E_{DP} + E_k , \qquad -\vartriangle\delta E_p +\vartriangle E_{EQ} =\vartriangle E_{DP} +\vartriangle E_k \qquad (1)$$

Note that this equation is also applicable to rain-induced slides if $E_{EQ} = 0$.

According to Eq. (1), once failure starts, the amount of the dissipated energy or mobilized friction coefficient is critical to decide how far it flows. In time increments when earthquake has already ended or for rain-induced failure, ($\Delta E_{EQ} = 0$ or $-\Delta\delta E_p = \Delta E_{DP} + \Delta E_K$), if ΔE_{DP} is smaller than $-\Delta\delta E_p$, then it is clear that ΔE_K is positive and the soil mass accelerates. A shift from slow slide to fast flow may occur not only due to an increase in $-\Delta\delta E_p$ but also due to a decrease of ΔE_{DP} caused by pore-pressure buildup in liquefiable soil and strength loss in high-sensitivity clay. In flow-type failures, soil mass will keep flowing unless the kinetic energy plus the subsequent potential energy change is all dissipated in the sliding soil mass. Namely, if $-\Delta\delta E_p$ is smaller than ΔE_{DP}, then ΔE_K is negative, hence the soil mass decelerates and comes to a halt when the reserved kinetic energy E_K is all consumed.

Thus, if the earthquake energy and the energy dissipation mechanism in flowing soil mass are known, it is possible to evaluate the run-out distance even in flow-type slides by using the energy balance.
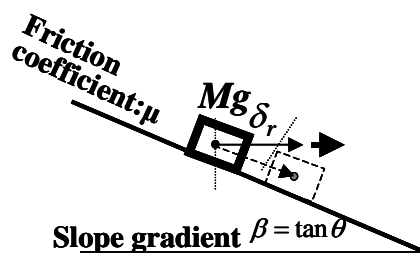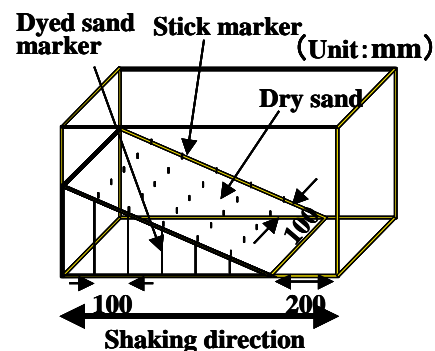
Fig 1. Comparison of models of rigid block and dry sand slope.

RUNOUT DISTANCE EVALUATION BASED ON RIGID BLOCK MODEL

A Newmark-type rigid block model was examined from the viewpoint of energy by Ko-kusho and Ishizawa (2007). The application of the energy balance in Eq. (1) for $E_K=0$ to the rigid block shown in Fig. 1(a) gives the potential energy change $-\delta E_p$ and the dissipated energy due to the block slippage E_{DP} to be correlated with horizontal residual displacement δ_r as;

$$-\delta E_p = \beta Mg\delta_r \ , \qquad E_{DP} = \frac{\mu(1+\beta^2)}{1+\mu\beta}Mg\delta_r \ , \quad E_{EQ} = -(-\delta E_p) + E_{DP} = \frac{\mu-\beta}{1+\mu\beta}Mg\delta_r \tag{2}$$

where M = mass of sliding soil block, $\beta = \tan\theta$ (θ = slope angle) is slope inclination and $\mu = \tan\phi$ (ϕ = friction angle) is friction coefficient. For saturated slip plane, Eq. (2) is replaced by Eq. (3) in which $\sigma_{n0} = Mg/[(1+\beta^2)A]$ is the total stress normal to the slip plane, σ'_{n0} is the corresponding effective stress and A is the horizontal area of the sliding soil mass (Kokusho and Ishizawa 2007).

$$-\delta E_p = \beta\sigma_{n0}\delta_r A(1+\beta^2), \ \ E_{DP} = \mu\sigma'_{n0}\delta_r A(1+\beta^2), \ \ E_{EQ} = \left(\mu\frac{\sigma'_{n0}}{\sigma_{n0}}-\beta\right)Mg\delta_r \tag{3}$$

From Eqs. (2) and (3), the residual displacement δ_r of the rigid block can be formulated for the unsaturated and saturated slip plane, respectively, as;

$$\delta_r = \frac{1+\mu\beta}{\mu-\beta}\frac{E_{EQ}}{Mg} \ , \qquad \delta_r = \frac{1}{\mu(\sigma'_{n0}/\sigma_{n0})-\beta}\frac{E_{EQ}}{Mg} \tag{4}$$

This simple model was compared with shaking table tests of dry sand slope schematically shown in Fig. 1 (b). The residual displacements δ_r obtained by a number of tests for different slope angles θ (10º~29º) and different input frequencies (f =2.0~2.7 Hz) are plotted versus the normalized earthquake energies E_{EQ}/Mg. It is remarkable that if μ =0.857 is chosen, Eq. (4) (unsaturated) can predict the residual slope displacement almost perfectly for all slope angles and input frequencies (Kokusho and Ishizawa 2007). This indicates that if an appropriate μ is known in advance, the simple rigid block model in Fig. 1(a), with quite different mechanism from the sand slope in Fig. 1(b), can successfully simulate the realistic failure.

From Eqs. (2) and (3), the following equations hold for unsaturated and saturated slip planes, respectively (Kokusho et al. 2011).

$$\frac{-\delta E_p/Mg + E_{EQ}/Mg}{\delta_r} = \tan\theta + \tan(\phi-\theta), \quad \frac{-\delta E_p/Mg + E_{EQ}/Mg}{\delta_r} = (\sigma'_{n0}/\sigma_{n0})\tan\phi \tag{5}$$

This indicates that runout distances δ_r for slopes of arbitrary cross-sections can be easily evaluated by a graphical method as illustrated in Fig. 3, if potentially unstable soil block with its mass, M, centroid P, together with mobilized friction coefficient $\mu = \tan\phi$ and earthquake energy for slope failure E_{EQ} are given. The energy E_{EQ} may be roughly evaluated from earthquake magnitude, hypocenter distance, im-
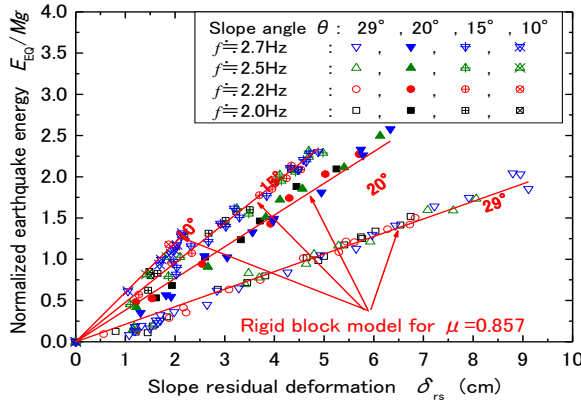
Fig. 2. Earthquake energy versus residual slope displacement for different slope angles by different input frequencies obtained by shake table tests.
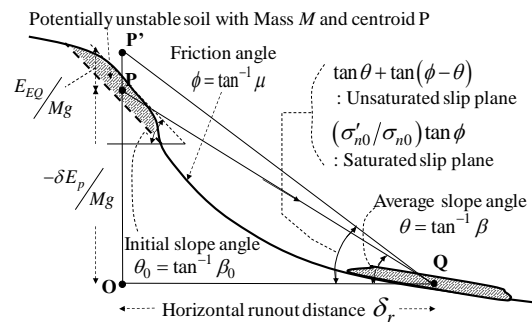
Fig. 3. Graphical evaluation method for run-out distance of seismically induced slope failure.

41

pedance ratio between a sloping layer and the underlying base layer (Kokusho et al 2011, Kokusho & Suzuki, 2012, Kokusho et al. 2014).

Thus, a simple method for evaluating the runout distance was developed, though the mobilized friction coefficient $\mu = \tan \phi$ has to be properly determined in advance.

CASE STUDIES IN VIEW OF ENERGY

In order to give friction coefficients properly, back-calculations of case histories as many as possible would be more robust than other methods due to complexity of actual slope failures in the field. The 2004 Niigataken-Chuetsu earthquake (M_J 6.8) and the 2008 Iwate-Miyagi Inland earthquake (M_J7.2) were studied in view of the energy balance for 68 natural slope failures. Failure types were classified according to failure modes into intact block-type slide (Type-A or Type-a for the two earthquakes, respectively) and non-intact disintegrated debris type slides (Type-B, C or Type-b, c). In addition, failures of 16 embankment slopes during the 2004 earthquake and 2005 Noto-peninsula earthquake (M_J6.9) were also studied. Failed slopes in complex shapes were simplified into a rectangular solid before and after failures based on air-photographs, and movements of the centroids were incorporated in Eq. (5). The following is the major findings obtained from the case histories.

1) The energy ratio $-\delta E_p/E_{EQ}$ is larger than unity even for small scale failures in terms of runout distance and failed volume, indicating only a small contribution of the earthquake energy E_{EQ} compared to the potential energy $-\delta E_p$ for larger failures in particular (Fig.4). This indicate that Newmark-type time-history analyses are not meaningful for slope fail-
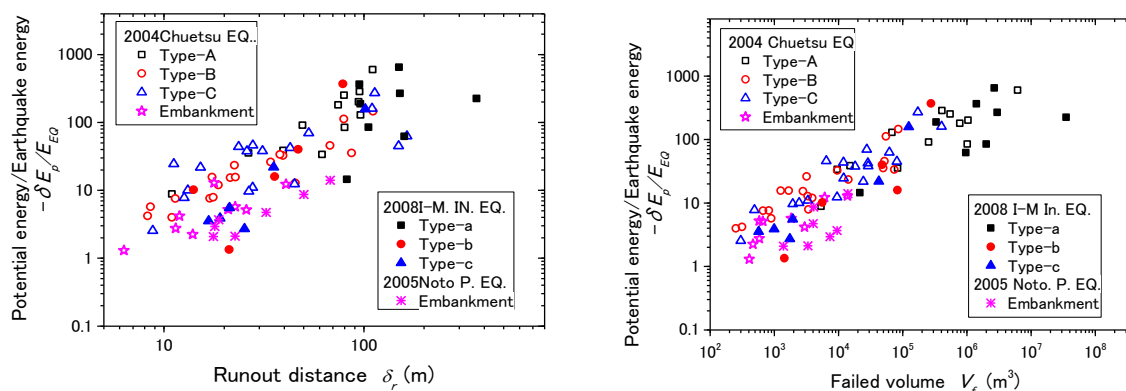
Fig.4. Energy ratio $-\delta E_p/E_{EQ}$ versus runout distance (left) or failed volume (right) in slope failure case histories during recent earthquakes in Japan.
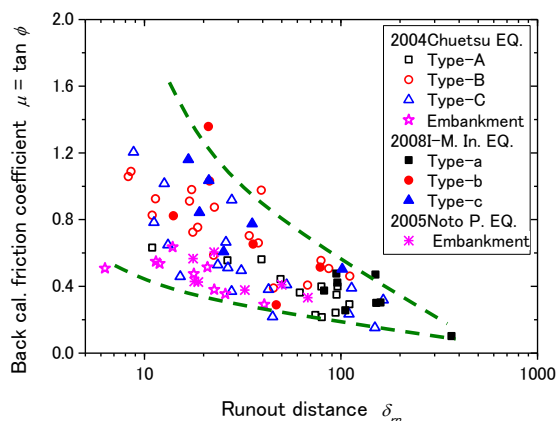
Fig. 5. Back-calculated friction coeff. versus runout distances for recent slope failure case histories.
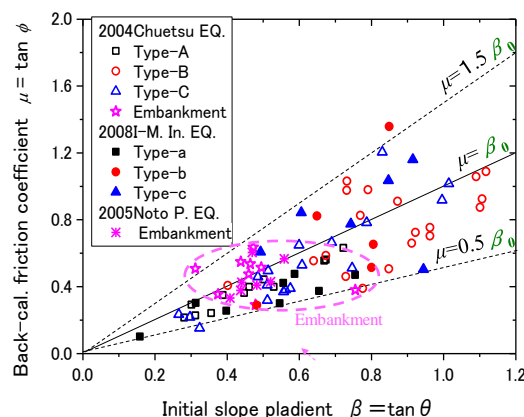
Fig. 6. Back-calculated friction coeff. versus slope gradients for recent slope failure case histories.

42
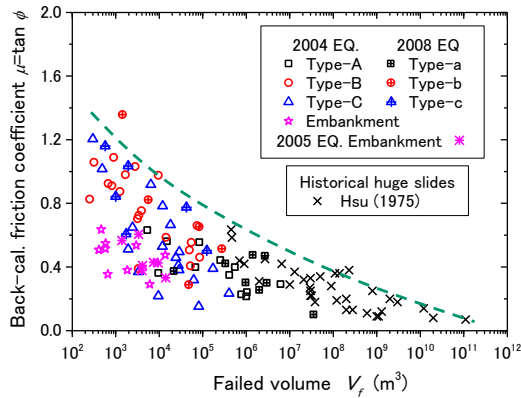
Fig. 7. Back-calculated friction coefficients versus failed soil volumes for recent slope failure case histories compared with historical huge slides.
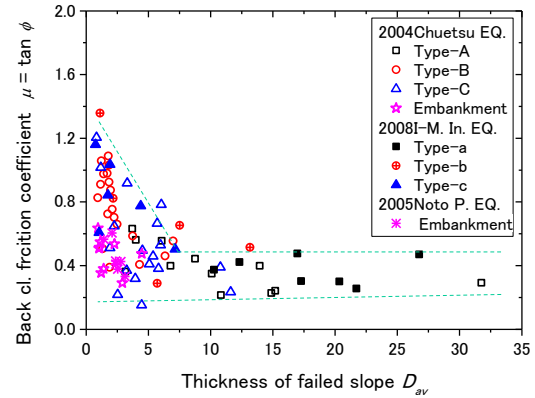
Fig. 8. Back-calculated friction coefficients versus thickness of failed slope for recent slope failure case histories.

ures exceeding a few meter displacements. This may also minimize the effect of uncertainties involved in evaluating earthquake energy E_{EQ} in the energy-based evaluation. Despite this finding, the earthquake energy still plays an important role as a trigger of the failure by reducing soil shear resistance rather than by directly driving the soil mass.

2) The back-calculated friction coefficients μ tend to decrease clearly with increasing runout distances (Fig. 5). This may reflect a quite unexpected observation that gentler slopes, if failed, tend to travel longer distances than steeper slopes (Kokusho et al. 2011).

3) The back-calculated friction coefficients μ are highly dependent on the slope gradient β and increase with increasing β for natural slopes, presumably reflecting long-term exposures to previous rains and earthquakes (Fig. 6). This seems different from manmade embankments for which μ is essentially unchanged as indicated in the same diagram.

4) On the $\mu \sim \beta$ plane (Fig. 6), many of the back-calculated μ-values are plotted below the line $\mu = \beta$ in intact block-type failures (Type-A, a) in particular, indicating that the back-calculated μ, originally larger than β, decreases when earthquake starts, indicating that the failed debris accelerated first and then decelerated in down-slope sections.

5) A clear decreasing trend in μ can be recognized as the failed soil volume increases from 10^3 to 10^7 m^3 irrespective of the failure types. This decreasing trend in this research is consistent with previous research results on huge landslides in the world by Hsu (1975) (Fig. 7), providing the global decreasing trend from 10^3 to 10^{11} m^3.

6) As shown in Fig. 8, the average thickness of failed slopes D_{av} seems to be promising as a key parameter to evaluate the friction coefficient among variables associated with slope failures, wherein μ tends to stay in lower values than 0.5 for D several meters or larger.

REFERENCES

Kokusho, T, and K. Kabasawa, K. (2003). Energy approach to flow failure and its application to flow due to water film in liquefied deposits, Proc. of International Conference on Fast Slope Movements, Prediction and Prevention for Risk Mitigation, Naples, 297-302.

Kokusho, T. and Ishizawa, T. (2007), "Energy approach to earthquake-induced slope failures and its implications", *Journal of Geotechnical and Geoenvironmental Engineering*, ASCE,133(7), 828-840.

Kokusho, T., Ishizawa, T. and Koizumi, K, (2011): Energy approach to seismically induced slope failure and its application to case histories, *Engineering Geology*, Elsevier, Vol. 122 (1-2), 115-128.

Kokusho, T. and Suzuki, T. (2012): Energy flow in shallow depth based on vertical array records during recent strong earthquakes(Supplement), Soil Dynamics & Earthquake Engineering 42, 138-142.

Kokusho, T., Koyanagi, T. and Yamada, T. (2014): Energy approach to seismically induced slope failure and its application to case histories –Supplement-, *Engineering Geology* 181, 290–296.

Hsu. J. (1975). Catastrophic debris streams generated by rockfalls, *Geological Society of America Bulletin* 86, No.50117, 129-140.

MODELING DYNAMIC PROGRESSIVE FAILURE OF SOIL SLOPES

Ga Zhang
Tsinghua University, China

BRIEF INRODUCTION

Dynamic loading has triggered a number of landslides that have caused great life and property losses, such as the Wenchuan earthquake in western China and the Aysn Fjord earthquake in southern Chile. In practice, slopes often experienced a diverse range of dynamic loads, such as inertia forces of structures on slopes under earthquake or machine vibration conditions, traffic loads on roads, railways, and airfield runways on slopes, cyclic loads of foundations induced by wind turbines. Dynamic loading is a major cause of landslides with significantly different behavior from the landslides caused by static loading. It is of great importance to accurately evaluate the stability level of soil slopes under dynamic loading conditions.

FAILURE MECHANISM ANALYSIS

A series of centrifuge model tests was conducted to investigate the progressive failure behavior of slopes under dynamic loading conditions, with a focus on the effect of cyclic loading. The cyclic effect induced significant deformation and final failure of the slope, which was influenced by the cyclic loading patterns. Displacement histories were measured accurately throughout the slope and were used to quantify the slope failure process. The slip surface developed from the top of the slope downward to the lower part under the application of the loading.

An integrated analysis of deformation process and failure process was used to investigate the behavior and mechanism of slope failure (Wang et al. 2011; Wang and Zhang 2014; Zhang et al. 2015; Zhang and Wang 2016). The failure process of the slope exhibited a significant coupling with the deformation localization under dynamic loading conditions. The deformation localization developed in the slope during loading and resulted in the development of the slip surface. Simultaneously, the local failure caused stronger deformation localization near the slip surface. The cyclic loading pattern had a significant effect on the slip surface and limit bearing capacity of the slope, which was essentially dependent on the diversity of the deformation behavior of the slopes under different cyclic loading conditions.

A new concept, shear zone, was introduced to provide a clear description of the shear deformation localization of the slope (Zhang et al. 2015). The slip surface of the slope was located in the shear zone that was established prior to slope failure (Fig. 1). The size of the shear zone was of the same order of magnitude as that of the slope and can be determined from the macroscopic measurement of displacement. The shear deformation of the shear zone exhibited a significant orientation during loading. On the basis of the concept of shear zone with three features, the slope failure process can be captured and simulated in a macroscopic view.
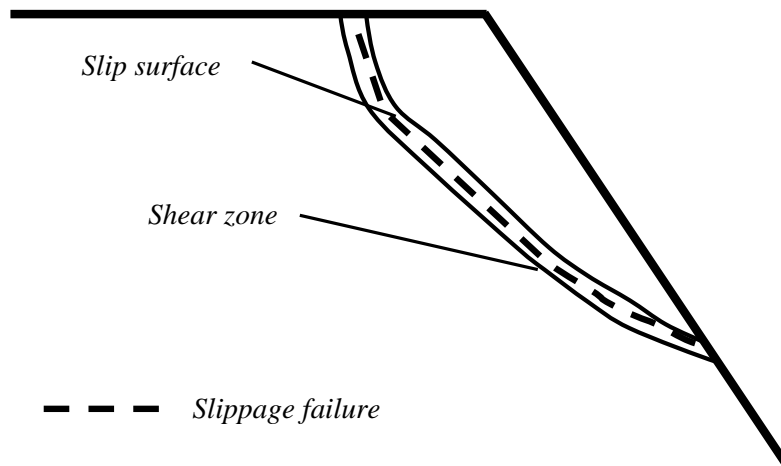
Fig. 1: Shear zones and slip surfaces of the slope under the surface loading condition.

NUMERICAL SCHEME

A finite element analysis program was developed to analyze the progressive failure of a soil slope based on the progressive failure mechanism. The shear element was developed to comprehensively characterize the shear zone, which described the soil shear deformation localization of progressive failure. The formulation of the shear element was derived using a format similar to that of the soil-structure interface element and incorporated into the traditional finite element method to macroscopically simulate the deformation and failure processes of the slope. A series of algorithms, including the combination and transformation of the shear element and the entity element, was proposed to obtain the full solutions for the progressive failure of soil slopes. The simulation results using the developed program for the slip surface, failure process, and displacement distribution match the observations of centrifuge model tests well.

CONCLUSIONS

1. An integrated analysis of deformation process and failure process was used to investigate the behavior and mechanism of slope failure under dynamic loading conditions. The failure process of the slope exhibited a significant coupling with the deformation localization
2. A finite element analysis scheme was proposed to capture the progressive dynamic failure of a soil slope using the shear element that was developed to comprehensively characterize the shear zone.

ACKNOWLEDGEMENTS

REFERENCES

Wang, L.P., Zhang, G. (2014). "Centrifuge model test study on pile reinforcement behavior of cohesive soil slopes under earthquake conditions." *Landslides* 11(2), pp. 213-223.

Wang, L.P., Zhang, G., Zhang, J.M. (2011). "Centrifuge model tests of geotextile-reinforced soil embankments during an earthquake." *Geotextiles and Geomembranes* 29 (3), pp. 222-232.

Zhang, G., Hu, Y., Wang, L.P. (2015). "Behaviour and mechanism of failure process of soil slopes." *Environmental Earth Sciences* 73(4), pp. 1701-1713.

Zhang, G., Wang, L.P. (2016). "Integrated analysis of a coupled mechanism for the failure processes of pile-reinforced slopes." *Acta Geotechnica*, doi: 10.1007/s11440-015-0410-z.

LARGE-SCALE EARTHQUAKE SIMULATION FOR SEISMIC HAZARD ANALYSIS OF SITES

Jin-Ting Wang, Chun-Hui He and Chu-Han Zhang
Department of Hydraulic Engineering, Tsinghua University, Beijing 100084, China

BRIEF INRODUCTION, METHODOLOGY AND KEY RESULTS

For the safety of engineering projects, seismic hazard analyses (SHA) for sites are of high importance. Currently in SHA, the ground motions are generally predicted by attenuation relationships (or ground motion prediction equations, GMPEs), which are based on the statistics against seismological records from a huge amount of earthquake events. When a specific site of a vital project is concerned, attenuation relationships may bring considerable uncertainties to the estimated ground motion parameters.

As the development of computation technology and numerical solution theory, the large-scale numerical simulation of an earthquake from the source to the site offers us an alternative to determine the ground motion parameters at a specific site. The advantage of the numerical simulation is that the source mechanism, propagation path, and local site effect may be explicitly taken into account, as shown in Figure 1. Among the various numerical approaches, the spectral element method (SEM) has been increasingly adopted in seismological research since introduced in the late 1990s. SEM combines the flexibility of the finite element method and the accuracy of pseudo-spectral method, and is highly suitable for parallel computing due to its diagonal mass matrix.
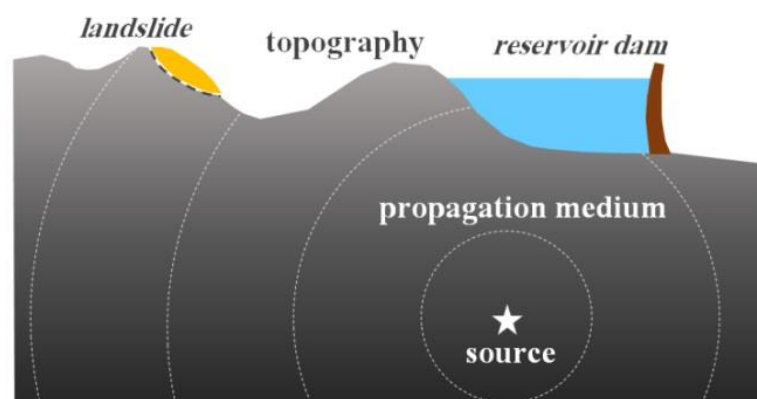
Figure 1: Schematic map of the simulation from the source to the site

The nonlinear spectral element analysis model adopted herein for seismic wave simulation integrates models of sources, propagation media and local site conditions. This allows us perform a deterministic simulation of earthquake including all the physical processes:

(1) The source can be simulated as points or finite fault ones. The spatial and temporal characteristics can be given by actual inversion results or hypothetic models.

(2) The propagation path is usually modeled as velocity and Q structures. These data are abundant and precise enough for some areas. However, it needs to be improved for places such as southwestern China.

(3) The local site conditions mainly refer to two aspects: non-uniform medium and topography. The former could be naturally considered due to SEM's advantage in dealing with complexly distributed material and the latter, which is highly concerned in engineering, is implemented with high resolution digital elevation model (up to 30 meters in global scale).

Based on the numerical approach of SHA and the integrated SEM model, three key factors of the source-path-site process of wave propagation can be separately researched for a specific site.

(1) Source effects. For causative fault whose movement information has been revealed, the effects of source mechanism on ground motions can be studied by physically modeling the source using moment tensors. Another problem involves the influence of fault rupture directivity, which is studied using finite fault modeling by considering the rupture propagation on the fault plane (Figure 2).
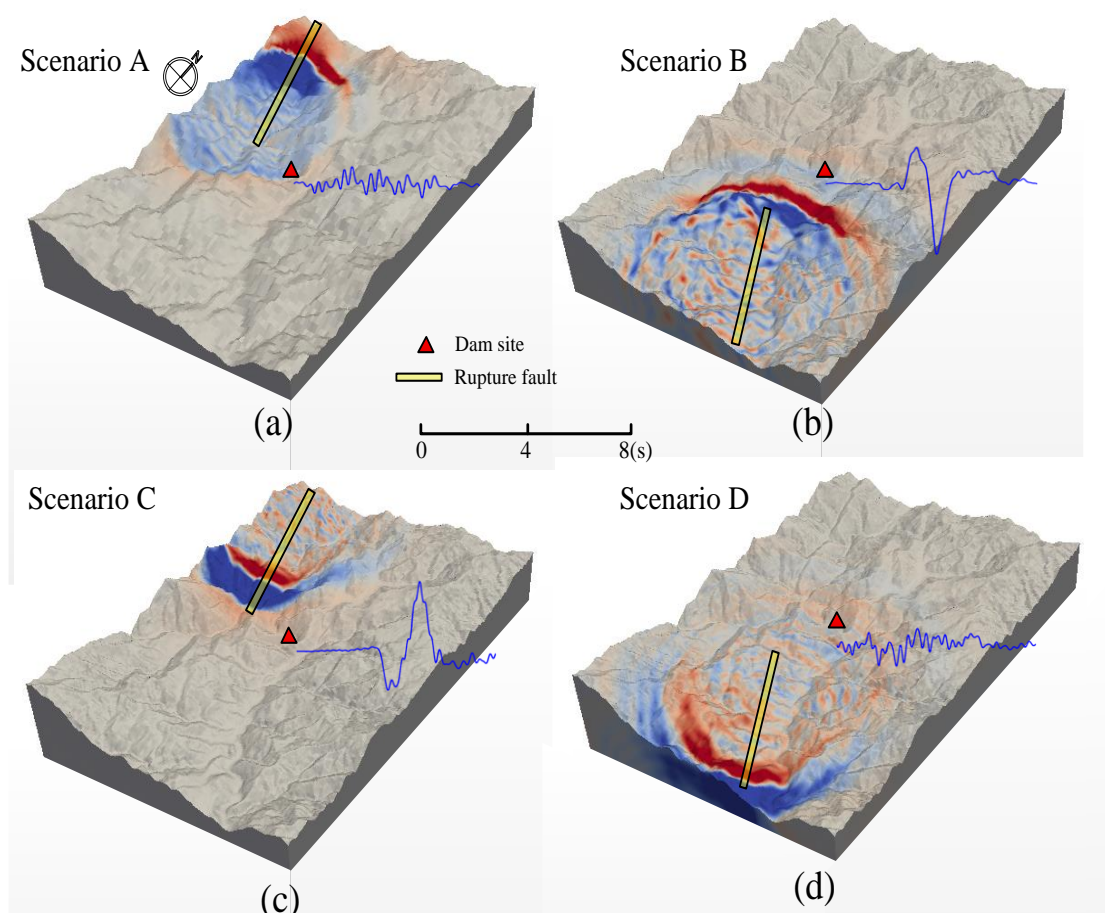
Figure 2: Simulation of rupture directivity with finite fault model

(2) Propagation path effects. The wave velocity of medium is given as 3D structure (Figure 3). The non-uniform medium such as the fault systems or covering layers may be incorporated by directly assigning the parameters for spatial points.

The Newhall earthquake on 28 October 2012 with hypocentral depth 4m, magnitude 3.9, source mechanism (strike 139°, dip 68°, and rake 137°), and seismic moment 4.03×10^{21} dyn cm.
In the right figure, upper line: recorded data; lower line: synthetic velocity
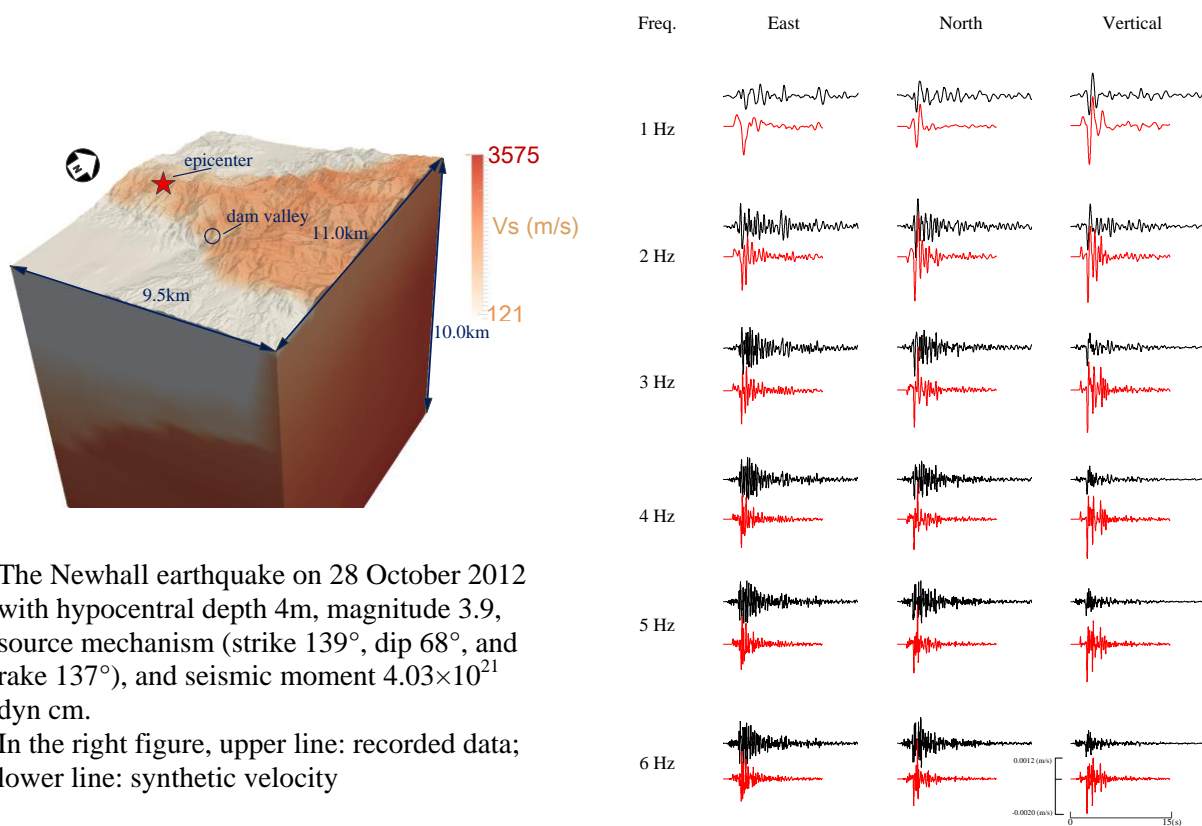
Figure 3: 3D velocity structure model and broadband simulation results

(3) Site effects. Topography is modeled to include the amplification of seismic waves (Figure 4), which is important for structures, such as high dams, long span bridges, and tunnels.
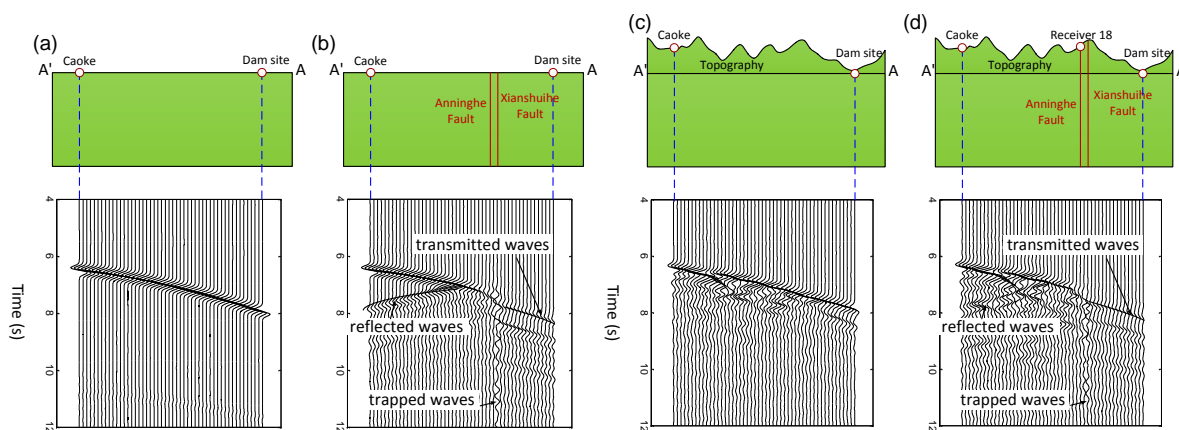
Figure 4: Site effects: influences of topography and near faults

CONCLUSIONS

Numeric simulation for earthquake from the source to the site has some advantages over the conventional empirical approaches.

1. Three factors, i.e., the source, the propagation path and the site conditions, can dramatically affect the ground motions. For key projects, using empirical equations to perform the SHA may suppress the characteristics of earthquake events. Herein, the deterministic analysis approach with the numerical model herein is proposed to stress the influences of all the physical processes in a specific earthquake event.

2. Utilizing the high-performance computer, numerical models with huge amount of DOFs can be solved in a short time. However, the simulation accuracy still depends on the quality of models such as the resolution of the velocity structure and more work on it needs to be conducted.

ACKNOWLEDGEMENTS

REFERENCES

Komatitsch, D., Tromp, J., (1999). "Introduction to the spectral element method for three-dimensional seismic wave propagation. " *Geophysical Journal International*, 139(3):806-822.

He, C. H., Wang, J. T., Zhang, C. H. and Jin, F. (2015). "Simulation of broadband seismic ground motions at dam canyons by using a deterministic numerical approach. " *Soil Dynamics and Earthquake Engineering*, 76:136-144.

He, C. H., Wang, J. T. and Zhang, C. H. (2016). "Nonlinear spectral element method for three-dimensional seismic wave propagation." *Bulletin of the Seismological Society of America*, 106(3): 1074-1087.

BRIDGE PILE FOUNDATIONS IN LATERALLY SPREADING GROUND IN COLD REGION: PERFORMANCE AND ANALYSES

Zhaohui Joey Yang[1], Xiaoyu Zhang[2] and Fujun Niu[3]

[1] Professor, Dept. of Civil Engineering, University of Alaska, 3211 Providence Dr., Anchorage, AK 99508, USA; zyang2@uaa.alaska.edu
[2] Staff Engineer, Mueser Rutledge Consulting Engineers, New York, NY 10122; rzhang@mrce.com
[3] Professor, State Key Laboratory of Frozen Soil Engineering, Chinese Academy of Science, Lanzhou, China; niufujun@lzb.ac.cn

INTRODUCTION

Liquefaction and associated ground failures have been commonly observed in past major earthquakes across the world. A substantial portion of these ground failures and structural damages was direct results of or related to liquefaction and lateral spreading of the ground crust. Lateral spreading is particularly damaging if a non-liquefiable crust rides on top of the liquefied soil (Hamada *et al.* 1986; JGS 1996, 1998). One of the lessons learned from two major earthquakes in Alaska was that the freezing of ground crust can generate greater lateral forces that are crucial to consider in northern-area foundation design (Ross *et al.* 1973, Shannon and Wilson 2009).

METHODOLOGY AND RESULTS

This study focus on how the frozen ground crust typically existing in cold regions in winter season affects the seismic performance of bridge pile foundations and how to estimate the loads imposed on pile foundations during earthquake induced liquefaction. A shake table experiment was conducted to gain an in-depth understanding of the mechanism of frozen ground crust-pile foundation interaction. A model pile of 5 cm diameter and 0.175 cm wall thickness was embedded in loose to medium dense sands underlying a frozen ground crust, which was simulated by cemented sands. This model was tested on a shake table to investigate the frozen ground crust-pile interaction. Partial liquefaction was induced in the sands, and lateral spreading of 2.1 cm, or 40% of the pile diameter, was induced in the frozen ground crust for loading Stage 2. Pore pressure, acceleration, strain of piles, and frozen ground crust lateral spreading data were collected. A fluid-solid coupled Finite Element (FE) model of the model pile was created using OpenseesPL (Lu *et al.* 2016) and the results show a FE model can capture the interaction mechanism of piles with laterally spreading frozen ground crust. It was concluded that during the lateral spreading of frozen crust, two plastic hinges formed on the model pile: one was formed at crust-liquefiable soil interface and was found induced by the large distributed load (soil resistance) in the crust; the other one was located at middle of the liquefied sand and it was caused by lateral spreading of the ground crust.

Based on a typical bridge from the Alaska Department of Transportation &Public Facilities (AK DOT&PF) bridge inventory, supported on commonly used pile foundations that penetrate a liquefiable sand layer, three dimensional fluid-solid coupled FE models of a

foundation embedded in a typical soil profile was created using the OpenseesPL platform. Figure 1 presents such a typical bridge foundation and soil profile. The soil profile has a 2-m thick ground crust layer consisting of clayey silt that freezes in winter and thaws in summer (also referred to as the active layer). The active layer overlies a 6-m thick loose sand layer that rests on a 6-m thick medium dense sand layer and a 7 m thick dense sand layer. A 3° sloping ground surface is assumed. All the soil layers except for the active layer are assumed saturated. A concrete-filled steel pipe (CSP) pile of 24 m long was embedded in the soil profile with 3 m remaining above the ground surface. The CSP pile has an outer diameter of 0.9 m and a wall thickness of 0.019 m, and the fill concrete has a reinforcing ratio of 1.52%. Two Finite Element (FE) models of the same soil-foundation system were created: one named "frozen case" (with a frozen ground crust) representing the typical winter conditions in Alaska, and the other named "unfrozen case" (with an unfrozen ground crust) representing the summer conditions in Alaska.

These two cases were analyzed with selected ground motion excitation. Soil response and pile performance for both the frozen and unfrozen conditions were presented to illustrate the key characteristics of pile performance in liquefiable soils underlying a frozen or unfrozen crust. The hinge rotation/plastic deformation demand were much higher in the frozen case than in the unfrozen case under similar seismic loading conditions. Results also show that the large-size CSP pile would not be able to survive the lateral spreading in the frozen case, but would otherwise survive in the unfrozen case. Additionally the modeling result further confirmed the forming of the two plastic hinges on pile in a full-size soil – pile system and the mechanisms responsible for these plastic hinges.

For practice purpose, a Beam-on-Nonlinear-Winkler-Foundation (BNWF) approach, or p-y approach, was used to predict the pile response of the full-size CSP pile under lateral loading, and the predicted results were compared with the fluid-solid coupled FE modeling results. Frozen soil p-y model developed by Yang et al. (2016) was used. Soil degradation due to liquefaction is modeled by utilizing p-multiplier method. A good agreement in terms of pile deformation, shear force, and bending moment was found between the results obtained from the p-y approach and those from fluid-solid coupled FE modeling. It is therefore concluded that the p-y approach is quite effective in modeling the performance of pile foundations subject to lateral spreading with the presence of a frozen crust.
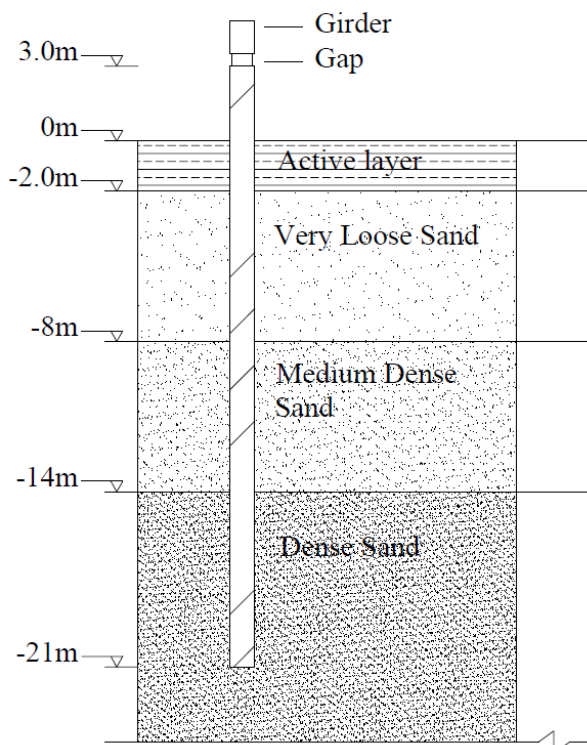
Figure 1 The soil-pile system of a typical bridge foundation system used in Alaska

CONCLUSIONS

In summary, both the shake table test and fluid-solid coupled FE analysis results show that laterally spreading ground crust can form two plastic hinges on the pile for both frozen

(with a frozen active layer) and unfrozen (with an unfrozen active layer) cases: one located near the frozen ground crust-loose sand interface (referred to as the upper plastic hinge) and the other within the medium dense sand layer (referred to as the lower plastic hinge). The plastic deformation and hinge rotation demand are much higher in the frozen case than in the unfrozen case under similar seismic loading conditions. The p-y approach is effective in predicting the location and plastic deformation demand at the upper plastic hinge, and the location of the lower plastic hinge. However, it underestimates the plastic deformation demand in the lower plastic hinge. Guidelines are proposed for design practitioners to analyze the response of piles embedded in liquefiable soils subjected to frozen ground crust lateral spreading by the p-y approach. This includes how to obtain free-field displacement, select p-multipliers, model the frozen soil resistance, and account for the restraint offered by the superstructure.

ACKNOWLEDGEMENTS

REFERENCES

Hamada, M., Yasuda, S, Isoyama, R, and Emoto, K. (1986). "Study on liquefaction induced permanent ground displacement." Report for the development of earthquake prediction. Tokyo, Japan.

Japanese Geotechnical Association (JGS) (1996). "Special issues on geotechnical aspects of the January 17, 1995, Hyogoken-Nambu Earthquake." *Soils and Foundations*, 1, 359.

Japanese Geotechnical Association (JGS) (1998). "Special Issues No. 2 on geotechnical aspects of the January 17, 1995, Hyogoken-Nambu Earthquake." *Soils and Foundations*, 2, 216.

Ross, G.A, H.B. Seed and R.R. Migliaccio (1973). "Performance of highway bridge foundations." The Great Alaska Earthquake of 1964 (Engineering), National Academy of Sciences, 190-242.

Shannon and Wilson Inc. "Documentation of geotechnical damages of the Magnitude 7.9 Denali Earthquake of Nov. 3, 2002." http://clients.shanwil.net/project.php?projectid= Quake_2002. Retrieved on Feb. 27, 2009.

Lu, J., Yang, Z., and Elgamal, A. (2006). "Openseespl three-dimensional lateral pile-ground interaction version 1.00 user's manual." Report No. SSRP-06/03, Department of Structural Engineering, University of California, San Diego.

Yang, Z., Li, Q., Jacob Horazdovsky, J.L. Hulsey, and Elmer Marx (2016). "Analysis of laterally loaded piles in frozen silts: a p-y approach." ASCE *Journal of Geotechnical and Geoenvironmental Engineering*. In press.

EXPERIMENTAL AND NUMERICAL STUDY OF GROUND VIBRATIONS INDUCED BY HIGH SPEED TRAIN

S.J. Feng, X. L. Zhang, H. X. Chen and Lei Wang
Department of Geotechnical Engineering, Tongji University, Shanghai 200092, China

INTRODUCTION

High speed railway, which acts as a safer and faster means of transportation, has grown rapidly around the world, especially in China. Meanwhile, the vibrations induced by high speed train (HST) arouse increasing concerns and cannot be ignored (Connolly *et al.*, 2015). Analytical method (Sheng, 1999) is confined to its simplification, which is not suitable for complex situations. Experimental study (Zhai *et al.* 2015) can take the complexity, inhomogeneity and uncertainty of the system into account, however, it is restricted to the specific configuration. Numerical method (Connolly *et al.*, 2013) seems to be eclectic and can be applicable to geotechnical engineering with enough accuracy.

This paper is organized as follows. Firstly, in-situ experimental study was conducted for an embankment section, including monitoring and analysis of the HST-induced ground vibrations in time domain and frequency domains. Secondly, a three dimensional model was formulated using the finite element method (FEM) to predict the ground vibrations. Finally, the effect of sub-soil treatment on vibration mitigation was discussed based the FEM model.

EXPERIMENTAL STUDY

The test site was located at Fengyang County. The vertical, transversal as well as longitudinal vibrations were all simultaneously measured at various distances from the track central line. A representative case of CRH380BL train, passing the embankment section at 300 km/h, is presented in this part.
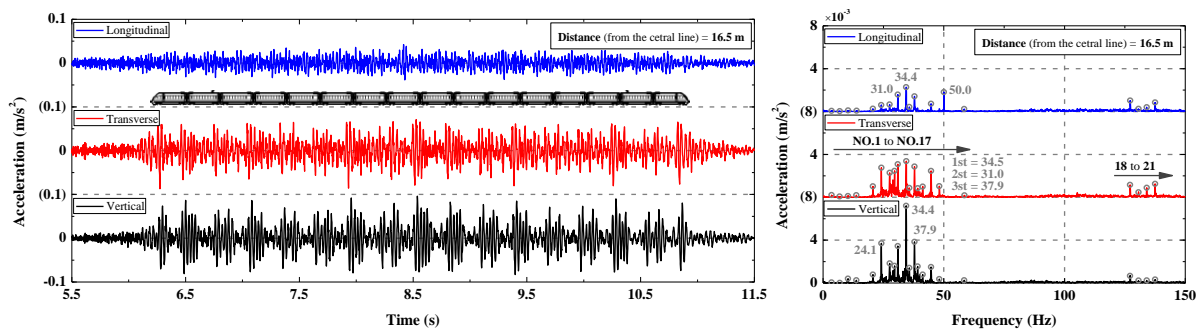
Fig. 1 Characteristics of three directional ground vibration: (a) time domain, (b) frequency domain

The three directional ground vibrations at 16.5 m from the central line in time and frequency domains are shown in Fig. 1 as an example. Due to superposition effect of adjacent

bogies, the three directional peak values, from the second to the penultimate, are commonly a little larger than the first and last ones (Fig. 1a). The vertical vibration peak values (a_{pz}) are typically the largest and the longitudinal vibration peak values (a_{py}) are obviously the least, the transversal vibration peak values (a_{px}) are a little weaker than the vertical.

All the corresponding dominant frequencies are depicted in Fig. 1b, varying from about 3.5 to 137.5 Hz. Moreover, the results indicate that all the dominant frequencies are n times at least one of the train characteristic frequencies, ground characteristic frequencies and intersectional frequencies. The vertical vibration, transversal vibration and longitudinal vibration have almost the same frequency. And their remarkable frequency components are between 20 and 50 Hz.
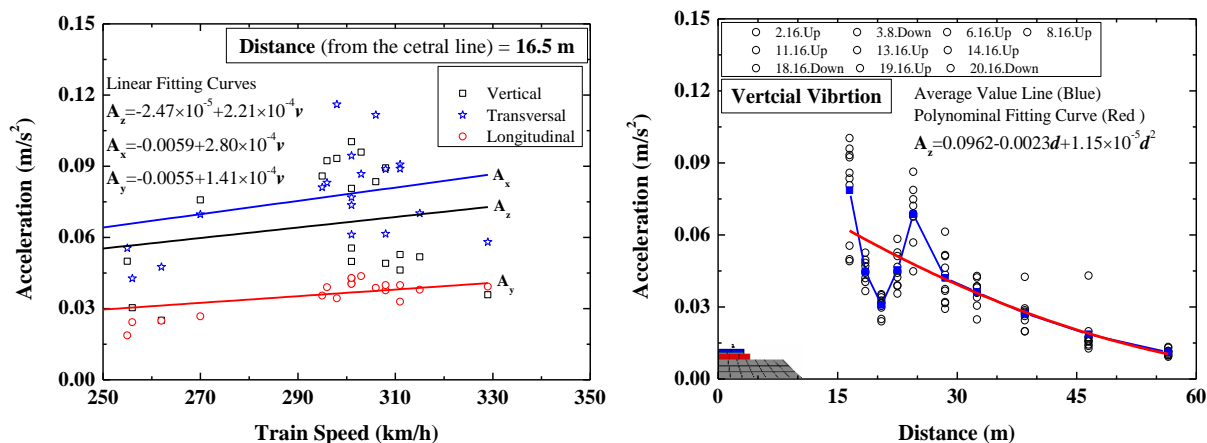
Fig. 2 Variations of time-domain peak value of acceleration with: (a) train speed, (b) distance from the track centerline

Figure 2a shows the variations of ground vibration acceleration amplitudes with train speed (v_t) varying from 250 to 350 km/h. With the increase of v_t, the acceleration amplitudes in the three directions display linearly uptrends at all the measuring points. Meanwhile, with the increase of observation distance (from track centerline), the slope of the fitting lines becomes gentler. The variation of vertical acceleration amplitudes with observation distance is show in Fig. 2b as an example. As expected, the vibration acceleration amplitudes overall decrease with distance. Nevertheless, an obvious amplification zone can be found at about 24 m. The reason is as follows. When the cover depth of bed rock is shallow, smaller propagation distance leads to more complex wave scattering and diffraction between the ground surface and the bed rock, leading to amplification in somewhere beyond the embankment.

NUMERICAL METHODOLOGY

A three dimensional model using the finite element method (FEM) was developed as shown in Fig. 3a. The rail was simulated by discrete supported Euler beams. The ballast-less track was composed of track slab, CA mortar, concrete slab and embankment, and was represented by 8-noded brick elements. Each car of the HST was modelled using a lamped mass model with ten degrees of freedom. The carriage, bogies and wheel were assumed to be rigid bodies and were connected via primary and secondary suspension system. The wheel and rail were coupled using the linear Hertz contact theory. Absorbing boundaries and Rayleigh damping approach were used to prevent wave reflections from the artificial edges and to simulate the material damping, respectively.

Investigations of ground vibrations caused by unit load under different speeds and frequencies are depicted in Fig. 4. The maximum vertical displacements ($u_{z\max}$) of these points remain stable before approximately 60 m/s (Fig. 4a). The $u_{z\max}$ then increases continuously with increasing speed until about the Rayleigh wave speed (v_R) of the surface ground. When it comes to a higher speed, the results tend to be classified into three categories. Generally, the closer a point to the central line, the larger the maximum vertical displacement is.
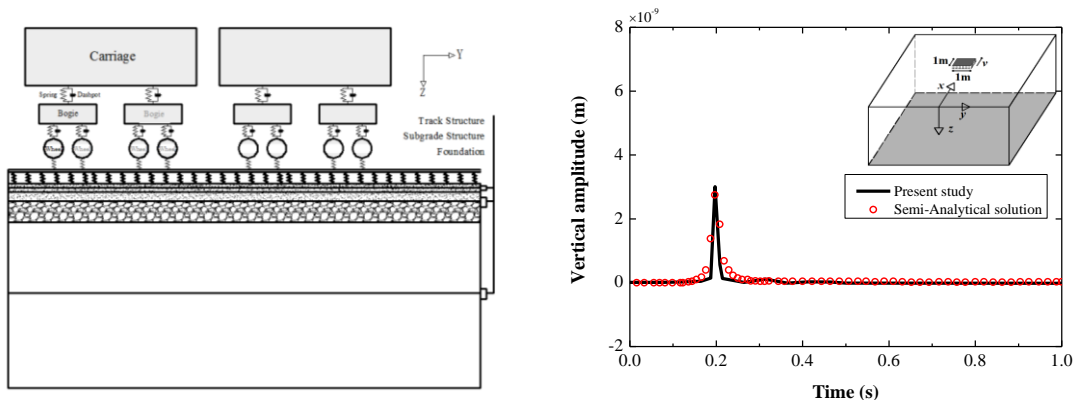
Fig. 3 Schematic diagram of the HST-track-embankment-ground model (a), and its verification (b)
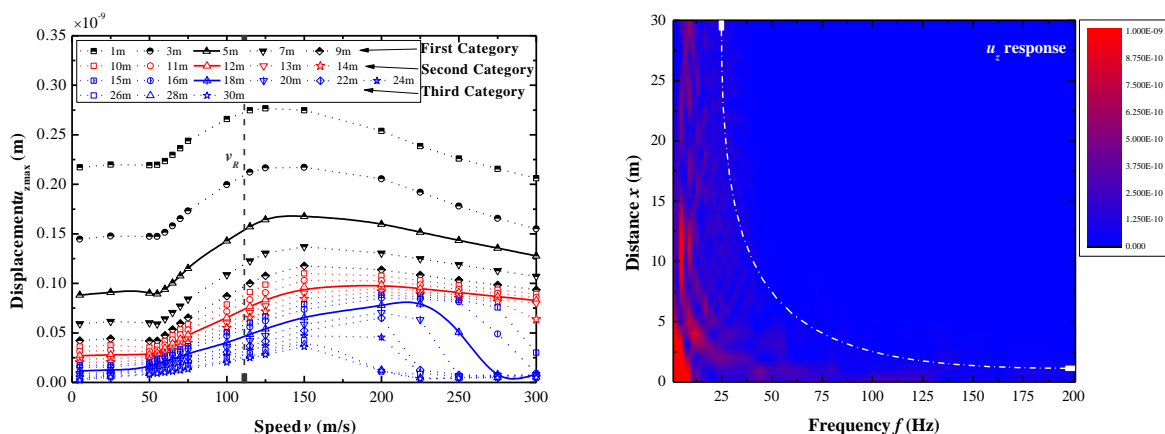
Fig. 4 Maximum vertical displacement of the surface ground: (a) at different speeds, (b) under different frequencies

The ground vibrations subjected to a unit load under different loading frequencies are investigated in Fig. 4b to distinguish the sensitive frequency range of the ground. For the vertical vibration, a low loading frequency range under around 30 Hz stimulates the largest vertical displacement of all the zones. Moreover, another loading frequency range from about 65 to 150 Hz is only efficacious for the zone just under or near the subgrade (within approximately 5 m). Thus, a "logarithmic" type curve is adopted to distinguish the effective loading frequency range (Fig. 4b).

VIBRATION MITIGATION

The treatment depth (d) in the ground is set as 5, 10, 15 and 20 m. With the increase of the treatment depth, the effect of sub-soil treatment on surface ground vibration isolation increases consistently (Fig. 5a). Meanwhile, the effective zone for vibration reduction also expands from about 6 m to 20 m with d increasing from 5 m to 20 m. Figure 5b shows the

effect of treatment width (*w*) on vibration reduction. With the increase of *w*, an increasing ground vibration reduction can be achieved within about 10 m, beyond which the increased vibration reduction is not significant. The benefits of cases with different treatment width are all less than the "*d*=10 m" case (shown with a green solid line in Fig. 5b), which indicates that treating the subgrade along the vertical direction is more effective.
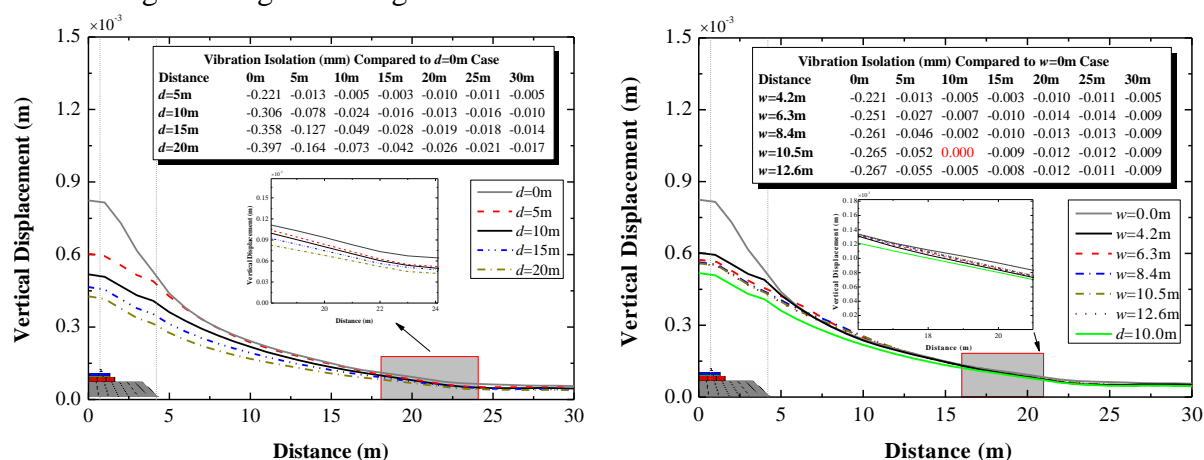
Fig. 5 Effect of sub-soil treatment on ground vibration mitigation: (a) with different treatment depth, (b) with different treatment width

CONCLUSIONS

1. Generally, the vertical vibration is the largest and the longitudinal is the least in the near field.
2. When the cover depth of bed rock is shallow, an obvious amplification zone would be found.
3. The first dominant frequency is generally determined by the distance between wheelsets or distance between the bogies at the very train speed.
4. The u_{zmax} would increase significantly with loading velocity until around the v_R of the ground.
5. The high frequencies played an important role especially under or near the subgrade, but would not work in the far field.
6. As for the benefits of sub-soil treatment on surface ground vibration mitigation, a deeper treatment under the subgrade is preferred.

REFERENCES

Connolly D.P., Marecki G.P., Kouroussis G., Thalassinakis I., Woodward P.K. (2015). The growth of railway ground vibration problems-A review, *The Science of the Total Environment*, (2015), in press.

Sheng X. (1999). Ground vibration generated by a load moving along a railway track, *Journal of Sound and Vibration*, 228 (1999) 129-156.

Zhai W., Wei K., Song X., Shao M. (2015). Experimental investigation into ground vibrations induced by very high speed trains on a non-ballasted track, *Soil Dynamics and Earthquake Engineering*, 72 (2015) 24-36.

Connolly D., Giannopoulos A., Forde M.C. (2013). Numerical modelling of ground borne vibrations from high speed rail lines on embankments, *Soil Dynamics and Earthquake Engineering*, 46 (2013) 13-19.

SEISMIC RESPONSES OF REINFORCED SOIL RETAINING WALLS SUBJECTED TO PULSE-TYPE GROUND MOTIONS

Huabei Liu*
* Huazhong University of Science and Technology, China

BRIEF INRODUCTION, METHODOLOGY AND KEY RESULTS

Strong earthquakes in recent years show that near-fault ground motions generally exhibit some unique characteristics, one of which is the pulse-type horizontal accelerations. Pulse-type strong ground motions have been shown to cause signifcant damages to buildings and bridge structures, while their devastating effects on geotechnical structures have seldom been investigated. Particularly, reinforced soil structures have been employed extensively in earthquake-active areas as the permanent components of critical infrastrures, thank to their good seismic performance during past earthquakes. However, the seismic designs of reinforced soil structures at present are simplistic, which generally do not take into account the frequency characteristics of the structures and the ground motions. While it has been known that reinforced soil structures are generally flexible, their behavior under the seismic loading from pulse-type motion deserves indepth investigations.

In this study, a calibrated Finite Element procedure was employed to analyze the seismic responses of modular-block reinforced soil retaining walls subjected to pulse-type ground motions. The model wall was 6 meter high, reinforced with geogrid reinforcements at a vertical spacing of 0.4 m. The backfill soil was assumed to be one type of dense sandy soil, which is modeled by a generalized plasticity model. The soil-geosynthetic interfaces were simulated by thin-layer elements, the constitutive behavior of which was also modeled by the generalized plasticity model, but the strength and stiffness parameters were reduced by 1/3. The aforementioned Finite Element procedure has been calibrated and used for seismic analysis of reinforced soil structures in a number of previous studies. 25 pulse-type horizontal acceleration time histories, which were recorded from the Chi-Chi Earthquake (1999) and Imperial Valley Earthquake (1979), were scaled to a peak acceleration of 0.4 g, and employed as the input motions in the numerical analyses.

The analysis results showed that pulse-type ground motions led to large seismic responses in the reinforced soil retaining walls. Although the input motions had the same peak accelerations, the responses of the reinforced soil retaining walls, including facing displacement, backfill compression, reinforcement load, and dynamic earth pressure were very different. These results indicate that employing the peak acceleration of
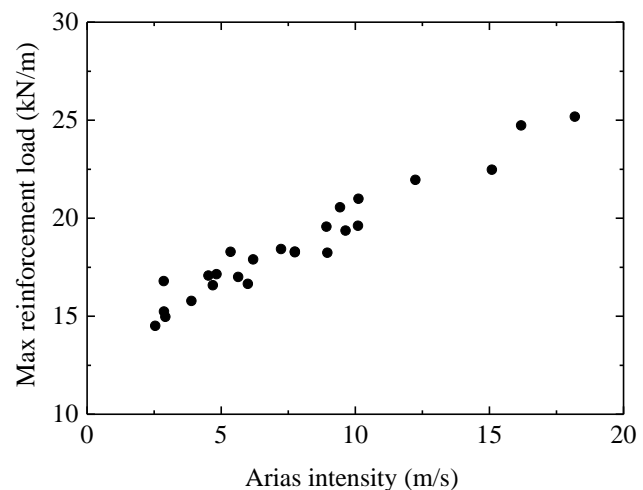
Figure 1: Relationship between reinforcement load and Arias intensity at the top of reinforced soil

the input motion as the design loading is not adequate, and may even result in erroneous interpretation of the seismic behavior of reinforced soil walls. In order to understand the relationship between the seismic loading and the seismic performances of the reinforced soil retaining walls, the Arias Intensity of the input motions were obtained. However, the correlation between the Arias Intensities of the input motions and the seismic responses of the retaining walls is not satisfactory. Much better correlation was obtained using the Arias Intensities of the horizontal accelerations at the top of the reinforced soil zone. Fig. 1 shows the relationship between the maximum reinforcement loads and the Arias Intensities at the top of the reinforced soil. It can be seen that the maximum reinforcement load increased almost linearly with the Arias Intensity.

CONCLUSIONS

1. A calibrated Finite Element procedure was employed to analyze the seismic responses of reinforced soil retaining walls subjected to pulse-type ground motions. It was found that pulse-type seismic motions resulted in very large seismic responses of the reinforced soil retaining walls.
2. The numerical results showed that the seismic performance of reinforced soil retaining walls was not only related to the peak ground acceleration, but also the frequency characteristics of the input, as well as the flexibility of the structures.
3. The maximum reinforcement load in the reinforced soil retaining wall was found to correlate well with the Arias Intensity at the top of the reinforced soil. It increased almost linearly with the Arias intensity.

REFERENCES

Champion, C., and Liel, A. (2012). "The effect of near-fault directivity on building seismic collapse risk." *Earthquake Engineering and Structural Dynamics* 41, pp. 1391-1409.

Ling, H.I., and Liu, H. (2003). "Pressure dependancy and densification behavior of sand through a generalized plasticity model." *Journal of Engineering Mechanics*, ASCE 129(8), pp. 851-860.

Ling, H.I., Leshchinsky, D., and Chou, N.N.S. (2001). "Post-earthquake investigation on several geosynthetic-reinforced soil retaining walls and slopes during 1999 Ji-Ji Earthquake of Taiwan." *Soil Dyn Earthq Eng* 21(4), pp.297–313.

Ling, H.I., Liu, H., Kaliakin, V.N., and Leshchinsky, D. (2004). "Analyzing dynamic behavior of geosynthetic-reinforced soil retaining walls." *Journal of Engineering Mechanics*, ASCE 130(8), pp. 911-920.

Liu, H., and Ling, H.I. (2012). "Seismic responses of reinforced soil retaining walls and the strain-softening of backfill soils." *International Journal of Geomechanics*, ASCE 12(4), pp. 351-356.

A RATIONAL CPT-BASED LIQUEFACTION SCREENING METHOD – EFFECT OF SILT CONTENT

S. Thevanayagam, U. Sivaratnarajah and Q. Huang
University at Buffalo, State Univ. of New York, Buffalo, NY, USA

INRODUCTION

Current liquefaction screening techniques rely on knowledge from extensive laboratory research conducted on liquefaction resistance of clean sands, and extrapolations of observed field performances during past earthquakes (NCEER 1997, Youd *et al.* 2001). Such observations have been documented in the form of normalized penetration resistances (SPT $(N_1)_{60}$, CPT q_{c1N}) (Seed et al. 1983, Robertson and Wride 1998), and shear wave velocity (v_{s1}) (Andrus and Stokoe, 2000) versus cyclic stress ratio (CSR) induced by the earthquakes, corrected for a standard earthquake magnitude of 7.5, for many soil deposits where occurrence or non-occurrence of liquefaction were recorded during the earthquakes (Fig.1). For liquefaction screening applications, the cyclic resistance ratio (CRR) of a soil deposit, applicable for number of cycles and frequency content relevant for a standard earthquake magnitude of 7.5, with a known value of $(N_1)_{60}$, q_{c1N} or v_{s1} for the site is obtained from a demarcation line drawn between the past field-observation-based data points which correspond to liquefied deposits and those that did not liquefy in Fig.1. This is denoted as $CRR_{7.5}$. This $CRR_{7.5}$ value is compared against the anticipated cyclic stress ratio (CSR) for that deposit due to a design earthquake of the same magnitude to determine whether or not that deposit would liquefy. Factor of safety (FS) against liquefaction is defined as $FS=CRR_{7.5}/CSR$. If a different design earthquake magnitude is expected, the $CRR_{7.5}$ is multiplied by a magnitude scaling factor (MSF) to obtain the cyclic resistance ratio CRR applicable for the deposit for the relevant number of cycles, frequency content, etc. of the design earthquake. The factor of safety is $FS= MSF*CRR_{7.5}/CSR$.

Practitioners and researchers have observed that the $CRR_{7.5}$ determined in this manner depends on silt content of the soil for a given $(N_1)_{60}$, q_{c1N} or v_{s1}. For the same values of $(N_1)_{60}$, q_{c1N} or v_{s1}, silty sands show higher $CRR_{7.5}$ than for sands (Fig.1). Demarcation lines have been developed for silt content less than 5, 15 and 35%, respectively. In the case of cone penetration, an equivalent cone index I_c which is considered to represent the apparent effects of silt content has been introduced to obtain these demarcation lines (Fig.1b). These different demarcation lines are used to determine most probable $CRR_{7.5}$ for a deposit, depending on the silt content (or I_c) of the soil deposit. While this approach has been routinely used in practice, a rational understanding of this procedure has been lagging.

As evident in Figs. 1b-d, these silt-content-dependent screening demarcation lines in the charts continue to evolve based upon the engineers' experience (e.g. Robertson and Wride 1998, Idriss and Boulanger 2008, Boulanger and Idriss 2014). One of the main sources of uncertainty is that the effects of presence of silt among sand grains on liquefaction resistance (CRR), q_{c1N}, and the interrelationship between silt content, silt-soil characteristics (such as permeability k, compressibility m_v, and coefficient of consolidation c_v), CRR, and q_{c1N} remain largely unexplored and unknown. Successful application of the current screening charts to other sites calls for significant judgment on the part of the practitioner. A rational approach to liquefaction screening requires a fundamental understanding of the above '*silt-phenomenon*'

observed in these charts (viz. the interrelationship between silt content, k, m_v, CRR, q_{c1N}), and development of revised/new charts that incorporates this new understanding for it to be applied successfully with a high degree of confidence for all sites.
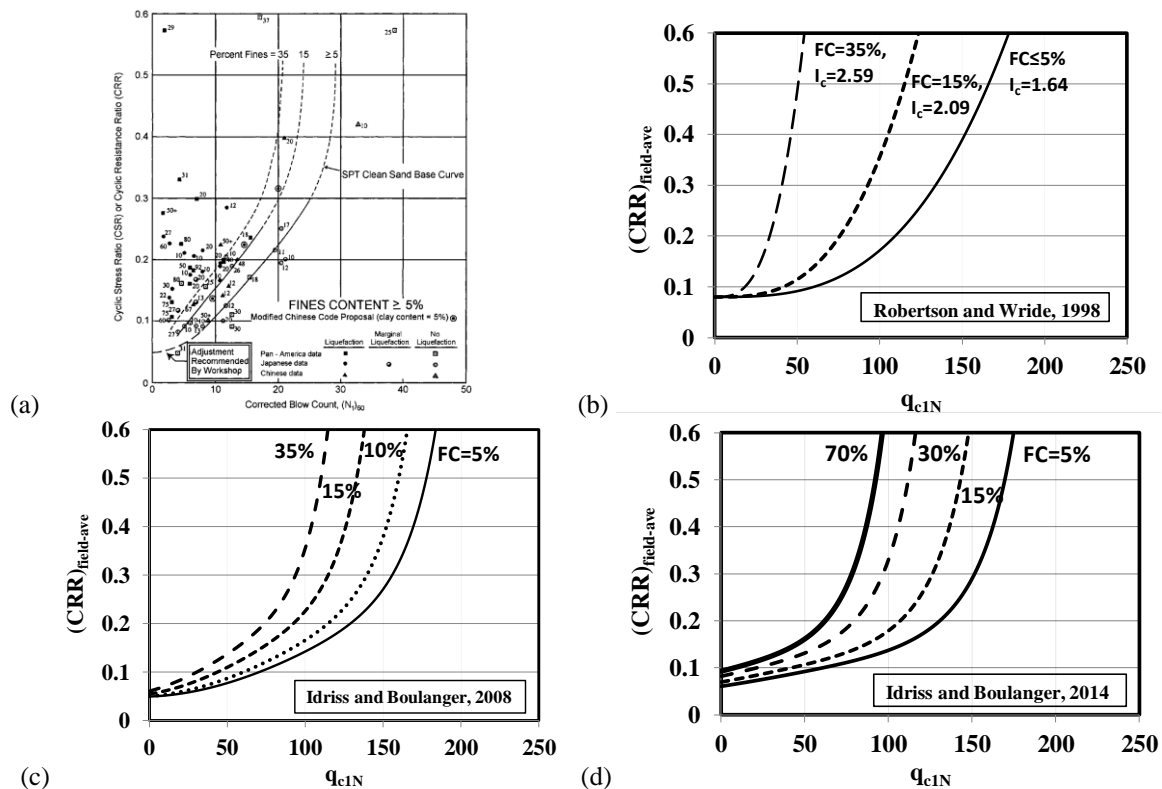
Fig.1 Examples of Silt-Content-Dependent Field Liquefaction Screening Charts

RECENT RESEARCH AND KEY RESULTS

Recent research shows that the silt-phenomenon affecting the liquefaction screening relationship (CRR versus q_{c1N}) is as follows (Thevanayagam and Martin 2002, Thevanayagam et al. 2006, 2008, 2015).

- Silt particles in a silty sand do not fully contribute to the cyclic strength and cone resistance as much as they contribute to the density of the silty sand. For this reason, a silty sand may appear dense and can have low void ratio. But it may not be as high resistant to liquefaction and as high resistant to cone penetration as a clean sand at the same void ratio.

- Silt particles contribute to the reduction in porosity and pore opening size and therefore reduce k and coefficient of consolidation c_v. Therefore, a cone penetration process in a saturated silty sand produces significant excess pore pressure that does not rapidly dissipate during penetration, and as a result contribute to a reduction cone resistance. On contrary, a clean sand is highly permeable, and therefore cone penetration produces low excess pore pressure, due to rapid dissipation of pore pressures around the cone due to large permeability of the sand. Furthermore, cone diameter (d) and penetration velocity (v) also affect the pore pressure regime and its dissipation rates during penetration, and therefore affects the measured q_{c1N}.

- The above combined effects influence the CRR-q_{c1N} relationship to a different degree for silty sand than for a clean sand. This phenomenon is not just a function of the amount of silt content only, but rather highly depends on k and c_v as well.

- A refined screening method can be developed that takes into account the effects of c_v, which can be measured using piezo-cone tests, on cone resistance q_{c1N} and the effect of silt content on CRR. Progress to date (presented below) indicates that it is highly likely there exists a rational relationship between CRR-q_{c1N}-T (where T = vd/c_v).

(a) Laboratory CRR vs q_{c1N} (b) Comparison with field liquefaction screening chart
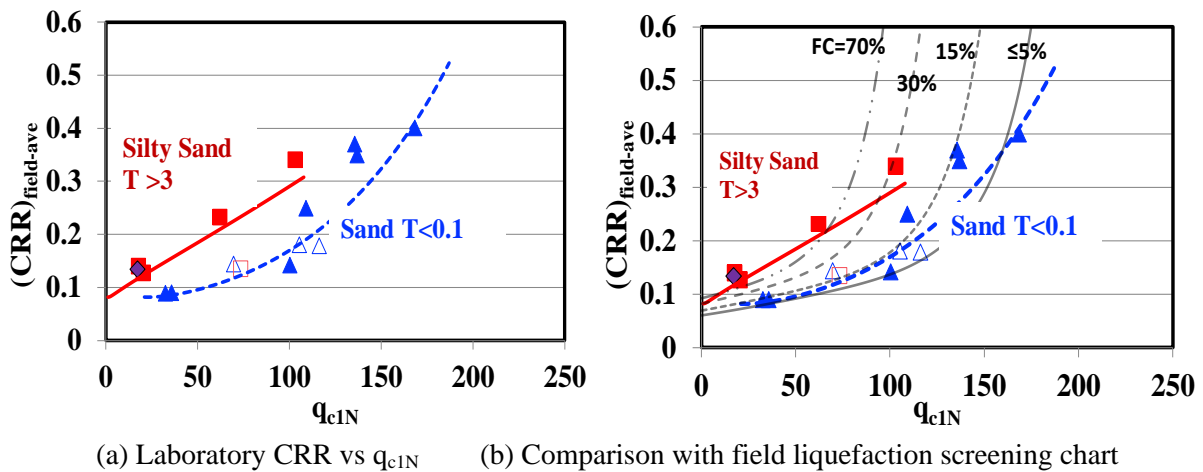
Fig. 2. Effect of silty sand (T) on CRR vs q_{c1N}

A preliminary series of experiments were conducted on a clean sands and silty sand at 25% silt content. They involved cone penetration tests with pore pressure measurements, cone-pore pressure dissipation tests, and undrained cyclic triaxial tests. The measured $(CRR)_{tx}$ were corrected for multi-shaking effects (Seed et al. 1978) to obtain an equivalent $(CRR)_{field}$.

Results showed that the sand and silty sand exhibited similar CRR at the same equivalent intergranular void ratio $(e_c)_{eq}$ (Thevanayagam et al. 2002). However, q_{c1N} was dependent on T and it was smaller for saturated silty sand compared to sand at the same $(e_c)_{eq}$ (Thevanayagam et al. 2015, 2016). Fig.2a shows the CRR-q_{c1N}-T relationship corresponding to each cone test, and the associated T values.

- The dashed blue line (T<0.1) in Fig.2a shows the relationship for saturated sand. The red line (T>3) shows the relationship for saturated silty sand at 25% silt content.
- The T values for saturated sand (blue dash line) are less than 0.1 whereas the T values for the saturated silty sand (red line) are greater than 3. As T increases the CRR-q_{c1N} curve shifts to the left, for the same CRR, due to excess pore pressures developed around the cone in silty sands. For the same CRR, saturated silty sand (red line) shows a smaller q_{c1N} than saturated sand.

Fig.2b shows the CRR-q_{c1N}-T relationship superimposed on the CRR-q_{c1N}-FC liquefaction screening chart from Boulanger-Idriss-2014 (black lines for FC of 5, 15, 30 and 70%).

- The dash-blue line (T<0.1) which corresponds to saturated sand follows the of B-I-2014 curve trend for sand.
- The red line (T>3) that corresponds to saturated sand-silt mix (prepared at FC=25%) follows the B-I-2014 trend for high silt content.
- This indicates that the different screening curves for different silt contents in screening charts (Fig.1) are indeed manifestations of the effect of k and c_v (reflected in T), not just the gross amount of silt content.
- As the silt content increases, typically k and c_v decreases and T increases and hence q_{c1N} decreases for the same CRR. The reduction in q_{c1N} for silty sand is due to lack of rapid pore pressure dissipation around the cone in silty sand compared to the case for a clean sand at the same CRR.

CONCLUSIONS

As evident from Fig.2, it appears what separates the CRR-q_{c1N} relationship for silty sands from sand are the effects of silt content on CRR, and the additional effects of silt content (namely permeability and consolidation characteristics) on q_{c1N}. A liquefaction screening relationship between CRR-q_{c1N}-T is likely. Such a screening method could be implemented in the field using piezocone penetration to measure q_{c1N} and dissipation (or hold) tests to measure c_v by stopping the penetration for just a few seconds when the cone tip reads notably high excess pore pressures during penetration through silty sands zones, excluding clayey zones. Such a rational CRR-q_{c1N}-T liquefaction screening method could help reduce the level of uncertainty in the current screening methods and advance the state of practice in liquefaction triggering analysis.

ACKNOWLEDGEMENTS

REFERENCES

Andrus, R.D. and Stokoe, K.H. (2000) "Liquefaction resistance of soils from shear-wave velocity", *J. Geotech. and Geoenv. Eng.*, ASCE, 126(11): 1015-25.

Boulanger, R and Idriss, I-M. (2014) "CPT and SPT based liquefaction triggering procedure", *Report No. UCD/CGM-14-01*. University of California, Davis. 138p.

Idriss, I. M., and Boulanger, R. W. (2008). Soil liquefaction during earthquakes. *Monograph MNO-12*, EERI, Oakland, CA, 261p.

NCEER (1997) Proc., NCEER workshop on Evaluation of liquefaction resistance of soils, *NCEER Tech. Report NCEER-97-0022*, prepared by Youd, T.L, and Idriss, I.M; 276p

Robertson, P.K., and Wride, C.E. (1998) "Evaluation of cyclic liquefaction potential using the cone penetration test," *Canadian Geotechnical Journal*, Ottawa, 35(3), 442-459.

Seed, H. B., Martin, G. R., and Pyke, C. K. (1978) "Effects of multi-directional shaking on pore pressure development in sands", *J. Geotech. Eng. Div.*, ASCE, 104(1), 27-44.

Seed, H.B., Idriss, I.M, and Arango, I. (1983) "Evaluation of liquefaction potential using field performance data", *J. Geotech. Eng.*, ASCE, 109(3): 458-482.

Thevanayagam, S., Shenthan, T., Mohan, S. and Liang, J. (2002), "Undrained fragility of sands, silty sands and silt", *J. Geotech. & Geoenv. Eng.*, ASCE, 128 (10), 849-859.

Thevanayagam, S. and Martin, G. R. (2002) "Liquefaction in silty soils - screening and remediation issues", *J. Soil Dyn. and Earthquake. Eng.*, 22, 1034-1042.

Thevanayagam, S. Ecemis, N., Kanagalingam, T., and Martin, G. R. (2006) "Liquefaction screening of silty soils using Cone penetration tests" Proc. 8th National Conf. Earthq. Eng., San Francisco, CA.

Thevanayagam, S. and Ecemis, N. (2008) "Effects of permeability on liquefaction resistance and cone resistance", *Geotechnical Special Publication 181*, ASCE, 11p.

Thevanayagam, S. Veluchamy, V, Huang, Q, and Sivaratnarajah, U. (2015) "Silty sand liquefaction, screening, and remediation", *Proc. 6th ICEGE*, New Zealand.

Thevanayagam, S. Veluchamy, V, Huang, Q, and Sivaratnarajah, U. (2016) "Silty sand liquefaction, screening, and remediation", *J. Soil Dyn.and Earthq. Eng.*, (in review).

Youd, T.L., et al. (2001) Liquefaction resistance of soils: Summary Report from the 1996 NCEER and 1998 NCEER/NSF Workshops on Evaluation of Liquefaction Resistance of Soils, *J. Geotech. and Geoenv.Eng.*, ASCE, 127(10), 817-833.

PILE-SOIL CYCLIC INTERACTION OF OFFSHORE WIND TURBINES' FOUNDATIONS

Bin Zhu, Z. J. Zhu and Jie Ren
Institute of Geotechnical Engineering, Zhejiang University, China

BRIEF INRODUCTION, METHODOLOGY AND KEY RESULTS

The single pile foundations and the piled jacket foundations are widely used in offshore wind turbines and oil/gas platforms, mainly because they are easily constructed and relatively low-cost. Usually constructed in severe environment and subjected to lateral loads of wind, wave, current, earthquake, etc., they must meet the requirements for the bearing capacity and deformation. A series of centrifuge model tests on single piles with different diameters and on jacket foundations in saturated sand have been carried out, to investigate behaviors of the piles subjected to laterally monotonic and cyclic loading. Both static and cyclic *p-y* curves of the piles are derived from the measured bending moments of the pile shaft. The calculated hyperbolic *p-y* curves with the modified initial modulus of subgrade reaction of the API *p-y* curves are in good agreement with these derived static *p-y* curves.
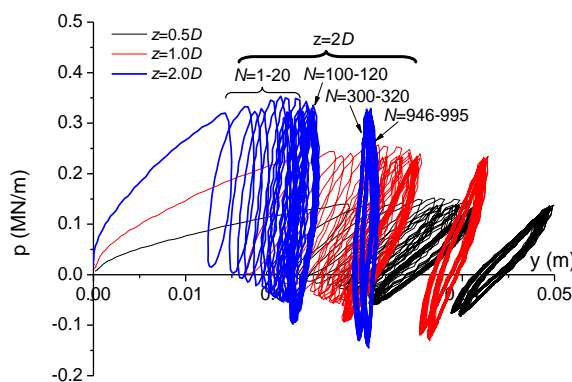
Fig. 1 Cyclic *p-y* curves at different depths
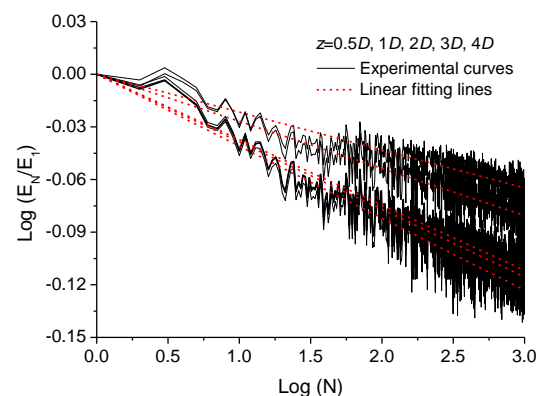
Fig. 2 Ratio of the secant stiffness

For the large-diameter pile under laterally cyclic loading, it is indicated that the deflection, the maximum moment and the unloading stiffness of the pile increase in a certain degree with respect to the number of cycles, while the pore water pressure of soil around pile don't have an obvious accumulation for the used Fujian sand with a relative density of 60%. The accumulated horizontal displacement at the loaded position on the pile shaft approximately increases 100-150% after 1000 cycles compared with the one after the first cycle. The cyclic *p-y* curves derived from the measured bending moments of the pile shaft in each cycle are obtained and given in Fig. 1, and the cyclic degradation factor of these *p-y* curves at different depths is calculated. It is found that the cyclic degradation factor increases as the increase of the soil depth and the decrease of the cyclic ratio of soil reaction, as shown in Fig. 2. Finally, a group of cyclic *p-y* curves related to the number of cycles and the cyclic ratio of soil reaction are presented, and a corresponding analysis approach is proposed for engineering design.

For jacket foundations, the test results show that the uplifted piles of a jacket foundation will be pulled out more easily under the horizontal loads along the diagonal direction rather than loading along the side direction. The maximum bending moment of the pile shaft, the shear force and bending moment at the top of the front-row pile(s) are apparently larger than those of the back-row pile(s) while their lateral deflection is close to each other. As shown in Fig. 3, it is found that within the soil depth of 2.5 times the pile diameter, the horizontal subgrade reaction per unit length on the back-row pile(s) is approximately 60% of that of the front-row pile(s) when loading along the side direction, while this value decreases to about 40% when loading along the diagonal direction. The decrease is mainly attributed to the decrease of effective stress in soil around the uplifting pile(s) caused by the pile group effect and the uplifting axial force of the pile shaft. In view of this, modified p-multipliers depending on the pile spacing, the loading height, the loading direction, and the pile deformation are proposed for lateral response analysis of the tetrapod jacket foundation of offshore wind turbines.

(a) Loading along side direction   (b) Loading along diagonal direction
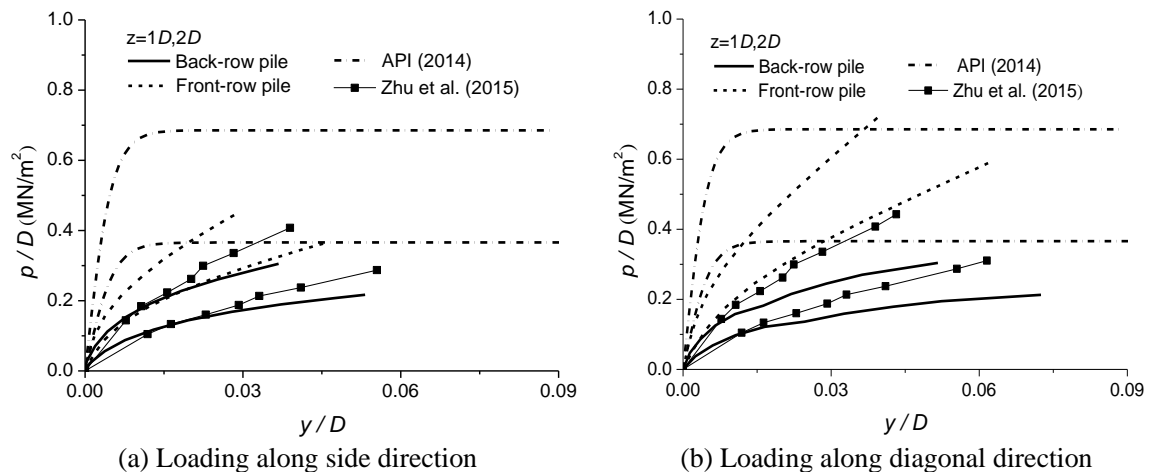
Figure 3 Comparison of static p-y curves

CONCLUSIONS

1. For the single pile under lateral monotonic loads, in the first 1000 cycles in the present cyclic loading tests, both the accumulated horizontal displacement and the unloading stiffness at the loaded position could approximately increases 100-150% and 50-150% with respect to the number of cycles, and the variation of the maximum bending moment of the pile shaft can be 10% for different cyclic loading amplitudes and frequencies. The cyclic degradation factor increases as the decrease of the soil depth and the increase of the cyclic ratio of soil reaction.
2. For jacket foundations, when loading in different directions, the pile group effect and the uplifting axial force of the pile shaft are the main reasons for the decrease of horizontal subgrade reaction in soil around the uplifted pile(s). The value of the back-row pile(s) is approximately 60% of that of the front-row pile(s) when loading along the side direction, while this value decreases to about 40% when loading along the diagonal direction.

REFERENCES

American Petroleum Institute (API). (2007). "Recommended Practice for Planning, Designing and Constructing Fixed Offshore Platforms-Working Stress Design." API Recommended Practice 2A-WSD (RP2A-WSD), Errata and Supplement 3.

Chen, Y. M., Kong, L. G., Zhou, Y. G., Jiang, J. Q., Tang, X. W., and Niu, B. (2010). "Development of a large geotechnical centrifuge at Zhejiang University." 7th

International Conference on Physcial Modeling in Geotechnics, Zurich, 28 June-1 July, pp.223-228.

Craig, W. H. (1983). "Simulation of foundations for offshore structures using centrifuge modelling." Developments in Soil Mechanics and Foundation Engineering-Model Studies, London, 1-27.

Mirza, U. A., and Maclaren, D. J. (1992). "Jacket performance due to foundation-degraded response", Offshore Technology Conference, Houston, 311-322.

Mostafa, Y. E., and El Naggar, M. H. (2004). "Response of fixed offshore platforms to wave and current loading including soil-structure interaction." *Soil Dynamics and Earthquake Engineering*, 24(4): 357-368.

Poulos, H. G. (1982). "Single pile response to cyclic lateral load." *Journal of the Geotechnical Engineering Division*, ASCE, 108(3): 355-375.

Zhong, C., Mao, D. F., Duan, M. L., Li, Z. G., Yuan, Z. L., and Wang, J. G. (2013). Experiment study of horizontal vibration characteristics of fixed jacket platform considering degradation of pile foundation. *Rock and Soil Mechanics*. 34(1): 53-60.

Zhu, B., Chen, R. P., Guo, J. F., Kong, L. G., and Chen, Y. M. (2012). "Large-scale model and theoretical investigations on lateral collisions to elevated piles." *Journal of Geotechnical and Geoenvironmental Engineering*, ASCE, 138(4): 461-471.

WAVE & CURRENT-INDUCED PROGRESSIVE LIQUEFACTION IN LOOSELY DEPOSITED SEABED

Jianhong Ye* Kunpeng He*+ Lijie Zhou*+ Guoxiang Yang++

*Institute of Rock and Soil Mechanics, Chinese Academy of Sciences

+School of Resources & Environment, Wuhan University of Technology

++Department of Civil Engineering, China University of Geosciences (Beijing)

BRIEF INRODUCTION, METHODOLOGY AND KEY RESULTS

In offshore environments, newly deposited Quaternary seabed soil is widely distributed, for example, the loose silty soil in the zone of estuary of Yellow River in China. Actually, a great number of offshore structures have been built on Quaternary sediments. The particle arrangement of Quaternary seabed soil generally is relatively loose, far from being very dense. Under cyclic ocean wave loading (magnitude is greater than a critical value), soil particles re-arrange their relative positions to a more dense status, accompanying a pore water drainage process. In this process, pore water pressure builds up, making soil liquefy, or soften. Therefore, it is very dangerous to build a marine structure on newly deposited Quaternary seabed floors. In this study, the wave & Current-induced dynamic response characteristics of newly deposited loose seabed soil, rather than very dense seabed soil (elastic deformation is dominant) is exactly the focus. Understanding of the dynamic response characteristics of seabed foundation to ocean wave is a key factor when evaluating the stability of offshore structures during their service period.

Taking an integrated numerical model FSSI-CAS 2D (Ye et al., 2013) as the tool, the wave & current-induced liquefaction mechanism of newly deposited loose seabed soil is investigated. The advanced soil constitutive model–Pastor-Zienkiewicz Mark III (PZIII) proposed by Pastor et al. (1990) is used to describe the complicated nonlinear dynamic behaviour of loose seabed soil. The variation of void ratio e, and corresponding permeability k of soil is considered in this computation. Additionally, the stiffness matrix [K] highly depending on effective stress state is also updated using current effective stress in computation, to fully consider the nonlinearity of dynamics of loose seabed to ocean wave. A flat seabed with 400m long and 20m thick is chosen as the computational domain. The progressive wave & current-induced dynamic pressure acting on the seabed is applied adopting third-order formulation (first explicitly formulated by Ye and Jeng (2012)). The parameters of loosely deposited seabed soil for PZIII constitutive model are listed in Table 1, which were determined by Zienkiewicz et al. (1999) for Nevada sand (D$_r$=60%).

The initial void ratio e, saturation of seabed soil used in computation is 0.333, and 98%, respectively. Correspondingly, the initial permeability of seabed soil is 1.0×10^{-5}m/s. The initial water depth d_0 of sea water over seabed floor is 10m. Wave height and wave period is set as 1.5m and 8.0s, respectively. Current velocity U$_0$=0.5m/s. Computational results

Table 1 Parameters for PZIII model

Iterm	Nevada dense sand	Unit
K_{evo}	2,000	[kPa]
G_{eso}	2,600	[kPa]
p'_0	4	[kPa]
M_g	1.32	-
M_f	1.3	-
α_f	0.45	-
α_g	0.45	-
β_0	4.2	-
β_1	0.2	-
H_0	750	-
H_{U0}	40,000	[kPa]
γ_u	2.0	-
γ_{DM}	4.0	-

on symmetrical lines x=200m are recorded, taking as representatives to demonstrate the dynamics of loose seabed soil to progressive wave & current.

Figure 1 shows the time history of wave & current-induced excess pore pressure and effective stress at a typical buried depth. It is observed that pore pressure builds up under ocean wave & current loading in loose seabed floor. There are two components of pore pressure: residual component and oscillatory component. Wave & current-induced residual pore pressure cannot build up unlimitedly. After its peak value being reach, Residual pore pressure basically keeps its state in this case. Corresponding to the build-up of residual pore pressure, effective stress in loose seabed floor reduces from its initial consolidation state. When effective stress approach zero stress state, seabed soil will lost its shear strength and bearing capacity, resulting in collapse of offshore structures if it is as a foundation. As illustrated in Figure 1, the mean effective stress $I_1/3$ at z=18.5m approaches the zero stress state at about t=150s, becoming partially liquefied. At t=300s, $I_1/3$ becomes zero. It means that the seabed soil at z=18.5m becomes fully liquefied. In the process of effective stress decreasing, the amplitude of shear stress also reduces. When seabed soil at z=18.5m becoming fully liquefied, wave & current-induced shear stress also becomes zero due to the fact that a fully liquefied soil behaviors like a kind of heavy fluid. As we know, fluid has not ability to transmit shear stress in nature. Our model can clearly captures this phenomenon.
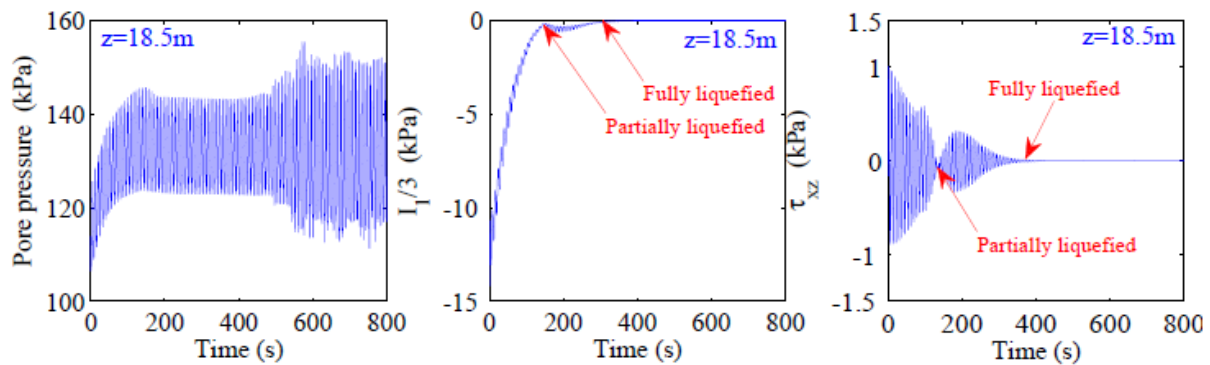
Figure 1: Time history of wave & current-induced pore pressure and mean effective stress I1/3 at a typical buried depth.

The essence of residual soil liquefaction in loose seabed is the build-up of residual pore pressure under hydrodynamic loading. When excess residual pore pressure is equal to or greater than the initial contact effective stress between soil particles, sandy soil become liquefied. It is highly necessary to understand the vertical distribution characteristics of residual pore pressure under wave & current loading. In Figure 2, this vertical distribution characteristics of residual pore pressure at different times on x=200m are shown. It is clearly observed that residual pore pressure in loose seabed continuously builds up with time. However, there is a limitation line to constrain the build-up of residual pore pressure. Residual pore pressure cannot exceed this limitation line. Actually, this limitation line is the liquefaction resistance line (LRL). When wave & current-induced residual pore pressure reaches to LRL at a depth, the seabed soil at this depth becomes liquefied. It is shown that the time needed for residual pore pressure reaching LRL is positively related to buried depth of seabed
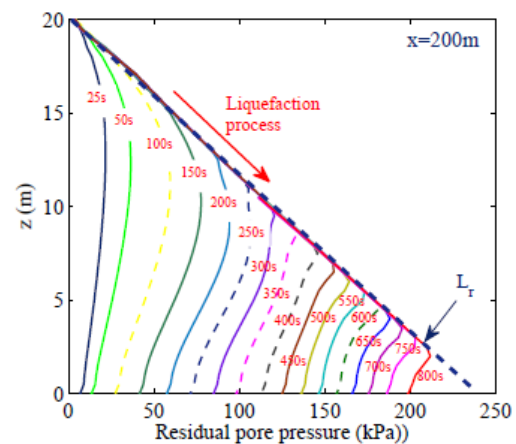
Figure 2: Vertical distribution of wave & current-induced residual pore pressure.

soil. It means that hydrodynamic loading-induced liquefaction in loose seabed is a progressive process, initiating at surface, and gradually propagating downward, as illustrated in Figure 3. Liquefaction zone shown in Figure 3 is predicted based on the definition of liquefaction potential. When liquefaction potential is greater than 0.86 at a position, then it is predicted that seabed soil here become liquefied. In Figure 3, it is observed that the liquefaction zone in loose seabed floor gradually enlarges with time. The shape of liquefaction zone frontier is wavy affected by the motion of ocean wave. To t/T=100, most of the loose seabed floor become liquefied, the liquefaction depth reaches 18m.
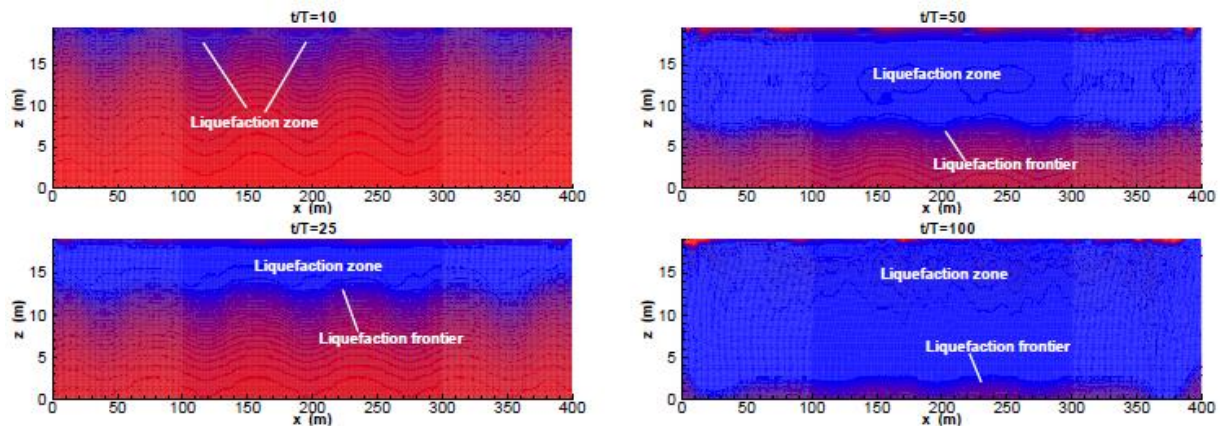
Figure 3 Wave & current-induced residual liquefaction zone in loose seabed floor at typical time t/T=10, 25, 50, 100 (It is noted that zone with blue color presents the liquefaction zone)

CONCLUSIONS

Wave & current-induced residual liquefaction has been investigated deeply and comprehensively adopting a validated integrated numerical model. It is shown that the integrated numerical model FSSI-CAS 2D incorporating PZIII soil model can effectively and precisely capture a series of nonlinear dynamic response characteristics of loose seabed floor under wave & current loading. The computational results further confirm the wave-induced liquefaction in loose seabed soil is progressively downward, initiating at seabed surface. Besides, it is also found that the progressive liquefaction process is significantly affected by wave height, permeability and saturation of the seabed soil.

ACKNOWLEDGEMENTS

REFERENCES

Ye, J. H., Jeng, D.-S., Wang, R., and Zhu, C.-Q. (2013). "Validation of a 2D semi-coupled numericalmodel for Fluid-Structures-Seabed Interaction". *Journal of Fluids and Structures*, 42, pp. 333–357.

Pastor, M., Zienkiewicz, O. C., and Chan, A. H. C. (1990). "Generalized plasticity and the modelling of soil behavior". *International Journal for Numerical and Analytical Methods in Geomechanics*, 14, pp. 151–190.

Ye, J. H. and Jeng, D. S. (2012). "Response of porous seabed to nature loadings: Waves and currents". *Journal of Engineering Mechanics*, ASCE, 138, No. 6, pp. 601–613.

GEOTECHNICAL ENGINEERING ASPECT OF THE 2015 GORKHA, NEPAL, EARTHQUAKE

K. Sharma, Lijun Deng
Department of Civil & Env Eng, University of Alberta, Canada

INTRODUCTION

The Gorkha Nepal earthquake of moment magnitude M_w 7.8 occurred at 11:56 a.m. NST (6:11 a.m. UTC) on April 25, 2015, with the epicenter (N: 28.1470; E: 84.7080) 77 km northwest of Kathmandu at a focal depth of approximately 15 km (USGS, 2015). Tremor that lasted for 55 sec was felt in Nepal, India, Bhutan, Bangladesh, and China. Another earthquake of M_w 7.3 shook the region on May 12, having the epicentral location in Kodari (N: 27.8368; E: 86.0772), northeast of Kathmandu, and caused additional damage to rural towns and villages in the northern part of central Nepal. These seismic events in the central Himalaya were the strongest after the 1934 earthquake that was located northeast of Kathmandu. As of June 1, 2016, a total of 455 aftershocks with a magnitude above 4 had been observed, 49 with a magnitude above 5, and 5 above 6.

The Himalaya was formed by the collision of Indian plate and Eurasian plate starting from 40 million years ago. The Himalayan arc, which marks an active boundary between Indian and Eurasian plates, has caused numerous major earthquakes of moment magnitude 7.5 or greater in past centuries (Bilham et al, 2001). The 2015 Gorkha earthquake were the result of thrust faulting between the subducting India plate and the Eurasia plate to the north, where the Indian plate converges with the Eurasian plate at a rate of approximately 45 mm/year towards the north-northeast, driving the uplift of the Himalayas and the Tibetan Plateau [Copeland, 1997].

A field reconnaissance of the Gorkha earthquake was carried out by the authors in April and May 2015. This paper briefly explains recorded ground, case studies of landslides, ground failure, liquefaction, and local site effects on the observed damage severity due to the soil properties, basin, and basin ridge.

Figure 1: Accelerograms at KATNP for the (a) Mw 7.8 main shock, (b) Mw 7.3 aftershock, (c) 5%-damped acceleration response spectra (ARS) of the accelerograms.

GROUND MOTION AND RESPONSE SEPCTRA

The peak ground acceleration (PGA) of the recorded ground motions was 184 gal and 87 gal (Figs. 1a and 1b) for the M_w 7.8 main shock and the M_w 7.3 aftershock, respectively

(USGS, 2015). It is seen that the acceleration records are broadband and contain the long-period components at 5 sec which may be resulted from the effects of the deep soft sediment in the valley on the duration and amplification of shaking. However, due to the lack of rock outcrop recordings, comparison between the outcrop and ground surface responses are not readily available. The 5%-damped response spectra of the accelerograms for the M_w 7.8 main shock and the M_w 7.3 aftershock are calculated and compared in Fig. 1c. It is seen that the NS component of the main shock has two prominent peaks, one at about 0.47 sec and another one at about 5 sec.

GEOTECHNICAL ASPECT OF THE EARTHQUAKE

Geotechnical failures observed during the field reconnaissance were mainly landslides and ground fissures. Liquefaction, lateral spreading, and settlement triggered by the main shock appears to be limited and localized. Case studies of geotechnical failure and damages are detailed as follows. Figure 2 shows the survey route from Kathmandu to the epicentral area of the main shock and nearby areas.

Following the main shock and aftershock, about 3,600 landslides of small to mega scales were induced within 200 km stretch of the epicenter causing enormous economic and socio-environmental loss (ICIMOD 2015). The pattern of mass movements was similar to those observed in the 1999 Chi-Chi earthquake and 2008 Wenchuan earthquake. Numerous earthquake induced landslides were observed as the team travelled toward epicentre through the mountainous terrain. A major rock fall occurred near Baluwa village at the distance about 2.5 km from the epicentre of main sock and obstructed the Daraudi link road connecting to Barpak village as shown in Fig. 3. A small village on the left of rock fall was destructed. Fortunately, there are only minor cracks on the newly constructed reinforced cement concrete (RCC) bridge near the rock fall.

The M_w 7.8 main shock caused minimal damages to major highways. However, side access road to the remote areas suffered significantly from the earthquake and still remains blocked. Although building structures suffered severely in the Kathmandu Valley, roadway damage was minor. The Arniko highway north to Tibet (China), suffered numerous landslides and rock falls due to M_w 7.3 aftershock.

Figure 4a shows the location and types of damage observed in Lokanthali along the Araniko highway. The embankment suffered from substantial settlement of approximately 1 m due to the main shock, as shown in Figs 4b and 4d. Ground fissures, settlement, tilting of buildings and road pavement damage were also observed in the surrounding areas. The ground fissures extend hundreds of meters diagonally across the highway (Figs. 4a and 4d), damaging and tilting a number of buildings and boundary walls. Apart from the subsidence, the embankment did not suffer from major structural damage. Only minor damage such as cracks and fissures, slight tilting, and differential settlement (Fig. 4c) was observed in reinforced soil retaining wall. Overall, the
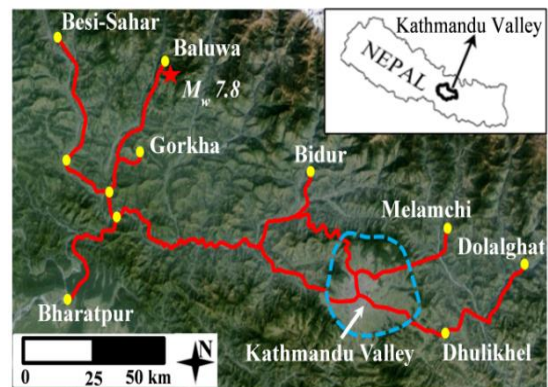
Figure 2: Survey route and locations of investigation sites in the epicentral area
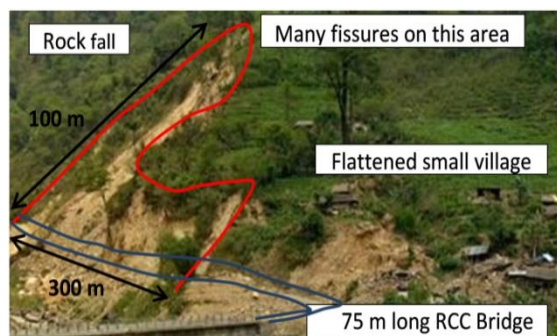
Figure 3: A major rock fall near Baluwa at 2.5 km from the epicenter

71

reinforced retaining walls and earth embankment demonstrated good performance against the earthquake.
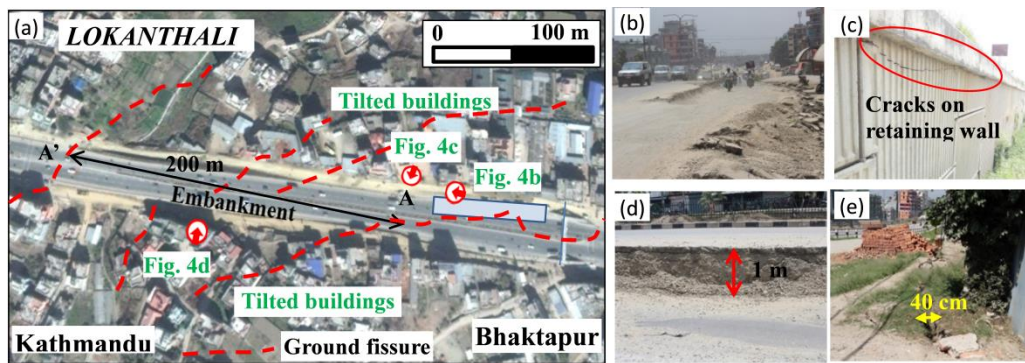
Figure 4: (a) Location of damage observed in Lokanthali along the Arniko highway, (b) Subsidence of left side lane of the highway, (b) close-up view of Fig. 13a, (c) cracks and deformation on retaining wall, and (d) diagonal cracks across the highway.

Liquefaction triggered by the Mw 7.8 Gorkha earthquake appears to be fairly limited and localized (Fig. 5). Observed liquefaction cases were evident sporadically along the edge of the Kathmandu basin. The low liquefaction occurrence in the valley may be attributed to low PGA of 0.17 g in the valley that is much smaller than the design PGA of 0.3 g in the studies of the liquefaction susceptibility maps (JICA, 2002). In addition, the low groundwater table during the dry season may reduce the liquefaction potentials of the valley soils.

It was observed that one of the main reasons for extensive damages to building structures was local geological and geotechnical effects and the construction quality. The effect of loose fill was evident from the extensive damages in Gongabu, Balaju, Machha Pokhari, Ramkot, Naikap and the surrounding areas in Kathmandu city. Most of the four- to five-storey reinforced-concrete (RC) buildings in this region had experienced severe damage or failure completely (Sharma et al, 2016). Since these RC buildings have the predominant period of approximately 0.5 sec, the severity may be attributed to the predominant period of 0.45 sec (Fig. 1c) of the horizontal component of the main shock. The destruction of the building structures supported on shallow foundations in Ramkot, Naikap and Sipadol can also be interpreted by the local site amplification because most of these structures were constructed on loosely compacted fill.

The effect of low frequency amplification caused by the Kathmandu Valley basin is evident from the severe damage to well-designed high-rise buildings in Kathmandu city (Keshab et al, 2016). It was observed that most of the one- and two-story masonry houses constructed more than 50 years ago were literally intact, with only few houses suffering minor cracks, while newly constructed multi-storey buildings suffered from severe damage (Figs. 6a and 6b). Similarly, both structural damage and ground failure patterns observed during the Gorkha earthquake sequence clearly indicate that the ridge effects dominated ground motion intensity, on the basis of the contrast in the severity of damage on the hill and in the nearby valley. Figure 6c shows the distribution of damage (red) and partially damage building (yellow) in the hilly area of Nepal. It is evident that the severe damages are aligned with the ridge lines.

Severe damages were observed adjacent to basin edges around the Kathmandu Valley after the main shock and subsequent aftershocks. It is evident that basin edge effect has had the impacts

Figure 5: Liquefaction in small scale in Lalitpur

on the performance of buildings because of the geological features of the Kathmandu Valley. Towns such as Duwakot, Kapan, Manmaiju, Budhanilkantha, Jorpati, and Sakhu located at the edge of the valley basin were severely affected as compared to other old towns with many non-engineered masonry buildings such as Asan and Patan located in the center of the Kathmandu Valley.

Figure 6: Overview of high rise apartment and low rise residential building in Buddanagar, Kathmandu, (b) severe cracks on high rise apartment, and (c)) Ridge-top damage interpreted from satellite image decorrelation before and after the main shock (ARIA/JPL-Caltech)

CONCLUSION

The aim of this paper is to investigate the geotechnical aspect of 2015 Gorkha earthquake that struck Nepal on April 25, 2015, followed by a series of aftershocks. The paper described the geological and geotechnical characteristics of the affected areas and presented geotechnical case studies of landslides, road embankment, bridges, and liquefaction.

The recorded accelerograms showed that the max shaking at the ground shaking was 184 gal. The ground motions contained long-period component at the predominant period of 0.47 sec and secondary period of 5.0 sec. A large number of slope failures and rocks fall occurred at shallow depth in Gorkha district. The M_w 7.3 aftershock added large number of slopes failures along Araniko highway and in Kodari region. Shallow landslide and numerous ground fissures were found in devastated area. Liquefaction cases triggered by the M_w 7.8 Gorkha earthquake appeared to be limited and localized, although the valley soils are susceptible to liquefaction. The damage patterns revealed strong influence of local site conditions on the severity of the damage at many places. Building damage in the Kathmandu Valley and nearby villages was caused not only by the poor quality of non-engineered buildings but also by local site effects induced by soft alluvial soil deposits, ridge effect and basin effect.

REFERENCES

Bilham, R., Gaur, V. K. and Molnar P. (2001). "Himalayan Seismic Hazard." *Science* 293, pp. 1442-1444.

Copeland, P. (1997). "The when and where of the growth of the Himalaya and the Tibetan Plateau. In: Ruddiman, W.F. (Ed.), *Tectonic Up lift and Climate Change*. Plenum Press, New York, pp. 19–40.

Japan International Cooperation Agency (JICA) (2002). "The study of earthquake disaster mitigation in the Kathmandu Valley, Kingdom of Nepal." *Final Report*. I-IV.

Sharma, K., Deng, L. and Cruz-Noguez, C. (2016). "Field investigation on the performance of building structures during the April 25, 2015, Gorkha earthquake in Nepal." *Eng Struct*.121, pp. 61-74.

United States Geological Survey (USGS). http://earthquake.usgs.gov/realtime/product/finite-fault/us 20002926/us/1429969841288/20002926.html (accessed on May 27, 2015).

EFFECTS OF PARTICLE BREAKAGE ON THE MOVEMENT AND DEPOSIT CHARACTERISTICS OF ROCKSLIDES

Y.D. Zhou*, J. Sun, and H. Jiang
Department of Hydraulic Engineering, Tsinghua University, Beijing, China

BRIEF INRODUCTION, METHODOLOGY AND KEY RESULTS

Rock avalanches are commonly described as extremely rapid, massive, flow-like motion of fragmented rock from a large rock slide or rock fall, with controlling factors mainly from discontinuities and lithostratigraphy features. Reasonably, rock fragmentation behaviour, owing to particle-particle collision or particle-bedrock impact, can contribute significantly to the progressive movement and final deposit formation of a rockslide event. Field observations show that the mobilized deposits, which may vary with geological and geomorphological conditions of the source mountainsides, are composed of rock fragments of broad particle size range characterized by intense heterogeneity and porosity. Rockslide avalanches are one of the most common natural disasters in China. During the 2008 Wenchuan earthquake, numerous rock avalanches were triggered and have killed more people than any other type of landslide by this seismic event. Furthermore, similar geo-structures made up of fragmented rock aggregates are quite common in hydraulic and mining as well as minerals engineering. It is of great significance to investigate the complex behaviour of rock debris under various loading conditions.

Although much attention has been paid to the kinematic and kinetic analysis of rock avalanche, most of previous studies are based on phenomenological approaches, and the rock debris are mostly considered as continuum media. Various types of motion mechanism, including air theories, frictional heating, mechanical fluidisation, acoustic fluidisation, and grain kinematic flow, were proposed and adopted for modelling of rock avalanche processes and mechanisms. For more realistically incorporating the fragmentation behaviour of rock fragments during the sliding process, a debondable rigid finite element approach was proposed in this study. The maternal fragments that may disintegrate into smaller particles, are simulated by an assembly of rigid finite elements of prescribed feed particle size, and beam elements are introduced as bonding adhesive between adjacent pieces. The beam elements are made of material that can damage and break under given failure criteria, such as time, displacement, stress, as well as other internal variables.

A series of parametric numerical study has been carried out to investigate the effect of particle breakage on the movement and deposit formation of a typical sliding block under gravity loading condition. An initial square rock fragment of 10 m $\times$ 10 m was selected for numerical sliding experiments on a 45° inclined slope of 60m long and a joining flat ground surface. Numerical models were established to incorporate the influence of various breakage modes, disintegration efficiency, as well as the friction coefficient of the bedrock. Three types of breakage modes, namely, uniform, peripheral, and bottom-biased, were considered, whilst three breakage events, namely, forming 1×1, 5×5, and 10×10 fragments of equal size, were simulated accounting for different disintegration efficiency. To consider variable roughness of bedrock along the sliding path, three friction coefficients of 0.5, 0.7 and 0.9 were respectively adopted. A friction coefficient of 0.7 was taken for all contact interfaces

between adjacent rock fragments, maternal or new-born, in all numerical cases. It should be noted that the initial conditions in all cases are the same, assuming a geo-static state, and the potential breakage event would be triggered after one-second-long sliding downward the bedrock.

Based on the numerical results, Figure 1 shows a typical comparison of the deposits formed after a 20-second-long sliding of the rock block. The cases considering different breakage efficiency and friction coefficients of bedrock surface were chosen and the results show quite interesting findings. Figure 1a shows the effect of variable breakage efficiency on the movement of the sliding rock. It can be seen that with the rock mass kept intact, the sliding distance on the horizontal ground surface is much shorter than the other two cases with breakage incorporated (5×5 or 10×10 fragments formed), and a limited number of new-born fragments can even travel 150m away from the corner of the sloping surface. From the comparison given in Figure 1b, it can be seen that with the friction coefficient enlarged from 0.5 to 0.9, the movements of the fragmented pieces are only influenced to a small extent, and each case presents a similar run-out of the front of the deposits.

Intact block

Breakage into 5×5 blocks

Breakage into 10×10 blocks

(a)

f=0.5, breakage into 10×10 blocks

f=0.7, breakage into 10×10 blocks

f=0.9, breakage into 10×10 blocks

(b)
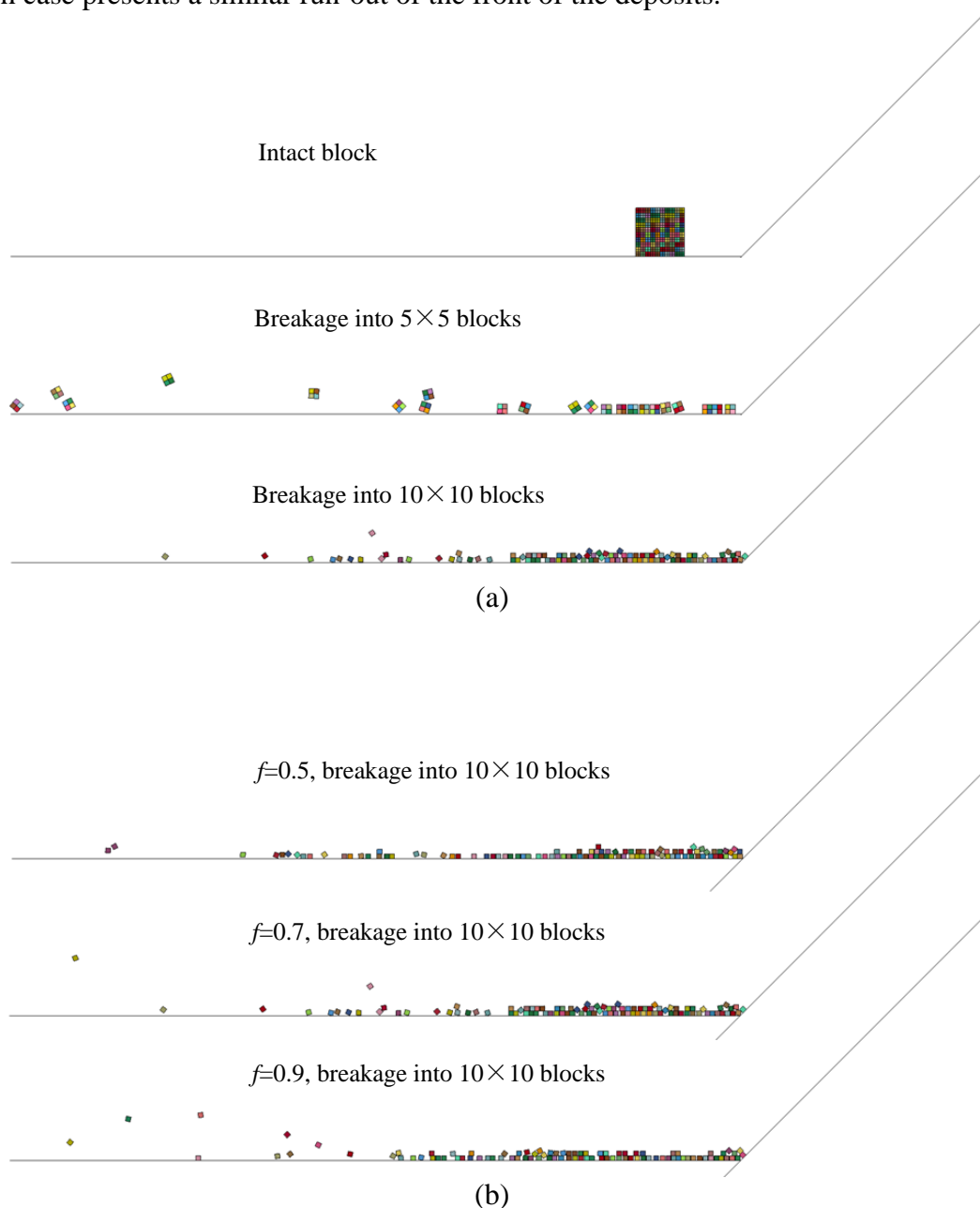
Figure 1 Comparison of simulated run-outs and deposits considering variable (a) breakage efficiency and (b) friction coefficient of bedrock surface

CONCLUSIONS

1. A series of numerical analyses were carried out to investigate the influence of particle breakage on the movement and deposit formation by rockslide avalanche. A debondable rigid finite element technique was developed for simulating potential breakage of rock blocks and different criteria can be adopted. Typical sliding cases of a rock block on a 45˚ inclined slope joined by a flat ground surface were modelled. Numerical models considering variable breakage modes, breakage efficiency, and the friction coefficient of bedrock surfaces were established and the run-out process were simulated. The rolling of particle fragments, collision between adjacent pieces, and impact of pieces with bedrock can all be considered in the numerical model.
2. When the breakage of sliding rockmass is considered, numerical results in our study demonstrate that the run-out and deposit would be less influenced by the bedrock roughness, and the rolling as well as the collision between fragments would mobilize a fluid-like flow of the sliding mass. With the breakage mode changed, the deposit formed by the sliding avalanche can be quite different, whilst the run-out distances remain basically the same if the breakage efficiency is unchanged.

ACKNOWLEDGEMENTS

REFERENCES

Bowman, E. T., Take, W. A., Rait, K. L., et al. (2012). "Physical models of rock avalanche spreading behaviour with dynamic fragmentation." *Canadian Geotechnical Journal*, 49(4), pp. 460-476.

Davies, T. R., and McSaveney, M. J. (1999). "Runout of dry granular avalanches." *Canadian Geotechnical Journal*, 36(2), pp. 313–320.

Davies, T. R., and McSaveney, M. J. (2002). "Dynamic simulation of the motion of fragmenting rock avalanches." *Canadian Geotechnical Journal*, 39(4), pp. 789-798.

Hungr O, Evans SG, Bovis M, and Hutchinson JN (2001). "Review of the classification of landslides of the flow type." *Environmental and Engineering Geoscience*, VII, pp. 221-238.

Imre, B., Laue, J., and Springman, S. M. (2010). "Fractal fragmentation of rocks within Sturzstroms: insights derived from physical experiments within the ETH geotechnical drum centrifuge." Granular Matter, 12(3), pp. 267–285.

Mudge, M. R. (1965). "Rockfall-avalanche and rockslide-avalanche deposits at Sawtooth Ridge, Montana." *Geological Society of America Bulletin* 76.9, pp. 1003-1014.

Qi, S., Xu, Q., Zhang, B., Zhou, Y., Lan, H., & Li, L. (2011). "Source characteristics of long runout rock avalanches triggered by the 2008 Wenchuan earthquake, China." *Journal of Asian Earth Sciences*, 40(4), pp. 896-906.

Wang, Yu-feng, Cheng Qian-gong, and Zhu Qi. (2015) "Surface microscopic examination of quartz grains from rock avalanche basal facies." *Canadian Geotechnical Journal*, 52, pp. 167-181.

SEISMIC ANALYSIS ON SOIL-FOUNDATION-SUPERSTRUCTURE SYSTEM CONSIDERING LARGE DEFORMATION

Guanlin Ye[1], Yonglin Xiong[2], Yuanfeng Bao[3], Bin Ye[2] and Feng Zhang[4]
[1] Shanghai Jiao Tong University, China
[2] Tongji University, China
[3] Xi'an Jiaotong-Liverpool University, China
[4] Nagoya Institute of Technology, Japan

BRIEF INRODUCTION, METHODOLOGY AND KEY RESULTS

In considering boundary value problems related to soil-structure interaction, both the structure and the soil are involved in the calculation. It is important to consider properly the geometric and material nonlinearities of both the structures and the soils. Unfortunately, due to the different aims between geotechnical engineering and structural engineering, geotechnical engineers usually pay more attention to the soil properties than to the structures. Vise verse, structural engineers usually pay more attention to the structural properties than to the soils. As the results, in simulating the soil-structure interaction problems, sophisticated models describing geometric and material nonlinearities are usually applied only in one aspect and another aspect is neglected. Therefore, in order to increase the accuracy of numerical analysis for soil-structure interaction problems to a satisfactory level that can be accepted both by geotechnical and structural engineering, it is needed to develop a numerical method in which the geometric and material nonlinearities of both the soils and the structures are properly modeled.

In this study, a rigorous numerical scheme for space beam element that can properly take the geometric and the material nonlinearities of structures into consideration was introduced and embedded into the DBLEAVES (Ye, 2007; Ye, 2011). Furthermore, soil-water coupled dynamic analyses, in the finite deformation schemes of both soils and structures, were conducted on a soil-group pile foundation-superstructure system to investigate the seismic behavior of an elevated bridge with a 12-pile foundation during a major earthquake, in which strong nonlinear behaviors of geometry and material are expected for both the soils and the structures.

As shown in Fig.1, the full system of an elevated bridge consists of a steel pier with box cross-section as the superstructure, a reinforced concrete group-pile foundation and a four-layered ground. In the analysis, the material nonlinearity of soils is described by a model named the cyclic mobility model (Zhang et al.,2007, 2011). Because of the geometric symmetry of the full system, the system is split along the direction of earthquake vibration, and only half of the system is taken out and meshed as the analytical model. The boundary condition of the ground is that: (a) the bottom of the ground is fixed; (b) the vertical boundaries parallel to the XOZ plane are fixed in the y direction and free in the x and z directions; (c) an equal-displacement-boundary condition is used between the two side boundaries whose normal direction is parallel to the x-axis to simulate the infinite boundary in real situation. The boundary condition of the piles in the calculation is that the head of the pile is fixed with the RC footing and the toe of the pile is free. The boundary condition of the pier is that the bottom of the pier is fixed with the RC footing.

Fig. 2 shows the input earthquake wave used in the analyses, which is a part of an earthquake wave recorded in Nagoya area and has the maximum acceleration of 494 gal in the horizontal direction.

In order to investigate the influence of the nonlinearity of superstructure described by different models on soil-structure interaction, three cases are conducted:

Case 1: the pier is modeled by elastic linear beam elements based on infinitesimal deformation theory (called as *Elastic Model*).

Case 2: the pier is modeled by trilinear beam elements based on infinitesimal deformation theory (called as *Trilinear Model*).

Case 3: the pier is modeled by box thin-walled beam elements which can take both material and geometric nonlinearity into consideration (called as *Goto's Model*).
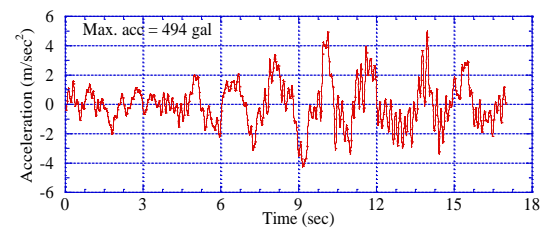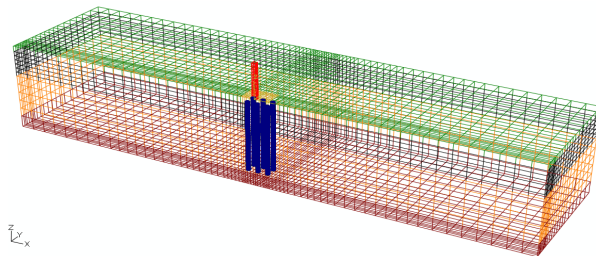
Fig. 1 Axonometric view of the analytical model   Fig.2 Input earthquake wave

Fig. 3 gives out the bending moments at the bottom of pier for all three cases. Because of no energy absorption due to hysteresis attenuation in the case of the Elastic Model, serious vibration will occur and consequently the moment and the shear forces are much larger than those in the case of the Trilinear Model or Goto's Model (Goto et al, 1995). Obviously, beam elements based on infinitesimal deformation scheme can't trace the finite deformation of pier in the process of earthquake action. As a result, the extra moment of superstructure respected to the bottom of pier due to the nodal mass and the finite deformation can't be taken into account. In the calculation, the maximum moment acting on the bottom of pier in the case of Goto's Model is 3.50 MN*m, whereas the moment in the case of Trilinear Model is only 1.30 MN*m. This notable difference will cause great different internal forces in the piles as described subsequently.
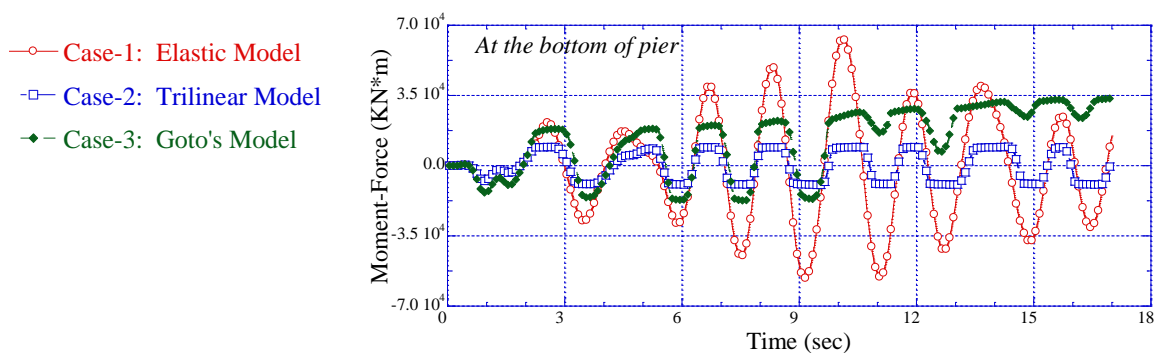
Fig.3 Bending moments at the bottom of pier

Fig. 4 shows the distributions of sectional force in different piles at the times of 7.26 and 15.52 sec respectively, from the calculation of all three cases. Pile 1 is a front pile and Pile 3 is a back pile. Because of improperly evaluating the inertia forces of superstructure, the sectional forces of group piles can't be evaluated correctly in the case of Elastic Model, which can be identified from the figures. By comparing the sectional forces of piles in the

case of Trilinear Model and Goto's Model at different times, difference of sectional forces between two cases develops with the process of earthquake action. At the time of 7.26 sec, the sectional forces of piles almost coincide with each other between Trilinear Model and Goto's Model. However, at the time of 15.52 sec, the sectional forces of piles between these two cases are totally different. Especially, the directions of axial force are even different. This is because that the extra moment of superstructure respected to the bottom of pier due to the gravitation of nodal mass will become remarkable as the finite deformation increasing. As a result, the difference of axial force between the cases of Trilinear Model and Goto's Model will also become considerable.
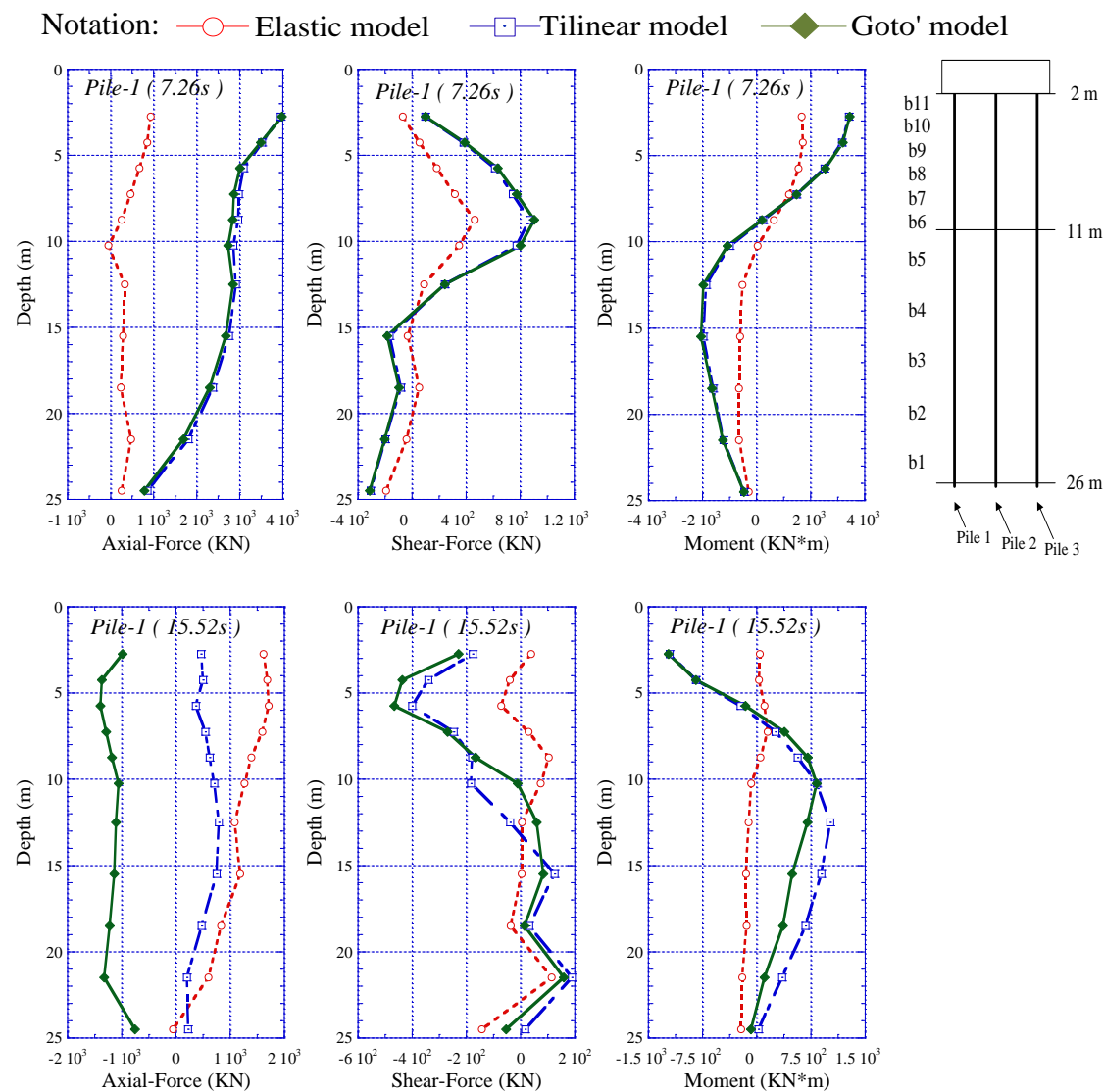
Fig.4 Distributions of sectional force of group piles at t = 7.26 sec and 15.52 sec

CONCLUSIONS

1. By introducing a beam element which can take into consideration the material and geometric nonlinearity of superstructure, any large deformation of the super- structure can be traced in the process of earthquake action. It was shown that, because of the large deformation of the superstructure due to earthquake motion, the extra moment of superstructure at the bottom of pier becomes remarkable, and this can only be simulated properly with the proposed numerical method. It is obvious that without adopting the

finite deformation scheme for the superstructure, it is impossible to describe the extra moment.

2. The cyclic mobility model was adopted to describe the behavior of ground subjected to seismic loading. The Jaumann rate strain tensor was used in the cyclic mobility model to deal with the finite deformation of soils. In the simulation, the EPWP in sandy soils increased very quickly and the soils entered into the cyclic mobility state with large deformation occurring. The soils near to the group-pile foundation showed very large shear strain compared with the soils in other areas. The soils more far afield, however, were less influenced by the soil–structure interaction.

3. For the problems involving soil–structure interaction encountered in geotechnical engineering, a full system consisting of the ground, the foundation and the superstructure should be modeled. Moreover, both the material and geometric nonlinearities of the soils and the structures should be taken into consideration by introducing proper constitutive models and finite deformation schemes.

ACKNOWLEDGEMENTS

REFERENCES

Goto, Y., Li, X. S., Kasugai, T. and Obata, M. (1995). "Analysis of Greenhill Problem by a Co-rotational Method." *Journal of Structural Engineering*, Vol.41A, 411-420.

Ye, B., Ye, G., Zhang, F. and Yashima, A. (2007). "Experiment and numerical simulation of repeated liquefaction-consolidation of sand." *Soils and Foundations*, Vol.47, No.3,

Ye, G. L. (2011): DBLEAVES: User's manual, Version 1.6, Shanghai Jaotong University, China (In Japanese and Chinese).

Zhang, F., Ye, B., Noda, T., Nakano, M. and Nakai, K. (2007). "Explanation of cyclic mobility of soils: approach by stress-induced anisotropy." *Soils and Foundations*, 47(4), 635-648.

Zhang, F., Ye, B. and Ye, G. L. (2011). "Unified description of sand behaviour." *Frontiers of Architecture and Civil Engineering in China*, Vol.5, No.2, 121–150.

DISCUSSION ON SOIL LIQUEFACTION DISCRIMINANT BY INTRODUCING FLOWABILITY INDEX

Yun-mei Zhang and Zhi-hua Wang
Nanjing Tech University, China

BRIEF INRODUCTION, METHODOLOGY AND KEY RESULTS

Soil seismic liquefaction problem gradually becomes a hot topic in the field of geotechnical engineering since the 1970s. At present, the seismic liquefaction mechanism that is the process of soil transferring from the solid to liquid, has not been fully understood. The popular method of discriminating the seismic liquefaction in practical engineering is based on the empirical knowledge obtained by the analysis and summary of existing seismic damage. However, this method is lack of an exact physical mechanism explanation and support, and it lacks the scientific basis. It is urgent to study and put forward the relevant liquefaction discrimination method based on intrinsic physical mechanism of soil liquefaction, so as to supplement and improve the existing empirical methods.

The definite method using shear wave velocity as an index is a very popular empirical liquefaction discrimination method. It is obtained on the basis of the site liquefaction critical curve according to modified shear wave velocity. However, this kind of method is lack of reasonable explanation regarding its physical mechanism. The evaluation method on the seismic equivalent shear stress in the NCEER method is used for reference in this study. It is based on the principle of Dobry strain method to calculate the potential flowability levels for all kinds of site soil under seismic equivalent shear stress. Accordingly, the liquefaction discriminant based on the flowability criterion and shear wave velocity is established using the seismic liquefaction database from Kayen & Andrus, and the seismic liquefaction data from Saygili, combined with the data of total 606 sites in 49 earthquakes. It will provide a new method for evaluating the liquefaction effect in engineering practice.

According to the simplified method proposed by Seed (1971), the equivalent seismic shear stress of soil is given by:

$$\tau_{av} = 0.65 \frac{a_{h\max}}{g} \cdot \sigma_{v0} \cdot r_d \tag{1}$$

where $a_{h\max}$ is maximum horizontal acceleration in the ground surface ($\mathrm{m/s^2}$), σ_{v0} is the total vertical stress (kPa), r_d is the reduction coefficient with depth and g is the acceleration of gravity ($\mathrm{m/s^2}$).

Changing Formula (1) gets the corresponding soil shear strain as:

$$\gamma_c = \frac{0.65 \, a_{h\max} \cdot \sigma_{v0} \cdot r_d}{g \cdot \rho \cdot V_s^2 \cdot \left(\dfrac{G}{G_{\max}} \right)_{\gamma_c}} \tag{2}$$

where ρ is bulk density of soil ($\mathrm{kg/m^3}$), V_s is soil shear wave velocity (m/s), $\left(\dfrac{G}{G_{\max}} \right)_{\gamma_c}$ is modulus ratio of critical shear strain.

Introducing the fitting formula of dynamic shear modulus ratio as:

$$\left(\frac{G}{G_{\max}}\right)_{\gamma_c} = A_2 + \frac{A_1 - A_2}{1 + e^{\frac{\gamma_c - \gamma_0}{d_\gamma}}} \tag{3}$$

where $A_1(0.928)$, $A_2(0.027)$, $\gamma_0(0.061)$ and $d_\gamma(0.008)$ are fitting parameters. A derivative of shear wave velocity with respect to the time is obtained as:

$$\dot{\gamma}_c = \frac{1.3a_{h\max}^2 \cdot d_\gamma \cdot r_d \cdot E \cdot k(A_2E + A_1 - A_2)}{0.65V_s \cdot a_{h\max} \cdot r_d (A_1 - A_2)(E-1) - d_\gamma \cdot V_s^{-3}(A_2E + A_1 - A_2)/Z} \tag{4}$$

$$E = 1 + e^{\frac{\gamma_c - \gamma_0}{d_\gamma}} \tag{5}$$

$$k = 100\frac{\sigma_v'}{\sigma_{v0}} \tag{6}$$

where k is correction factor of the effective overburden pressure σ_v' and z is soil depth (m). According to the stress-strain rate curve to get the ratio of vertical and horizontal coordinates, the apparent viscosity of the sand after liquefaction under different strain rates can be given by:

$$\eta = \frac{\tau_{av}}{\dot{\gamma}_c} \tag{7}$$

where η is apparent viscosity and τ_{av} is shear stress. The apparent viscosity in the soil caused by earthquake is expressed as:

$$\eta = \frac{0.65V_s \cdot a_{h\max} \cdot \sigma_{v0} \cdot r_d(A_1 - A_2)(E-1) - d_\gamma \cdot V_s^{-3}(A_2E + A_1 - A_2)}{2g \cdot a_{h\max} \cdot d_\gamma \cdot E \cdot k(A_2E + A_1 - A_2)} \tag{8}$$
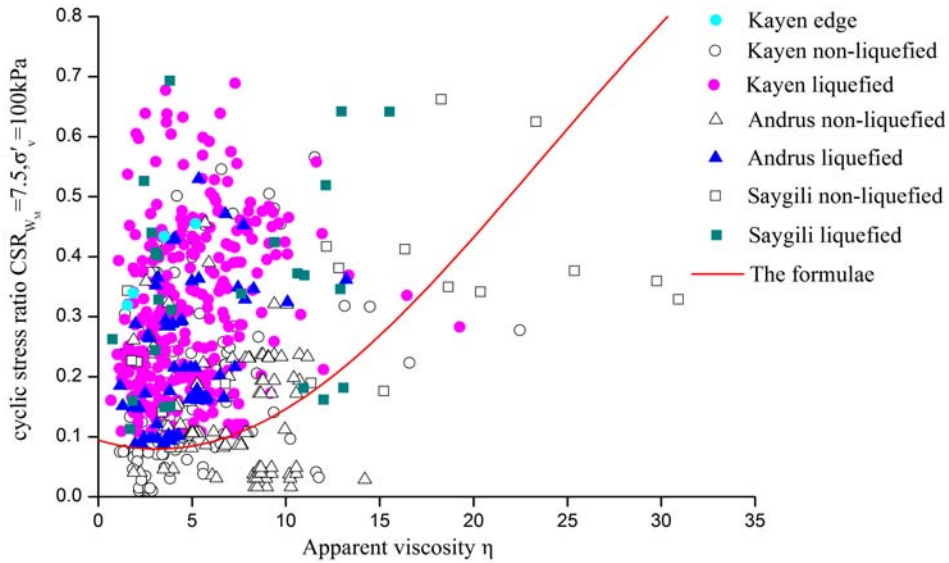
Fig.1.Relationship between case histories of database and the liquefaction triggering curves versus η with equations proposed by this paper.

According to the 150 cases of site liquefaction data from the 17 earthquakes of Andrus etc database, 415 cases from the 35 earthquakes of Kayen etc database and 41 cases from the 2 earthquakes of Kayen etc database, the scatter plot of soil layer seismic cyclic stress ratio CSR and apparent viscosity η is drawn as shown in Fig. 1. In the diagram, CSR values are normalized by the moment magnitude $M_W = 7.5$ and effective overburden pressure $\sigma_v' = 100\text{kPa}$. Hereby, the site liquefaction curve can be expressed as:

$$CRR_{M_W=7.5,\ \sigma'_V=100\text{kPa}} = 1.3 - 1.2 \cdot \exp\left[-2 \cdot \left(\frac{\eta-3.1}{41.1}\right)^2\right] \tag{9}$$

CONCLUSIONS

It is shown from Fig.1 that there are three liquefaction data points below the critical curve of liquefaction and six non-liquefaction data points fitly on the liquefaction critical curve. By the calculation and analysis, the liquefaction discrimination success rate of suggested liquefaction critical curve is 99% and the non-liquefaction discrimination success rate is 32%. The result of non-liquefaction discrimination is conservative. It is concluded that the liquefaction critical curve established in this study as Formula (9) is reasonable.

REFERENCES

Idriss, I. M., Boulanger, R. W. (2006). "Semi-empirical procedures for evaluating liquefaction potential during earthquake." *Soil Dynamics and Earthquake Engineering* pp. *No. 26. ASCE*,115-130.

Kayer, R., Thompson, E. M., et al. (2010). "Shear-ware velocity-based probabilistic and deterministic assessment of seismic soil liquefaction potential." *Journal of Geotechnical and Geoenvironmental Engineering* ASCE, 139(3), 407-419.

Kong, Meng-yun, Chen, GUO-xing., et al. (2015)."Shear ware velocity and peak ground acceleration based deterministic and probabilistic assessment of seismic soil liquefaction potential." *Rock and Soil Mechanics,* Vol.36, No.5, pp. 1239-1260.

Seed, H. B., Idriss, I. M. (1971)."Simplified procedure for evaluating soil liquefaction potential." *Journal of Soil Mechanics and Foundations Divisions* ASCE, No. 97 (SM9), 1249-1273.

MODELLING SPIKY ACCELERATION RESPONSES OF SAND DEPOSITS USING A LARGE POST-LIQUEFACTION CONSTITUTIVE MODEL

*Gang Wang, [+]Xing Wei and [+]John Zhao
* Chongqing University, Chongqing 40045, China
[+] Southwest Jiaotong University, Chengdu 610031, China

BRIEF INRODUCTION, METHODOLOGY AND KEY RESULTS

The acceleration records at some liquefied sand deposits during past earthquakes have shown that the surface acceleration time-series exhibited a distinctive spiky waveform, characterizing with the strong amplification and the remaining of high-frequency components. This is contrary to the expected amplification reduction and shaking-period enlargement in liquefied soil. Previous studies (e.g. Zeghal and Elgamal, 1994) confirmed that the spiky acceleration is attributed to the cyclic mobility of sand after initial liquefaction. However, in what circumstances the spiky acceleration would occur still remains an unanswered question due to the lack of a deep understanding of the post-liquefaction behavior of sand and corresponding constitutive models.

Sands over a wide density range from loose, medium to dense and even the densest state exhibit cyclic mobility behavior, charactering with developing fluid-like shear strain and solid-like shear strain alternately. To reproduce the seismic response of liquefied soil deposits during earthquakes, the employed model must capture both the fluid-like shear strain and the solid-like strain of sand, especially the gradually increase of the fluid-like shear strain with the increasing number of cycles. Wang and Zhang (2007 and 2012) presents a theoretical framework for predicting the post-liquefaction deformation of saturated sand under undrained cyclic loading. They decomposed the volumetric strain into three components with distinctive physical background, and then found that the interplay among these three volumetric strain components characterizes three physical states alternating in the liquefaction process and governs the development of the fluid-like shear strain.

In order to understand the mechanism of post-liquefaction spiky acceleration response, a SDF system is designed, in which the cyclic force-displacement relationship of the spring follows the stress-strain behavior of saturated sand under undrained condition. Figure 1 presents the acceleration response of the SDF system for the dense sand. It is observed that the spiky waveform appears after 4 cycles. The amplitude of the spike increases gradually with the excitation continuing, reaches its maximum, then decreases progressively, and eventually becomes zero. Besides, the time interval between two adjacent spikes enlarges gradually; the time lag between the response acceleration peak and its counterpart in the input time series also increases gradually. The mechanism of the spikes and time lag can be explained by the non-linear force-deformation behavior of the equivalent spring. The calculated stress-strain response indicates that the spikes are associated with the strain hardening behavior at non-zero effective stress state. The strain hardening causes a sharp increase in the stiffness, and the sharp increase in the stiffness results in a sharp amplification of acceleration. While, the enlargement of time interval between two spikes is associated with the fluid-like shear strain occurred at zero effective stress state. As the magnitude of the fluid-like shear strain increases gradually during cyclic shearing, more time is needed in the

following cycle for the mass to run farther in order to generate larger shear strain than the preceding cycle to exceed the fluid-like shear strain.
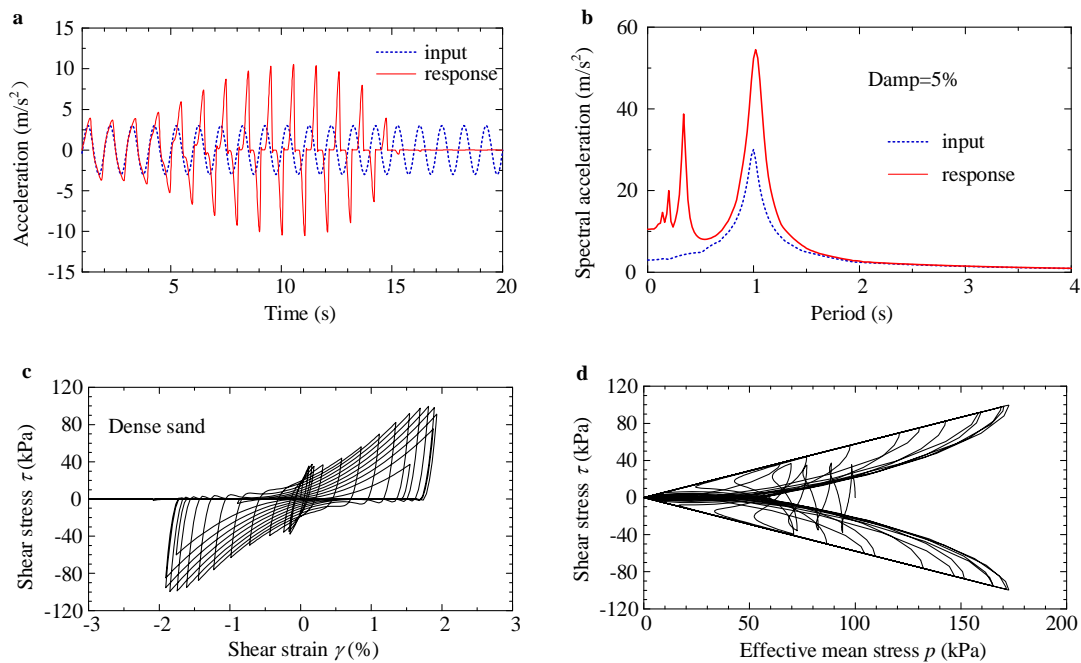
Fig.1. Response of the equivalent SDF system for the dense sand subjected harmonic excitation of vibration period 1s. (a) comparison of input and response acceleration time series, (b) response spectra of input and response acceleration, (c) stress-strain hysteretic curve of sand, and (d) effective stress path of sand. Note the spikes after 4 cycles.
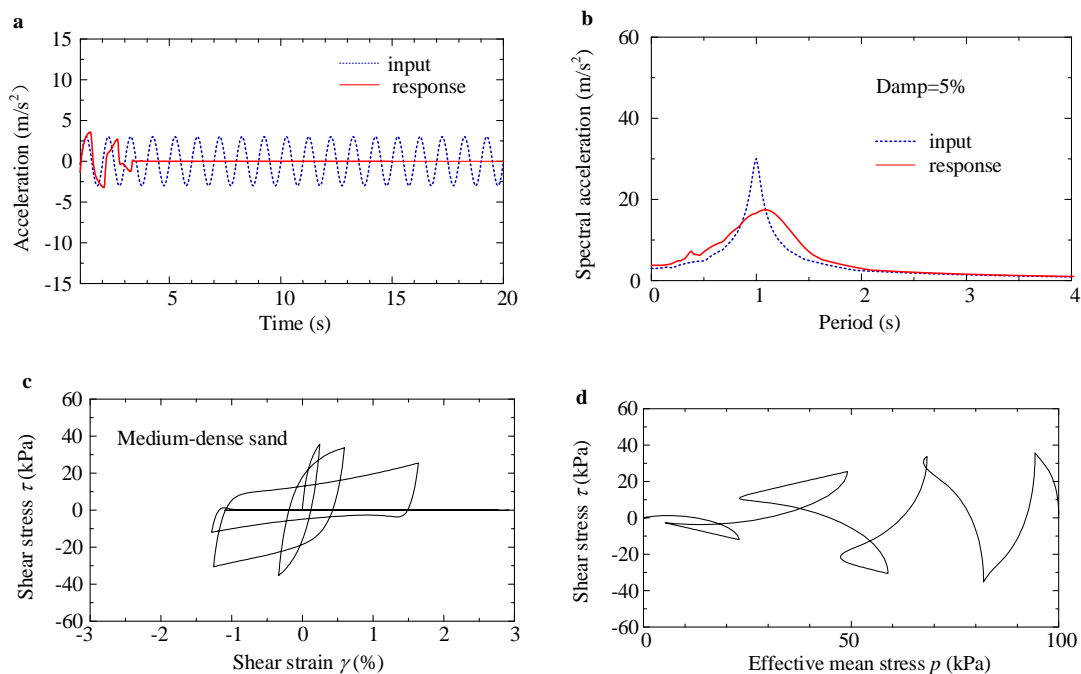
Fig.2. Response of the equivalent SDF system for the medium dense sand subjected harmonic excitation of vibration period 1s. (a) comparison of input and response acceleration time series, (b) response spectra of input and response acceleration, (c) stress-strain hysteretic curve of sand, and (d) effective stress path of sand. Note that no obvious spiky acceleration and high frequency component developed.

When the shear strain generated during shaking cannot exceed current fluid-like shear strain, the sand is sheared cyclically at zero effective stress state and cannot transfer shear force to excite the top mass. Consequently, the acceleration response at the top mass vanished

eventually. To further validate this mechanism, Figure 2 presents the acceleration response of the SDF system with the element assigned as the medium-dense sand. It can be seen that after 2 cycles the top nodes become rest and do not vibrate along with the input motion, implying that the boundary vibration cannot be transmitted by the element. Figure 2c and 2d give the stress-strain history and effective stress path of the element. It can be seen that the fluid-like shear strain increases so quickly that just after 2 cycles the amplitude of the shear strain becomes not enough to bring the sand back into non-zero effective stress state and thus the sand cannot bearing shear stress. This example explains the reason why the recorded ground surface motion reduces or diminishes in most liquefied cases with loose to medium-dense sand deposits.

Furthermore, the recorded earthquake response respectively at Kushiro Port site and Port Island site during past earthquakes are simulated through fully coupled method to validate the presented mechanism.

CONCLUSIONS

Through analysis of an idealized SDF system and two practical cases during past earthquakes, this study demonstrated that the spikes observed in the acceleration records are directly related to the cyclic hardening behavior of sand, and more interestingly, following new findings were revealed.

1) There exists a threshold shear strain amplitude to cause spiky acceleration, which increases gradually with the cyclic shearing goes on. Only when the shear strain generated in seismic response exceeds this threshold shear strain the spiky acceleration can occur, otherwise the acceleration response would be attenuated. The looser the sand is, and the larger the threshold shear strain. Consequently, the spiky acceleration responses are more often observed in dense sand deposits, and however, for loose sand deposits, long period excitation also can cause large spiky acceleration response because of its large displacement amplitude.

2) The time intervals between the acceleration spikes increase gradually because more time is needed to generate larger shear strain to exceed the threshold shear strain amplitude.

3) The threshold shear strain amplitude is associated with the fluid-like shear strain of liquefied sand generated in zero effective stress state, which depends on stress history. So the constitutive model employed to evaluate the seismic response of liquefied strata must be able to realistically simulate the fluid-like shear strain generated at zero effective stress state.

ACKNOWLEDGEMENTS

REFERENCES

Zeghal M, Elgamal A. (1994). "Analysis of site liquefaction using earthquake records." *Journal of Geotechnical Engineering*, 20(6): 996-1017.

Wang G, Zhang JM. (2007). "A cyclic elasto-plastic constitutive model for evaluating large liquefaction-induced deformation of sand." *Chinese Journal of Geotechnical Engineering*, 29(1): 51-59. (in Chinese)

Zhang JM, Wang G. (2012). "Large post-liquefaction deformation of sand, part I: Physical mechanism, constitutive description and numerical algorithm." *Acta Geotechnica*, 7(2):69-113.

ELECTRICITY RESISTANCE: A NEW INDEX OF SATURATION FOR DESATURATED SAND

Y.M. Chen*, S.K. He*, Z. Fang* and H.Y. Qin[+]
* Hohai University, China
[+] Flinders University, Australia

BRIEF INTRODUCTION, METHODOLOGY AND KEY RESULTS

Desaturation is a process of decreasing the degree of saturation of liquefiable sandy soils to a low level by engineering measures (Okamura and Teraoka 2006; Tomida and Okamura 2013). The liquefaction resistance of the desaturated sand can be enhanced to 2 – 3 times of the original value of the fully saturated sand (See Figure 1). Sherif et al. conducted the torsional simple shear tests on the partially saturated sand to analyze the saturation effects on the initial soil liquefaction, because they believed that most natural geological soils deposits were not fully saturated (Sherif et al. 1977). Afterwards, more tests were carried out to obtain the increased liquefaction resistance of partially saturated sand (Goto and Shamoto 2002; Huang et al. 1999; Ishihara et al. 2001; Yasuda et al. 1999; Yoshimi et al. 1989). According to the results, as shown in Figure 1, it is possible to mitigate the liquefaction disaster of the fully saturated sand by a desaturation process.
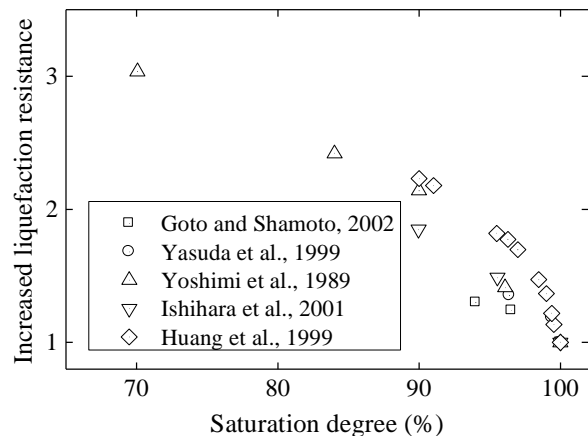
Figure 1: Relation between liquefaction strength ratio and the degree of saturation

For a liquefiable sandy foundation, a saturated porous material combine with sand particles and pore water, a direct way to decrease the degree of saturation is to replace some pore water with air bubbles. The desaturation methods of air injection (Okamura et al. 2011), chemical reactions (Eseller-Bayat et al. 2012), biogas (He et al. 2013) and electrolysis (Yegian et al. 2007) were proposed in recent years. However, the most significant problem of desaturation is how to calculate the degree of saturation precisely and economically. The degree of saturation of sandy soil cannot be measured directly, so some different indexes of it are proposed, including the coefficient of pore water pressure, the bulk modulus of aerating water and the velocity of the compressional wave.

In Japan, the degree of saturation of the foundation after air injection can be measured in a triaxial laboratory apparatus using a frozen sample taken from the in-situ field (Okamura et al. 2011), which is a very expensive procedure. The coefficient of pore water pressure, B, can be obtained in a conventional triaxial test on a partially saturated sand sample under a confining stress. The relationship between the B value and the degree of saturation is shown in Figure 2 (Yang et al. 2004a; c; Yoshimi et al. 1989), and this figure shows that the B value decreases dramatically with the increase of the degree of saturation. However, the effective range of the degree of saturation is only between 96% to 99.5%. If the degree of saturation is less than

96%, the *B* value will decrease to almost zero. Therefore, the *B* value is not an effective index to judge the degree of saturation in the desaturation process. Meanwhile, the *B* value can be only obtained in a triaxial laboratory apparatus; it is difficult to be implemented in a shaking table test or in-situ condition.
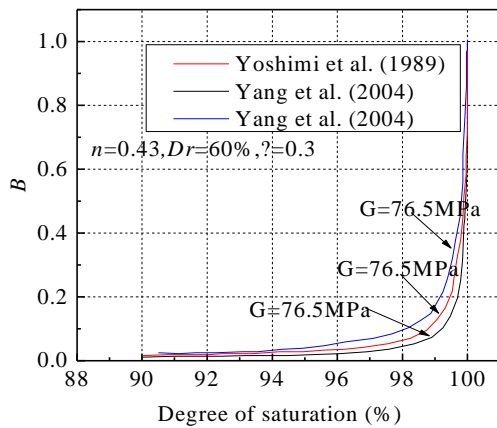
Figure 2: Relationship between the *B* value with and degree of saturation
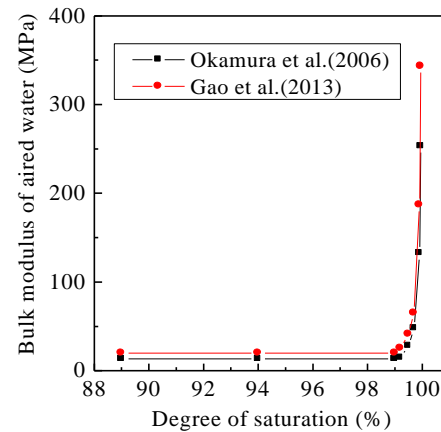
Figure 3: Relationship between the bulk modulus and the degree of saturation

Another index of the degree of saturation is the bulk modulus of the pore water, that is air-mixed water, in the desaturated sand. Okamura et al. and Gao et al. presented the relationship between the bulk modulus of the air-mixed water and the degree of saturation as shown in Figure 3 (Gao et al. 2013; Okamura and Soga 2006). As Figure 3 shows, the bulk modulus of the air-mixed water changes significantly with the degree of saturation within the range of 100 % to 94.4 %. However, when the degree of saturation decreases to less than 94.4 %, the

bulk modulus of the air-mixed water drops very slowly. Meanwhile, the bulk modulus of the pore air-mixed water is also difficult to measure in the site or laboratory. Therefore, it is not a reasonable index of the degree of saturation.

The third option of the index of the degree of saturation is the velocity of the compression wave. Figure 4 shows the relationship between the velocity of compression wave and the degree of saturation of different kinds of sandy soils (Eseller-bayat et al. 2013; Hatanaka and Masuda 2008; Yang et al. 2004b). The

Figure 4: Relationship between the velocity of compression wave and degree of saturation

velocity of the compressive wave of partially saturated sand decreases dramatically with the reducing of the degree of saturation from 100 %. The sensitive range of the degree of saturation in Figure 4 is from 92 % to 100%. So, the velocity of the compressive wave is also not a good index of the degree of saturation.

Electrolytic desaturation method is proposed in recent years, as an innovative mitigation of soil liquefaction. It produces the tiny bubbles of hydrogen (H_2) and oxygen (O_2) by electrolyzing the pore water inside the saturated sandy soils and reduces the saturation degree of the soil and then improves its liquefaction resistance. Serials of model tests on the electricity resistance of partially saturated sand are carried out in the sand box shown in Figure 5. The electrodes driven vertically in the sandy foundation are arranged in a triangle configuration. There are eight electrodes including two positive ones in the center of the box

and other 6 surrounding negative ones. The distance between each two electrodes is 200 mm. The Silicon No. 7 sand (Orense et al. 2014), which has a similar size distribution with Toyoura Sand (Ishihara 1993), is adopted in the test. The degree of saturation is calculated by the water level in the sand box after the electrolysis process with a stable electric current of 0.6 A, 0.8 A and 1.0 A, respectively. The relationship between the electricity resistance and the degree of saturation is shown in Figure 6. As it shows, the electricity resistance increases gradually with the decrease of the degree of saturation. At the end of three cases, the degree of saturation of the sandy foundation decreases as same as 89 % with no effect of the electric current. Meanwhile, the electric current has litter influence on the curves of the electricity resistance with the degree of saturation, especially when the degree of saturation is in the range from 100 % to 95 %.
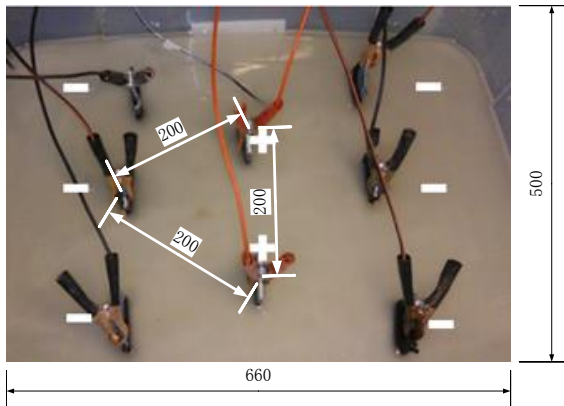
Figure 5: Electrode arrangement in the model box (Unit: mm)
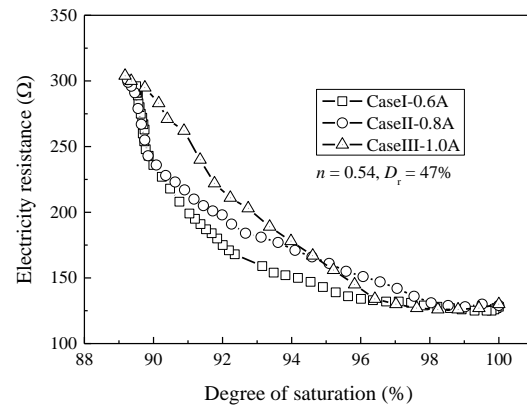
Figure 6: Relationship between the electrical resistance and the degree of saturation

CONCLUSIONS

1. Serials of model tests on the electricity resistance of desaturated sand are carried out. In the tests, the velocity of the compressive wave is also measured to confirm the degree of saturation after the electrolysis process.
2. The results show that at the initial stage of electrolytic desaturation, the decreasing rate of saturation increases linearly with the currency intensity; then the saturation continues to decrease, and the rate decreases gradually, and finally the saturation reduces to 89.5% which is independent of the current intensity.
3. In the process of electrolysis, the electrical resistance of the foundation increased with the decreases of the saturation of sand. In the practical engineering application, it can accelerate the initial decline rate of saturation degree in the condition of high current intensity; then it can weaken the electric current in the later stage, which can achieve the purpose of economic and environment protection.
4. Four kinds of the index to evaluate the state of desaturation of the sandy foundation were analysed, including the pore water pressure coefficient B, the gas bearing water bulk modulus K_{wa}, the compression wave velocity v_p and the electricity resistance. The results show that the electricity resistance is most easily measurable, and has a largest sensitive range of sand saturation. Therefore, the foundation electricity resistance can be adopted as an effective index to evaluate the state of desaturation of the sandy foundation.

ACKNOWLEDGEMENTS

REFERENCES

Eseller-bayat, E., Asce, M., Yegian, M. K., Asce, F., and Alshawabkeh, A. (2013). "Liquefaction Response of Partially Saturated Sands . I : Experimental Results." Journal Article, (7), 863–871.

Eseller-Bayat, E., Asce, M., Yegian, M. K., Asce, F., Alshawabkeh, A., and Gokyer, S. (2012). "Liquefaction response of partially saturated sands. I: Experimental results." *International Journal of Geotechnical and Geoenviromental Engineering*, 139(7), 863–871.

Gao, Q., Zhen, L., and Xiong, Y. (2013). "Computer Simulations on the Effects of Desaturation on Soil Liquefaction Resistance." *International Conference on Geotechnical and Earthquake Engineering*, 786–795.

Goto, S., and Shamoto, Y. (2002). "Estimation method for the liquefaction strength of unsaturated sandy soil (part 2)." *Procedding of 37th Japanese National Conference of Geotechnical Engneering*, 1987–1988.

Hatanaka, M., and Masuda, T. (2008). "Experiment study on the relationship between degree of saturation and P-wave." *Geotechnical Engineering for Disaster Mitigation and Rehabilitation*, 346–351.

He, J., Chu, J., and Ivanov, V. (2013). "Remediation of Liquefaction Potential of Sand Using the Biogas Method." *Geo-Congress 2013@ sStability and Performance of ...*, 879–887.

Huang, Y., Tsuchiya, H., and Ishihara, K. (1999). "Estimation of partial saturation effect on liquefaction resistance of sand using P-wave velocity." *Proceedings of Japanese Geotechnical Society*, 431–434.

Ishihara, K. (1993). "Liquefaction and flow failure during earthquakes." *Géotechnique*, 43(3), 351–451.

Ishihara, K., Tsuchiya, H., Huang, Y., and Kamada, K. (2001). "Recent studies on liquefaction studied on sand - effect of saturation." *Proceedings of 4th International Conference on Recent Advance in Geotechnical Earthquake Engineering and Soil Dynamics*, San Diego, California, 1–7.

Okamura, M., and Soga, Y. (2006). "Effects on pore fluid compressibility on liquefaction resistance of partially saturated sand." *Soils and Foundations*, Journal Article, 46(5), 695–700.

Okamura, M., Takebayashi, M., Nishida, K., Fujii, N., Jinguji, M., Imasato, T., Yasuhara, H., and Nakagawa, E. (2011). "In-Situ Desaturation Test by Air Injection and Its Evaluation through Field Monitoring and Multiphase Flow Simulation." *Journal of Geotechnical and Geoenvironmental Engineering*, Generic, 137(7), 643–652.

Okamura, M., and Teraoka, T. (2006). "Shaking table tests to investigate soil desaturation as a liquefaction countermeasure." *Geotechnical Special Publication*, JOUR, Reston, VA; American Society of Civil Engineers; 1998, 145, 282.

Orense, R. P., Towhata, I., and Chouw, N. (2014). *Soil Liquefaction During Recent Large-scale Earthquakes*. Taylor & Francis Group.

Sherif, M. A., Ishibashi, I., and Tsuchiya, C. (1977). "Saturation effects on initial soil liquefaction. Journal of the Geotechnical Engineering Division.pdf." *Journal of Geotechnical Engineering Division*, Generic, 103(GT8), 914–917.

Tomida, Y., and Okamura, M. (2013). "Verification of Desaturation Technique as a Liquefaction Countermeasure for Existing Embankments." *International Journal of Landslide and Enviroment*, 1(1), 111–112.

Yang, J., Savidis, S., and Roemer, M. (2004a). "Evaluating liquefaction strength of partially saturated sand." *Journal of geotechnical and ...*, 130(September), 975–979.

Yang, J., Savidis, S., and Roemer, M. (2004b). "Evaluating liquefaction strength of partially saturated sand." *Journal of geotechnical and ...*, Journal Article, 130(September), 975–979.

Yang, J., Savidis, S., Roemer, M., Asce, M., Savidis, S., and Roemer, M. (2004c). "Evaluating liquefaction strength of partially saturated sand." *Journal of geotechnical and ...*, 130(September), 975–979.

Yasuda, S., Kobayashi, T., Fukushima, Y., Kohari, M., and Simazaki, T. (1999). "Effect of degree of saturation on the liquefaction strength of Masa." *Proceedings of 34th Japanese National Conference Geotechnical Engineering*, Tokyo, 2071–2072.

Yegian, M. K., Eseller-Bayat, E., Alshawabkeh, A., and Ali, S. (2007). "Induced-Partial Saturation for Liquefaction Mitigation: Experimental Investigation." *Journal of Geotechnical and Geoenvironmental Engineering*, 133(4), 372–380.

Yoshimi, Y., Tanaka, K., and Tokimatsu, K. (1989). "Liquefaction resistance of partially saturated sand." *Soils and Foundations*, 29(3), 157–162.

DETERMINATION OF DYNAMIC SOIL PROPERTIES IN HONG KONG

E.H.Y. Sze*, J.S.H. Kwan*, R.C.H. Koo*, E.H.Y. Leung[+], M.M.L. So[+] and K.K.S. Ho*
* Geotechnical Engineering Office, Civil Engineering and Development Department,
The Government of the Hong Kong SAR, China
[+] Arup, Hong Kong

BRIEF INTRODUCTION, METHODOLOGY AND KEY RESULTS

Determination of dynamic soil properties is an important step in geotechnical earthquake engineering analysis and design. Key properties including the bulk density of soil (ρ), small-strain shear modulus (G_0) and the degradation of shear modulus (G/G_0) with increasing amplitude of cyclic shear strain are required for seismic site response analysis. Except for the soil density, determination of other properties requires unconventional laboratory testing equipment such as the resonant column and cyclic triaxial tests. It is, therefore, common to correlate the dynamic soil properties with the shear wave propagation velocity (V_s), e.g. $G_0 = \rho V_s^2$. Nevertheless, V_s measurement in the field by geophysics testing or laboratory by bender element testing is again unconventional. Hence, its estimation via empirical correlation with the SPT N-value is usually adopted in design practice. In this regard, the establishment of the G/G_0 curve and V_s-N relationship using local soil data is of practical significance.

In this study, various laboratory and in-situ geophysics testing results obtained from Hong Kong were collected and reviewed. Based on the results, the shear modulus degradation curve and V_s-N correlations for different types of soils are established empirically. Data adopted in this study comprised results extracted from Leung et al. (2010), who studied dynamic properties of soils in Hong Kong, and the data of the ground investigation (GI) works for the seismic microzonation assessment of the North-west New Territories by Arup (2012). The GI works consisted of 27 vertical boreholes, 47 geophysics field tests and 6 laboratory cyclic triaxial tests. The results have been used to evaluate the site response to earthquake ground motions and develop the site classification. Details of the geophysics testing techniques including down-hole seismic, PS suspension logging, cross-hole seismic and multi-analysis of surface wave tests were discussed by So et al. (2013).

The shear modulus degradation curves presented in form of normalised shear modulus (G/G_0) against shear strain (γ) were derived based on the cyclic triaxial test data by Arup (2012). In the tests, shear wave velocity measurement by the internally mounted bender element was made. The test information is briefly summarised in Table 1. The results are presented in Figures 1 to 3 for Estuarine / Marine Deposits (MD), Alluvium (ALL), and Completely Decomposed Sedimentary Rock (CDS) respectively. The shear modulus degradation curves proposed

Table 1: Cyclic triaxial test information

Test ID	Soil Type
CW1	CD-metasiltstone
CW2	Alluvium
CW3	CD-metasiltstone
CW4	Alluvium
CW5	Estuarine/Marine Deposit
CW6	Alluvium

by Leung et al. (2010) are also shown in the figures for comparison. By categorising the data by soil types, a reasonable match was observed. The degradation curve for alluvial clay by Leung et al. (2010) matches quite well with Arup's data on clayey soils (Estuarine and MD) but not that on alluvium, which is mainly a sandy soil. This different modulus reduction behaviour of coarse-grained and fine-grained soils has also been reported by EPRI (1993). The reduction characteristic is represented by a family of shear modulus degradation curves for gravels to clays as shown in the background of each of the figures for reference.
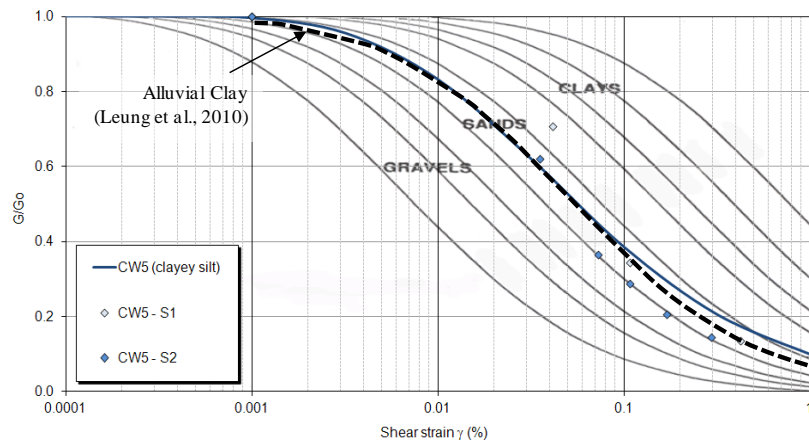
Figure 1: Shear modulus degradation curve for Estuarine/Marine Deposit
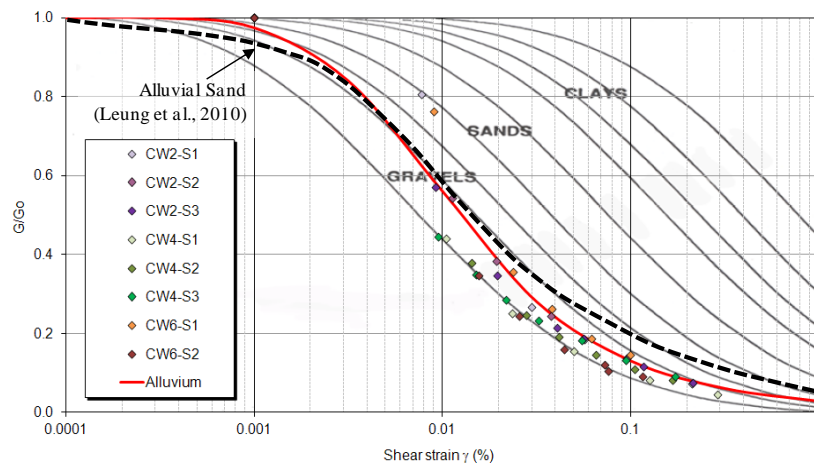
Figure 2: Shear modulus degradation curve for Alluvium
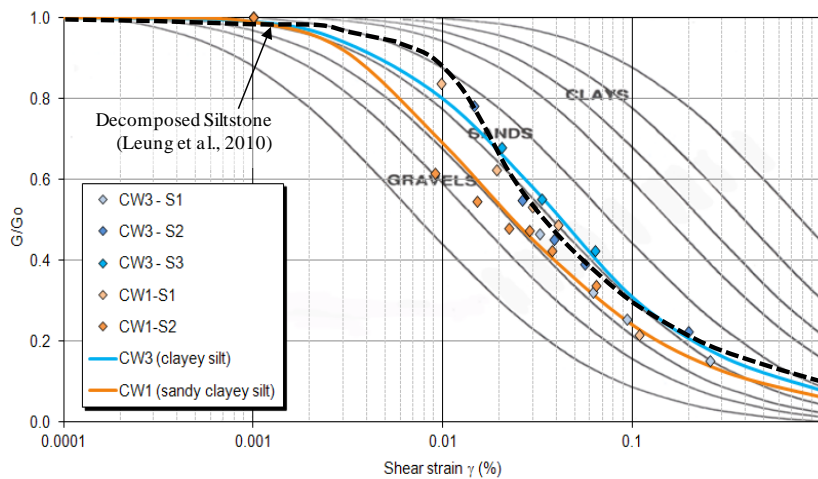
Figure 3: Shear modulus degradation curve for Decomposed Sedimentary Rock

In-situ measurements of V_s and SPT N-value for all soil types are plotted in Figure 4. The data from the same soil strata are plotted in Figures 5 to 8 for Fill (FILL), Alluvial Clay (ALL(C)) / MD, Alluvial Silt/Sand (ALL(S)) and Saprolitic soils (CDS / Completely Decomposed Granite (CDG) / Completely Decomposed Volcanic Tuff (CDV)) respectively.

Data of Arup (2012) generally matched the previous data from Leung et al. (2010) despite the scattering of data points. A new empirical correlation was derived for each soil type by least square analysis. The soil specific correlations are summarised as follows:

a. All Soils: $V_s = 99.9 \, N^{0.282}$
b. FILL: $V_s = 103.6 \, N^{0.231}$
c. ALL(C)/MD: $V_s = 93.7 \, N^{0.371}$
d. ALL(S): $V_s = 146.9 \, N^{0.189}$
e. Saprolitic Soils: $V_s = 109.8 \, N^{0.264}$
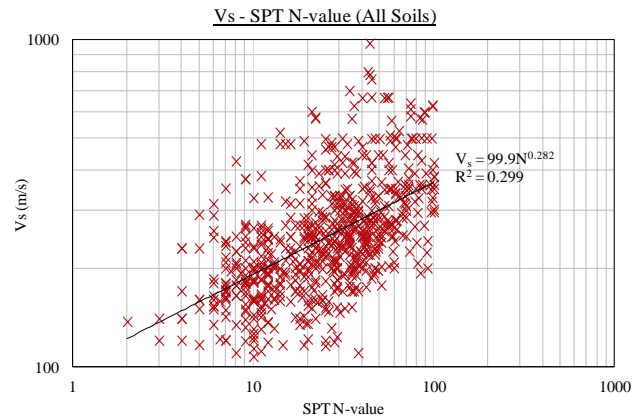
Figure 4: V_s – N correlation for all soils
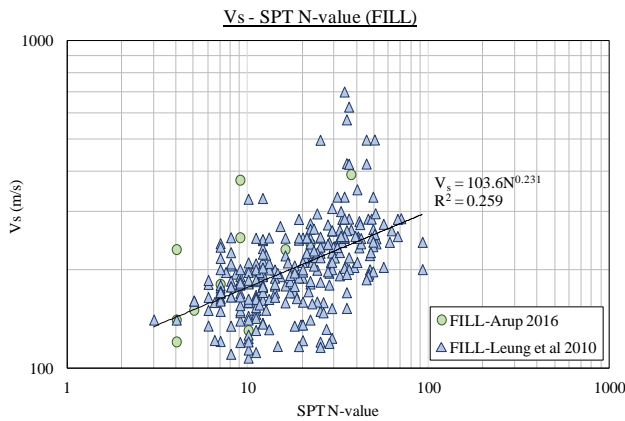
Figure 5: V_s – N correlation for Fill
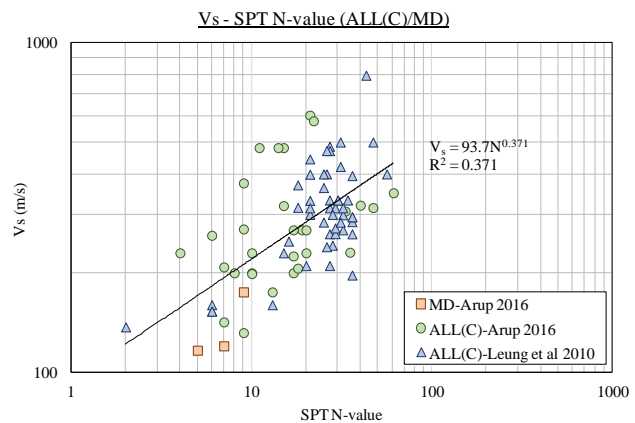
Figure 6: V_s – N correlation for Alluvial Clay and Marine Deposit
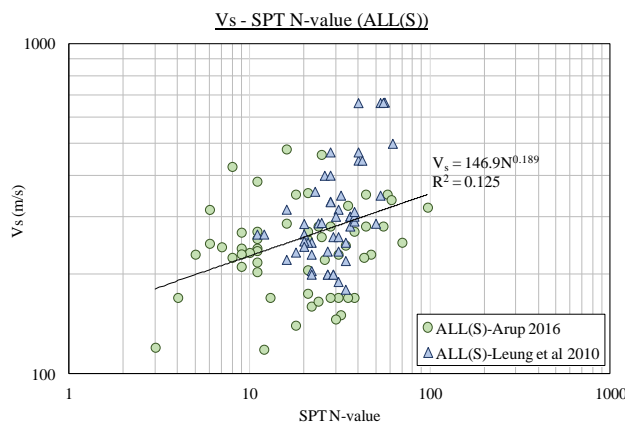
Figure 7: V_s – N correlation for Alluvial Silt / Sand
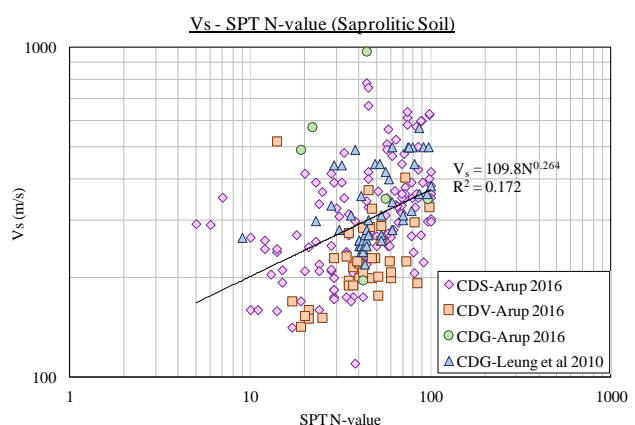
Figure 8: V_s – N correlation for Saprolitic Soils

CONCLUSIONS

1. Field and laboratory data for determination of dynamic properties of soils obtained in different locations of Hong Kong were collected and reviewed. Data including laboratory cyclic triaxial test results for shear modulus determination and in-situ shear wave propagation velocity measurements by geophysics testing were used to derive the empirical correlations for the shear modulus degradation curves (G/G_0) as well as the shear wave propagation velocity and SPT N-value relationship $(V_s\text{-}N)$ for different types of soil.
2. Data adopted in this study are highly scattered. Probably, they are sensitive to the locality from which the soil data were obtained. The correlations may provide information for a general appreciation of the dynamic soil properties of Hong Kong. For engineering design purpose for specific projects, it is recommended to obtain site-specific data from GI and laboratory tests.

ACKNOWLEDGEMENTS

REFERENCES

Arup (2012). "Final report on Seismic Microzonation Assessment, Pilot Seismic Microzonation Study in North-west New Territories for the Study of Potential Effect of Earthquake on Natural Terrain." *CEDD Agreement No. CE49/2008(GE)*, for the Geotechnical Engineering Office, Civil Engineering and Development Department, Government of the Hong Kong SAR, China, 257 p.

Electric Power Research Institute (EPRI) (1993). "Guidelines for determining design basis ground moitions." *Final Rep. No. TR-102293,* Palo Alto, Calif.

Leung, E.H.Y., Pappin, J.W., and R.C.H. Koo (2010). "Determination of small strain modulus and degradation for in-situ weathered rock and old alluvium deposits." *In Proc. of 5th Int. Conf. on Recent Adv. In Geot. Earthq. Engrg. and Soil Dyn. and Symp. In Honor of Prof. I.M. Idriss,* San Diego, California, Paper No. 1.20a.

So, M.M.L., Pappin, J.W., Mote, T.I., and R.C.H. Koo (2013). "Determination of small strain soil properties in Hong Kong by Geophysics Testing." *In Proc. of Aust. Earthq. Engrg. Soc. 2013 Conf.,* Hobart, Tasmania.

DESIGN EARTHQUAKE GROUND MOTIONS USING STOCHASTIC SIMULATIONS OF THE SEISMOLOGICAL MODEL

N.T.K. Lam*, R.C.H. Koo[+], J.S.H. Kwan[+] and K.K.S. Ho[+]
* Infrastructure Engineering, The University of Melbourne, Parkville 3010,
Victoria, Australia
[+] Geotechnical Engineering Office, Civil Engineering and Development Department,
The Government of the Hong Kong SAR, China

BRIEF INRODUCTION, METHODOLOGY AND KEY RESULTS

This paper discusses the selection and generation of appropriate accelerograms in bedrock for input into dynamic analyses of soil sites and structures for Hong Kong conditions. Due to the limited earthquake data for rock sites in open access databases and the lack of recorded strong motion time histories in the Hong Kong region, establishment of accelorograms based on the recorded ground motions of previous earthquake events is not technically straightforward. Artificial accelerograms composed using stochastic simulations may provide a credible and practicable option for design purposes.

Research into the seismic hazard of Hong Kong has commenced for more than two decades. Probabilistic seismic hazard analysis (PSHA) conducted by ARUP and The University of Hong Kong in recent years has culminated in the development of Uniform Hazard Spectrum (UHS) models that can be codified for the structural design of buildings and other types of structures. However, there is a paucity of instrumented strong motion records of accelerograms collected from within the region that can be used for engineering design. This paper introduces artificial accelerograms that are generated from stochastic simulation based on a representative seismological model for Hong Kong.

Research into the seismic hazard affecting Hong Kong dates back to the early 1990's (e.g. Pun and Ambraseys, 1992; Lee et al., 1998). In those early investigations, ground motion predictive expressions employed in hazard predictions were mainly based on empirical relationships developed from the tectonically active environment of California. Little evidence was available to support that the attenuation relationships used in the modeling were relevant to local conditions.

Uniform hazard spectrum (UHS) models for Hong Kong have been developed throughout the last 15 years with updated attenuation models. The UHS model was first published by ARUP (2002). Later, Tsang and Lam (2010) employed the HKU-UHS model to assess the seismic hazard of Hong Kong based on Direct Amplitude-Based (DAB) PSHA methodology. The latest seismic hazard assessment of Hong Kong was carried out by Arup (2015) with input from the Earthquake Administration of Guangdong Province. Good consistency between the independently developed HKU-UHS and the ARUP (2015) models in the medium, and high, natural period range was observed (see Figure 1). Su et al. (2015) also presented a design envelope which incorporated findings from both the HKU-UHS and the ARUP (2015) UHS models.

Both of the above seismic hazard studies used the ARUP-HKU (2006) attenuation relationship, which was underpinned by stochastic simulations of the seismological model developed by Lam (1999). It is a technique that enables reliable predictions to be made based on utilizing regional information that is related to the wave generation, transmission, and

properties of the earth crust (Lam et al., 2000). This technique was adopted for modeling ground motions in South China including regions surrounding Hong Kong (Lam et al., 2002; Chandler et al., 2006). A program, GENQKE, was developed to generate ground motions using this technique. The seismological attenuation model of Mak et al. (2004), which was specifically developed based on the tectonic conditions surrounding Hong Kong, has been incorporated into the program. Several example time series of accelerograms produced by GENQKE are shown in Figure 2. They were generated using seismological parameters pertinent to Hong Kong conditions (see Table 1).
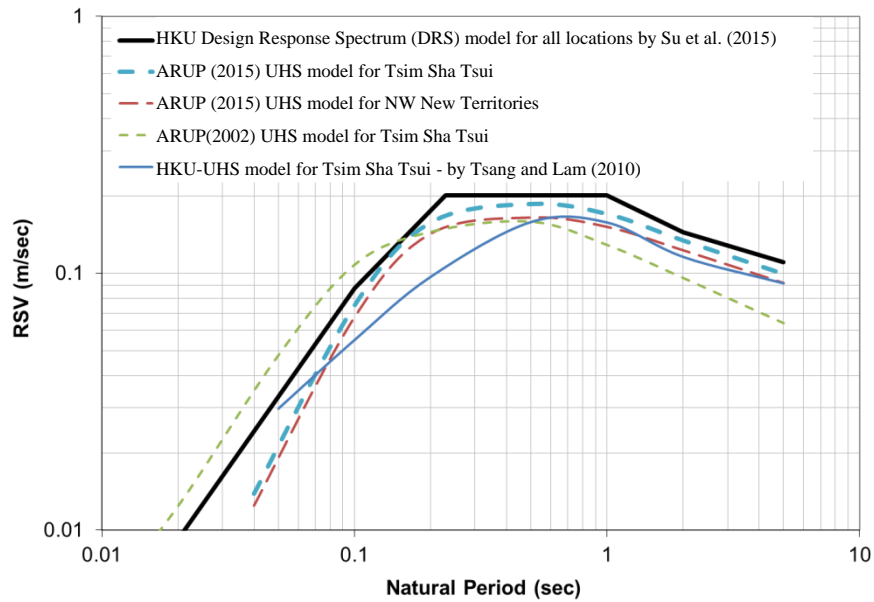
Figure 1: Uniform Hazard Spectrum (UHS) models for Hong Kong rock sites (RSV is response spectral velocity)
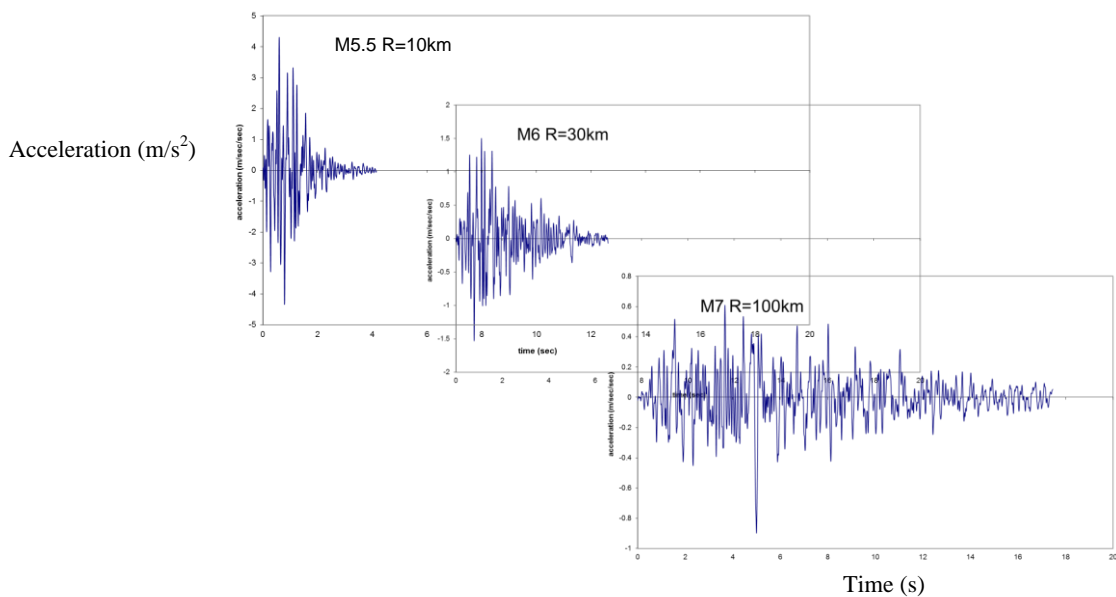
Figure 2: Example accelerograms generated by program GENQKE

96

Table 1   Seismological parameters applicable for Hong Kong conditions
(extracted from Pappin et al., 2015)

Seismological Parameters		The University of Hong Kong (Tsang, 2006; Tsang and Lam, 2010)
Source Model		CENA model, S(M,f) M is the moment magnitude and f is frequency of seismic wave.
Geometrical Spreading		$30 / R$ $\qquad$ (R ≤ 45 km) 0.667 $\qquad$ (45 km < R ≤ 75 km) $5.77 / R^{0.5}$ $\qquad$ (R > 75 km) where R is hypocentral distance
Anelastic Attenuation		Southeast China: $\quad Q = 256f^{0.7}$ $\qquad$ (R < 200 km) $\quad Q = 348f^{0.54}$ $\qquad$ (200 km < R < 500 km) $\quad Q = 384f^{0.51}$ $\qquad$ (R > 500 km) where Q is the wave transmission quality factor
Crustal Effect	Mid-Crust	$\beta = 3.5$ km/s where β is the average shear wave velocity at mid-crust (~10 km depth)
	Upper-crust	$\kappa = 0.03$ and $v_{30} = 2,000$ m/s where v_{30} is the average shear wave velocity within the upper 30 m

CONCLUSIONS

1. In a site specific hazard analysis, accelerograms recorded on the rock surface, or on bedrock, are required for input into the dynamic analysis. However, the amount of accelerograms that were recorded on rock to serve this purpose is scarce.
2. Stochastically simulated artificial accelerograms based on suitable seismological models could provide alternatives to the recorded accelerograms. A further review will be carried out to confirm the applicability of the artificial accelerograms.

ACKNOWLEDGEMENTS

REFERENCES

Arup (2002). "Final Report on Evaluation of Seismic Response of Buildings." Consultancy to Study The Seismic Effects on Buildings in Hong Kong, Agreement No. CAO K49, Building Department, The Government of the HKSAR.

Arup (2015). "Seismic Hazard Analysis of the Hong Kong Region" (GEO Report No. 311), Geotechnical Engineering Office, Civil Engineering and Development Department, Hong Kong, 325 p.

Arup-HKU (2006). Internal Study Report on Attenuation Ground Motion Model for Southeast China Based on Research by the University of Hong Kong jointly with the University of Melbourne, 50 p.

Chandler, A.M., Lam, N.T.K. and Tsang, H.H. (2006). "Regional and Local Factors in Attenuation Modelling." *Journal of Asian Earth Sciences* 27, 892 - 906.

Dowrick D.J. (2009). Earthquake Resistant Design and Risk Reduction. John Wiley and Sons.

Lam, N.T.K. (1999). Program 'GENQKE' user's Guide. Department of Civil and Environmental Engineering, The University of Melbourne, Australia.

Lam, N.T.K., Wilson, J.L. and Hutchinson, G.L. (2000). "Generation of Synthetic Earthquake Accelerograms Using Seismological Modelling: A Review." *Journal of Earthquake Engineering*, 4:3, 321-354.

Lam, N.T.K., Wilson, J.L. and Chandler, A.M. and Hutchinson, G.L. (2002). "Response Spectrum Predictions for Potential Near-Field and Far-Field Earthquakes Affecting Hong Kong : Rock Sites." *Soil Dynamics and Earthquake Engineering*. 22, 47-72

Lee, C.F., Ding, Y.Z., Huang, R.H., Yu, Y.B., Guo, G.A., Chen, P.L. and Huang, X.H. (1998). "Seismic Hazard Analysis of the Hong Kong Region." (GEO Report No. 65). Geotechnical Engineering Office, Civil Engineering Department, Government of the Hong Kong SAR, 145 p.

Mak, S., Chan, L.S., Chandler A.M. and Koo, R.C.H. (2004). "Coda Q estimates in the Hong Kong region." *Journal of Asian Earth Sciences* 24,127-136.

Pappin, J.W., Jiang, H., Koo, R.C.H., Yu, Y.B., Kwan, J.S.H., So, M.M.L., Shiu, Y.K., Ho, K.S. and Pun, W.K. (2015). "An updated seismic hazard analysis of the Hong Kong region", HKIE Transactions, 22(15).

Pun, W.K. and Ambraseys, N.N. (1992). "Earthquake Data Review and Seismic Hazard Analysis for the Hong Kong Region." *Earthquake Engineering and Structural Dynamics* 21, 433-443.

Su, R.K.L., Lee, C.L., He, C.H., Tsang, H.H., Law, C.W. (2015). "Rare Earthquake Response Spectra for Typical Site Conditions in Hong Kong." *HKIE Transactions*, 22(3):179-191.

Tsang, H.H., Lam, N.T.K. (2010). Seismic Hazard Assessment in Regions of Low-to-Moderate Seismicity. LAP Lambert Academic Publishing, Koln, Germany.

A SITE-AMPLIFICATION MODEL FOR BEDROCK GMPEs OF SINGAPORE

Wenqi Du* and Tso-Chien Pan*,+

* Institute of Catastrophe Risk Management, Nanyang Technological University, Singapore

+ School of Civil and Environmental Engineering, Nanyang Technological University, Singapore

Singapore is a modern island city-state located in a low-to-moderate seismicity zone. It frequently felt the shakings by long-distance giant earthquakes originated from the Sumatran fault systems (Pan and Sun, 1996). The main seismic sources in this region consist of the Sumatra mega-thrust and the Sumatran strike-slip fault. The Sumatra mega-thrust represents a part of the Sunda trench, which was formed by the subduction of Indian-Australian plate underneath southeastern Eurasian plate. Based on documented records, 6 great earthquakes with Mw larger than 8 have occurred along the Sumatra mega-thrust in the past 200 years, including the devastating Mw 9.1 Aceh-Andaman earthquake in 2004 (Megawati and Pan, 2010).

The Sumatran strike-slip fault lies about 250 km northeast of the Sunda trench (Figure 1). It has been identified as a 1,900-km long right-lateral strike-slip fault. This fault is highly segmented by many discontinuities, with width ranging from 4 to 12 km (Sieh and Natawidjaja, 2000). The Sumatran fault is divided in 20 major segments and the length of the faults ranges from 35 to 200 km. The locations of these segments are also shown in Figure 1. More than a dozen of earthquakes larger than magnitude 7 have occurred historically along this fault (Natawidjaja and Triyoso, 2007). The largest earthquake magnitude occurred at the Angkola segment (Ms = 7.7) in 1892, followed by the Sumani segment (Ms = 7.6) in 1943.

Figure 1: The locations of Sumatra megathrust and the Sumatran-fault segments

Recently, the Defence Science and Technology Agency (DSTA, 2009) provided detailed geological formations of Singapore, as shown in Figure 2. The geology of Singapore can be broadly classified into five major formations i.e., Gombak Norite (GN), Bukit Timah Granite (BTG), Jurong Formation (JF), Old Alluvium (OA) and Kallang Formation (KF). In particular, KF is the youngest formation, and it is located most abundantly on the coastline of the island with larger area coverage at the southeast part. The KF category consists of marine and littoral sediments with silt and clay lenses. In addition, a large portion of Reclaimed Land (RL) has been extended outwards to coast. Based on ground types classification of Eurocode 8 (Eurocode 8, 2004), the dominant site classifications in Singapore are mainly ground types B, C, D and S_1, respectively.

The soft clay and reclaimed areas of Singapore, where includes dense population and infrastructures, would significantly amplify seismic intensities due to site effect. Since currently the existing ground motion prediction equations (GMPEs) in Singapore can only predict peak ground acceleration (PGA) and spectral accelerations at the bedrock level (Megawati et al, 2003; Megawati and Pan, 2010), there is a strong need to develop a site amplification model, in order to evaluate the surface seismic hazard. In total, 555 soil profiles are collected in Singapore. The dataset provides the description of soil layers, including geological conditions, the unit weight and shear wave velocity (V_s) profiles. At each site, the time-averaged shear wave velocity in the top 30 meters (V_{s30}) can be computed using the V_s profiles or inferred based on some empirical relations (e.g., Wair and DeJong, 2012). The histogram of the estimated Vs30 values are is shown in Figure 3.

Bedrock ground motions are simulated using a kinematic model, in which the source rupture is represented

Figure 2: Geological map of Singapore (DSTA, 2009)
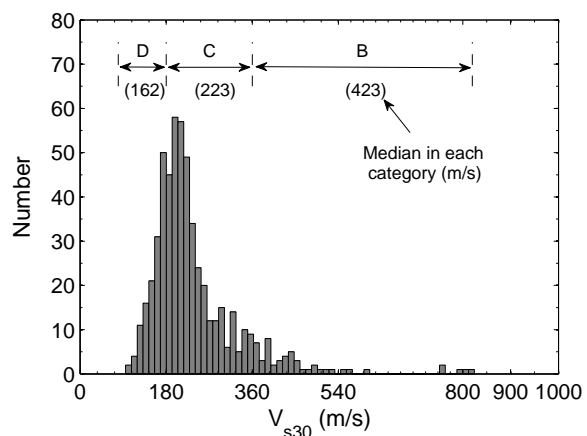
Figure 3: Histogram of Vs30 values for sites used in this study.

using a finite-fault model (Kohketsu, 1985). For a given scenario, the entire fault plane is divided into several regular subfaults, whereby each subfault can be considered as a point source. This method models the rupture initiation at one point of the plane (hypocenter) and it propagates radially to all parts of the subfaults with a certain rupture velocity. Six representative earthquake scenarios (moment magnitude M_w as 6, 6.5, 7, 7.5, 8, 8.5 and 9) from the Sumatran subduction fault and six earthquakes with M_W in the range of 5-8 from the strike-slip fault are considered in the study. For each considered earthquake event, 120 pairs of time series resulting from various rupture models and various locations in Singapore can be simulated. In total, there are 1440 pairs of time series simulated.

SHAKE program (Schnabel et al, 1972) is used to compute the surface ground motions of the 555 sites, based on the computed bedrock ground motions. One-dimensional analysis (upward propagation of seismic waves) is performed by this program, and an equivalent linear approximation method in the frequency domain is implemented. A number of applications show that the SHAKE program can fairly predict the seismic site response, and therefore it is widely used in geotechnical earthquake engineering (Kramer, 1996). For each earthquake scenario at each site, the site-amplification factors at different periods can be computed using the ratios of bedrock spectra and surface spectra. Finally, an empirical model can be developed based on the V_{S30} and the PGA on rock with the following form:

$$\ln(AF) = \begin{cases} a(T) \cdot \ln(V_{s30}/V_{eff}) + b(T) \cdot \left\{ \ln\left[\dfrac{PGA_{ref} + c \cdot (V_{s30}/V_{eff})^n}{PGA_{ref} + c} \right] \right\}; & V_{s30} < V_{eff} \\ \left[a(T) + b(T) \cdot n \right] \cdot \ln(V_{s30}/V_{eff}); & V_{s30} \geq V_{eff} \end{cases} \quad (1)$$

where $a(T)$, $b(T)$, c and n are regressed coefficients for a specific period T. V_{eff} is a reference velocity above which the site effect is linear. PGA_{ref} is the PGA value at the corresponding reference-rock site condition. The functional form in Eq. (1) is widely used in recently nonlinear site amplification studies (e.g., Sandıkkaya et al, 2013; Seyhan and Stewart, 2014). In this study, V_{eff} is taken as 760 m/s; and c and n are assigned as 2 and 1.82 for all periods. The corresponding standard deviations of the site-amplification model are also estimated. Table 1 shows the obtained regression coefficients and the corresponding standard deviations σ for some selected periods T. The estimated amplification factors for PGA for different V_{s30} values are demonstrated in Figure 4.

Table 1: Regression coefficients for the proposed site-amplification model

Period (s)	a	b	σ
PGA	-0.237	-0.176	0.421
0.1	-0.121	-0.244	0.424
0.5	-0.532	-0.120	0.435
1	-0.428	0	0.424
2	-0.152	0	0.230
5	-0.035	0	0.061
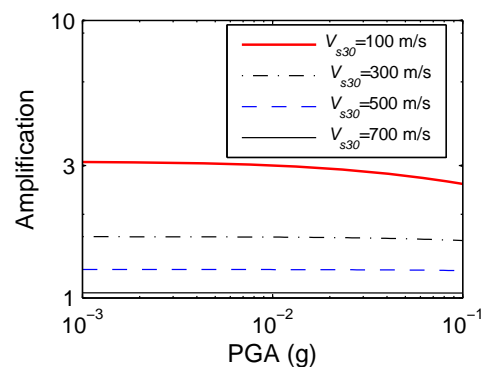
Figure 4: Example of the amplification factors for different V_{S30} values for PGA.

CONCLUSIONS

1. A comprehensive site response analyses were performed to investigate the seismic site amplifications in Singapore. A number of 555 sites with V_{s30} values in the range of 87 m/s to 460 m/s were collected. More than 1400 ground motion time series, covering M_w up to 9 and 8 for the Sumatran subduction and strike-slip faults respectively, have been simulated at bedrock layers using a finite-fault model. The computed site amplifications of the response spectra for various sites were used to develop a site-amplification model for Singapore.
2. The proposed site-amplification model, together with the existing GMPEs at bedrock layers, can be used to estimate the surface seismic hazard of Singapore. The proposed model indicates the important role of site effects in the seismic hazard of Singapore. It can be further used in seismic risk assessment or loss estimates of this region.

ACKNOWLEDGEMENTS

REFERENCES

CEN Eurocode 8. (2004). "Design of structures for earthquake resistance-Part 1: general rules, seismic actions and rules for buildings." *EN 1998-1:2004*. Comité Européen de Normalisation, Brussels.

DSTA. (2009). "Geology of Singapore, (2nd edition)." Defence Science and Technology Agency (DSTA): Singapore.

Kohketsu K. (1985). "The extended reflectivity method for synthetic near-field seismograms." *Journal of Physics of the Earth*, 33, No. 2, pp 121-131.

Kramer S.L. (1996). "Geotechnical earthquake engineering." Practice Hall, New Jersey.

Megawati K., Pan T.C., Koketsu K. (2003). "Response spectral attenuation relationships for Singapore and the Malay Peninsula due to distant Sumatran-fault earthquakes." *Earthquake Engineering and Structural Dynamics*, 32, No. 14, pp 2241-2265.

Megawati K., and Pan T.C. (2010). "Ground-motion attenuation relationship for the Sumatran megathrust earthquakes." *Earthquake Engineering and Structural Dynamics*, 39, No. 8, pp 827-845.

Natawidjaja D.H., and Triyoso W. (2007). "The Sumatran fault zone-from source to hazard." *Journal of Earthquake and Tsunami*, 1, No. 1, pp 21-47.

Pan, T.C. and Sun, J. (1996). "Historical earthquakes felt in Singapore." *Bulletin of the Seismological Society of America*, 86, No. 4, pp.1173-1178.

Schnabel P.B., Lysmer J., Seed H.B. (1972). "SHAKE, A computer program for earthquake response analysis of horizontally layered sites." Report No. EERC 72-12, *Earthquake Engineering Research Center*, College of Engineering, University of California, Berkeley.

Sieh K., and Natawidjaja D. (2000). "Neotectonics of the Sumatran fault, Indonesia." *Journal of Geophysical Research: Solid Earth*, 105, No. B12, pp 28295-28326.

Wair, B.R., and DeJong J.T. (2012). "Guidelines for Estimation of Shear Wave Velocity Profiles" *Pacific Earthquake Engineering Research Center*'s Report, 08/2012.

Sandıkkaya, M.A., Akkar, S., and Bard, P. Y. (2013). "A nonlinear site-amplification model for the next pan-European ground-motion prediction equations." *Bulletin of the Seismological Society of America*, *103*(1), 19-32.

Seyhan, E., and Stewart, J.P. (2014). "Semi-empirical nonlinear site amplification from NGA-West2 data and simulations." *Earthquake Spectra*, *30*(3), 1241-1256.

EFFECTIVE PARAMETERS IN SLOPE-BURIED PIPELING INTERACTIN UNDER DYNAMIC CONDITION

F. Jafarzadeh[1] and H. Farahi[2]

[1] Associate Professor of Geotechnical Engineering (fardin@sharif.edu), [2] PhD Candidate
Sharif University of Technology, Tehran Iran

INTRODUCTION

Since earthquakes have functionally suppressed the operation or physically destroyed embedded pipelines in slopes, many research projects have been performed to reveal the effective parameters in soil slope- pipeline interactions.

Sharif University of Technology, as the consultant, has conducted many 1 g shaking table tests for Tehran Gas Company as client; to clarify the phenomenon in Tehran condition. While, pipelines have been influenced by three major factors including ground conditions, seismic scale and intensity, and lifeline features; this research considers the constant situation for first two factors. The ground conditions and seismic parameters were extracted from related geological, geotechnical and seismological reports. While many features of pipelines have remained unchanged, each test contained on alternatives parameter for evaluation.

Thus, Tehran potential landslides were studied and a typical slope, was selected. The effective parameters, extracted from literature have been "relative geometry of pipe insertion location to slope", "the intersection angle of pipe to sliding direction", "pipe burial depth" and "foam usage in pipe trench as a shelter to reduce pipe deformation".

LOADING PARAMETERS

Seismic parameter were calculated from Kijko- Sellevoll (1992) and Kijko-Graham (1998) methods. The earthquake catalog, allotted to 150 km distribution from the base point (Tehran center), and six attenuation relations were used to reach the maximum base acceleration. 975 years return period earthquake along with 50 years life time of the structure were considered in the analysis. Several seismic sources (line and aria sources) were selected and the parameters were assessed and engaged in seismic hazard calculations. The results showed a peak acceleration amplitude of 0.493 g with 3.8 Hz frequency record.
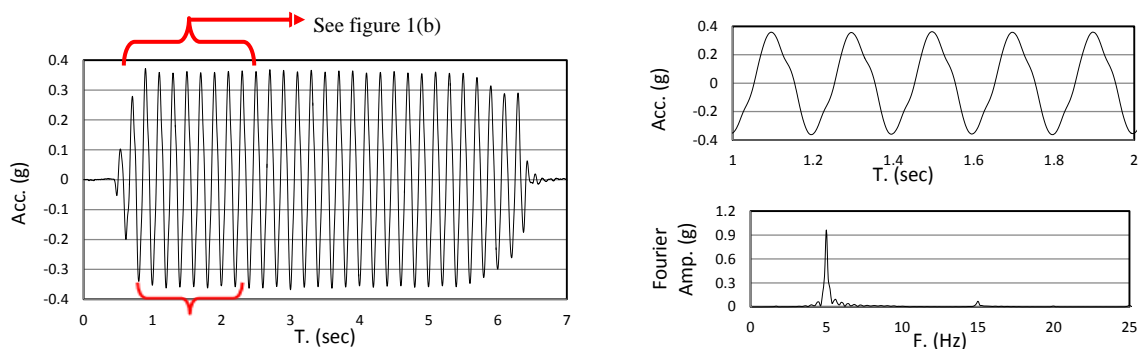
Figure 1. (a) Acceleration time history induced on slope base, (b) Detailed acceleration time history during 1 second, (c) Fourier amplitude of induced record (Test 1)

Since required for converting prototype values to laboratory ones, similitude analysis was performed based on so called Iai method (Iai, 1989 & 2005). By the assumption of the geometrical scaling factor (λ=10), the shear wave velocity of the model and prototype (50 and 375 m/s; respectively), and similar soil densities, laboratory model parameters were calculated. Extracted loading parameters from PSHA were altered to a 5 Hz frequency, 0.32 g amplitude and 25 cycles record with regard to Seed method (Kramer, 1996). Figure 1 shows the induced slope base acceleration time history and Fourier amplitude of test 1.

EXPERIMENTAL SETUP

A one dimensional rigid box having 3 m length, 1 m width and 1.5 m height was designed and constructed with steel profiles. It could tolerate up to 2 g amplitude excitation in longitudinal direction. A one side transparent Plexiglas sheet allowed deformation observation and displacement video record. Also, the pictures taken from this clear side were used for slip surface depth evaluation. Figure 2 depicted a constructed soil slope in the rigid box (model 2).

The model soil parameters (coastal sand) which resembled the prototype material were measured by routine index tests (soil gradation, maximum and minimum soil dry density and natural soil moisture). The poorly graded sand had less than 3 % fine content, 1.453 and 1.732, minimum and maximum density (t/m3) and 2 % moisture content in laboratory. The uniform gradation curve in Figure 3 shows SP-SM soil characteristics according to USGS (Figure 3).

As the model and prototype soil had similar densities, ($\lambda\rho$=1, ρ=15.5 kN/m^3 & Dr=45%), the air pluviation method was calibrated and 70 cm pouring height was selected. In order to visually observe soil horizontal and vertical displacements and to detect the failure plane during and after dynamic excitations, a plaster strip was poured each 10 cm layer next to the Plexiglas side. These layers can be easily distinguished in Figure 2.

Figure 2. Constructed soil slope and plaster-strips in model 2
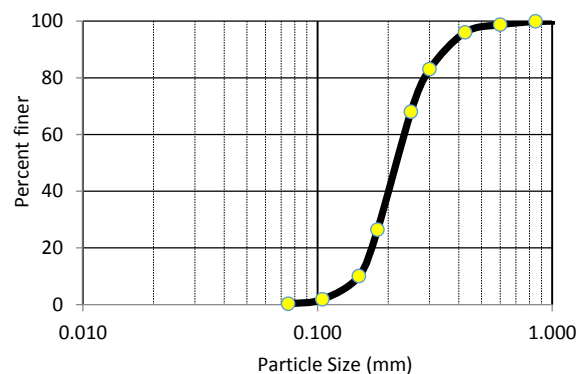
Figure 3. Babolsar coastal Sand gradation curve

Three sensor types, accelerometer, LVDT and strain gauge were used to record slope response and pipe deformations in dynamic tests. The accelerometers were arranged in different positions of the slope to record acceleration responses through height (Figure 4). In order to record the soil subsidence and to check the induced and desired record, two LVDTs were placed on slope crest and next to the side wall of the rigid box respectively (Figure 4). In addition, many strain gauges, arranged to record pure bending or axial deformations, were installed on aluminum pipes (Figure 5).

Since, Tehran Gas network mainly includes steel material, it has been altered by aluminum pipe in physical models. The real case (prototype) continuous pipeline having 20" diameter

and 0.25" thickness was changed to a 16 mm diameter and 1 mm thickness aluminum model pipe.

8 physical models were constructed and tested. Each model contained 2 to 4 pipes inside. The number of pipes was selected based on geometrical limitations of soil container. Figure 4 typically depicted the 1st model arrangements in plan and section views. The slope had 150 cm length with 100 cm width and 86 cm height. It had 91.5 and 60 cm length in crest and toe respectively. The basic difference of models refers to pipes arrangement. Table 1 summarizes the model characteristics in each test.

While, strain gauges were placed on various sections of pipes length, each section had 2 pairs of sensors to report pure bending in either horizontal or vertical directions. The horizontal and vertical strains represents the lateral soil pressure (due to slope horizontal displacement) or overburden changes respectively.

Figure 5 depicts the strain gauge positions on aluminum pipes in models. Furtheremore, the strains have been combimed to form the resulatant ones.
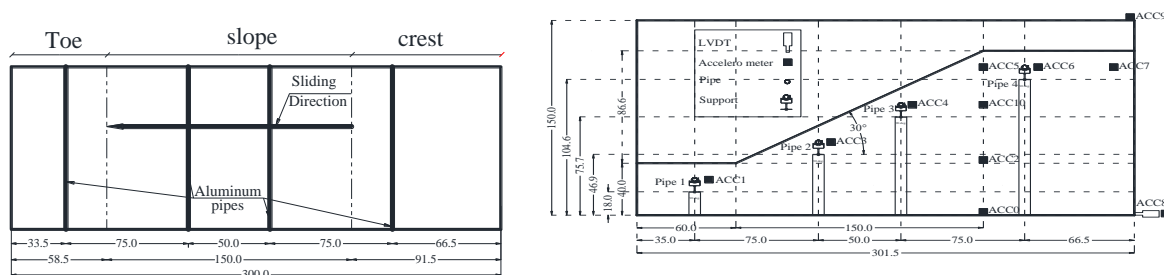
Figure 4. Sandy slope and pipe arrangements in models
(a) Plan view with aluminum pipes showing the pipe positions and sliding direction
(b) model sections with sensors and pipe supports
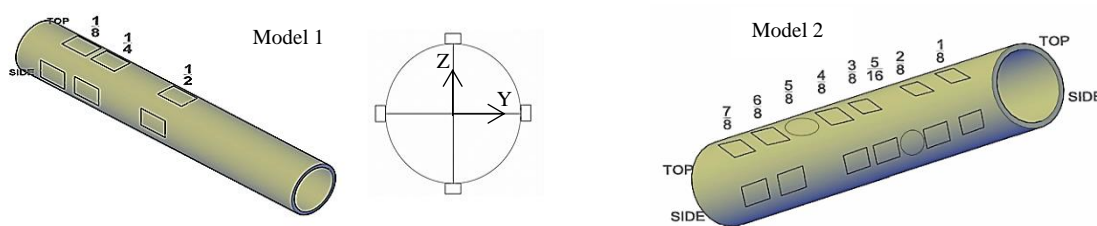
Figure 5. Strain gauges arrangement in buried aluminum pipes

Table 1- Characteristics of shaking table tests

Model No.	Number of buried pipes	Model characteristics		The basic goal of test
		Pipe-slope intersection angle	Burial depth	
1	4	90 °	11 cm	Evaluation of intersection angle and pipe placement zone effect on pipe deformations
2	2	30 °		
3	4	70 °		
4	2	0 °		
5	-	-	-	Evaluation of sliding algorithm and soil displacements
6	4	90 °	21 cm	Evaluation of pipe burial depth on deformations
7	4		31 cm	
8	4		11 cm	Usage of foam material to mitigate pipe deformations

OBSERVED RESULTS

Accordingly, 8 model slopes including buried pipes were constructed and tested under resembled earthquake condition in laboratory scaled situation, using three degree of freedom shaking table of Earthquake Centre of Sharif University. While after test condition and acceleration time histories of slope-crest in test 1 are shown in Figure 6, Figure 7 typically summarizes the strain time history of 3rd pip in model 2. The recorded strains were divided to dynamic, final and peak classes, they are categorized in horizontal-vertical bending and axial ones.
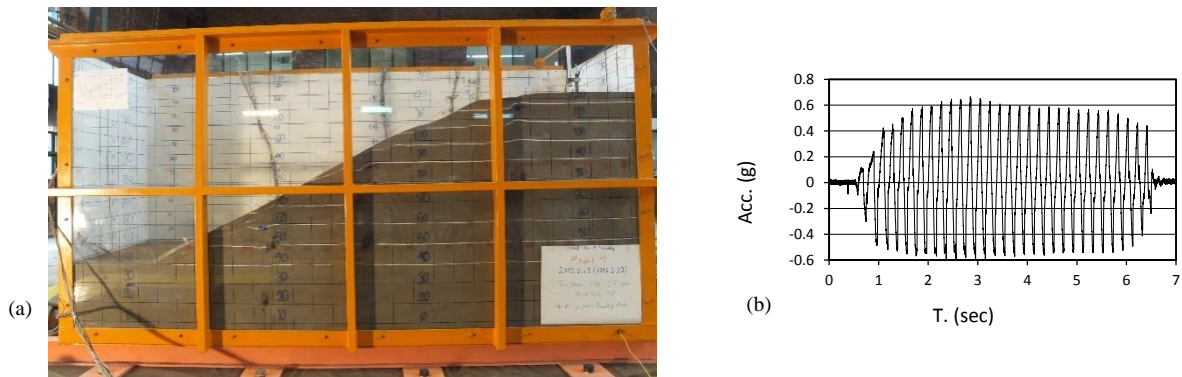
Figure 6. After test condition (a) and acceleration time histories of slope crest in test 1 (b**)**
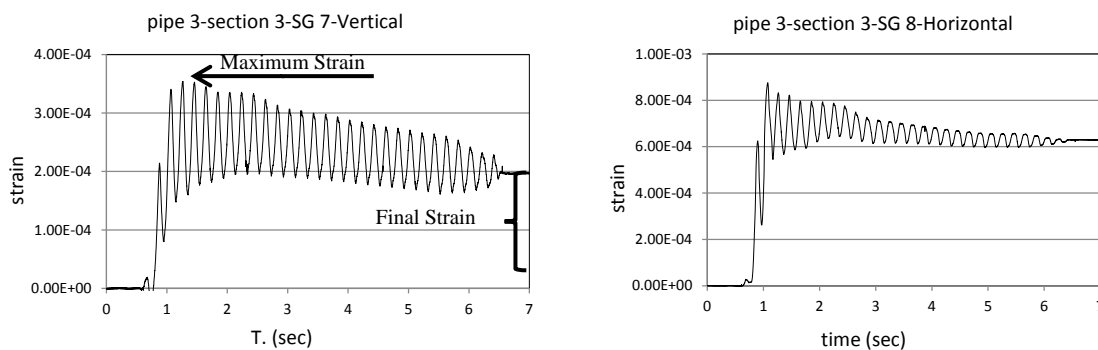
Figure 7. Bending strains in pipe 3 (model 5)

CONCLUSIONS

The research project has been performed to reveal the important parameters affecting buried pipe response in a slope under resembled earthquake condition. The test basically evaluated three major factors as following:

1. Pipe intersection angle with sliding direction

The results show that buried pipe deformations are basically affected by the intersection angle. Since for an equal strain record location, higher intersection angle have resulted larger pipe deformations. Figure 8 show the intersection angle effect on pipe deformations.

2. Pipe placement zone in the slope

The slope has been divided to four zones as toe, lower part, upper part and crest section. In each test the strain of various pipe have been compared and the results have shown that:

b-1) In pipes which are in parallel to sliding direction and extend from crest section to slope toe, the crest and lower slope part had maximum and moderate deformation zones respectively. The upper slope and toe sections are considered low strain part.

b-2) In pipes which are not in parallel to sliding direction, maximum deformation zone moves from lower slope part in β=90o (bending mode) to mid slope section, in β=70o, and to upper slope part, in β=30° (buckling mode). Figure 9 compares the pipe deformations in different slope parts to two 90 and 70 degree intersection angle.
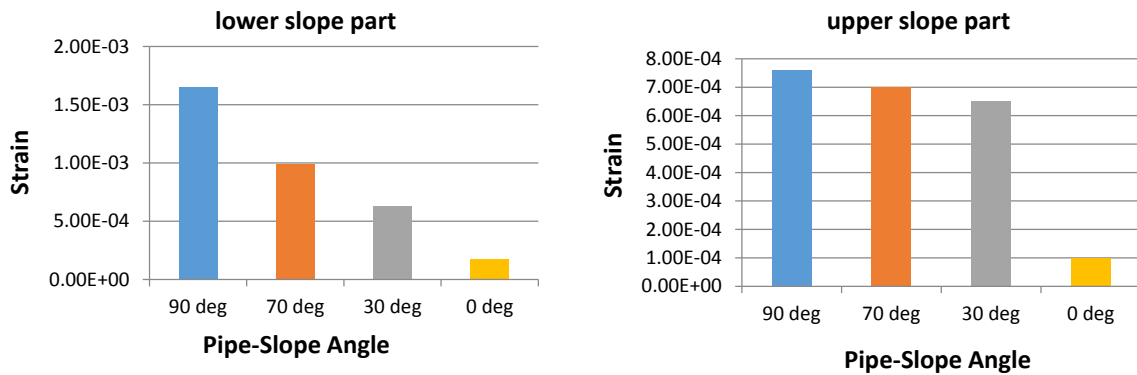
Figure 8. maximum strain comparison in lower and upper slope part for four intersection angles
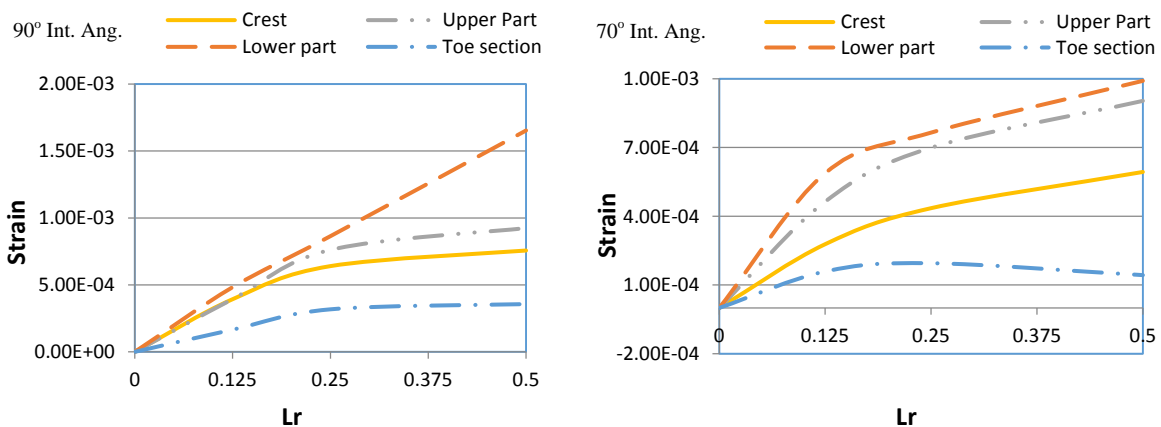
Figure 9. Resultant maximum strains in models in 90° and 70° intersection angle

3. Pipe burial depth

Burial depth effects on embedded pipe deformations is dependent on pipe passage route in a slope. Three burial depths have been considered in tests and the results have been compared. The standard burial depth, 1.1 m and two experienced alternatives, 2.1 and 3.1 m, have been changed to 11, 21 and 31 cm overburden soil in laboratory.

Where the pipe is going to pass the slope with less subsidence, particularly lower part and toe section, increasing burial depth is a helpful action, however in the area having higher subsidence value (upper slope part and crest section) increasing burial depth is not suggested. Figure 10 summarized the bending strains for three burial depths in four slope zones.
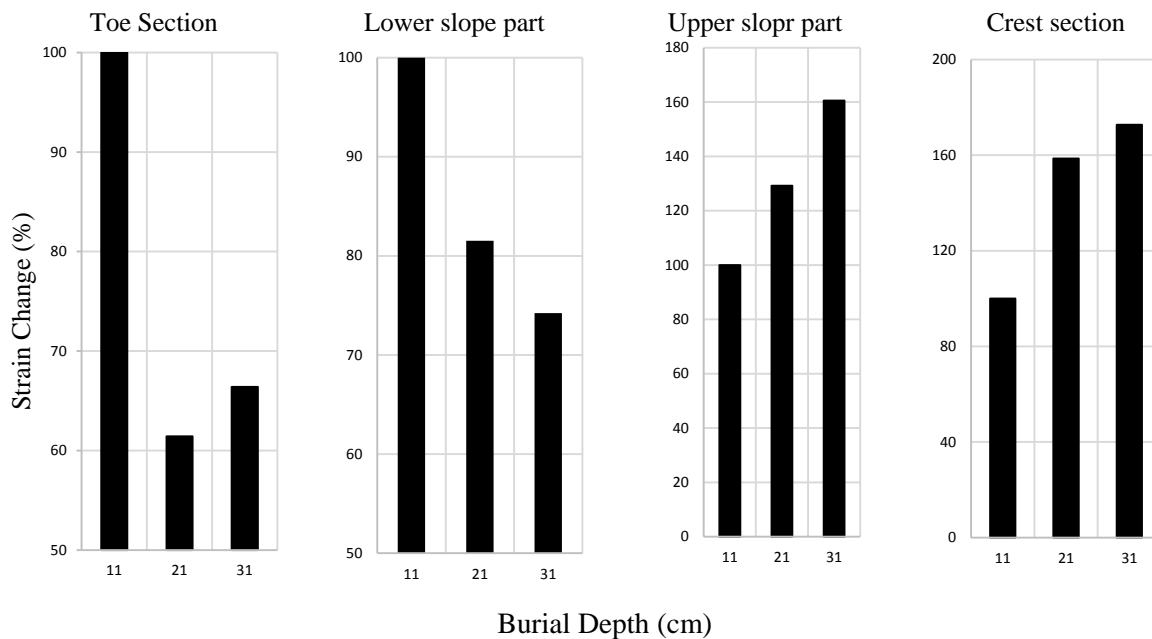
Figure 10. Bending strain change (%) with refence to standard burial depth

REFERENCES

Boivin R.P., Cavanagh P.C. and Clarke R.G. 1993. Directional drilling solves unstable slope along Canadian pipeline. *Oil & Gas Journal* 91, 36.

Challamel N. and de Buhan. P. 2003. Mixed modelling applied to soil–pipe interaction. *Computers and Geotechnics*. Vol. 30: 205–216.

Cocchetti G. di Prisco. C. Galli. A. and Nova. R. 2009. Soil–Pipeline Interaction along Unstable Slopes: A Coupled Three-Dimensional Approach. Part 1: Theoretical Formulation. *Can. Geotech. J.* 46: 1289–1304.

Cocchetti G. di Prisco. C. Galli. A. 2009. Soil–Pipeline Interaction along Unstable Slopes: A Coupled Three-Dimensional Approach. Part 2: Numerical Analyses. *Can. Geotech. J.* 46: 1305–1321.

Iai. S. 1989. Similitude for Shaking Table Tests on Soil-Structure-Fluid Model in 1g gravitational field. *Soil and Foundations*. Vol. 29 (1): 105-118.

Iai. S. Tobita.T and Nakahara.T. 2005. Generalized Scaling Relations for Dynamic Centrifuge tests. *Geotechniques*. Vol 55 (5): 355-362.

Kijko. A and Sellevoll. M. A. 1992. Estimation of earthquake hazard parameters from incomplete data files. Part II. Incorporation of magnitude heterogeneity. *Bulletin of the Seismological Society of America*. Vol 82: 120-134.

Kijko. A and Graham. G. 1998. Parametric-historic procedure for probabilistic seismic hazard analysis Part I: estimation of maximum regional magnitude mmax. *Pure and Applied Geophysics*. Vol 152: 413-442.

Kijko. A and Graham. G. 1998. Parametric-historic procedure for probabilistic seismic hazard analysis Part II: estimation of maximum regional magnitude mmax. *Pure and Applied Geophysics*. Vol 154: 1-22.

Kramer. S. 1996. Geotechnical earthquake engineering. Prentice Hall, Upper Saddle River, New Jersey 07458.

Li Y., Zhao B., Wang Y., Zhang H., Zeng Z. and Sun Y. 2009. Research on some Problems about Oil and Gas Pipelines Crossing the Loess Gully or Slope. ICPTT. ASCE 648.

O'Rourke. T.D. Jezerski. J.M. Olson. N. A. Bonneau. A.L. Palmer. M.C. Stewart. H.E. O'Rourke M. J. Abdoun. T. 2008. Geotechnics of Pipeline System Response to Earthquakes. Keynote Paper. Proceedings Geotechnical Earthquake Engineering and Soil Dynamics IV, Sacramento, CA.

ENERGY-COMPATIBLE AND SPECTRUM-COMPATIBLE SYNTHETIC MOTIONS FOR SEISMIC SLOPE DISPLACEMENT ANALYSES

Duruo Huang and Gang Wang

Department of Civil and Environmental Engineering, The Hong Kong University of Science and Technology, Clear Water Bay, Hong Kong

BRIEF INRODUCTION, METHODOLOGY AND KEY RESULTS

Ground motion effects on structures are commonly represented by spectral acceleration, which reflects frequency content of a ground motion. For design purposes, ground motions can be stochastically simulated to be compatible with a prescribed design response spectrum. However, it is known that ground motions that match a target spectrum are not unique, since the linear response spectrum does not reflect some other important aspects of a ground motion, such as duration, energy content and nonstationary characteristics. These intensity measures have been demonstrated to be important in dynamic analyses of structures and geotechnical systems. For example, Wang (2012) showed that the Arias intensity (Ia), in addition to spectral acceleration, is critical for estimating seismic slope displacements.

Recently, a generalized conditional intensity measure (GCIM) method has been developed for ground-motion selection (Bradley 2010). The method constructs conditional distribution of multiple ground-motion intensity measures (IMs) and selects ground motion suite following the GCIM distribution. The accuracy of GCIM framework has been evaluated using nonlinear time-history analysis of structures, which highlights the significance of conditioning multiple IMs in ground-motion selection process (Kwong and Chopra, 2015).

Following this line, a wavelet-packet based ground-motion simulation and modification technique has been recently developed by the author (Huang and Wang 2015a, 2015b; Huang, 2016) to generate energy-compatible and spectrum-compatible (ECSC) synthetic ground motions. The ECSC method significantly advances traditional ground-motion modification methods, because it generates ground-motion time histories that not only match target spectral accelerations, but also match other important ground-motion IMs such as total energy and its temporal accumulation, as well as ground-motion duration (ref. Figure 1). The ECSC simulation method includes three major steps: (1) predict a seed motion using seismological constraints (M, R, Vs_{30}), (2) iterative adjustment of the wavelet-packet spectrum in both time and frequency domain, and (3) evaluate compatibility of response
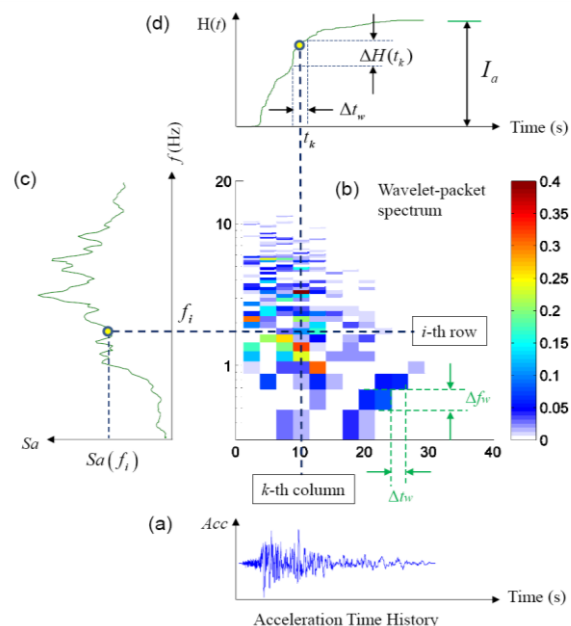
Figure 1: Wavelet-packet spectrum, showing the distribution of squared wavelet-packet coefficients of a recorded ground-motion time history (Huang 2016)

spectrum and accumulative energy of the simulated motion with targets.

Given an earthquake scenario, the statistical distribution of target spectral accelerations, significant durations and Arias intensity can be determined following the GCIM procedure (Bradley, 2010). Empirical cross-correlation between these *IMs* is preserved through multivariate random realizations. Figure 2 (a) shows 60 randomly realized target spectral accelerations for an earthquake scenario (M_w=7, R_{rup}=10 km, strike-slip faulting) conditioned on T = 1s with epsilon = 0. Correspondingly, the cumulative distribution of significant duration parameters, D_{5-75}, D_{5-95}, and Arias intensity are shown in Figure 2(b) for this scenario. A single realization of the spectral acceleration, its corresponding significant duration values D_{5-75}, D_{5-95} and Arias intensity is also highlighted in Figure 2(b)(c) using open circles. These values are used as the *targets* for the ECSC simulation. It is also worth noting that a target Arias intensity build-up can be easily established using D_{5-75}, D_{5-95} and Arias intensity by

Figure 2: (a) Distribution of *Sa* and the selected target; (b) CDF of D_{5-75}, D_{5-95} and (c) CDF of Arias intensity. The open circle represents the selected target values for ECSC simulation.

assuming the Arias intensity build-up process follows a lognormal *CDF* distribution. Figure 3 shows the simulated ECSC ground motion following this selected target. By comparing *IMs* of the ECSC simulated ground motion with the specified targets, it can be observed that both response spectrum and Arias intensity build-up of the simulated motion agree well with the targets. The ECSC ground-motion simulation procedure can be repeated for other selected targets of *Sa*, D_{5-75}, D_{5-95} and *Ia* such that a full set of simulated motions can be generated to follow the targeted distribution of these multiple *IMs* for a specific earthquake scenario.
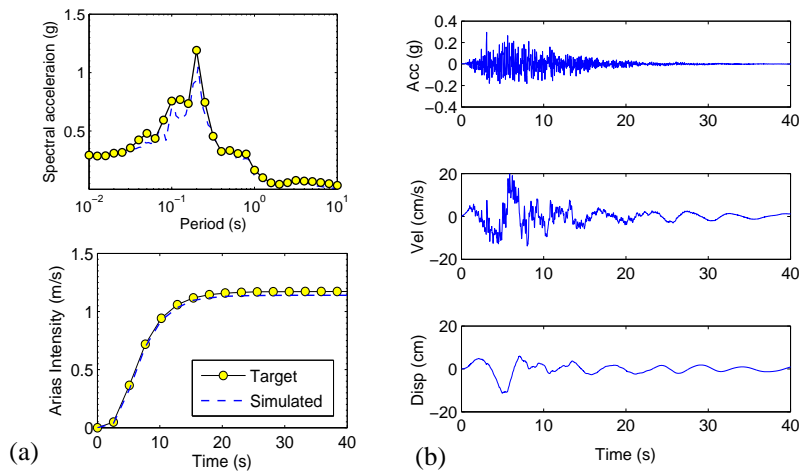
Figure 3 (a) Target and simulated spectral acceleration, Arias intensity build-up. (b) Acceleration, velocity and displacement time histories of the simulated ground motion using ECSC method.

Although the ECSC synthetic ground motions can match multiple *IM* targets, its capability of producing similar nonlinear dynamic responses with realistic ground motions need to be validated. For this purpose, we select a total of 562 ground-motion records from three large earthquakes in California to perform the sliding block analyses. They are ground motions recorded during the 1979 Imperial Valley earthquake, the 1989 Loma Prieta earthquake and the 1994 Northridge earthquake. Ground motions are recorded in both strike-normal and strike-parallel directions and are retrieved from the PEER-NGA strong-motion database. Figure 4 shows locations of seismograph stations and epicenters of the three events. Using the ECSC simulation method, each

Figure 4: Epicenters of earthquake events and locations of recording stations used in this study

actual recorded motion is stochastically simulated using seismological variables (M, R, V_{s30}) associated with that record. In this way, all 562 waveforms are "reproduced" and referred to as the ECSC simulated dataset.

Estimating seismic displacement of natural slopes is important for risk assessment of earthquake-induced landslides. In this study, the Newmark sliding block analysis (Newmark 1965) is used to predict the seismically induced slope displacements using the 562 ECSC simulated motion set, compared with that calculated using real recorded ground motions. The Newmark model assumes sliding of a rigid block is initialized when the shaking acceleration exceeds the yield acceleration (a_c) of the sliding surface, and the block continues
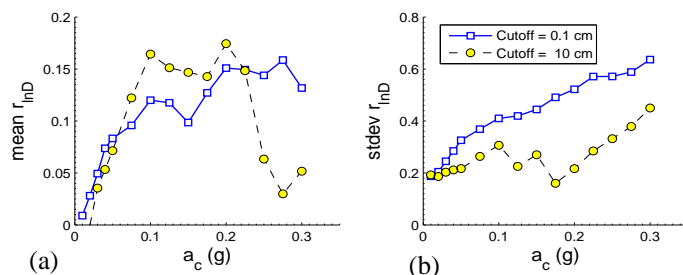
Figure 5: (a) Mean and (b) standard deviation of displacement residuals versus yield accelerations. Cut-off displacement of 0.1 cm and 10 cm are used.

to slide until the relative velocity between the block and ground reaches zero. The velocity-time history of the block is then calculated by integrating the relative acceleration within that time range, and the sliding displacement is determined by integrating the velocity time history of the block. We define the one-to-one difference (residual) of the Newmark displacements in natural log scale, as follows:

$$r_{\ln D} = \ln\left(\text{Disp}_{NGA}\right) - \ln\left(\text{Disp}_{ECSC}\right) \tag{1}$$

Figure 5 shows mean and standard deviation of displacement residuals using two cut-off thresholds (1 cm and 10 cm). It can be observed that the mean of displacement residual $r_{\ln D}$ increases from 0 to around 0.1 ~ 0.15 when the yield acceleration a_c increases from 0.01 to 0.5 g. This means, on average, the ECSC ground motions slightly under-predict the Newmark displacement up to 10-15%. The standard deviation of $r_{\ln D}$ increases from 0.2 to 0.5 when the yield acceleration increases from 0.01 to 0.5 g. It is also interesting to notice that the standard deviation will be reduced to around 0.2 if analysis is performed only on displacement data

greater than 10 cm, which implies the increased scatter of displacement residuals is mainly contributed by smaller displacement data.

CONCLUSIONS

A new ground-motion simulation and modification procedure is developed that allows the generation of energy-compatible and spectrum-compatible (ECSC) ground motions through wavelet-packet characterization and modification. The ECSC procedure can be regarded as stochastic ground-motion simulation conditioned on a specific seismological environment and multiple *IM*s, including spectra acceleration, duration and cumulative energy. This study demonstrates that the ECSC technique can be implemented in the GCIM framework to directly simulate ground-motion suite for performance-based earthquake design.

Seismic slope displacement analyses have been performed to compare the nonlinear seismic response of earth structures using simulated ECSC ground-motion dataset and its recorded counterpart in the NGA database. The tests validated the general performance of simulated ECSC motions are comparable with that of the recorded motions.

ACKNOWLEDGEMENTS

REFERENCES

Bradley, B.A. (2010). "A generalized conditional intensity measure approach and holistic ground-motion selection." *Earthquake Engineering & Structural Dynamics* 39(12), pp. 1321–1342.

Newmark, N.M. (1965). "Effects of earthquakes on dams and embankments." *Geotechnique* 15(2), pp. 139–160.

Huang, D. and Wang, G. (2015a). "Stochastic simulation of regionalized ground motions using spatial cross-correlation model and cokriging analysis." *Earthquake Engineering & Structural Dynamics* 44, pp. 775-794.

Huang, D. and Wang, G. (2015b). "Regional-specific spatial cross-correlation model for stochastic simulation of ground-motion time histories." *Bulletin of the Seismological Society of America*, 105 (1), pp. 272-284.

Huang, D. (2016). *Stochastic simulation of spatially correlated earthquake time histories, and energy-compatible and spectrum-compatible ground motion modification using wavelet packets.* Ph.D. thesis, Department of Civil and Environmental Engineering, Hong Kong University of Science and Technology.

Kwong, N.S., and Chopra, A.K. (2015). "Evaluation of the exact conditional spectrum and generalized conditional intensity measure methods for ground motion selection." *Earthquake Engineering & Structural Dynamics* online.

Wang, G. (2011). "A ground motion selection and modification method capturing response spectrum characteristics and variability of scenario earthquake." *Soil Dynamics and Earthquake Engineering*. 31, pp. 611-625.

Wang, G. (2012). "Efficiency of scalar and vector intensity measures for seismic slope displacements." *Frontiers of Structural and Civil Engineering*. 6(1), pp. 44-52.

NUMERICAL MODELING OF LATERAL BEHAVIOR OF HELICAL PILES

Weidong Li and Lijun Deng
University of Alberta, Edmonton, Canada

BRIEF INRODUCTION, METHODOLOGY AND KEY RESULTS

Helical piles are extensively used in Western Canada to support vertical loads because of the effective contribution of helical plate embedded at depth. The influence of helical plates on the lateral behaviour when used for lateral resistance is yet to be determined. The overturning capacity of helical plates may be dependent of many factors such as the size of the helix, the embedment depth of the helix, and the soil strength. To find out the influence of helix on the lateral capacity will substantially improve the design practice of helical piles used to resist large lateral loads due to winds or earthquake loads.

In the present research, a 3-D Beam-on-Nonlinear-Winkler-Foundation (BNWF) model was developed in the Open System for Earthquake Engineering Simulation (OpenSees) to simulate the lateral behaviour of helical piles in a soft clay soil and a dense sand soil; the model was calibrated against the results of several existing axial and lateral load tests in the literature. A series of parametric analyses was carried out using the BNWF model to evaluate the factors that influence the lateral capacity. In the parametric analyses, the diameter of helix D, embedment depth of helix H, and dimeter of pile shaft d were altered to observe the response of the lateral capacity. Besides helical piles, the bucket pile, an innovative helical pile whose upper shaft is partially enlarged (the bucket) to provide extra lateral resistance, was also accounted in the analyses; the length l_B and diameter d_B of the bucket were altered in the analyses.

Figure 1 and Figure 2 show the results of the parametric analyses. In the analyses, the soft clay soil had an undrained shear strength s_u of 3 kPa, the dense sand soil had an effective friction angle ϕ' of 38°, D was varied from $4d$ to $8d$, H was varied from 10% to 90% of the pile embedment depth E, d_B was varied from $2d$ to $5d$, and l_B was varied from $0.2E$ to $0.4E$.
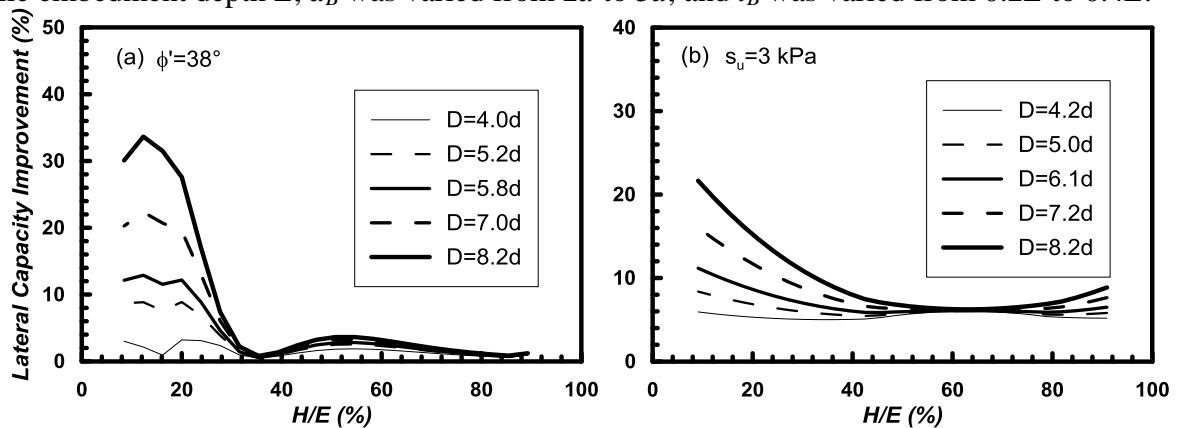
Figure 1: Lateral capacity improvement vs. helix diameter and helix embedment

It is found that the improvement of lateral capacity showed different tendency in the soft clay and the dense sand; the parametric variables adopted in the analyses have nonlinear

impacts on the lateral capacity; the helical pile dimensions may be optimized to obtain the most effective improvement of lateral capacity.
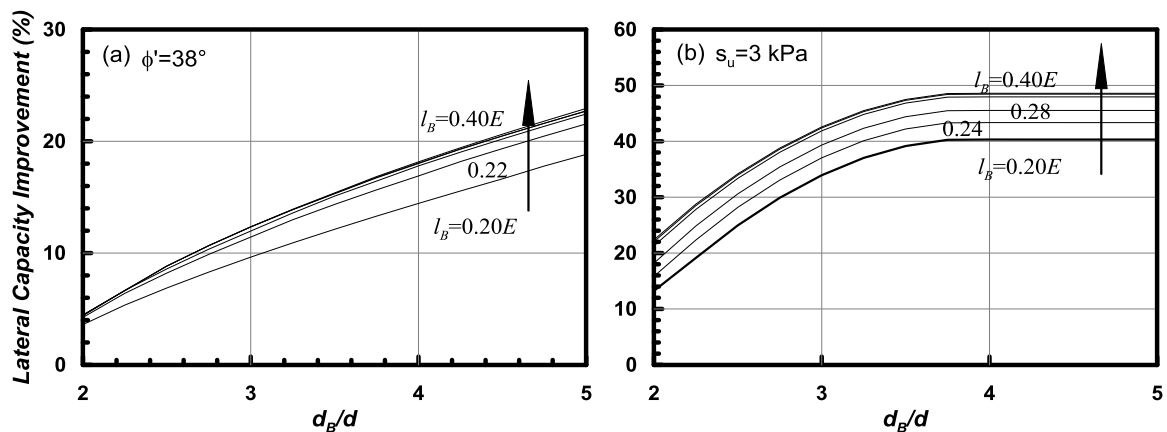
Figure 2: Lateral capacity improvement vs. bucket diameter and bucket length

CONCLUSIONS

1. In the dense sand scenario, the contribution of the helix to the total lateral resistance is negligible when it is embedded at a great depth. An optimum embedment of the helix is about 12% of the pile embedment. The optimum improvement by a single helix, whose diameter is 5 times of shaft diameter, is about 9%.
2. In the soft clay scenario, both deeply and shallowly embedded helices can improve the lateral capacity. Theoretically the helix installed right below the surface of soft clay is the most effective design to enhance the lateral capacity. In the practice, the helix has to be embedded to a proper depth such that the cohesion on the upper surface of helix can develop. The optimum improvement by a single helix, whose diameter is 5 times of shaft diameter, is also about 9%.
3. The effect of bucket diameter yielded at about 3.7d in the soft clay, but not yet in the dense sand. The lateral capacity improvement becomes less effective when the bucket length increases, and almost ineffective at 40% of the pile embedment depth.

ACKNOWLEDGEMENTS

REFERENCES

Prasad, Y. V., and Rao, S. N. 1996. Lateral capacity of helical piles in clays. *Journal of Geotechnical Engineering*, 122(11), 938-941.

Sakr, M. 2009. Performance of helical piles in oil sand. *Canadian Geotechnical Journal*, 46(9): 1046-1061.

API 1993. Recommended practice for planning, designing and constructing fixed offshore platforms – Working stress design. 20th Edition, American Petroleum Institute, Washington, D.C.

Coyle, H. M., and Reese, L. C. 1966. Load transfer for axially loaded pile in clay. *Proc. ASCE*, SM2.

Aschenbrenner, T. B., and Olson, R. E. 1984. Prediction of settlement of single piles in clay, Analysis and design of pile foundations. American Society of Civil Engineers, J. R. Meyer, ed., 1984.

EFFECT OF ROUGH BEDROCK SURFACE ON DEFORMATION AND FAILURE OF SOIL SLOPES

Yiying Zhao, Huite Wu, Zewei Ma and Ga Zhang
Tsinghua University, China

BRIEF INRODUCTION

A great proportion of slopes are located on the bedrock. The bedrock has been proven to affect the deformation and failure significantly. The influential mechanism has not been clarified though numerical and physical simulations were conducted to investigate the behavior of slopes on the bedrock. Centrifuge modeling has been widely used to studies on the failure behavior of slopes under different loading conditions (Zornberg et al. 1998; Viswanadham and Rajesh 2009; Wang and Zhang 2014; Zhang et al. 2015). In this paper, centrifuge model tests were performed to compare the response of the slope with rough bedrock with that of the pure slope. The effect of rough bedrock surface on deformation and failure of soil slopes was analyzed on the basis of test observations.

METHODOLOGY

The centrifuge model tests were conducted using the centrifuge at Tsinghua University. The soil used in the tests was a type of silty clay with a specific gravity of 2.7. The dry density and water content of the soil were 1.4 g/cm^3 and 17%, respectively. The cohesion of the soil was 24 kPa, and the internal frictional angle was 27°. The bedrock was simulated by the organic glass, and a piece of sandpaper was pasted on the surface to simulate the rough surface property. The slope of the bedrock was 2:1 (Fig. 1).

The slope model was 25 cm high with a gradient of 1.5:1 (Fig. 1). The bedrock was placed behind the slope. A 5-cm-thick soil layer was placed under the slope to diminish the effect of the model container. The soil slope without bedrock was in the same condition as the one with rough bedrock, except that the bedrock was replaced by the soil.

During the centrifuge model tests, the centrifugal acceleration increased from 1 g gradually to 50 g. An image record system was used to capture a series of photographs of the lateral side of the slope during loading through the transparent organic glass of the model container. The displacement of the slope was analyzed according to the photograph series.

KEY RESULTS

A slip surface appeared through the slope with bedrock at the 42 g level, and a rapid landslide consequently occurred. The height of the prototype slope was 10.5m when the landslide occurred. On the other hand, the pure slope did not fail even if the centrifugal acceleration reached the 75 g though it exhibited evident deformation. The photograph of the failure morphology of slope with bedrock is shown in Fig. 1.

In order to show the effect of the rough bedrock, the slippage along the bedrock was compared with the displacement at the same position of the pure slope (Fig. 2). It can be seen that both types of soil slopes exhibited evident slippage displacement with similar

development tendency as the centrifugal acceleration increased. It is easy to find that at the two elevations, the displacements of the slope with bedrock were both smaller than those of the pure slope, especially at the higher location. This demonstrated that the rough bedrock reduced the deformation of the slope near the bedrock surface. Such reduction became greater with increasing altitude.
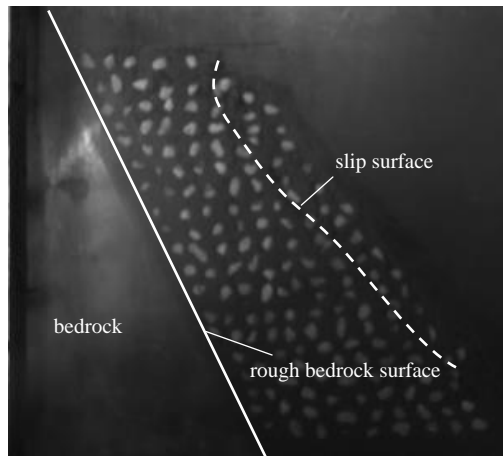
Figure 1: Photograph of slope model and morphology of slope failure.
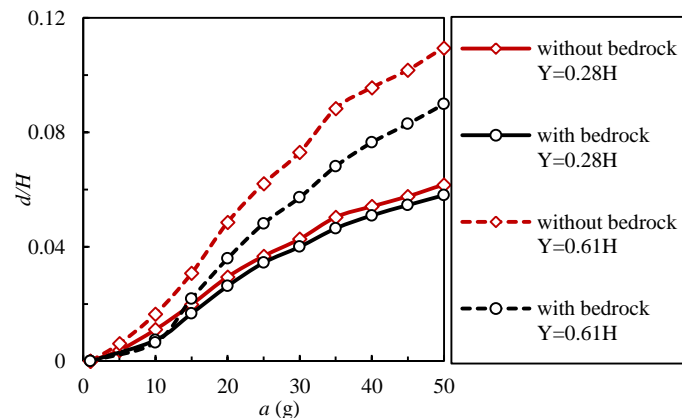
Figure 2: Displacement histories along the bedrock. d, displacement along bedrock surface; H, slope height; a, centrifugal acceleration; Y, vertical distance from slope toe.

For further analysis of the effect of bedrock surface on deformation of soil slope, the total horizontal displacement, u, could be decomposed into two components, namely the horizontal slippage along the bedrock, u_0, and the horizontal displacement relative to the bedrock, u'. That is,

$$u=u_0+u' \tag{1}$$

Figure 3 shows distribution of horizontal displacement of the two types of soil slopes at different elevations and g levels. It can be seen that for the upper part of the slope ($0.61H$ elevation), both the total horizontal displacement, u, and relative horizontal displacement, u', of the slope with bedrock were evidently larger than those of the pure slope. It can be seen that for the slope with bedrock, there was a rapid increase at a certain range near the bedrock, which indicates that the bedrock affected the displacement of the soil next to the bedrock. The bedrock not only exacerbates the horizontal displacement of the soil slope, but also changes the displacement distribution inside the soil slope. While for the lower part of the slope ($0.28H$ elevation), the total displacement u and relative displacement u' of slope with bedrock and those of the pure slope were similar. This indicates that the effect of the bedrock is significant in the upper and middle of the slope. The bedrock reduces the slippage along the bedrock, however, it increases the horizontal displacement of the slope. This may be the cause to the failure of the slope with bedrock.

Figure 4 shows horizontal gradient of horizontal displacement of soil slopes. The gradient could be used to indicate the degree of the deformation localization of the slope. For the slope with bedrock, the gradient of horizontal displacement was all small at the 35 g level (Fig. 4a). As the centrifugal acceleration continued to increase, the gradient of horizontal displacement increased rapidly within a certain area, and there was an evident peak. After the peak appeared, the deformation localization near it increased significantly with increasing the centrifugal acceleration. As a result, the slip surface turned up at this position where the peak appeared. It manifests that the deformation localization of soil slope with bedrock emerges and enhances, and leads to the failure of the slope finally. After the sliding body appeared, the gradient of horizontal displacement near the slip surface continued to increase

significantly, and there was still evident deformation inside the sliding body. The appearance of the slip surface further enhances the degree of the deformation localization of the slope. This indicates a significant coupling of deformation localization and failure. The deformation localization of the slope develops and leads to local failure, and the new deformation localization is induced by the local failure.

For the pure slope without bedrock, the degrees of deformation localization were evidently smaller than those of the soil slope with bedrock, and there was no evident peak of the gradient. (Fig.4). This indicates that the bedrock exacerbates the emergence and development of deformation localization because of the effect of the deformation distribution of the soil slope. Therefore, the bedrock reduces the stability level of slope.

(a) 30g   (b) 40g
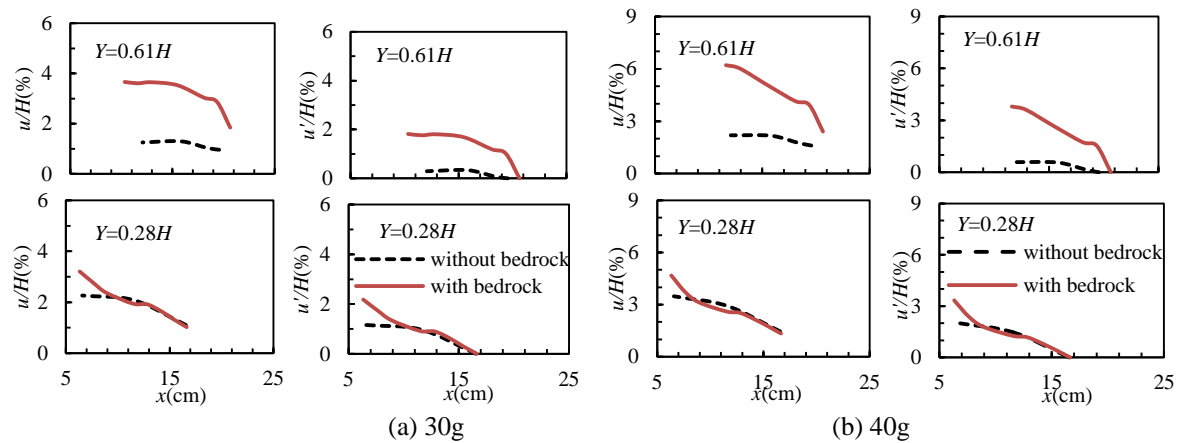
Figure 3: Distribution of horizontal displacement of soil slope of typical moment. *u*, horizontal displacement; *H*, slope height; *Y*, vertical distance from slope toe; *x*, horizontal distance from slope toe.

(a) soil slope with rough bedrock   (b) soil slope without bedrock
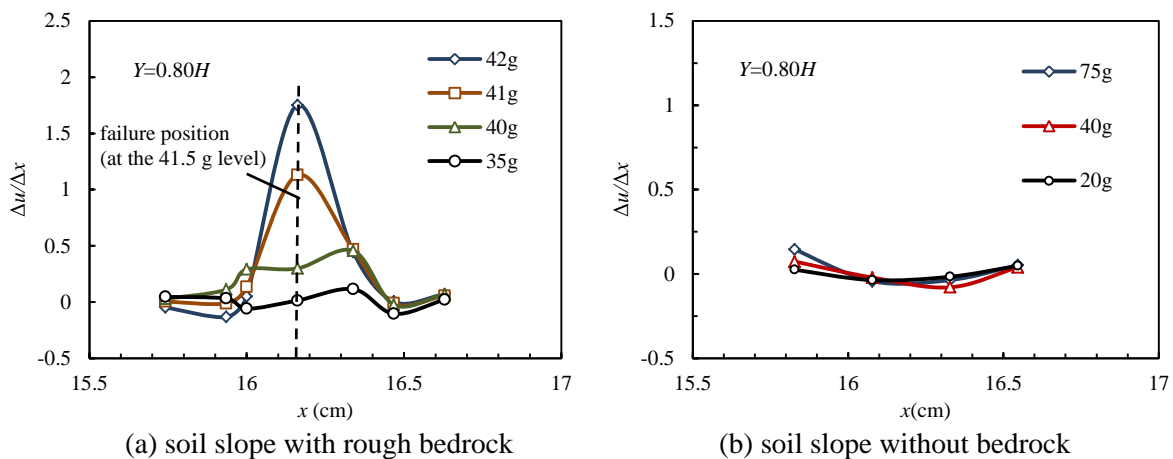
Figure 4: Horizontal gradient of horizontal displacement of soil slopes. *u*, horizontal displacement; *x*, horizontal distance from slope toe; *H*, slope height; *Y*, vertical distance from slope toe.

CONCLUSIONS

1. The rough bedrock has a significant effect on the deformation of the soil slope. It not only exacerbates the horizontal displacement of the soil slope, but also changes the displacement distribution inside the soil slope. Such effect increases with increasing altitude.

2. The soil slope with rough bedrock shows an evident coupling of deformation localization and failure. In other words, the deformation localization of the slope develops and leads to local failure, and the new deformation localization is induced by the local failure.
3. The bedrock exacerbates the emergence and development of deformation localization because of the effect of the deformation distribution of the soil slope. Therefore, the bedrock reduces the stability level of slope.

ACKNOWLEDGEMENTS

REFERENCES

Viswanadham, B.V.S., Rajesh, S. (2009). "Centrifuge model tests on clay based engineered barriers subjected to differential settlements." *Apply Clay Science* 42(3-4), pp. 460-472.

Zhang, G., Hu, Y., Wang, L.P. (2015). "Behaviour and mechanism of failure process of soil slopes." *Environmental Earth Sciences* 73(4), pp. 1701-1713.

Zornberg, J.G., Sitar, N., Mitchell, J.K. (1998). "Performance of geosynthetic reinforced slopes at failure." *Journal Geotechnical and Geoenvironmental Engineering* 124(8), pp. 670-683.

Wang, L.P., Zhang, G. (2014). "Progressive failure behavior of pile-reinforced clay slopes under surface load conditions." *Environmental Earth Sciences* 71(12), pp. 5007-5016.

Zhang, G., Hu, Y., Zhang, J.M. (2009). "New image analysis-based displacement-measurement system for geotechnical centrifuge modeling tests." *Measurement* 42(1), pp. 87-96.

CENTRIFUGE MODEL TESTS OF HETEROGENEOUS SLOPES UNDER RAPID DRAWDOWN CONDITION

Jiahao Zhang, Weisa Meng and Ga Zhang
Department of Hydraulic Engineering, Tsinghua university, Beijing, China

BRIEF INTODUCTION

There are many slopes adjacent to water in nature. Rapid drawdown of water levels often induces landslides of this kind of slopes (Jia et al. 2009), which causes great loss of life and property. Many researches have been conducted to investigate the slope failure. However, most previous studies ignored slope's heterogeneity. It's necessary to study the effect of slope's heterogeneity in slope failure. This essay is based on centrifuge model test to study heterogeneous slope's failure behavior under drawdown condition.

METHODOLOGY

Fig. 1 shows the profile of the model slope. The slope was constructed to have a height of 35 cm. From the top to the bottom, it consisted of a 10-centimeter-thick soil layer with a gradient of 1:1, a 5-centimeter-thick sand layer with a gradient of 0.7:1 and a 20-centimeter-thick soil layer with a gradient of 1.2:1. The soil moisture and dry density of experimental slope were 18% and 1.55 g/cm^3, respectively. The plastic and liquid limits of the soil are 25% and 18.5%, respectively. The sand has moisture of 5% and a dry density of 1.6 g/cm^3. The model slope was made by compacting layers every 5 cm up to preset height.

During the test, the centrifugal acceleration gradually increased to 50g with suspended for 1min every 10g. When the deformation of the slope became stable at 50g-level, after around 20 min, the water was impounded to the preset water level, 280 mm. To have a good permeation and ensure the slope deformation stable, the water level was started to decrease to slope bottom after 30 min. The GeoImage analysis System for centrifuge was used to measure the slope displacement (Zhang et al. 2009).

KEY RESULTS

Fig. 2 shows the histories of water level and settlement at the slope top. It can be observed that the water level decreased at a nearly linear rate. The settlement at the slope top increased as the water level decreased. In the beginning of drawdown, the settlement increased little, which indicates that there is a time lag between drawdown and deformation of the slope.
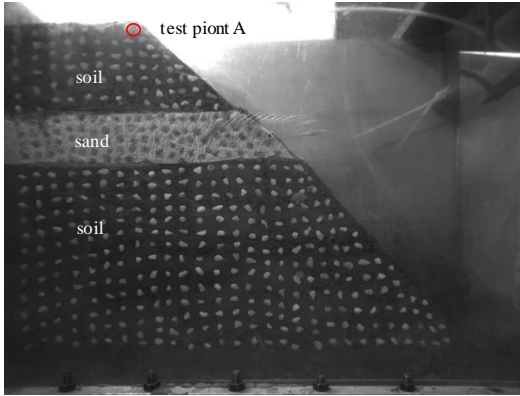
Fig.1 Photograph of the slope model.
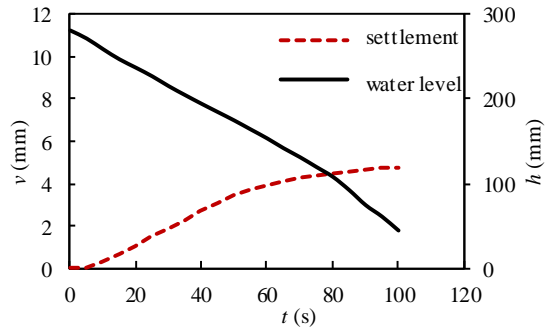
Fig.2 Histories of water level and settlement at the top of slope during drawdown. h, water level; v, settlement at the slope top; t, time.

Fig.3(a) shows the photograph of model slope after drawdown. The slope failed during drawdown and the slip surfaces are outlined in the photograph and also marked in the schematic diagram (Fig.3 (b)). Noticeably, there were two slip surfaces in the slope, which may be induced by the heterogeneity of the slope. Both of the slip surfaces ran through the three layers and connected smoothly in the interface without intersecting. Thus, the slope can be divided into three parts, base body, slipping body and sub-slipping body according to the slip surfaces. A coordinate system was established for clear illustration in Fig.3 (b).
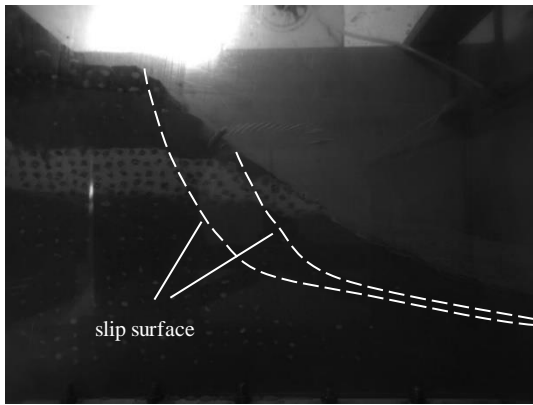
(a)
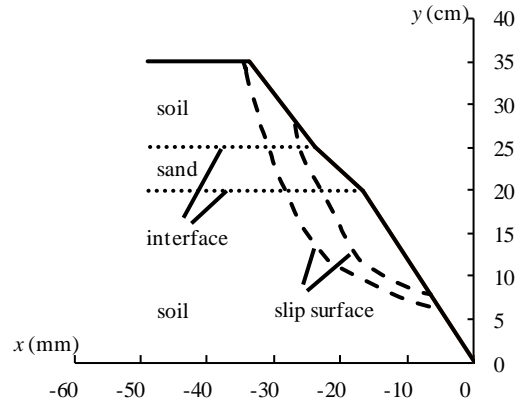
(b)

Fig.3 (a): Photograph of model slope after drawdown; (b): Schematic diagram of model slope.

Point couples were used to analyze the formation sequence of the slip surfaces. At the roughly same height, on both sides of slip surfaces, two points whose distance was about 10 mm were chosen as a point couple. The relative displacements of the point couples on the tangent and normal directions of slip surface were obtained using displacement measurements. Fig.4 shows the locations of point couples.
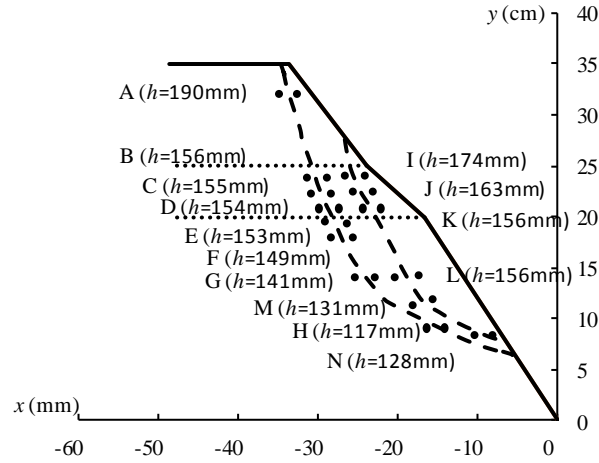
Fig.4 Point couples' positions and slip surfaces' formation process.

Fig.5 shows typical results of point couple measurements. It can be seen that the displacements on the tangent directions were greater than the ones on the normal directions to the slip surface. This suggested that the slope's exhibited majorly slippage failure. In the beginning of drawdown, the relative displacements were fairly small, and exhibited a sudden change at some moment. Such the moment could be regarded as the time when the slip surface formed there. The corresponding water level was figured out and marked in Fig.4. to show the forming process of the slip surfaces.

Fig.4 shows the two slip surfaces both formed from the slope top and developed downward. However, the occurrence times were different for the two slip surfaces. The deeper slip surface started at a water level of 190mm, while the shallower slip surface started at a water level of 174mm. This indicates that the slipping body formed before sub-slipping body. It should be noted that the water level of 174 mm was just the time that the water level reached lower interface between the soil and sand. It could be concluded that the shallower slip surface is largely due to the difference between the permeability of the cohesive soil and sand. This suggests that the heterogeneity of slope affects the failure process and caused the two slip surfaces.
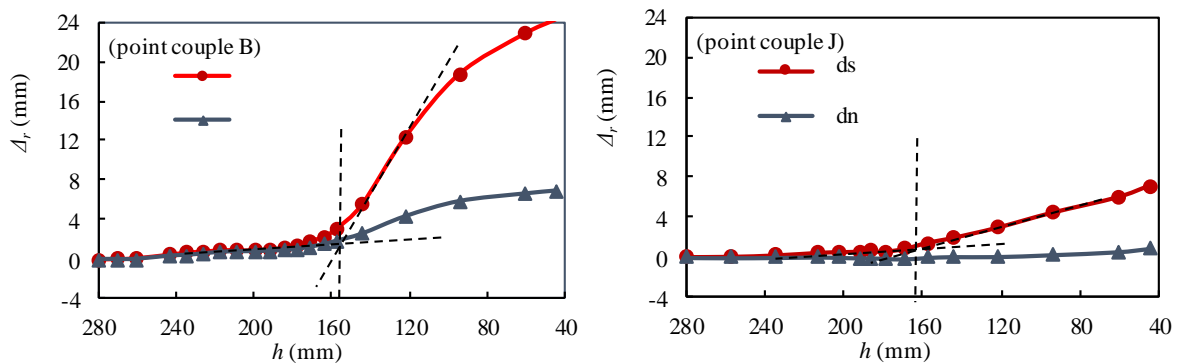
Fig.5 Histories of point couples' relative displacement and water level. Δ_r: relative displacement; ds: relative displacement on tangent direction; dn: relative displacement on normal direction; h: water level.

The horizontal displacement of some points in every layer at the same height was measured at different water level (Fig.6). The displacement increased when water level dropped, apart from those points in base body. The inflection points on the curves exhibited similar locations with the slip surfaces. Fig.6 also shows that the displacements varied little between the two inflection points or before the inflection points. This suggested that deformation localization appeared. It could be concluded that the deformation localization that led to the global failure of the slope.
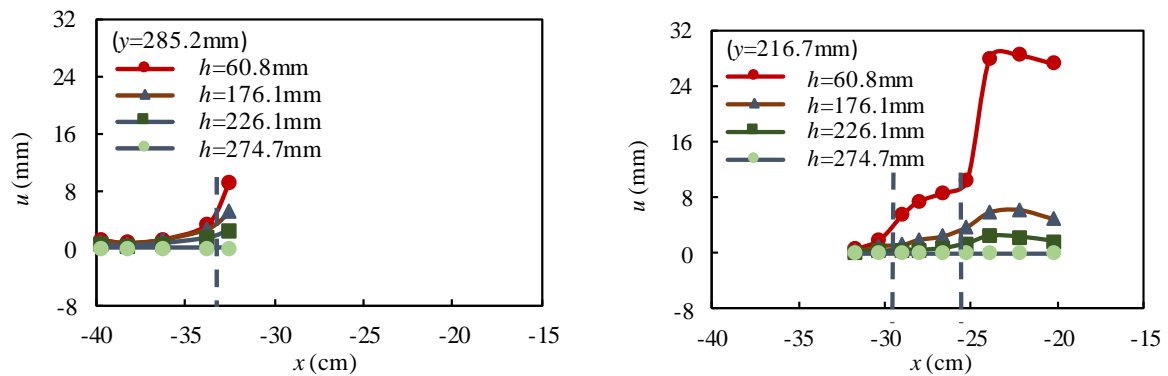
Fig.6 Horizontal displacement of the same height points at different water level. u: horizontal

CONCLUSIONS

1. Drawdown led to slope failure. Two slip surfaces were appeared due to the heterogeneity of the slope.
2. Two slip surface both formed from the slope top and developed downward.
3. Slope failure was majorly sliding failure and caused by the deformation localization under drawdown conditions.

ACKNOWLEDGEMENTS

REFFERENCE

Jia, G., Zhan, L., Chen, Y. (2009). Model Test Study of Slope Instability Induced by Rapid Drawdown of Water Level. *Chinese Journal of Rock Mechanics and Engineering*, 9, 010.

Wang, R., Zhang, G., Zhang, J. M. (2010). Centrifuge modelling of clay slope with montmorillonite weak layer under rainfall conditions. *Applied Clay Science*, 50(3), 386-394.

Zhang, G., Hu, Y., Zhang, J. M. (2009). New image analysis-based displacement-measurement system for geotechnical centrifuge modeling tests. *Measurement*, 42(1), 87-96.

REINFORCEMENT EFFECT OF CHEMICAL GROUTING MATERIAL ON NAIL-REINFOCED SLOPE

Teng Wang, Lv Lin and Ga Zhang
Tsinghua University, China

BRIEF INRODUCTION

Chemical grouting material (CGM) has been broadly applied in the geotechnical engineering, such as foundation treatment and soil slope reinforcement. Whereas, the reinforcement effect of CGM on nail-reinforced slopes has not been sufficiently clarified. Centrifugal modeling is a vital research approach of geotechnical engineering (Zornberg et al. 1998; Sommers and Viswanadham 2009; Wang et al. 2010). However, few centrifuge model tests have been achieved to understand the reinforcement effect of CGM on nail-reinforced slopes. In this paper, centrifuge model tests were performed to study the response of the nail-reinforced slope with the reinforcement of CGM. The reinforcement effect of CGM on deformation and failure of slopes was analyzed on the basis of test observations.

METHODOLOGY

All the tests were conducted on the geotechnical centrifuge at Tsinghua University. The model container used for the tests was made of aluminum alloy, 500 mm in length, 200 mm in width, and 350 mm in height. A vertical loading device was installed at the top of the model container. This device can provide a vertical load on the slope top with a capacity of 10 kN on the loading plate through the shaft, driven by an electric motor and a corresponding reducer (Figure 1(a)). CGM was applied to reinforce the nail-reinforced slope surface in the

| (a) Schematic view | (b) Photograph |
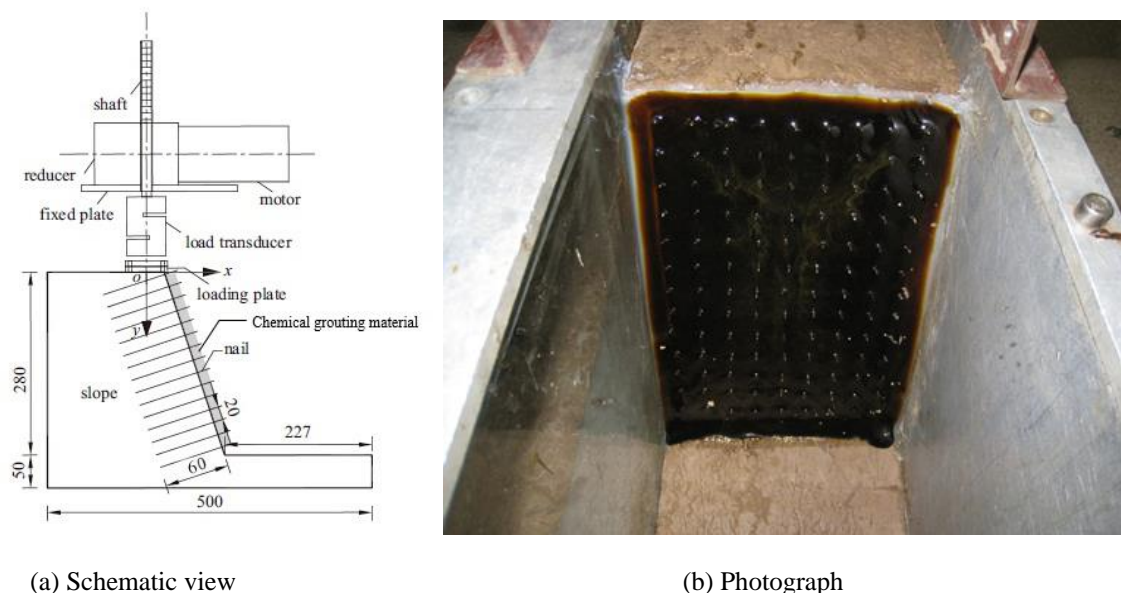
Figure 1: Model slope and device for centrifugal model test.

CGM test (Figure 1(b)) while the slope was only reinforced by nails in the non-CGM test. The other main factors remained the same in all the tests including: (1) the gradient of the slope (Vertical: Horizontal) equalled 3; (2) the nail length was 60 mm; (3) the plastic limit and the liquid limit of the soil were 15.5% and 33.7%, respectively. The dry density and the water content of the soil were controlled around 1.50 g/cm^3 and 17%; (4) the centrifuge acceleration level was maintained at 40 g.

KEY RESULTS

Figure 2 shows the load-settlement relationship of the loading plate on nail-reinforced soil slopes. It can be observed that the load pressure on the loading plate increased with a decreased rate as the settlement of the loading plate increased in both the tests during the initial loading period. For the slope with CGM, the curve appeared gentler when compared with that of the non-CGM slope. The value of loading pressure in the CGM test was larger than that in the non-CGM test when the loading pressure reached a stable stage, which indicates that CGM can increase the bearing capacity of soil slopes.
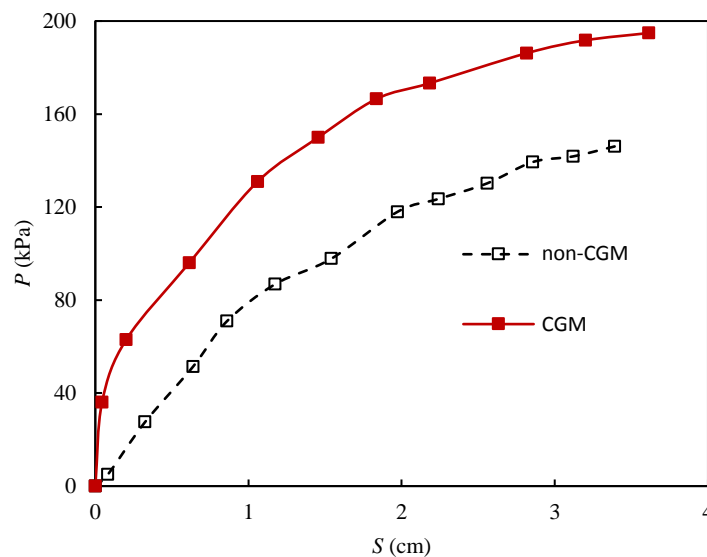
Figure 2: Load-settlement curves for reinforced slopes. *P*, vertical load pressure; *S*, settlement of loading plate.

Figure 3 shows distribution of horizontal displacement of the two types of soil slopes under the same vertical load pressure. It can be seen that the horizontal displacement of the slope with CGM was obviously smaller than that of the non-CGM slope at both the elevations. In addition, there was a rapid increase at a certain range in the middle part of the non-CGM slope, indicating that the failure might have emerged in this region. Meanwhile, the horizontal displacement curve exhibited a slower increase in the CGM test, suggesting that the deformation was not large enough to induce the slope failure.

The horizontal gradient of horizontal displacement of soil slopes which could be used to represent the degree of the deformation localization is exhibited in Figure 4. For the slope with CGM, the degree of deformation localization was evidently smaller than that of the soil slope without CGM. There was no obvious peak of the gradient in the CGM test, which was definitely different from the non-CGM test. This suggests that CGM can retard the emergence and development of deformation localization of the area under the loading plate. Therefore, CGM can improve the stability of soil slopes.

(a) Y=0.25H   (b) Y=0.5H
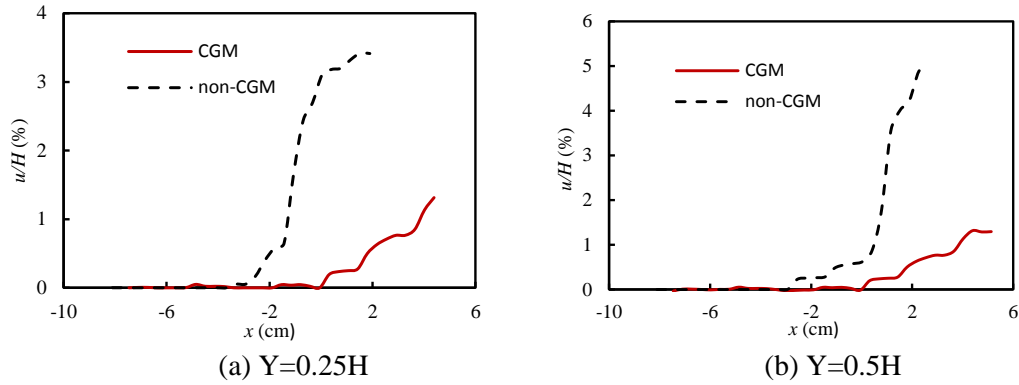
Figure 3: Distribution of horizontal displacement of soil slopes under a vertical load pressure of 120kPa. u, horizontal displacement; H, slope height; Y, vertical distance from the middle point of the loading plate; x, horizontal distance from the middle point of the loading plate.

(a) Y=0.25H   (b) Y=0.5H
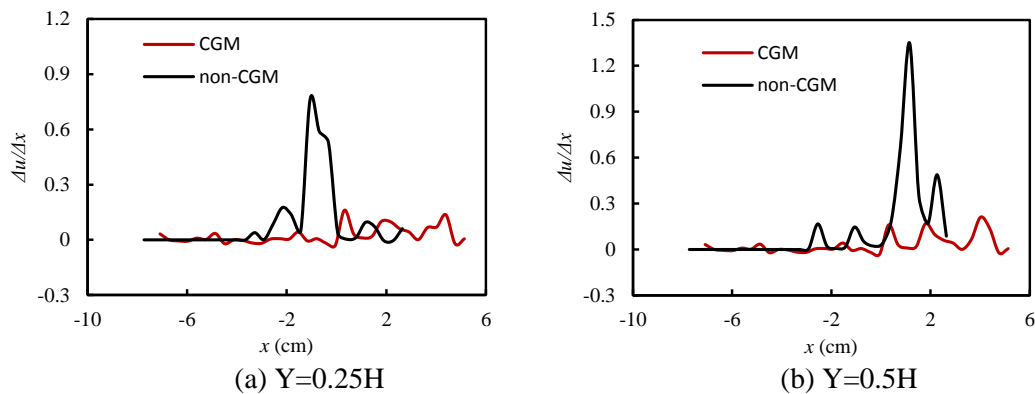
Figure 4: Horizontal strain of soil slopes under a vertical load pressure of 120kPa.

CONCLUSIONS

1. The CGM has a significant reinforcement effect on nail-reinforced soil slopes. The use of CGM can increase the bearing capacity of soil slopes.
2. The CGM reinforcement mechanism could be explained using the coupling of the failure and deformation localization of soil slopes. The CGM delays the development of the deformation localization of soil slopes during loading.

ACKNOWLEDGEMENTS

REFERENCES

Zornberg, J.G., Sitar, N., Mitchell, J.K. (1998). "Performance of geosynthetic reinforced slopes." *Journal Geotechnical and Geoenvironmental Engineering* 124(8), pp. 670-683.

Sommers, A.N., Viswanadham, B.V.S. (2009). "Centrifuge model tests on the behavior of strip footing on geotextile-reinforced slopes." *Geotextiles and Geomembranes* 27, pp. 497-505.

Wang, L.P., Zhang, G., Zhang, J.M. (2010). "Nail reinforcement mechanism of cohesive soil slopes under earthquake conditions." *Soil and Foundations* 50(4), pp. 459-469.

THE EFFECTS OF PARTICLE SHAPE AND INITIAL STATIC SHEAR STRESS ON LIQUEFACTION RESISTANCE OF SILTY SANDS

Xiao Wei and Jun Yang
Department of Civil Engineering, The University of Hong Kong

BRIEF INRODUCTION, METHODOLOGY AND KEY RESULTS

Recent earthquake events revealed that soil liquefaction remains an unsolved issue with uncertainties and difficulties in earthquake geotechnical engineering. For large projects involving earth dams, embankments and slopes, initial static shear stress plays an important role in liquefaction analysis. However, such effects on silty sands remain poorly understood, partially due to a lack of systematic experimental data (Wei and Yang, 2015). Among various factors, particle shape has a significant effect on mechanical behaviours of sands (Yang and Wei, 2012; Yang and Luo, 2015) but is less emphasized in liquefaction analysis.

In order to perform well-controlled experimental study, silty sands were prepared by adding angular crushed silica silt or rounded glass bead into Toyoura sand (TSS and TG, respectively). The two silty fines have similar particle size distribution but distinctly different particle shapes. Undrained cyclic triaxial tests were performed to evaluate liquefaction resistance of the moist-tamped silty sands under systematic combinations of initial static shear stress, void ratios and effective confining pressure.

Selected data are presented in Fig. 1 showing the effects of initial static shear stress ratio (α) on the cyclic resistance ratio (CRR) for different materials. The void ratio after consolidation (e_c) was controlled to be about 0.791 and 0.903, and the initial effective confining pressure (σ_{nc}') was 100 kPa. Clean sand data were extracted from Yang and Sze (2011a). Similar to that of clean Toyoura sand (TS), CRR of both TSS and TG specimens increased with increasing initial static shear stress ratio (α) before crossing the no-reversal line and then decreased with further

Figure 1: Effects of α on the cyclic resistance of silty sands with silts of different shapes

increase of α after crossing the no-reversal line. This indicates that CRR tends to reach a maximum value near the no-reversal line, and thus the concept of threshold of α (α_{th}), proposed by Yang and Sze (2011a) based on clean sand data, may be extended to silty sands. Moreover, the data in Fig. 1 also show that addition of silts decreased CRR of the sand. Particularly, addition of rounded glass bead led to more significant reduction of CRR under otherwise similar conditions.

One of the important features of α_{th} is its state dependency (Yang and Sze, 2011a, b). Fig. 2 shows that α_{th} decreases almost linearly with increasing state parameter (ψ) of Been and

Jefferies (1985). The TSS and TG data fall into the vicinity of the trend line for clean Toyoura sand, which may approximately serve as a unified trend line for all the materials. Detailed inspection of the data suggests that the TG data seem to form the lower boundary of all the data points whereas the TSS data seem to form the upper boundary, which implies the potential influence of particle shape on the $\alpha_{th} - \psi$ correlation.
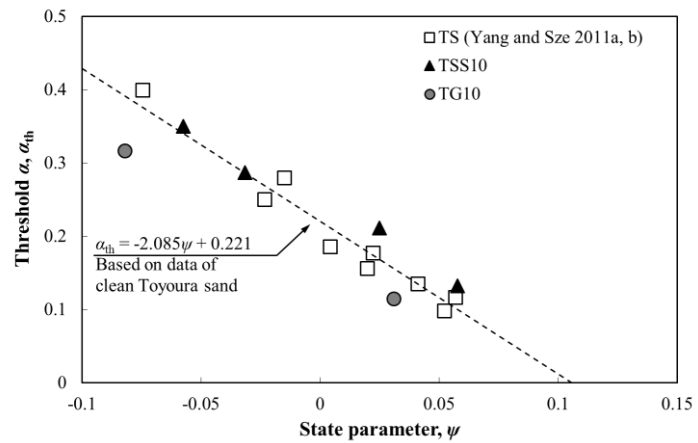
Figure 2: Dependency of α_{th} on the state parameter

CONCLUSIONS

1. A series of undrained cyclic triaxial tests was performed to investigate the combined effects of particle shape and initial static shear stress under various initial states. Addition of silts into clean Toyoura sand led to reduction of cyclic resistance. Such reduction was more significant if rounded silts (glass bead) were added other than angular silts (crushed silica).
2. The concept of threshold α proposed by Yang and Sze (2011a) can be extended to silty sands. The effects of initial shear stress can be either beneficial or detrimental depending on the initial state of the sand. A fairly good unified correlation has been found to exist between threshold α and state parameter for both clean and silty sands tested (TS, TSS and TG specimens), showing that the threshold α decreases with increasing state parameter.

ACKNOWLEDGEMENTS

REFERENCES

Been, K. and Jefferies, M. G. (1985). "A state parameter for sands." *Géotechnique* 35, No. 2, pp. 99-112.

Wei, X. and Yang, J. (2015). "The effects of initial static shear stress on liquefaction resistance of silty sand." In *Proc. 6th Int. Conf. Earthq. Geotech. Eng.*, Christchurch, N. Z., No. 145.

Yang, J. and Luo, X. D. (2015). "Exploring the relationship between critical state and particle shape for granular materials." *J. Mech. Phys. Solids.* 84, pp. 196-213.

Yang, J. and Sze, H. Y. (2011a). "Cyclic behaviour and resistance of saturated sand under non-symmetrical loading conditions." *Géotechnique* 61, No. 1, pp. 59-73.

Yang, J. and Sze, H. Y. (2011b). "Cyclic strength of sand under sustained shear stress." *J. Geotech. Geoenviron. Eng.* 137, No. 12, pp.1275-1285.

Yang, J. and Wei, L. M. (2012). "Collapse of loose sand with the addition of fines: the role of particle shape." *Géotechnique* 62, No. 12, pp. 1111-1125.

DEM SIMULATION OF SAND BEHAVIORS UNDER MULTI-DIRECTIONAL LOADING

Jiangtao Wei and Gang Wang
The Hong Kong University of Science and Technology, HKSAR

BRIEF INRODUCTION, METHODOLOGY AND KEY RESULTS

During earthquake shaking, the shear wave propagated through the ground is essentially irregular. As a consequence, cyclic load applied on the soil element is multi-directional, which involves variation in both loading direction and loading amplitude. In practice, uni-directional cyclic simple shear tests or triaxial tests are usually performed in laboratory or by numerical simulation to study cyclic behaviors of sands. The influence of loading direction variation to sand behaviors is often ignored. In laboratory, bi-directional simple shear device was designed and applied to conduct multidirectional loading. The laboratory tests found that both excess pore water pressure and shear deformation would increase faster under multi-directional loading compared with the uni-axial loading.

In this study, discrete element method is used to conduct numerical test and explore the evolution of fabric during multi-directional loading. In the numerical simulation, a sand packing made by spherical particles under a confining pressure is firstly prepared, as shown in Fig. 1(a). The packing is then subjected to an undrained multi-directional cyclic simple shear test as shown in Fig. 1(b). In the test, shear stress is decomposed into two components acting along mutually perpendicular directions. The two components are denoted by τ_x and τ_y, respectively. The amplitude of the shear stress vary with time according to the follows:

$$\tau_x = \tau_1 \cos(\omega_1 t) \tag{1}$$

$$\tau_y = \tau_2 \cos(\omega_2 t + \varphi) \tag{2}$$

where ω_1 and ω_2 are the angular frequency of cyclic loading along two directions. τ_1 and τ_2 are the cyclic shear stresses along x and y directions. φ is the phase lag.
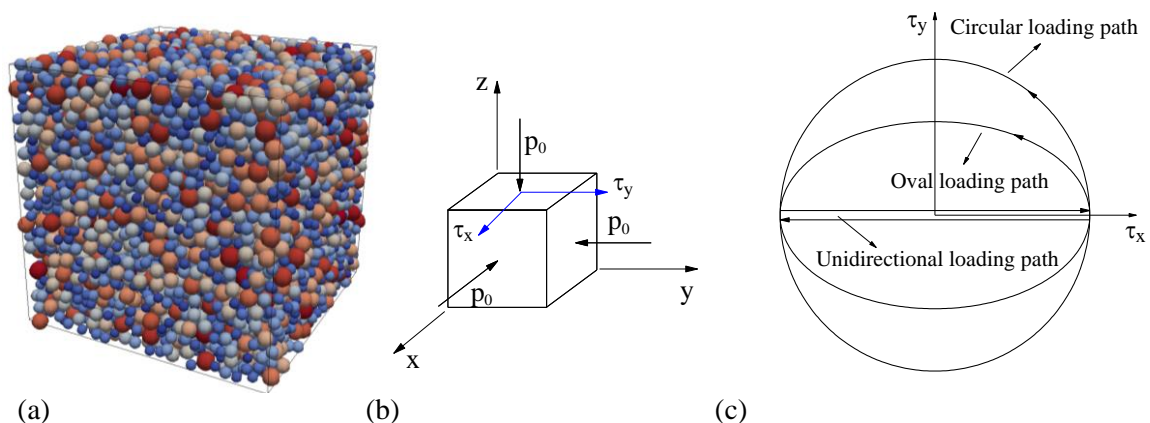
Figure 1: (a) Granular packing in simulation; (b) Stress state of granular packing after consolidation; (c) Different loading paths in simulation.

A variety of loading paths can be obtained using the above equations. In our numerical simulation, three typical loading paths are selected: uni-directional loading, oval and circular loading, which are consistent with laboratory tests by Kammerer *et al.* (2005). For the uni-directional loading, one component of shear stress is reduced to zero ($\tau_2 = 0$). In the oval loading path, $\omega_1 = \omega_2$ and $\varphi = -\pi/2$. The circular loading path is one special case of the oval loading if $\tau_1 = \tau_2$. These loading paths are schematically illustrated in Fig. 1(c). Note that shear stress along x direction for all loading conditions remains the same in our study. With two shear stress components τ_x and τ_y, the effective stress tensor can be expressed as:

$$\sigma'_{ij} = \begin{bmatrix} p' & 0 & \tau_x \\ 0 & p' & \tau_y \\ \tau_x & \tau_y & p' \end{bmatrix} \tag{3}$$

The DEM simulations of sands under a circular loading path are presented in Fig 2. The granular packing is a medium-dense sand consolidated under initial confining pressure of p_0=100kPa. Fig. 2(a) is the effective stress path ($\tau = \sqrt{\tau_x^2 + \tau_y^2}$). The cyclic stress ratio CSR=0.25 in both directions. Fig. 2 (b) is the development of excess pore water pressure as the number of loading cycle increases. Figs. 2(c) and (d) demonstrate circular-shaped shear stress path and the corresponding shear strain evolution. These macro behaviors are qualitatively similar to the laboratory observations. Excess pore water pressure gradually decreases in accompany with the increase of shear strain amplitude. In the uni-directional loading tests, the effective stress decreases to zero when initial liquefaction occurs (Wang and Wei, 2016). However, for the oval/circular loading tests, as shown in Fig. 2(a), the effective stress approaches the critical state line (CSL) instead of zero. As a result, the excess pore water pressure is always lower than initial confining pressure. This result is consistent with findings from laboratory tests (Ishihara and Yamazaki, 1980; Kammerer *et al.*, 2005).
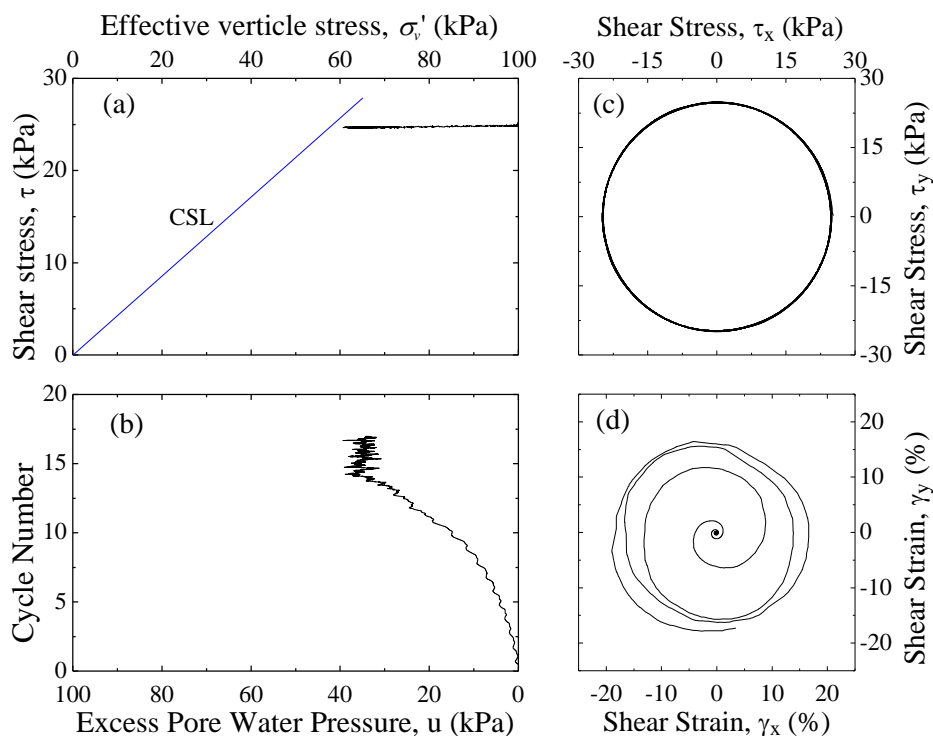
Figure 2: The macro behaviors of granular packing under circular loading path
($CSR_x = CSR_y = 0.25$)

Coordination number and contact-based fabric tensor are employed to quantify the internal structure of granular packing. Coordination number, defined as the ratio between total contact number and total particle number ($Z=2N_c/N_p$), describes the average number of contact for each particle. Contact-based fabric tensor adopted here is a second order tensor that constructed by the following equation:

$$\phi_{ij} = \frac{1}{N_c} \sum_{k=1}^{N_c} n_i^{(k)} n_j^{(k)} \tag{4}$$

where **n** is the contact normal. It can been verified from simulation results that the diagonal components ϕ_{xx}, ϕ_{yy} and ϕ_{zz} are close to 1/3 and variation of off-diagonal components ϕ_{xy} is negligible compared with ϕ_{zx} and ϕ_{zy}. Therefore, the contact-based fabric tensor ϕ_{ij} during cyclic loading can be approximated as

$$\phi_{ij} = \begin{bmatrix} 1/3 & 0 & \phi_{xz} \\ 0 & 1/3 & \phi_{yz} \\ \phi_{zx} & \phi_{zy} & 1/3 \end{bmatrix} \tag{5}$$

Therefore, the anisotropy degree of the tensor (Guo and Zhao, 2013) becomes:

$$a = 7.5\sqrt{3}\sqrt{\phi_{zx}^2 + \phi_{zy}^2} \tag{6}$$

Principal direction of tensor can be obtained by eigenvalue analysis. Note the stress tensor in Eq. (3) and fabric tensor in Eq. (5) have similar form. Their major principal directions are:

$$\mathbf{n} = (\sin\alpha\cos\beta, \sin\alpha\sin\beta, \cos\alpha) \tag{7}$$

where $\alpha = 45°$ (the angle between **n** and vertical direction). β is the angel between the projection vector of **n** on the horizontal plane (xy plane) and x axis. $\tan\beta_\sigma = \tau_y / \tau_x$ for the stress tensor and $\tan\beta_\phi = \phi_{zy} / \phi_{zx}$ for the fabric tensor. Therefore, the principal direction of stress tensor (and fabric tensor) can be simply represented by a single parameter β. Figure 3 shows the evolution of the principal direction of the stress tensor and fabric tensor under circular loading. These two directions virtually coincide.
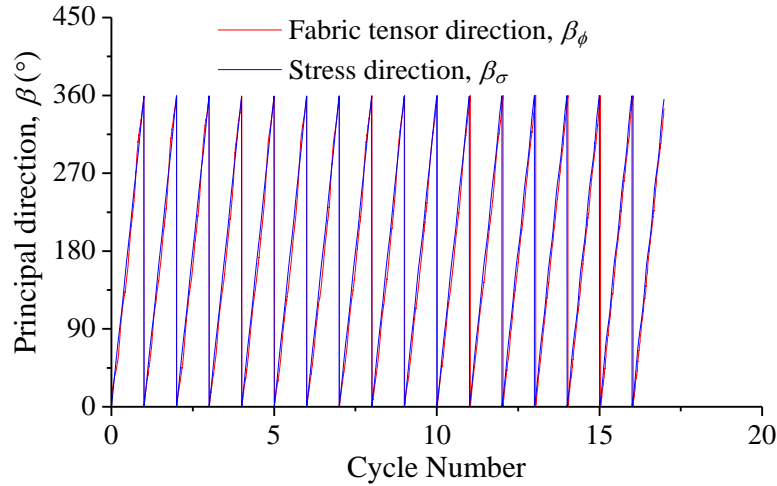
Figure 3: Evolution of principal direction of stress and fabric tensor under circular loading path.

During the circular loading, the evolution of anisotropy degree a and coordination number are plotted in Fig. 4. For easy comparison, the effective stress is also plotted beneath it.
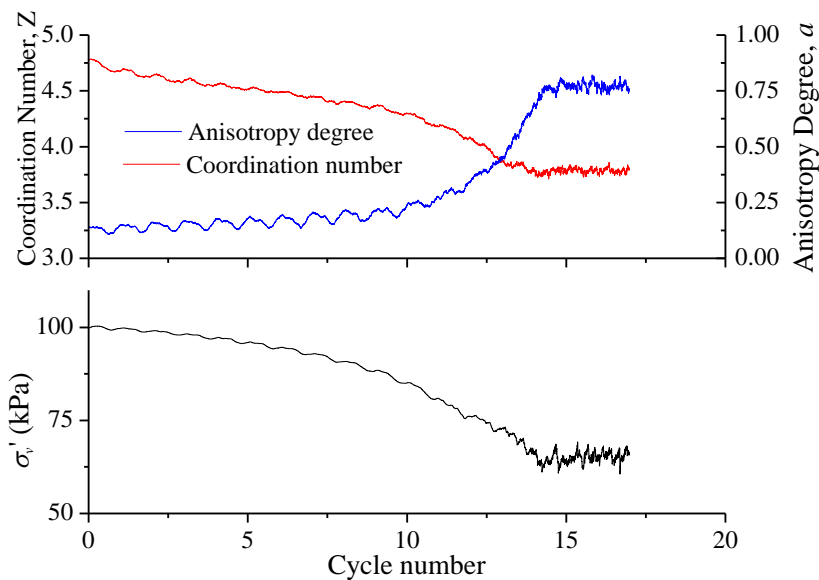
Figure 4: Evolution of coordination number and anisotropy degree under circular loading path

CONCLUSIONS

1. Sand behaviours during multi-directional loading were explored using DEM simulation. The simulation results are qualitatively similar to the laboratory observations. For rotational loading test, large shear deformation would be induced without occurrence of zero effective stress.
2. As shown in Fig. 4, when effective stress decreases, coordination number of the packing gradually decreases and the anisotropy degree increases. Both the coordination number and anisotropy degree will finally get stabilized without much change when the number of loading cycle further increases. At the same time, the effective stress reaches a minimum value approaching the critical state line. Evolution of the principal direction of fabric is almost identical to that of the principal stress.

REFERENCES

Guo, N., and Zhao, J. (2013). "The signature of shear-induced anisotropy in granular media". *Computers and Geotechnics*, 47, pp. 1-15.

Ishihara, K., and Yamazaki, F. (1980). "Cyclic simple shear tests on saturated sand in multi-directional loading." *Soils and Foundations*, 20(1), pp. 45-59.

Kammerer, A. M., Pestana, J. M., and Seed, R. B. (2005). "Behavior of Monterey 0/30 sand under multidirectional loading conditions". *In Geomechanics: Testing, Modeling, and Simulation*. pp. 154-173.

Oda, M. (1982). "Fabric Tensor for Discontinuous Geological Materials". *Soils and Foundations*. 22(4), pp. 96-108.

Wang, G., and Wei, J. (2016). "Microstructure evolution of granular soils in cyclic mobility and post-liquefaction process". *Granular Matter*, 18(3), pp. 1-13.

CYCLIC DEGRADATION AND NON-COAXIALITY OF SATURATED CLAY SUBJECTED TO CYCLIC PRINCIPAL STRESS ROTATION

Zibo Du and Jiangu Qian
Department of Geotechnical Engineering, Tongji University, Shanghai 200092, China
Key Laboratory of Geotechnical and Underground Engineering of Ministry of Education,
Tongji University, Shanghai 200092, China

BRIEF INRODUCTION, METHODOLOGY AND KEY RESULTS

Dynamic loads, such as wave loadings, earthquakes, and traffic loadings, will cause cyclic principal stress rotation (PSR) in soils (Ishihara 1983). This class of dynamic loads produce complicated deformation responses such as non-coaxiality, called non-coincidence of principal directions between stress and strain increment. In essence, non-coaxiality is triggered by PSR in anisotropic soil (Qian *et al.* 2013). Although previous experimental studies in granular soils under PSR have been carried out by many researchers (Ishihara and Towhata 1983; Yang et al. 2007; Tong et al. 2010), non-coaxiality under cyclic PSR remains unclear and need be further explored for saturated clay.

The test equipment TJ-5Hz hollow cylinder apparatus (HCA) at Tongji University was used to investigate cyclic responses of Shanghai clay under three distinct types of dynamic loads, as illustrated in Figure 1. The standard sample size in TJ-5Hz HCA is outer radii r_o=50mm, inner radii r_i=30mm, and height H=200mm. The soil (Shanghai clay) samples were obtained from a deep excavation site located 15m below ground surface. The physical properties of in-situ clay tested in laboratory are given by: natural water content w_n=38.4%, plasticity index I_P=18.2, liquidity index I_L=0.99, specific gravity G_s=2.75 and initial void ratio e_0=1.060. Pre-consolidation pressure p_c was about 148.6 kPa based on a set of oedometer tests.

50kPa back-pressure was applied to achieve Skempton's pore pressure coefficient B-value >0.96. Isotropic consolidation was first performed and subsequently deviatoric stress is applied under drained condition to a desired level so that specimen was anisotropically consolidated. Eventually, different designed cyclic deviatoric stress paths with and without PSR was commenced under undrained condition.

The stress path in the $\tau_{z\theta}$-$(\sigma_z-\sigma_\theta)/2$ plane is shown in Fig. 1. The first series without PSR was shown in Fig. 1(a), b, p and α_σ were kept constant, and only q varied (C-B-C). The
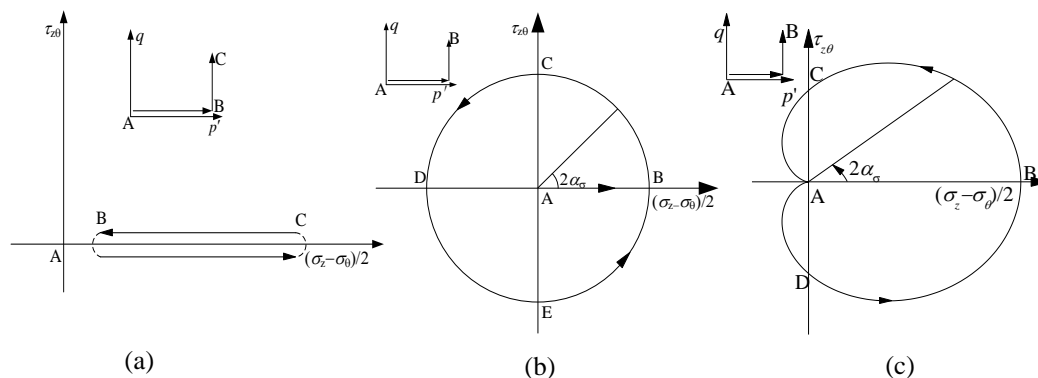
Fig.1. Stress path in deviatoric stress space: (a) test path without PSR; (b) pure principal stress rotation; (c) coupled loading with varying deviatoric stress and PSR

second test group was tested under pure principal stress rotation, as shown in Fig. 1(b), where p, b, and q were maintained constant, and only the directions of the principal stresses were rotated (B-C-D-E-B). The third stress path was shown in Fig. 1(c). The specimen were subjected to principal stress rotation as well as variation of deviatoric stress (B-C-D-B), while the intermediate principal stress parameter b and the mean total stress p were kept constant. In general, the stress paths given in Fig. 1(b) and Fig. 1(c) with PSR were used to simulate cyclic loading induced by wave loadings and traffic loadings, respectively (Ishihara, 1983). In total, 6 groups of undrained tests were conducted. According to the stress paths, all tests were divided into three series, as listed in Table 1.

Fig. 2 shows the variation of stiffness ratio G_j/G_1 with the number of cycles, where G_j is the secant modulus in the jth cycle of normal differential stress–strain curve,

Table 1. Test program

Test number		p' (kPa)	q (kPa)	b	α_σ (°)
Series I (no PSR)	TL05-1	150	4~30	0.5	0
	TH05-1	150	8~60	0.5	0
Series II (PSR & constant q)	RL05-2	150	30	0.5	0~1260
	RH05-2	150	60	0.5	0~720
Series III (PSR & varying q)	CL05-3	150	4~30	0.5	0~2160
	CH05-3	150	8~60	0.5	0~2160

respectively. The degradations of stiffness with PSR are much different from those without PSR. At a lower deviatoric stress as presented in Fig. 2(a), the stiffness for three cyclic loadings coincidently experience a slight hardening in the first 2 cycles and then remains approximately constant in subsequent cycles. However, hardening effects with PSR are more pronounced than that without PSR. On the other hand, at a higher level of q as shown in Fig. 2(b), nearly constant stiffness remains during cyclic loading without PSR. In contrast, significant stiffness degradations are observed for cyclic loading with PSR. One should note that cyclic pure PSR (Series II) results in more pronounced degradation of stiffness than cyclic coupled loading (Series III).

Figs. 3 and 4 compare non-coaxiality between cyclic loadings of series II and series III in the 1st cycle. Keep in mind deviation of strain increment indicates from outwards normal vector indicates its non-coaxiality (non-coincidence) from major principal stress, whose direction points along outwards normal vector. Non-coaxiality changes significantly in different sections of PSR path. It is clear that with increasing shear stress $\tau_{z\theta}$, non-coaxiality becomes weaker as the magnitude of strain increment is increasing, due primarily to

(a)

(b)

Fig. 2 The effects of PSR on variation of stiffness ratio G_j/G_1 (a) low deviatoric stress level; (b) high deviatoric stress level

the growing part of coaxial strain increment relative to total strain increment. Inversely, as $\tau_{z\theta}$ is decreased, coaxiality becomes stronger and the magnitude of strain increment is reducing. In addition, non-coaxiality significantly depends on the level of deviatoric stress. In addition, non-coaxiality tends to be weaker as the level of deviatoric stress increases. Eventually, comparison between Fig.2 and Fig.3 shows that non-coaxiality is more significant in the coupled loading (i.e., PSR and varying q) than pure PSR loading, although they share the same magnitude of peak deviatoric stress.

Fig. 3. Stress path and strain increment vector for test series II: (a) RL05-2; (b) RH05-2
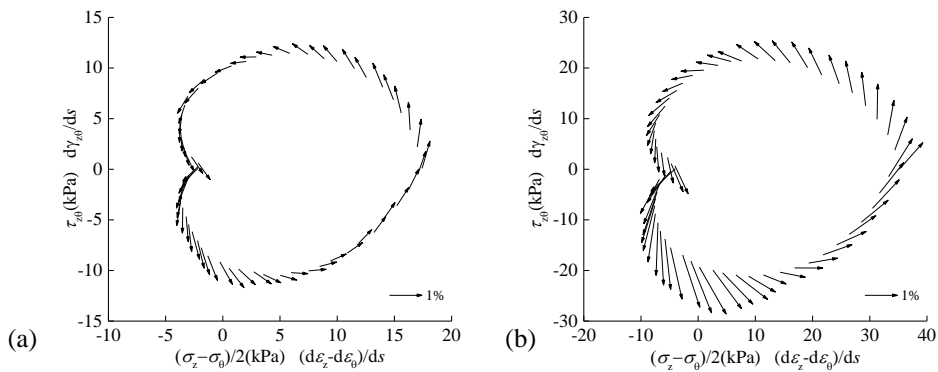
Fig. 4. Stress path and strain increment vector for test series III: (a) CL05-3; (b) CH05-3

CONCLUSIONS

1. Principal stress rotation (PSR) has a considerable weakening effect on the stiffness under cyclic loading. Among three dynamic loading manners, cyclic loading without PSR hardly produces any degradation of stiffness. As the levels of deviatoric stress increase, significant stiffness degradations are observed when PSR is involved.

2. PSR induces apparent non-coaxiality, which depends on the varying level of shear stress component as well as that of deviatoric stress. The degree of non-coaxiality is reducing as the magnitudes of shear stress component and deviatoric stress are increasing.

ACKNOWLEDGEMENTS

REFERENCES

Ishihara, K. "Soil response in cyclic loading induced by earthquakes, traffic and waves." *Proc. 7th Asian Reg. Conf. on Soil Mechanics and Foundation Engineering*, pp. 42–66.

Ishihara, K., and Towhata, K. (1983). "Sand response to cyclic rotation of principal stress directions as induced by wave loads." *Soils Found.*, 23, No. 4, pp. 11–26.

Qian, J., You, Z., Huang, M., and Gu, X. (2013). "A micromechanics-based model for estimating localized failure with effects of fabric anisotropy." *Comput. Geotech.*, 50, No. 3, pp. 90–100.

Tong Z. X., Zhang J. M., Yu Y. L., and Zhang G. (2010). "Drained deformation behavior of anisotropic sands during cyclic rotation of principal stress axes." *J. Geotech. Geoenviron. Eng.*, 136, No. 11, pp. 1509–1518

Yang, Z. X., Li, X. S., and Yang, J. (2007). "Undrained anisotropy and rotational shear in granular soil." *Geotechnique*, 57, No. 4, pp. 371–384.

COMPARATIVE ANALYSIS OF SEISMIC RESPONSE OF CONVENTIONAL AND COLUMN-FREE SUBWAY STATION

Ting-jin Liu*[+], Yue-yu Zheng*, Wen-bo Li*, Xin-wei Tang*[+]
* School of Civil Engineering and Transportation, South China University of Technology, Guangzhou, China
[+]State Key Laboratory of Subtropical Architecture Science, Guangzhou, China

BRIEF INTRODUCTION, METHODOLOGY AND KEY RESULTS

Restricted by surrounding soils and rocks, underground structure performed better in earthquake than floor structure. However, due to the difficulties in underground structure's restoration after earthquake and lessons from Hanshin earthquake, researchers had studied on mechanism of seismic damage and influencing factors. But aforementioned studies were mainly concentrated on conventional subway station compared with column-free subway station.

To evaluate the similarities and differences of seismic response properties between conventional and column-free subway station structures, ABAQUS was applied to simulate the horizontal nonlinear seismic response of these two structures. The response characteristics of these two types of structures under three seismic waves with diverse PGAs (0.10g, 0.20g, 0.40g) were compared and analyzed.

The results indicate that these two types of station structures had similar seismic response patterns and would both be severely damage under strong earthquake. Besides the connections between lateral wall and roof/base slab, the central column of conventional station and the base slab of column-free station were also the weak areas during vibration, which should be seriously considered in seismic design. The maximum relative horizontal displacement between roof and base slab had a linear increasing relationship with PGA of input seismic wave, and closely depends on its spectrum characteristics(Figure 1). In the

Figure 1: Maximum relative horizontal displacement between top and base plate of subway station

process of ground motion, unidirectional residual deformation was accumulated. The deformation along the height of lateral wall after earthquake was wavelike and its ultimate swing direction was consistent with the maximum amplitude (Figure 2). The acceleration time-histories of two structures had analogous forms and showed amplification effect significantly to input seismic waves of bedrock.

Figure 2: The residual deformation distribution curves along the lateral wall of subway station under PGA=0.4g Kobe ground motions

CONCLUSIONS

1. Both conventional and column-free subway station would be severely damaged under strong earthquake. And members' connections were the weak area, especially the connection between column and roof/base slab, lateral wall and top/base plate. Compared with conventional subway station, the base slab in column-free subway station had obvious damage and should be reinforced in design. However, the top plate performed better.
2. The maximum relative horizontal displacement between roof and base slab in both different types had a linear increasing relationship with PGA of input seismic wave and closely depended on its spectrum characteristics. Besides, the moment of maximum swing, the swing direction and displacement rule were nearly the same.
3. In the process of ground motion, unidirectional residual deformation in two different subway station types were accumulated and the rules were similar. The deformation along the height of lateral wall after earthquake was wavelike and its ultimate swing direction was consistent with the maximum amplitude. Sublayer of lateral wall had severer plastic damage than upper layer.
4. The acceleration time-histories of two structures' base slab had analogous forms and showed amplification effect significantly to input seismic waves of bedrock and roof slab was more obvious than base slab.

REFERENCES

Yang L. Recommendations on Seismic Design of Tunnels and Underground Structures[J]. Tunnel Construction, 2013, 09:707-714.

ZHUANG Hai-Yang, WANG Xiu-xing, CHEN Guo-xing. Earthquake responses of subway station with different depths of soft soil[J]. Chinese Journal of Geotechnical Engineering, 2009, 08:1258-1266.

XU Long-jun, XIE Li-Li, HU Jin-Jun. Analysis on engineering characteristics of sub-ground motions[J]. Chinese Journal of Geotechnical Engineering, 2006, 09:1106-1111.

CHEN Su, CHEN Guo-xing, QI Cheng-zhi, et al. A shaking table-based experimental study of seismic response of three-arch type's underground subway station in liquefiable ground [J]. Rock & Soil Mechanics, 2015, 07:1899-1914.2012.

Sang-Hyeok Nam, Ha-Won Song, Keun-Joo Byun, Koichi Maekawa. Seismic analysis of underground reinforced concrete structures considering elasto-plastic interface element with thickness. Engineering Structures, 2006. 28: 1122-1131.

ZHUANG Hai-Yang, CHENG Shao-ge, CHEN Guo-xing. Numerical simulation and analysis of earthquake damages of Dakai metro station caused by Kobe earthquake[J]. Rock & Soil Mechanics, 2008, 01:245-250.

Chen Lei, Chen Guo-xing, Chen Su, LOUNG Hui. 3D Refined Nonlinear Analysis on Seismic Responses of Three-arch and Two-column Subway Station Structure[J]. Journal of the China Railway Society, 2012, 11:100-107.

Xia Chen, Zhao Boming, Wang Zijun, Sun Fengbo. A study on affecting factors of seismically induced drift of subway station[J]. china Civil Engineering Journal, 2015, S1:132-136.

Zhong Bobo, Zhang Yongbin, Li Hong. Analysis of Seismic Response of Large-span Column-free Subway Station[J]. Chinese Journal of Underground Space and Engineering, 2015, S1:317-322.

LIU Jing-bo, GU Yin, DU Yi-xin. Consistent viscous-spring artificial boundaries and viscous-spring boundary elements. [J]. Chinese Journal of Geotechnical Engineering, 2006, 09:1070-1075.

ZHUANG Hai-Yang, LONG Hui, CHEN Guo-xing. Analysis of the nonlinear earthquake responses of a large complicated subway underground station[J]. Journal of Earthquake Engineering and Engineering Vibration, 2013, 02:192-199.

ZHUANG Hai-Yang, CHEN Guo-xing, Hu Xiaoming. Analysis of nonlinear earthquake response of two-layer double-column subway station structure. Chinese Journal of Rock Mechanics and Engineering, 2006,S1:3074-3079.

Chen Lei, CHEN Guo-xing, MAO Kung-ming. 3D refined nonlinear analysis of seismic response characteristics of frame metro station under near-field strong ground motion of large earthquake[J]. Chinese Journal of Geotechnical Engineering, 2012, 03:490-496.

Iida H., Hiroto T., Yoshida, N., Iwafuji, M. Damage to Dakai Subway Station[J]. Special Issue of Soils and Foundation, JSCE. Jan. 1996: 283-300.

ANALYSIS OF THE EFFECT OF SOIL-STRUCTURE INTERACTION ON LIQUEFACTION RESISTANCE

S. Montoya-Noguera*[+], F. Lopez-Caballero*
* MSSMat CNRS UMR 8579 laboratory, CentraleSupélec, Paris-Saclay University,
Châtenay-Malabry, France
[+] Current address: Department of Architecture and Civil Engineering, City University of
Hong Kong, Tat Chee Avenue, Kowloon, Hong Kong

BRIEF INRODUCTION, METHODOLOGY AND KEY RESULTS

With the current outburst in numerical tools, seismic design analysis has focused on nonlinear structure behavior while the foundation soil behavior is often simplified by a modification of the input acceleration depending on the expected site effects. When taking into account nonlinear soil behavior, the isolation of structure and soil is no longer valid and nonlinear soil-structure interaction has to be taken into account (Mylonakis and Gazetas, 2000). This means that the structure will be influenced by the soil, but also, that the soil will be affected by the structure. Additionally, when the soil is loose and saturated additional nonlinearity has been observed due to seismic liquefaction (Montoya-Noguera and Lopez-Caballero, 2016). In such cases, more robust models are needed to accurately describe the generation, redistribution and dissipation of excess pore pressure during and after earthquakes. Findings presented in this work illustrate the importance of accounting for both soil nonlinearity and for soil-structure interaction.

Evidently, the structure's weight affects the stress state (horizontal, vertical and shear) and also the volumetric deformations on the soil deposit. As the coefficient of earth pressure at rest (k_0) also increases with the building load, the surrounding soil is stiffened but without the effect of the shear stress. Thus the soil on this region will present higher liquefaction resistance. The initial effect of the structure on the soil deposit will depend on the total weight and its distribution through the foundation base. However, the overall effect of the structure on liquefaction and its consequences depends also on the seismic hazard. To account for both factors, two different structures and a wide range of real seismic motions were tested in a 2D finite element model with fully coupled effective stress analysis (Aubry et al., 1982; Hujeux, 1985; and Modaressi, 1987). Both the soil and the structure were modeled with nonlinear behavior and a modified width plane-strain condition is used to account for the interaction effects between the soil and the structure (Saez et al., 2013). For further details on the model used please refer to Lopez-Caballero and Modaressi (2011) and Montoya-Noguera (2016).

The spatial distribution of the liquefaction ratio at the end of shaking ($r_u = \Delta p_w / \sigma'_0$) is affected by the structure's influence on the stress state prior to the dynamic loading, as seen in Figure 1 for two different structures subjected to the same input motion. It can be noted that although the same soil properties are used throughout the deposit, due to the increase in mean stress and the stress ratio difference, pore pressure generation appears heterogeneously in the deposit. The effect of the structure on liquefaction will depend on the structure's properties as well as the seismic loading. For the two-story building in Figure 1a, the structure's effect is mild and is detrimental compared to free-field. In contrast, the higher influence of the three-story building in Figure 1b will cause a pore pressure migration from

below the structure to the surrounding. As the soil under the structure is stiffened, liquefaction (i.e. r_u near 1.0) is not presented there; however, around this area and due to the differences in the stress state, high r_u values appear beyond the structure's influence. The Q index, introduced by Shinozuka and Ohtomo (1989), is commonly used to quantify liquefaction on the deposit. Applied to a 2D model, it is a spatial average of r_u in a specific area. It can be seen in Figure 1 how the choice of this area will affect the result.
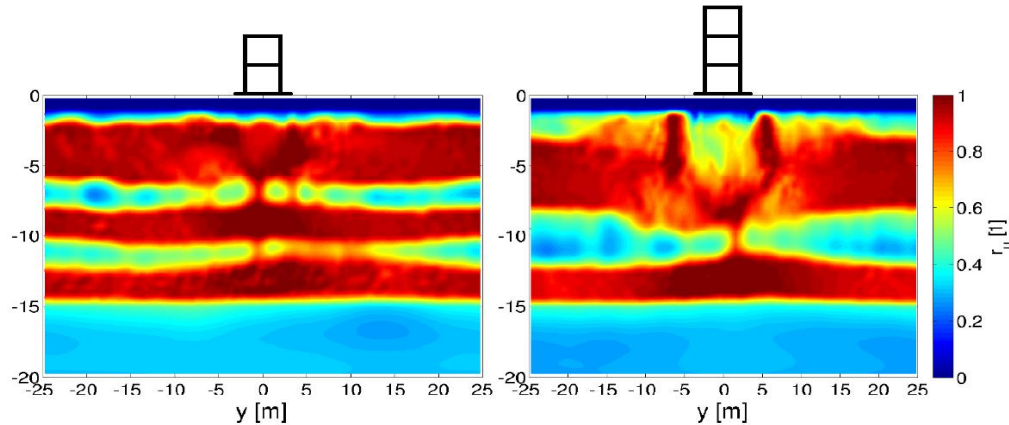
Figure 1: Liquefaction ratio at the end of shaking for a) a two-story and b) a three-story building.

To compare the different motions tested, two areas are used to evaluate the Q index and the results of the models with the structures (w/ str) are compared with a 2D model without structure (w/o str) in Figure 2. For almost all motions tested, the Q index for the entire model is increased when either of the structures is used and it is higher for the heavier structure. When only a small area is evaluated, the response varies greatly; therefore the need to accurately define the liquefiable susceptible area.
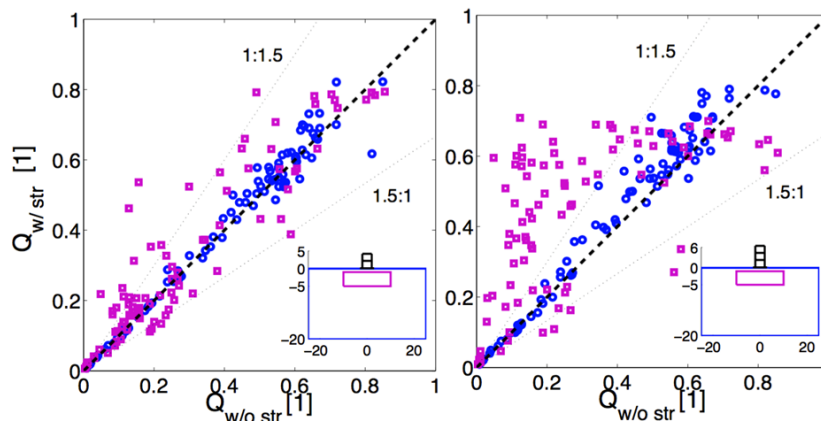
Figure 2: Structure effect on the Q index for a) a two-story and b) a three-story building. Comparison with structure (w/ str) and without (w/o str). The colors correspond to the size of the area depicted on the schema.

CONCLUSIONS

A finite element analysis was used to investigate the effect of soil-structure interaction on seismic liquefaction. Two structures were subjected to 90 unscaled earthquake motions. The use of nonlinear fully coupled soil models were proofed to be important in order to accurately evaluate liquefaction evolution and improve performance-based earthquake engineering (PBEE).

The effect of the structure on the soil can be observed on the increase on pore-pressure generation throughout the deposit with the structure's weight but also, and most importantly,

139

on the differences in its spatial distribution, especially when SSI effects are important which will affect the final failure mode of the main structure and the surrounding ones. The combined effect of input ground motion, nonlinear soil and nonlinear structure behavior makes the task of predicting the seismic performance very difficult. Hence for more realistic models with SSI both the structure and the soil nonlinearity should be taken into account.

Liquefaction evolution is shown to be very complex and while only the state at the end of shaking is shown here, the differences within the 2D model can be due to the motion's frequency evolution with time and the consequently pore-pressure migration and differential settlements. Thus, the overall effects of SSI in both soil and structure could be further evaluated for varying types of soils and structures in order to increase the reliability of the results. In addition to the SSI effects on the soil, the performance risk analysis could be further enriched comprehending the evaluation of damage and failure on the structure.

ACKNOWLEDGEMENTS

REFERENCES

Aubry, D., Hujeux, J.C., Lassoudiere, F. and Meimon, Y. (1982): "A double memory model with multiple mechanisms for cyclic soil behaviour". In *International Symposium on Numerical Modeling in Geomechanics*, pages 3– 13, Balkema ed.

Hujeux, J.C. (1985): "Une loi de comportement pour le chargement cyclique des sols". In *Génie Parasismique*, pages 278–302, France. Presses ENPC. Edited by V. Davidovici.

Lopez-Caballero, F. and Modaressi, A. (2011): "Numerical analysis: Specification and validation of used numerical methods". FP7-SME-2010-1-262161, *PREMISERI project*, Paris, France.

Modaressi, H. (1987): "Modélisation numérique de la propagation des ondes dans les milieux poreux anélastiques". PhD thesis. *LMSSMat, Ecole Centrale Paris*, Châtenay-Malabry, France.

Montoya-Noguera, S. and Lopez-Caballero, F. (2016): "Effect of coupling excess pore pressure and deformation on nonlinear seismic soil response". *Acta Geotechnica*, 11(1):191– 207, February.

Montoya-Noguera, S. (2016): "Assessment and mitigation of liquefaction seismic risk: Numerical modeling of their effects on SSI". PhD thesis. *MSSMat CNR UMR 8579 laboratory, CentraleSupélec, Paris-Saclay University*, Châtenay-Malabry, France.

Mylonakis, G. and Gazetas, G. (2000): "Seismic soil-structure interaction: beneficial or detrimental?" *Journal of Earthquake Engineering*, 4(3): 277–301.

Saez, E., Lopez-Caballero, F., and Modaressi-Farahmand-Razavi, A. (2013): "Inelastic dynamic soil-structure interaction effects on moment resisting frame buildings". *Engineering structures*, 51(1): 166–177.

Shinozuka, M. and Ohtomo, K. (1989): "Spatial severity of liquefaction". In *Proceedings of the 2nd US-Japan workshop in liquefaction, large ground deformation and their effects on lifelines*, 193–206, New York.

PROBABILISTIC LIQUEFACTION SEVERITY ASSESSMENT

C.W. Fu, Y. Wang and K. Huang
Department of Architecture and Civil Engineering, City University of Hong Kong, Tat Chee
Avenue, Kowloon, Hong Kong

INRODUCTION

Soil liquefaction refers to a phenomenon of transforming a granular material from a solid to a liquefied state due to the increased pore pressure and reduced effective stress (e.g., Youd et al. 2001; Cetin et al. 2002). Cone penetration test (CPT) is widely used as a tool to assess the liquefaction potential of soils. Whether or not the soils liquefy is determined by the seismic loading and resistance, which are expressed as cyclic stress ratio, CSR, and cyclic resistance ratio, CRR, respectively. Factor of safety, FS = CRR/CSR, is utilized to measure the liquefaction potential of soils. No liquefaction is expected to occur when FS > 1, and liquefaction is predicted if FS ≤ 1. Since the calculation models for estimating CRR and CSR were mainly developed from past observations and engineering experience (e.g., Seed and Idriss 1971; Robertson and Wride 1998; Juang et al. 2003), various uncertainties (e.g., measurement error, uncertainty in the model) should be considered for liquefaction assessment (e.g., Toprak et al. 1999; Juang et al. 2002). Furthermore, the spatial correlation of soil properties at different depths is ignored in the assessment.

In addition, the severity of liquefaction has attracted increasing research attentions (e.g., Iwasaki et al. 1982; Toprak and Holzer 2003). Since the liquefaction severity in these studies mainly relies on the thickness of the liquefiable soil layers, an important issue in the liquefaction severity assessment is how to properly determine the thicknesses of liquefiable soil layers, particularly when using the scattered test results from CPT.

This paper aims to develop a probabilistic approach to identify liquefiable soil layers and assess the liquefiable soil thickness using CPT, considering the spatial variability of CRR, the model uncertainty associated with the CPT-based RW method, and input parameter uncertainty in CSR calculation.

PROBABILISTIC FRAMEWORK FOR LIQUEFACTION SEVERITY ASSESSMENT

When CPT and other necessary data are obtained, the CRR and CSR can be calculated using the Robertson and Wride (1998), RW, model and the simplified procedure developed by Seed and Idriss (1971), respectively. Then, the assessment proceeds with characterization of various uncertainties, including input parameter uncertainty in CSR calculation, model uncertainty in the RW model and spatial variability of the CRR. In order to consider the parameter uncertainty in CSR calculation, four parameters (i.e., the peak horizontal ground surface acceleration a_{max}, the earthquake moment magnitude M_w, the total overburden stress σ_{v0} and effective overburden stress σ'_{v0}) involved in CSR expression are assumed to follow a lognormal distribution and modelled by their mean values and coefficients of variation

(COVs). In addition, the correlations between a_{max} and M_w and between σ_{v0} and σ'_{v0} are also included in the assessment (e.g., Juang et al. 2008).

Based on the results of Juang et al. (2004), the model uncertainty in the RW model can be characterized as a random variable with a mean and coefficient of variation (COV). Bayesian approaches are developed to characterize spatial variability of the CRR. The soil is divided into N statistically homogeneous layers and the inherent spatial variability of the CRR within each soil layer is modelled by one-dimensional and mutually independent lognormal random field along the vertical direction. An exponential correlation function is used to model the spatial correlation of the logarithms of the CRR at different depths (e.g., Fenton 1999). Then, Bayesian system identification and model class selection methods (e.g., Cao and Wang 2013; Wang et al. 2014) are developed to identify the probability distribution of the CRR and the thicknesses of soil layers with statistically homogeneous CRR.

Finally, for a given seismic loading, the thicknesses of liquefiable soil layers are estimated. A ratio of the liquefiable soil layer thickness over the total thickness of all soil layers considered is defined for assessment of liquefaction severity, and it is quantified probabilistically using Monte Carlo Simulations (MCS).

ILLUSTRATIVE EXAMPLE

The proposed approaches are illustrated using a set of real CPT data from a sand site at Dodd Farm, USA (Schneider and Mayne 1999). The site is comprised of five layers of sand and sandy silt extending from the ground surface to a depth of about 13.2m (See Figure 1). The groundwater table (GWT) was at about 4.4m below the ground surface. It is noted that liquefaction only occurs below the GWT. The distributions of the cone penetration resistance q_c and the sleeve friction f_s, and the calculated CRR and CSR values are shown in Figure 1. As a reference, the soil stratification identified by Schneider and Mayne (1999) is also illustrated in Figure 1.
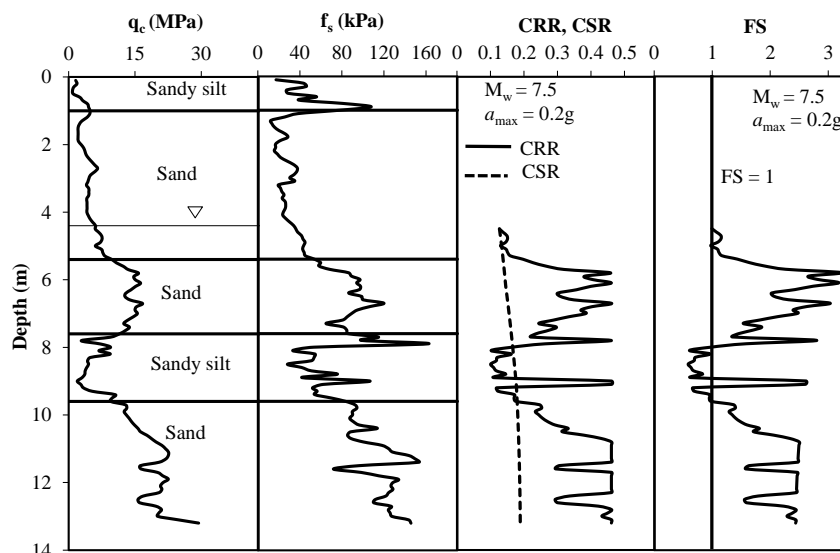
Figure 1 A set of real CPT data at the Dodd Farm, USA
(After Schneider and Mayne (1999))

Based on the proposed approach, the most probable boundaries of soil layers are delineated accordingly for the five model classes, as shown in Figure 2 using short dashed lines. The most probable boundaries (i.e., M_4^*) are consistent with those by Schneider and Mayne (1999).

Figure 3 illustrates a histogram of the percentage P of liquefiable soil thickness for all soil layers below the GWT from MCS. If the RW model is used deterministically without consideration of model uncertainty or spatial variability, the percentage of liquefied soil thickness is calculated as 19.3%, which is close to the mean value of P from MCS (e.g., 19.2%). In addition, the probabilistic approach provides a probabilistic distribution of P and quantifies the uncertainty in the liquefaction severity assessment results obtained. Furthermore, the liquefaction severity of each identified soil layer can be also assessed respectively using the proposed method.
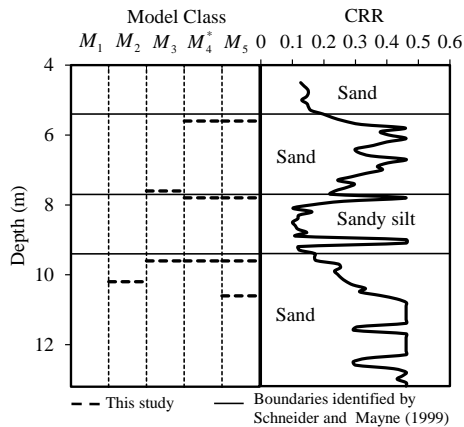
Figure 2 The most probable boundaries of soil layers in the Dodd Farm site example
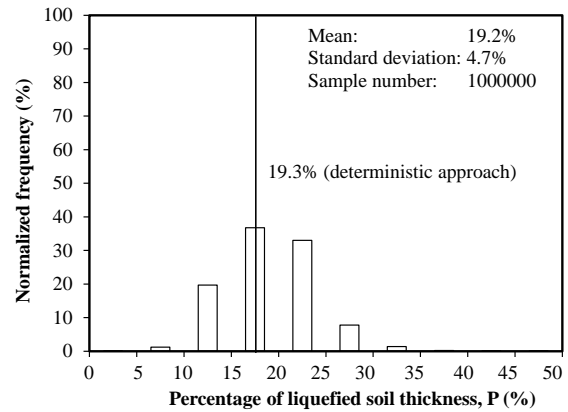
Figure 3 A histogram of the percentage P of liquefiable soil thickness

SUMMARY AND CONCLUSION

A probabilistic approach for assessment of the liquefaction severity of soil layers was developed using CPT data. The spatial variability of the CRR, the model uncertainty associated with the CPT-based RW method, and input parameter uncertainty in CSR calculation are taken into consideration explicitly in the proposed approach. MCS was performed to quantify the percentage P of liquefiable soil thickness for the assessment of liquefaction severity.

The proposed approach was illustrated using a set of real CPT data collected from USA. The proposed approach properly identifies the thicknesses of the liquefiable soil layers, quantifies their liquefiable soil thickness and associated uncertainty and offers a rational vehicle to properly assess liquefaction severity of soil layers.

ACKNOWLEDGEMENTS

REFERENCES

Cao, Z., and Wang, Y. 2013. Bayesian approach for probabilistic site characterization using cone penetration tests. *Journal of Geotechnical and Geoenvironmental Engineering*, 139(2): 267-276.

Cetin, K.O., Der Kiureghian, A., and Seed, R.B. 2002. Probabilistic models for the initiation of seismic soil liquefaction. *Structure Safety*, 24(1): 67-82.

Fenton, G. 1999. Estimation for stochastic soil models. *Journal of Geotechnical and Geoenvironmental Engineering*, 125(6): 470-485.

Iwasaki, T., Tokida, K., Tatsuoka, F., Watanabe, S., Yasuda, S., and Sato, H. 1982. Microzonation for soil liquefaction potential using simplified methods. Proc., 3rd Int. Earthquake Microzonation Conf., Seattle, 1319-1330.

Juang, C. H., Fang, S. Y., and Li, D. L. 2008. Reliability analysis of liquefaction potential of soils using standard penetration test. Edited by Phoon, K. K, in Reliability-Based Design in Geotechnical Engineering.

Juang, C.H., Jiang, T., and Andrus, R.D. 2002. Assessing probability-based methods for liquefaction potential evaluation. *Journal of Geotechnical and Geoenvironmental Engineering*, 128(7): 580-589.

Juang, C.H., Yang, S.H., Yuan, H., and Khor, E.H. 2004. Characterization of the uncertainty of Robertson and Wride model for liquefaction potential evaluation. *Soil Dynamics and Earthquake Engineering*, 24(9): 771-780.

Juang, C.H., Yuan, H.M., Lee, D.H., and Lin, P.S. 2003. Simplified cone penetration test-based method for evaluating liquefaction resistance of soils. *Journal of Geotechnical and Geoenvironmental Engineering*, 129(1): 66-80.

Robertson, P.K., and Wride, C.E. 1998. Evaluating cyclic liquefaction potential using the cone penetration test. *Canadian Geotechnical Journal*, 35(3):442-459. doi:10.1139/t98-017.

Schneider, J. A., and Mayne, P. W. 1999. Soil Liquefaction Response in Mid-America Evaluated by Piezocone Tests. Georgia Institute of Technology and MAE Center, Mid America Earthquake Report MAE-GT 3A.

Seed, H.B., and Idriss, I.M. 1971. Simplified procedure for evaluating soil liquefaction potential. *Journal of the Soil Mechanics and Foundation division*, ASCE, 97(SM9): 1249-1273.

Toprak, S. and Holzer, T.L. 2003. Liquefaction potential index: field assessment. *Journal of Geotechnical and Geoenvironmental Engineering*, 129(4): 315-322.

Toprak, S., Holzer, T.L., Bannett, M.J., and Tinslay, J.C. 1999. CPT and SPT-based probabilistic assessment of liquefaction potential. Proceedings of 7th U.S.–Japan Workshop on Earthquake Resistant Design of Lifeline Facilities and Countermeasures Against Liquefaction, Seattle, Technical Report MCEER-99-0019.

Wang, Y., Huang, K., and Cao, Z. 2014. Bayesian identification of soil strata in London Clay. *Geotechnique*, 64 (3): 239-246.

Youd, T. L., Idriss, I. M., Andrus, R. D., Arango, I., Castro, G., Christian, J. T., Dobry, R., Liam Finn, W. D., Harder, L. F. Jr, Hynes, M. E., Ishihara, K., Koester, J. P., Laio, S. S. C., Marcuson, W. F. III, Martin, G. R., Mitchell, J. K., Moriwaki, Y., Power, M. S., Robertson, P. K., Seed, R. B. and Stokoe, K. H. 2001. Liquefaction resistance of soils: summary report from the 1996 NCEER and 1998 NCEER/NSF workshops on evaluation of liquefaction resistance of soils. *Journal of Geotechnical and Geoenvironmental Engineering*, 127(10): 817-833.

EFFECT STUDY OF CYCLIC LOADING ON BEHAVIOR OF SOIL SLOPES USING CENTRIFUGE MODEL TESTS

Yaliang Wang and Ga Zhang
Tsinghua University, China

BRIEF INRODUCTION

Landslides triggered by earthquakes are serious natural disasters which cause great loss to people's properties and lives. It's of great significance to properly evaluate the dynamic stability of slopes. Pseudo-static method has been widely used since it was first proposed in 1950 (Terzaghi 1950). However, the simplification of seismic inertia force into permanent force often leads to inaccurate predictions of the dynamic stability of slopes (Chang 1984). Finite element method provides a basis for dynamic time-history analysis. But a shortcoming of finite element method is that the results are highly dependent on the accuracy of the model and parameters of the soil. Therefore, an understanding of the progressive failure process of slopes is essential for the evaluation of the dynamic stability of slopes. In this paper, centrifuge model tests were conducted to investigate the progressive failure behavior of slopes under cyclic loading conditions.

METHODOLOGY

The centrifuge model tests were conducted on the 50 g t geotechnical centrifuge at Tsinghua University. The plastic limit and the liquid limit of the soil were 18.5% and 25.0%, respectively. The dry density and the water content of the soil were controlled around 1.55 g/cm^3 and 18%. The model container used for the tests was made of aluminium alloy, 500 mm in length, 200 mm in width, and 350 mm in height. Fig. 1 shows the schematic view of the slope model. The height of the slope model is 250mm. The gradient of the slope model is 1.5:1(Vertical: Horizontal). A 50-mm-thick layer was under the slope to eliminate the
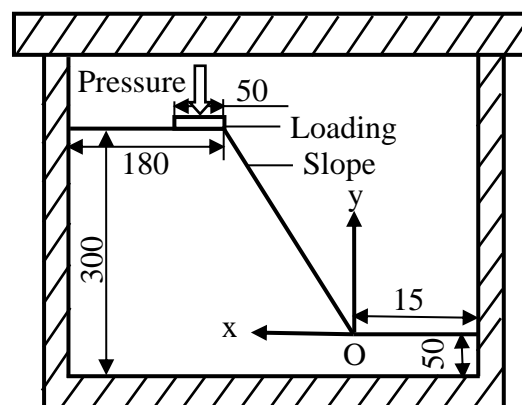
Figure 1: Schematic view of the slope model (unit: mm).

influence of the wall of the container. The load was generated by a hydraulic loading device and was applied at the slope crest through a rigid loading plate with a length of 200 mm and a width of 50 mm. The wave form of the cyclic load was triangular wave. The centrifuge acceleration was maintained at 50 g during tests. The load and the settlement of the slope crest were measured using a load transducer and a laser displacement sensor, respectively. The displacement field of the slope was determined through an image-based displacement measurement system (Zhang et al. 2009).

KEY RESULTS

Fig. 2 shows the relationship between the load pressure and the settlement of the slope crest. During the monotonic loading stage, the settlement of the slope crest increased as the load pressure increased. In the cyclic loading stage, the peak value of the cyclic load changed little, while the settlement of the slope crest kept increasing. Fig. 3 shows the ratio between the increment of the settlement of the slope crest and the peak value of the cyclic load. The increment of the settlement was counted from the beginning of the cyclic loading stage. It can be observed that the increasing rate of the settlement was nearly constant in every loading cycle. This result demonstrated that cyclic loading induced evident deformation in the slope, showing a significant cyclic effect.
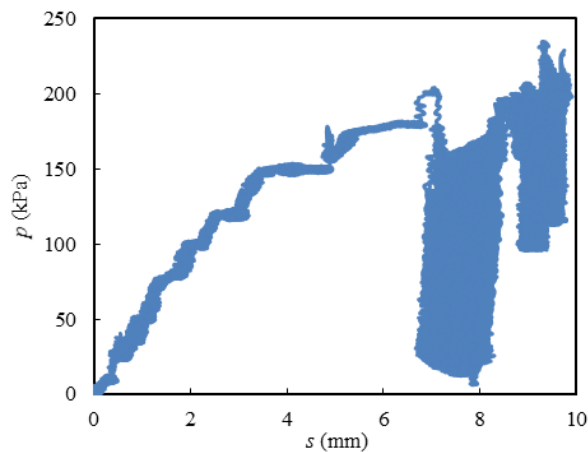
Figure 2: Relationship between the load pressure and the settlement of the slope crest. p, load increment of the slope crest.
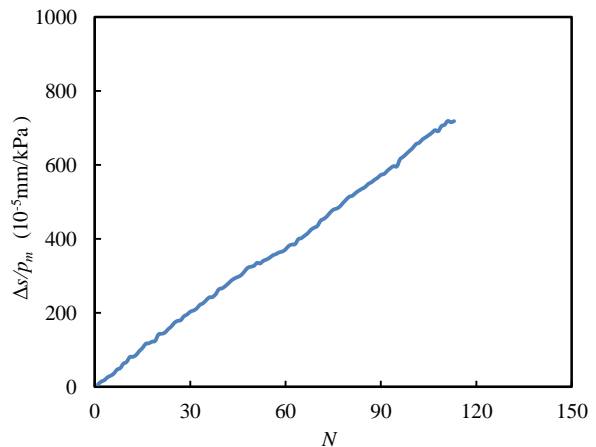
Figure 3: Ratio between the increment of the crest settlement and peak value of the cyclic. Δs, of settlement of the slope crest; p_m, peak value of cyclic load; N, number of loading cycles.

When the deformation of the slope accumulated to some extent, a slip surface can be observed (Fig. 4). Fig. 5 shows the schematic view of the slip surfaces under cyclic loading and static loading. The starting points of the two slip surfaces were both close to the inner edge of the loading plate. The slip surfaces gradually separated as they developed deeper in the slopes. The ending points of the slip surfaces were on the free surfaces of the slopes. It can be observed that the slip surface of the slope under cyclic loading was much deeper than that of the slope under static loading. This indicated that cyclic loading induced a larger affected area in the slope.

CONCLUSIONS

1. The settlement of the slope crest kept increasing during cyclic loading stage with the peak value of the load unchanged, demonstrating the cyclic effect.

2. A distinct slip surface appeared as the deformation of the slope accumulated to some extent under cyclic loading.
3. Compared with static loading, cyclic loading induced a deeper slip surface in the slope, indicating a larger loading-affected area in the slope.
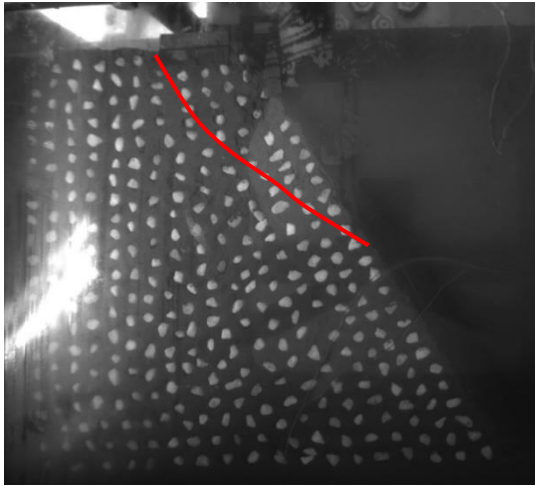
Figure 4: Slip surface of slope under cyclic loading.
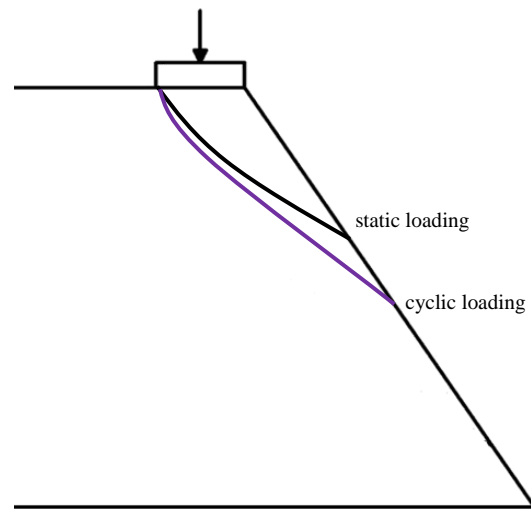
Figure 5: Schematic view of slip surfaces of slopes under different loading.

REFERENCES

Terzaghi, K. (1950). "Mechanisms of Landslides, Engineering Geology (Berdey)." *M.* Geological Society of America.

Chang, C. J., Chen, W. F., and Yao, J. T. P. (1984). "Seismic Displacements in Slopes by Limit Analysis." *J. Geotechnical & Geoenv. Engrg.,* Vol. 110(7), pp. 860-874.

Zhang, G., Hu, Y., and Zhang, J. M. (2009). "New image analysis-based displacement-measurement system for geotechnical centrifuge modeling tests." *Measurement. J.* 42(1), pp. 87-96.

SLOPE FAILURE MECHANISM UNDER DRAWDOWN CONDITIONS

Fangyue Luo, Yang Liu, Lv Lin and Ga Zhang
Tsinghua University, China

BRIEF INRODUCTION

The slope safety has been of great significance with more and more large reservoirs coming into service. The drawdown poses a threat to the slope safety. Numerical and physical modeling have been applied to the study of slope safety under drawdown conditions. However, the failure mechanism has not been clearly clarified yet. Centrifuge modeling has been widely used to invesigate the failure behavior of slopes under different loading conditions (Viswanadham and Mahajan 2007; Sommers and Viswanadham 2009; Wang and Zhang 2014). In this paper, centrifuge model tests were conducted to explore the failure mechanism of the slope under drawdown conditions. Analysis on the deformation and failure behaviors of the slope was presented on the basis of test results.

METHODOLOGY

The centrifuge model tests were conducted using the centrifuge at Tsinghua University. A soil, with a specific gravity of 2.7, was used in the tests. The plastic limit and liquid limit of the soil were 18.5% and 25%, respectively.

The model container, with a transparent organic glass on one lateral side, is 60 cm in length, 20 cm in width and 50 cm in depth. The water content of the soil is 18%. The soil was compacted to 5-cm-thick layers with a dry density of 1.55 g/cm^3 in the model container. The slope model was 35 cm in height with a gradient of 1:1. An extra layer under the slope was preserved to minimize the disturbance from the model container. The model container was equipped with a water-level-control system to realize a control of arbitrary water level during tests. The slope model and the water-level-control system is shown in Figure 1.
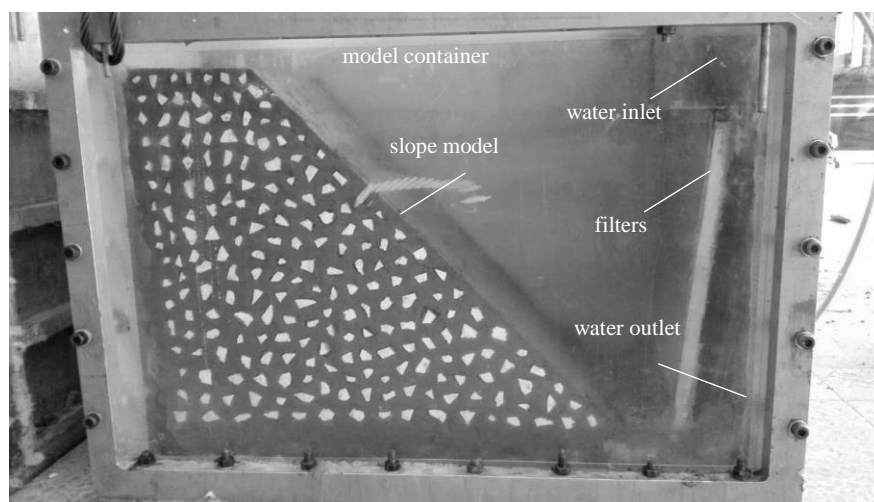
Figure 1: Photograph of the slope model

A rectangular Cartesian coordinate system was set up with the origin at the toe of the slope (Fig. 2). The positive directions were defined rightwards for x-axis and upwards for y-axis. The centrifugal acceleration increased to 50 g by a step of 5 g. Impoundment to a water level of 270mm was conducted at 50 g level using the water-level-control system after the deformation of the slope stablized. The water level began to drawdown to 40 mm after the slope reached a state of deformation balance. The images of the soil slopes were captured by an image record system during the tests. An image-measuring system was used to analyze the displacement of the soil slope and the water level according to the photograph series.

KEY RESULTS

The slip surface of the slope at the end of the test is portrayed with dashed line in the coordinate system (Fig. 2). It can be seen that the slip surface runs through the slope top and extends to an elevation of around 50 mm. The slope is divided into two parts, namely the sliding body and the base body, which are the right part and the left part, respectively. It can be observed during the test that the slip surface appeared from the top of slope to the toe.

Figure 3 shows the vertical displacements histories of typical points, of which the locations are marked out in Figure 2. It can be seen that the vertical displacements of all points keep increasing as the water level decreased and become stable at the end of the test. The vertical displacements of point B and D located in the sliding body are much larger than that of the point A and C located in the base body eventually. In each part of the slope, the vertical displacement appears to be much smaller with a lower elevation, which can be seen from point B and D, as well as point A and C. It should be noted that the inflection of the curve of point B appears earlier than that of point D, which confirms that the slip surface developed from the slope top downwards to the slope toe. The vertical displacement curves of point A and D also presents the same pattern.
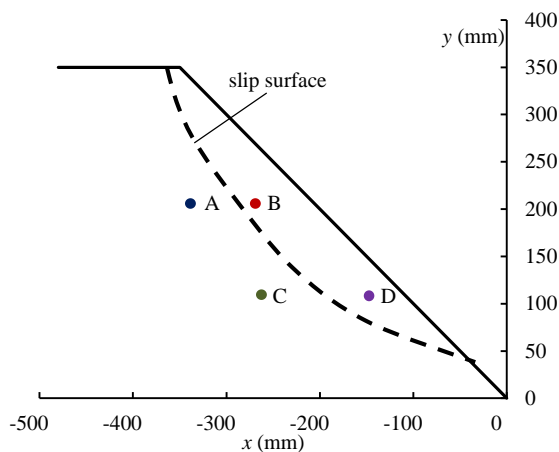
Figure 2: Slip surface of slope
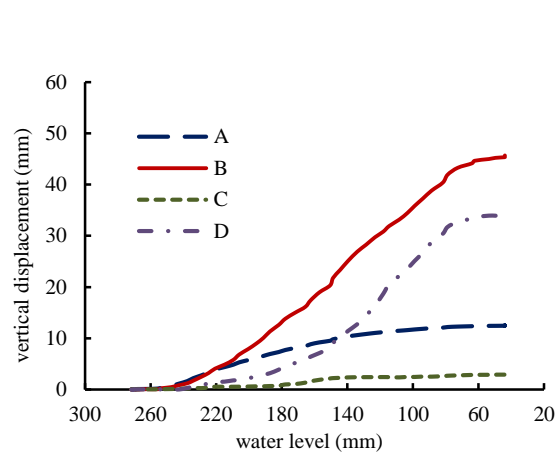
Figure 3: Vertical displacement histories of typical points (locations shown in Fig. 2)

Figure 4 shows the distribution of slope deformation at different water levels during drawdown, namely the distribution of horizontal displacements and the distribution of horizontal strain. It can be seen from Fig. 4(a) that the horizontal displacement of the slope increased from inside to outside of the slope during drawdown. The displacement grew larger as the water level decreased. The displacement soared in certain spots, namely where the deformation localization became obvious. The failure water level of the slope can be determined using the images captured during the test, which turns out to be 151 mm. By further analysis, it can be found in Fig. 4(b) that the deformation of the slope became larger

during drawdown. There is a peak on the strain curve of the slope at a water level of 180 mm, where the subsequent slip surface appeared. The strain curve at a water level of 120 mm also reveals that deformation localization of the slope induced failure. Remarkable deformation can be seen within the sliding body after slope failure implying that the local failure resulted in new deformation localization.
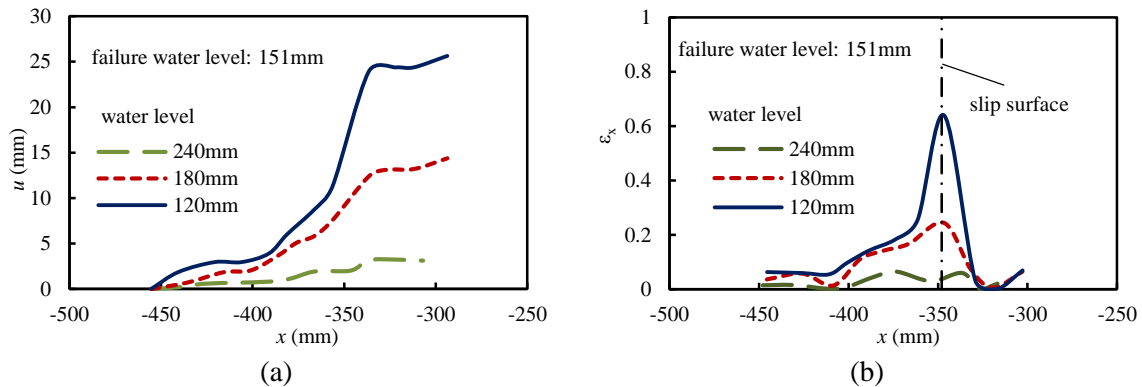
Figure 4: Distribution of deformation of soil slope at different water levels (y=300 mm). u, horizontal displacement; ε_x, horizontal strain.

CONCLUSIONS

1. The drawdown induced slope failure. The slip surface developed from the slope top downwards to the slope toe. Different parts of the slope exhibited different deformation characters during drawdown.
2. The displacement of the slope grew larger from inside to outside of the slope. There is an inflexion on each displacement curve, which implies the deformation localization became significant there.
3. The slope failure is coupled with the deformation localization. The slope failure occurred in the spot where deformation localization reached a peak. While the deformation localization kept developing because of the local failure appeared in later failure process.

ACKNOWLEDGEMENTS

REFERENCES

Sommers AN, Viswanadham BVS. Centrifuge model tests on the behavior of strip footing on geotextile-reinforced slopes. Geotextiles and Geomembranes, 2009, 27(6): 497-505.
Viswanadham BVS, Mahajan RR. Centrifuge model tests on geotextile reinforced slopes. Geosynthetics International, 2007, 14(6): 365-379.
Wang LP, Zhang G. Centrifuge model test study on pile reinforcement behavior of cohesive soil slopes under earthquake conditions. Landslides, 2014, 11(2): 213-223.

NUMERICAL STUDIES OF WAVE-INDUCED LIQUEFACTION OF SEABED AROUND A SINGLE PILE

J. Ren*, B. Zhu* and G. L. Ye[+]
* Zhejiang University, China
[+] Shanghai Jiao Tong University, China

BRIEF INRODUCTION, METHODOLOGY AND KEY RESULTS

The liquefaction of seabed under ocean waves is the main cause of the failure of offshore structures like wind turbines. Different from the situation in which no pile foundations are inserted, the seabed around the pile foundations is more likely to liquefy, due to the fact that it is subjected to two kinds of wave loads. Firstly, vertical wave pressure is directly loaded on the surface of the seabed, the value of which is usually calculated by wave theory. And secondly, the wave exerts a cyclic lateral load on the upper offshore structures, this load is transmitted to the seabed around the pile foundations through pile-soil interactions. However, this phenomenon hasn't been specifically discussed.

In this study, an effective stress-based, fully coupled finite element method (FEM) is used to simulate the soil behavior of seabed around a single pile under ocean waves. The behavior of the seabed is described by a cyclic mobility constitutive model based on the critical state theory and the pile is set as elastic. The wave load on the seabed is calculated by linear wave theory and the lateral cyclic load on the superstructure is calculated by Morison's equation. Three loading conditions are considered: (1) Loading condition 1, where only the pressure on the seabed is included. (2) Loading condition 2, where only the pile-soil interaction is included. And (3) Loading condition 3, where both of two loads are applied to the model. Soil responses of different positions around the pile are calculated. The influence of wave properties on soil responses is analyzed.

Fig. 1 shows the simulation results of seabed using either the Cam-clay model or the model proposed in the study. In this figure, σ_V, τ_{xz} represent the volumetric effective stress and shear stress in the x-z plane. No clear difference of pore pressure exists between the Cam-clay model and the model presented in the study, however, the results are quite different when it comes to the stress path in the $p - \tau$ plane. The mean stress p' falls continuously when using the Cam-clay model, until the liquefaction is reached ($p' = 0$). The reason why the present model can simulate the cyclic mobility phenomenon lies in the fact that in the proposed constitutive model the yield surface is able to rotate with the change of stress induced anisotropy.

Fig. 2 shows the pore pressure responses of seabed in these three load conditions. In Fig. 2 (a) where the water depth is set as 15m, there exists a huge difference between the load condition 1 and the load condition 3. On the other hand, it seems that only a tiny difference is found between the load condition 2 and 3, with the amplitude of oscillatory pressure of load condition 3 slightly larger. This indicates that the pile-soil interaction plays a vital role in the vicinity of the pile. However, when the water depth decreases to 10m (Fig. 2 (b)), the accumulation speed of pore pressure responses in loading conditions 1 and 2 are relatively slow, comparing with those in the loading condition 3. It indicates that in deep waters, the pile-soil interaction is critical for pore pressure responses, however, in shallow waters both

the wave pressure on the seabed and the pile-soil interaction should be considered. This is very important because most of the offshore wind turbines are built in relatively shallow waters.

(a) Pore water responses

(b) Stress path
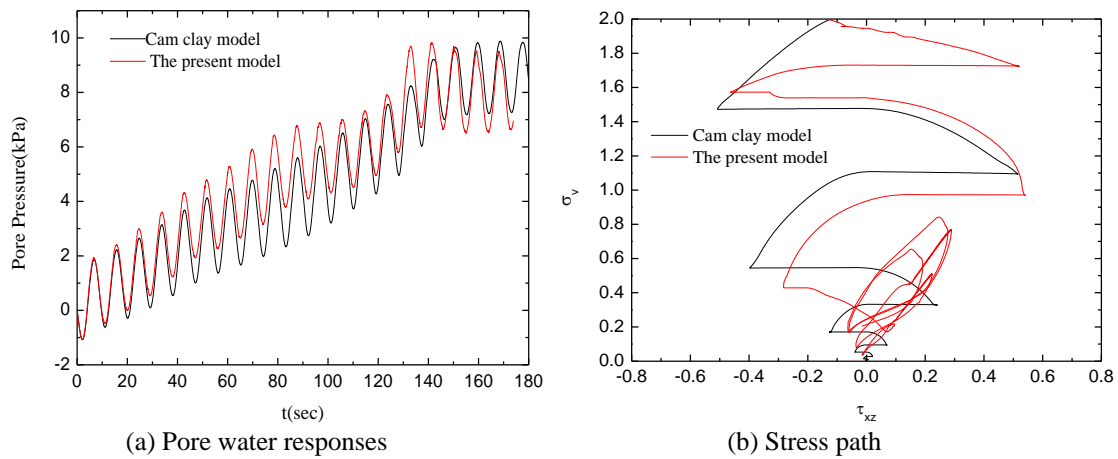
Figure 1: Comparison of different constitutive models

(a) Water depth of 15m

(b) Water depth of 10m
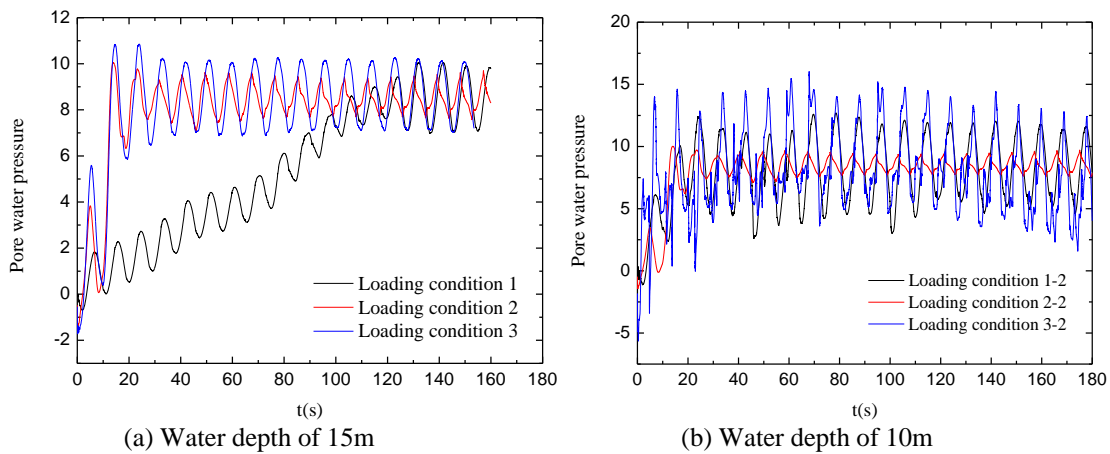
Figure 2: Loading conditions of the seabed around the pile

CONCLUSIONS

1. The pile-soil interaction exerts a substantial influence on the liquefaction behavior of seabed. The seabed around the pile is more likely to liquefy because of the pile-soil interactions, thus the methods that are based on the seabed without a pile will underestimate the liquefaction potential of seabed around the pile.
2. The influence of pile-soil interactions on soil behaviors depend heavily on water depth. In relative deep waters, the pile-soil interaction plays the key role in the accumulation of pore pressures, while the influence of the vertical wave pressure on the surface of the seabed is relatively small. However, in shallow waters, neither the effects of pile-soil interactions and the effects of vertical pressure on the surface of the seabed can't be neglected.

REFERENCES

Li X. J., Gao F. P., Yang B., et al. (2011). "Wave-induced pore pressure responses and soil liquefaction around pile foundation." *International Journal of Offshore and Polar Engineering.* 21, pp. 233-239.

Rosquoet F., Thorel L., Garnier J., et al. (2007). "Lateral cyclic loading of sand-installed piles." *Soils and Foundations*.47, pp. 821-832.

Sassa. S., Sekiguchi. H. (2001). "Analysis of wave-induced liquefaction of sand beds." *Geotechnique*. 51, pp. 115-126.

Ye. B., Ye. G. L., Zhang. F. (2012). "Numerical modeling of changes in anisotropy during liquefaction using a generalized constitutive model." *Computers and Geotechnics*. 42, pp. 62-72.

Zhang Y., Jeng D. S., Gao F. P., et al. (2001). "An analytical solution for response of a porous seabed to combined wave and current loading." *Ocean Engineering*. 51, pp. 115-126.

LARGE-SCALE SHAKING TABLE TEST ON THE ENERGY DISSIPATION OF THE RETAINING WALL BACKFILLED WITH EPS COMPOSITE SOIL

W. Zhou and H. M. Gao

Nanjing Tech University, China

BRIEF INTRODUCTION, METHODOLOGY AND KEY RESULTS

In recent years, the earthquake disasters in China are becoming more and more frequent. The related earthquake data show that the damage of retaining structure caused by the earthquake happened frequently. So the study on the stability of retaining wall under seismic loadings is urgent. The instability and failure phenomena of retaining wall include destruction, overturning and sliding, etc. The new idea to handle this problem is to decrease earth pressure behind the retaining wall. Therefore, the development of a light weight, high strength, strong, self-standing material will be an effective means to solve the retaining wall instability.

EPS composite soil is a new type filling material which is mixed with EPS beads, intact soil, water and cement. It has promising future due to its advantages, such as light weight, high strength, self-standing. Therefore, the application of EPS composite soil filled behind the retaining wall can reduce energy consumption and lessen vibration.

A series of large-scale shaking table tests on the retaining wall are carried out. EPS composite soil and sand are filled behind the retaining wall, respectively. The model retaining wall is made of C30 concrete. The test model is shown in Fig. 1. El-Centro wave and Taft wave are used as input seismic wave. Peak acceleration of El-Centro seismic wave is designed as 0.1g, 0.3g and 0.5g, and Taft seismic wave is designed as 0.1g, 0.3g, 0.5g and 0.7g.

Fig. 1. The layout of sensors embedded in the model (unit: mm)

The acceleration amplification factors of the retaining wall are shown in Fig. 2. It shows that the acceleration amplification factor of each measuring point decreases with the increase of the peak acceleration of the input ground motion.

(a) Wall 1 (El-Centro) (b) Wall 2 (El-Centro) (c) Wall 1 (Taft)
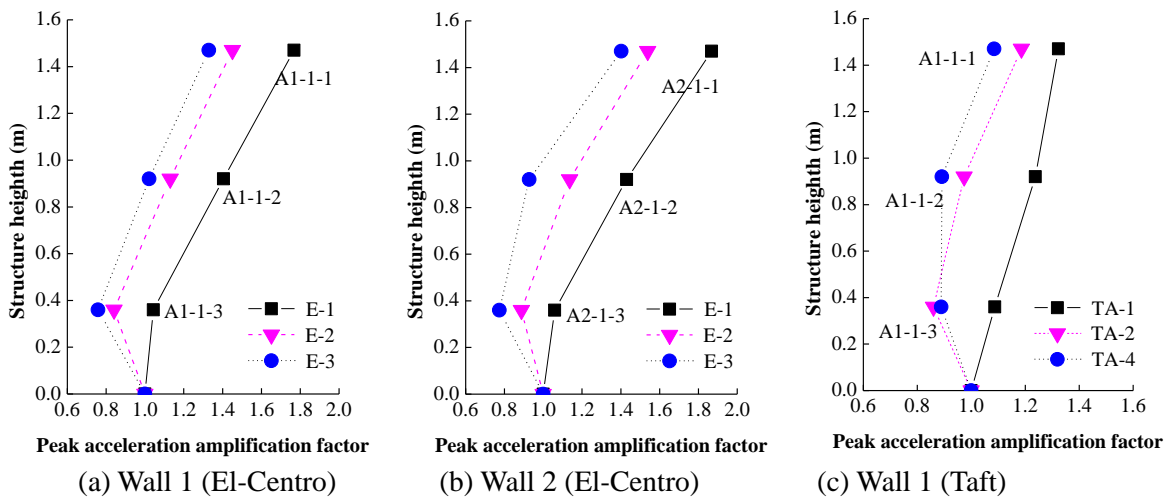
Fig. 2 PGA amplification factors with different height of retaining wall

The earth pressure increments behind the retaining wall under three conditions are given in Fig. 3. It can be seen that in the E-1 condition, the earth pressure of P1-1 to P1-3 increases with the increase of wall height, and for P2-1 to P2-3 decreases with the increase of wall height. In the E-2 and TA-2 conditions, the earth pressure at the P1-1 to P1-3 increases with the increase of wall height. The earth pressure from P2-1 to P2-3 increases firstly and then decrease with the increase of height. The earth pressure at P2-2 achieves the maximum value. There is a same phenomenon for the three conditions, that is, the earth pressure increment at P1-1 is much larger than other points.

(a) E-1 condition   (b) E-2 condition   (c) TA-2 condition
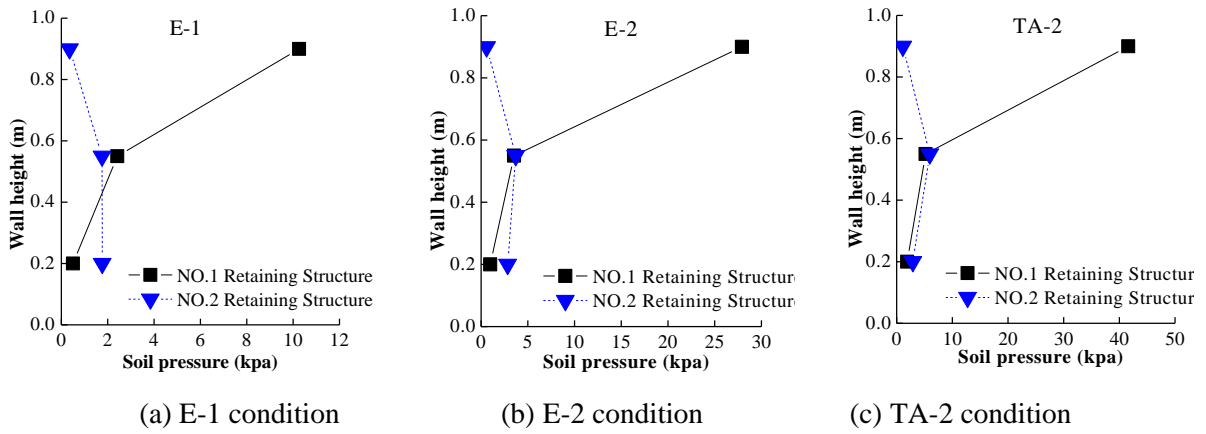
Fig. 3 Earth pressure at different measuring points under three ground motions

Wall collapse and wall slip are the commonly failure mode of retaining wall. It is of great significance to monitor the displacement response of retaining wall under seismic loadings for studying the stability of retaining wall. Fig. 4 shows the displacement on the top of the retaining wall under the condition of E-1 and TA-4. Under a small earthquake, the displacements of two retaining walls are almost the same. Under a large earthquake, the peak displacement at T1-1 is smaller than that at T2-1. In the end of seismic excitation, compared with T1-1, T2-1 has an obvious deflection.

(a) E-1 condition   (b) TA-4 condition
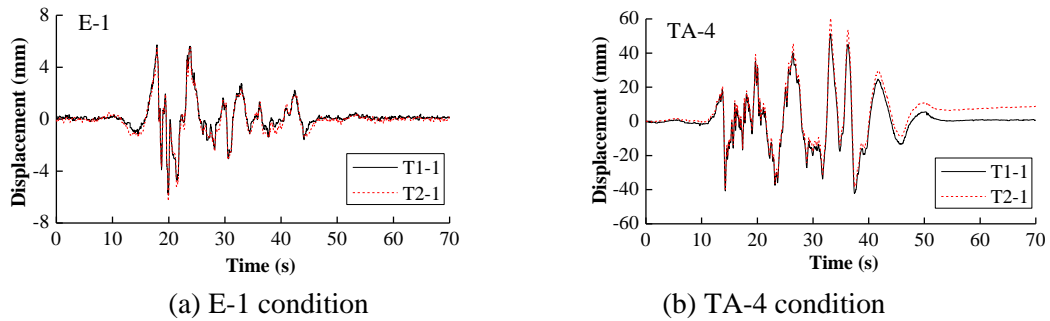
Fig. 4 Displacement on the top of retaining wall under different conditions

The non-contact dynamic displacement measurement method is used to obtain the displacement on the ground surface. Fig. 5 shows that no obvious displacement occurs on the ground surface of EPS composite soil foundation. The horizontal slip towards the retaining wall occurs for the sand foundation.

(a) E-1 condition   (b) TA-4 condition
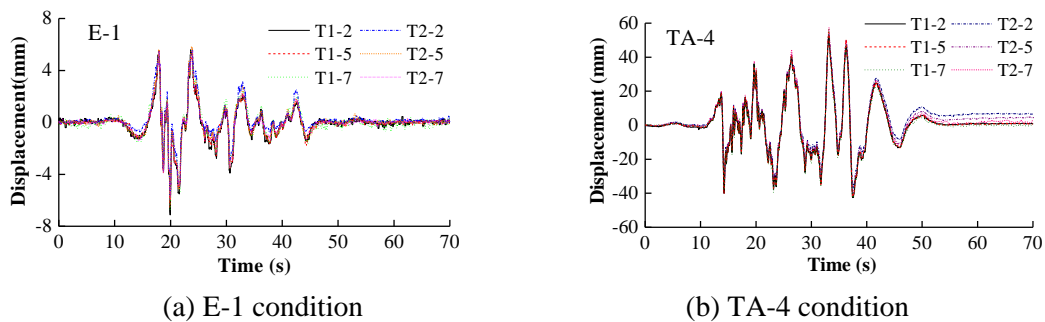
Fig. 5 Displacement on the ground surface under different conditions

156

CONCLUSIONS

Compared with the ordinary soil, EPS composite soil as filling material behind the retaining wall has an obvious energy dissipation effect, which can effectively reduce the peak acceleration of ground motion. The earth pressure acting behind the retaining wall differs obviously with the wall depth. The peak acceleration and the wall displacement for the retaining wall filled with EPS composite soil are smaller compared with sand. Therefore, EPS composite soil as backfill material behind the retaining wall can alleviate the influence of seismic loads on the stability of retaining wall.

REFERENCES

Watabe, Y., Tanaka, M., Saegusa, H., Shinsha, H., and Tsuchida, T. (2009). "Long-term properties of airfoam-treated lightweight soil made from dredged clay." *Journal of ASTM International,* No. 6(4).

Ling, H. I., Leshchinsky, D., Chou, N. S. (2001). "Post-earthquake investigation on several geosynthetic-reinfoced soil retaining walls and slops during the Ji-Ji earthquake of Taiwan." *Soil Dynamics and Earthquake Engineering*, No. 21(4), pp. 297-313.

Sandri, D. (1997). "Performance summary of reinforced soil structures in the Greater Los Angeles area after   the Northridge earthquake." *Geotextiles and Geomembranes*, No. 15(4-6), pp. 235-253.

Fang, Y. S., Yang, Y. C., and Chen. T. J. (2003). "Retaining walls damaged in the Chi-Chi earthquake." *Canadian Geotechnical Journal*, No. 40(6), pp. 1142-1153.

CYCLIC BEHAVIOR OF AN UNSATURATED EMBANKMENT FILLING SOIL

H.W. Li*, L.L. Zhang* and J. Xu[+]
* Shanghai Jiaotong University, China
[+] Hohai University, China

BRIEF INRODUCTION, METHODOLOGY AND KEY RESULTS

In the past ten years, the high-speed railway network has been dramatically developed in China. According to the long-term railway network plan of China, the total length of high-speed railway in service will be increased to 16,000 km in 2020. The railway embankment, which supports continuous dynamic loads of high-speed trains and track structure, is often unsaturated and subject to seasonal variations of moisture content or soil suction. Many theoretical and experimental studies have demonstrated that unsaturated soil behavior is highly dependent on soil suction. However, investigation of cyclic behavior for unsaturated soils, especially the high-speed railway embankment filling material, is very limited in the literature (Khoury at el. 2004; Yang at el. 2005, 2008; Ng at el. 2013, 2014).

In this study, the static/dynamic triaxial testing system in Shanghai Jiao Tong University is used to investigate the cyclic behavior of an unsaturated embankment filling soil. Based on the particle size distribution, the soil in this study is the Class B filling material based on the design code of railway embankment in China and is classified as a clayey sand (SC) according to the Unified Soil Classification System (ASTM, 2011). The effects of suction magnitude, form and amplitude of cyclic load, and the wetting and drying history on the accumulated plastic strain and resilient modulus of the unsaturated soil are evaluated. Totally eleven tests of four series are conducted. The testing program and detailed testing conditions are summarized in Table.1.

Table 1: Testing program and detailed testing conditions

Test series	Suction (kPa)	Cyclic load (kPa)	Cyclic load form	Test purpose
1	15, 50, 100, 200	70	Haversine	Suction level
2	15, 100	70	Haversine, triangular	Form of cyclic load
3	15, 100	70, 100	Haversine	Amplitude of cyclic load
4	$S_0^* \rightarrow 50 \rightarrow S_0$ $S_0 \rightarrow 100 \rightarrow 5$ $S_0 \rightarrow 200 \rightarrow S_0$	70	Haversine	Wetting-drying history

*: S_0 represents the initial suction of each specimen

Each soil specimen is compacted at the optimum water content (11.5%). The net mean stress is 20kPa. Matric suction is controlled by the axis-translation technique (Hilf, 1956) in this study. After suction equalization, each specimen is applied with an extra axial pressure of 15kPa that represents the load induced by the track or other structure. After consolidation of the unsaturated soil specimen, a dynamic triaxial test is carried out to investigate soil behavior

under cyclic loads. Generally, 10000 cycles of dynamic load is applied to each specimen with a frequency of 1Hz.
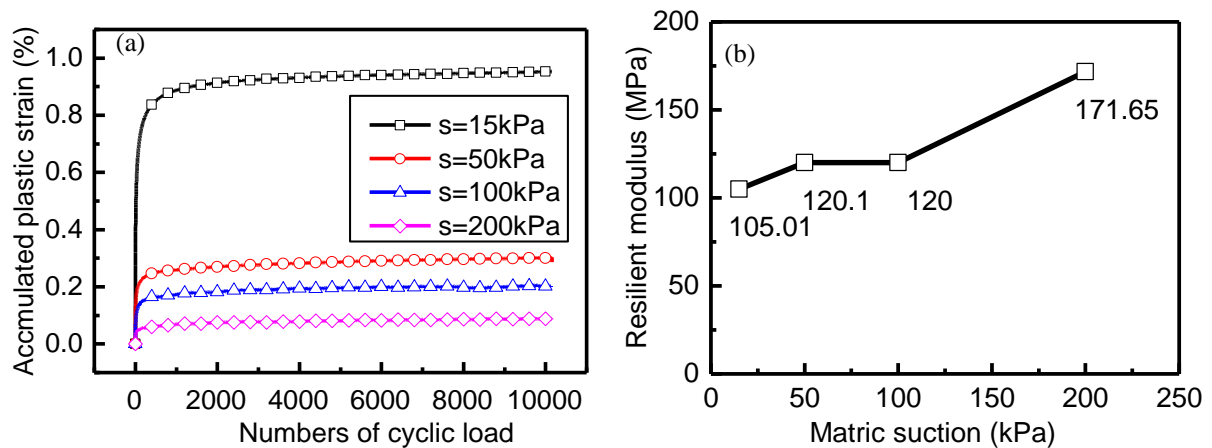
Figure 1: Effects of suction level on the (a) accumulated plastic strain and (b) resilient modulus of unsaturated soil

Figure 1 shows the effects of suction level on the accumulated plastic strain and resilient modulus for test series 1. The accumulated plastic strain is the plastic strain accumulated after each cyclic load, which will not recover after the test. The resilient modulus (M_R) was the ratio of cyclic load stress to axial recoverable strain. The accumulated plastic strain continually increases with the number of load cycles, but at a decreasing rate. The plastic strain accumulates very rapidly during the first 2000 cycles. The magnitude of accumulated plastic strain is consistently larger at a lower suction. When the suction is increased from 15 kPa to 50 kPa, the reduction of the accumulated plastic strain is significant. The resilient modulus increases generally with the increase of matric suction.
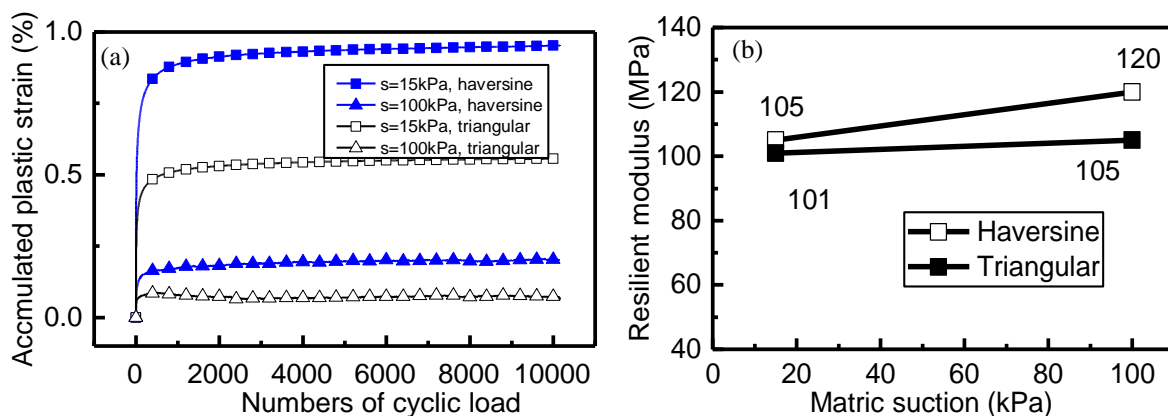
Figure 2: Effects of cyclic load form on the (a) accumulated plastic strain and (b) resilient modulus of unsaturated soil

Figure 2 shows the effects of cyclic load form on the accumulated plastic strain and resilient modulus. In this study, the haversine and triangular forms of cyclic load with the same amplitude are applied on the specimens. The test results show that the cyclic behavior of unsaturated soil under these two forms of cyclic load is similar. However, the plastic strain and resilient modulus are smaller under the triangular cyclic loads.

Figure 3 shows the effect of the amplitude of the cyclic loads on the cyclic behavior of the unsaturated fill material. In this study, two amplitudes, i.e., 70 kPa and 100 kPa are applied. As shown in Figure 3, with the increase of the cyclic stress level, the plastic strain and

resilient modulus also increase. In addition, the effect of stress level on the plastic strain is more significant when the soil suction is smaller.
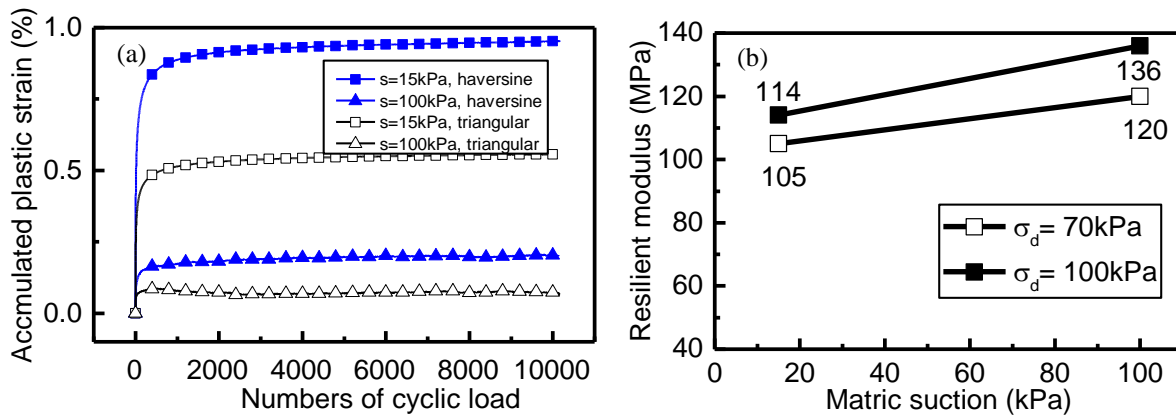
Figure 3: Effect of stress level of cyclic load on the (a) accumulated plastic strain and (b) resilient modulus in test group no. 3

In test series 4, each specimen is first applied with a designed suction (drying process). The suction is then decreased to the initial suction (S_0) and then the cyclic load is applied. Figure 4 shows the measured accumulated plastic strain and resilient modulus of specimens in test series 4. The specimens which experienced a smaller suction level during wetting-drying process yield relatively larger accumulated plastic strain and a lower resilient modulus.
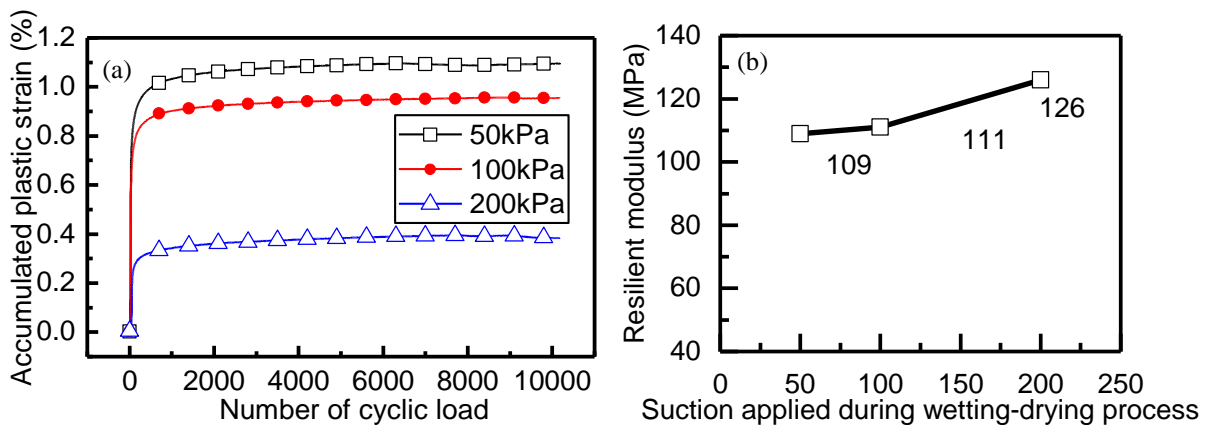
Figure 4: Effect of wetting-drying history on the (a) accumulated plastic strain and (b) resilient modulus of unsaturated soil

CONCLUSIONS

1. Four series of dynamic triaxial tests are carried out to investigate the cyclic behaviour of a high-speed railway embankment filling soil. The effects of suction level, form and amplitude of cyclic load, and the wetting and drying history on the accumulated plastic strain and resilient modulus of the unsaturated soil are investigated.
2. The specimen with a lower matric suction has a relatively higher accumulated plastic strain and a smaller resilient modulus. The plastic strain and resilient modulus under the triangular cyclic loads are smaller than those under the haversine cyclic load.
3. With the increase of the cyclic load amplitude, the accumulated plastic strain and resilient modulus increase. The effect of cyclic load amplitude on the plastic strain is more significant when the soil suction is smaller.
4. The specimen with a lower amplitude of wetting-drying process has relatively higher accumulated plastic strain and lower resilient modulus.

REFERENCES

ASTM. (2011). *Standard Practice for Classification of Soils for Engineering Purposes (Unified Soil Classification System),* American Society for Testing and Materials (ASTM).

Hilf, J. W. (1956). "An investigation of pore water pressure in compacted cohesive soils." *Technical Memo 654*, Bureau of Reclamation, Denver.

Khoury, N., and Zaman, M. (2004). "Correlation between resilient modulus, moisture variation, and soil suction for subgrade soils." *Transportation Res. Rec.: J. Transportation Res. Board* 1874, No. 1, 99–107.

Ng, C. W. W., & Zhou, C. (2014). "Cyclic behaviour of an unsaturated silt at various suctions and temperatures." *Géotechnique 64*(9), 709-720.

Ng, C. W. W., Zhou, C., Yuan, Q. & Xu, J. (2013). "Resilient modulus of unsaturated subgrade soil: Experimental and theoretical investigations." *Can. Geotech. J.* Vol. 50, No. 2, 223-232.

Yang, S. R., Huang, W. H., and Tai, Y. T. 2005. "Variation of resilient modulus with soil suction for compacted subgrade soils." *Transportation Research Record 1913*, Transportation Research Board, Washington, D.C., 99-106.

Yang, S. R., Lin, H. D., Kung, J. H. S. & Huang, W. H. (2008). "Suction-controlled laboratory test on resilient modulus of unsaturated compacted subgrade soils." *J. Geotech. Geoenviron. Eng., ASCE* 134, No. 9, 1375–1384.

APPLICATION OF 3D LASER SCANNING AND PRINTING IN GEOTECHICAL CONSTRUCTION

Z.B. Zuo*, J. Gong*, Y. L. Huang*, R. S. Li*, L. L. Zhang[+], and J.H. Wang[+]
* Shanghai Construction Group Co., Ltd., China
[+] Shanghai Jiaotong University, China

BRIEF INRODUCTION, METHODOLOGY AND KEY RESULTS

At present, geotechnical engineering lags behind other industries in its use of digitization and automation in construction. However, arguing that humans have an urgent need to exploit deep underground space. One example is the deep tunnel project of Shanghai. As the depth of excavation is more than 50 m, the traditional construction methods cannot guarantee safe and efficient geotechnical works. Therefore, it is necessary to introduce innovative technologies to improve the sustainability of geotechnical systems.

In this study, the applications of digital fabrication technology in geotechnical construction are introduced and some new ideas of the implementation of the digital fabrication technology for geotechnical sustainability are presented.

A new system for rapid monitoring and high prediction forecast of construction risk of geotechnical engineering based on 3D Laser Scanning is developed to solve the problem of low computational efficiency and reliability prediction using the traditional method of feedback analysis, and the flowchart as shown in Figure 1. The operation process can be summarized as follows: (1) Numerical analysis of the entire construction area is carried out using three-dimensional finite element method (3D FEM) before the construction of geotechnical engineering. Area of small changes due to construction disturbance (Small Changes Area), large changes due to construction disturbance and priority protected area (Priority Protected Area) are respectively defined as the general construction area (General Area), the critical construction area (Critical Area) according to the calculation results. (2) Stage one of construction (Stage *1*), the control parameters of the structure body and surrounding environment in General Area are monitored remotely in real time and the isolated discrete monitoring data (Discrete Data) is obtained using real-time monitoring module based on conventional sensors (CSRM Module). Meanwhile, the control parameters of the structure body and surrounding environment in Critical Area are monitored remotely in real time and the relatively continuous point cloud data (Cloud Data) is acquired quickly and
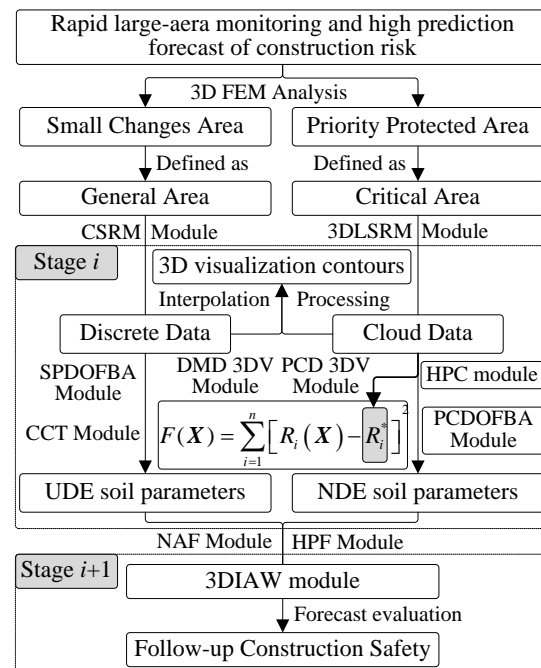
Figure 1 Flowchart of rapid large-area monitoring and high prediction forecast of construction risk of geotechnical engineering based on 3D Laser Scanning

widely using real-time monitoring module based on 3D laser scanning (3DLSRM Module). (3) Stage *1*, further, the collected Discrete Data in General Area is spatially interpolated using 3D visualization module based on isolated discrete monitoring data (DMD 3DV Module) and the collected Cloud Data in Critical is processed using 3D visualization module based on relatively continuous point cloud data (PCD 3DV Module) to achieve 3D visualization contours of monitoring data. (4) Stage *1*, still further, the back analysis and calculation of General Area is conducted using the conventional computing technology module (CCT module) and back analysis module based on single point data objective function (SPDOFBA Module). Afterwards, the uniform distributed equivalent soil parameters (UDE Soil Parameters) in General Area are well identified. Meanwhile, the back analysis and calculation of Critical Area is conducted using the high performance computing module (HPC Module) and back analysis module based on point cloud data objective function (PCDOFBA Module). Following, the non-uniform distributed equivalent soil parameters (UDE Soil Parameters) in Critical Area are also well identified. (5) Numerical analysis of General Area is carried out using numerical analysis and forecasting module (NAF Module) to predict the deflections of the structure body and surrounding environment in General Area during the later stage (Stage *2*). In addition, numerical analysis of Critical Area is carried out using high precision forecasting module (HPF Module) to predict the deflections of the structure body and surrounding environment in Critical Area during the later stage (Stage *2*). (6) The changes of entire construction area during Stage *2* are forecasted, the data is displayed in the form of 3D contours and the system can automatically alert when the data of certain areas exceeds a set value using 3D imagery automatic warning module (3DIAW Module) in order to ensure the entire construction area safety during Stage *2*. (7) Similarly, the back analysis and calculation during Stage *2* to *i* is conducted according to the above step (2) to (4). 3D FEM analysis and prediction calculation during Stage *3* to *i*+1 is conducted according to the above step (5) to (6). Thus, the monitoring and forecasting of geotechnical construction is carried out to ensure the safety of construction throughout the construction period.

Compared with the traditional method of feedback analysis, it can be seen that the biggest difference between the proposed method and traditional method are the objective function of back analysis $F(X)$ and computing technology as shown in Figure 1 (X is the vector of input soil parameters and $R_i(X)$ is the simulated result). That is, observed result R_i^* of $F(X)$ employing relatively continuous point cloud data obtained from the 3D laser scanning is adopt to improve the accuracy of prediction. The high performance computing technology which dramatically reduces the computational time is used to run numerical analysis.

A new idea of efficient, secure and automated construction in geotechnical engineering is presented based on digital fabrication technology. For instance, a digital fabrication technology of generating 3D full-scale structures of excavations directly in rapid hardening ultra-high performance concrete using 3D printing is proposed as illustrated in Figure 2. It shows that the specific technical route of the digital fabrication technology includes printing material, printing equipment, control technology and printing process. As we known, a high strength in compression, flexure tensile bond and low

(a) Printing material   (b) Printing equipment

(c) Control Technology   (d) Printing process
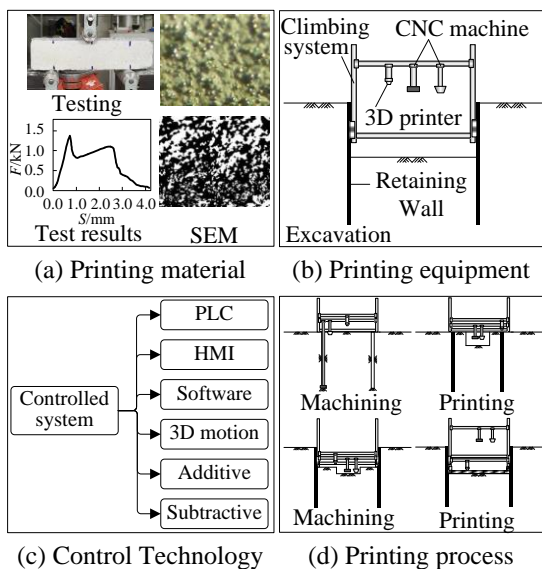
Figure 2 Digital fabrication technology of generating 3D structures of geotechnical engineering directly in rapid hardening ultra-high performance concrete using 3D

shrinkage as the freeform components are built without formwork is the main target in developing the printing material. A high performance printing concrete, such as the use of 3D printed fibers for the flexural reinforcement of a cement mortar developed by Farina et al, has the potential for wide applications in future geotechnical engineering structures. A new full-scale printing equipment of excavations, involving 3D printer, CNC machine and climbing system, is developed based on the additive and subtractive manufacturing. A control technology of 3D printing which consists of PLC (Programmable Logic Controller), HMI (Human Machine Interface), Software, 3D motion controllers, additive controllers, subtractive controllers, and other control systems is presented. Other control systems of 3D printing, including intelligent feedback system, monitoring and management system, etc., are the development direction. A printing process, including excavation of soil layer using CNC machine, construction of concrete layer using 3D printer and lifting of 3D printer using climbing system, is established while we only need to use 3D printer to construction of concrete layer in superstructure construction. The application of the digital fabrication technology in geotechnical construction may shorten the development cycle, reduce the production cost, and improve productivity.

CONCLUSIONS

1. A new system for rapid monitoring and high prediction forecast of construction risk of geotechnical engineering based on 3D Laser Scanning is developed to solve the problem of low computational efficiency and reliability prediction using the traditional method of feedback analysis. It is necessary to take seven major steps for the process of monitoring and forecasting using the developed system. Compared with the traditional method of feedback analysis, it is a great difference that the observed result R_i^* of $F(X)$ employing relatively continuous point cloud data obtained from the 3D laser scanning and the high performance computing technology are adopted in the proposed method.

2. A digital fabrication technology of generating 3D full-scale structures of excavations directly in rapid hardening ultra-high performance concrete using 3D printing is proposed. The specific technical route of the digital fabrication technology, including printing material, printing equipment, control technology and printing process is presented. A new full-scale printing equipment of excavations combined with 3D printing and CNC machining and the relevant construction technology are mainly discussed based on our previous research results. Perhaps the technology transfer from research to practice is very challenging, and is likely to be so for many years. However, the proposed basic technical framework of geotechnical construction using 3D printing in this study provides a new idea of geotechnical sustainability and makes it possible for wide applications in future geotechnical engineering structures. Furthermore, it may shorten the development cycle, reduce the production cost, and improve productivity.

ACKNOWLEDGEMENTS

REFERENCES

Simpson B., Tatsuoka F. (2008). "Geotechnics: the next 60 years." *Geotechnique*, Vol. 58, pp. 357-368.

Hanaor D. A. H., Gan Y., Revay M., et al. (2016). "3D printable geomaterials." *Geotechnique*, Vol. 66, pp. 323-332.

Sass, L. (2007). "Synthesis of design production with integrated digital fabrication." *Automation in Construction*, *No. 16*, pp. 298-310.

Gibbons, G. B., Williams R., Purnell P., Farahi E. (2010). "3D Printing of cement composites." *Advances in Applied Ceramics*, *Vol. 109*, pp. 287-290.

Bartlett, N. W., Tolley M. T., Overvelde J. T. B., et al. (2015). "A 3D-printed, functionally graded soft robot powered by combustion." *Science*, *Vol. 349*, pp. 161-165.

Farina, I., Fabbrocino F., Carpentieri G., et al. (2016). "On the reinforcement of cement mortars through 3D printed polymeric and metallic fibers." *Composites Part B*, *No. 90*, pp. 76-85.

Le, T. T., Austin S. A., Lim R. A., et al. (2012). "Hardened properties of high-performance printing concrete." *Cement and Concrete Research B*, *No. 42*, pp. 558-566.

Lloret, E., Lloret A. R., Lloret M., et al. (2015). "Complex concrete structures Merging existing casting techniques with digital fabrication." *Computer-Aided Design*, *No. 60*, pp. 40-49.